JUSTUS-LIEBIG-UNIVERSITÄT GIESSEN

AG BRINKMANN

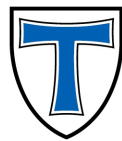

DISSERTATION

Series Testing, Quality Analysis and Implementation of Silicon Strip Sensor Parameters in $\overline{\text{P}}$ANDA's Slow-Control System

Serientests, Qualitätsanalyse und Implementierung der Silizium-Streifensensorparameter in das Slow-Control Steuerungssystem von $\overline{\text{P}}$ANDA

Nils Tröll

Supervisor: Prof. Dr. Kai-Thomas BRINKMANN

1st Reviewer: Prof. Dr. Kai-Thomas BRINKMANN
2nd Reviewer: Prof. Dr. Markus H. THOMA

Abstract

The $\overline{\mathrm{P}}$ANDA (antiProton ANnihilation at DArmstadt) experiment aims to investigate the strong interaction using an antiproton beam and a stationary cluster jet target, resulting in annihilation reactions. The Micro-Vertex Detector (MVD) is the innermost detector among $\overline{\mathrm{P}}$ANDA's sub-detectors and is positioned closest to the interaction point. It is designed for precise vertex and tracking detection, employing double-sided silicon strip and silicon pixel detectors. In conjunction with other sub-detector systems, $\overline{\mathrm{P}}$ANDA is capable of particle tracking, identification, and calorimetry. In addition to $\overline{\mathrm{P}}$ANDA, further applications of the MVD as well as the use of silicon strip sensors in different configurations are being discussed.

The double-sided silicon strip detectors allow high-precision spatial resolution, but require stringent compliance with specifications. Sensor characterization and detailed quality checks are conducted, including irradiation with protons at the Marburg Ion Beam Therapy Center (MIT) to assess radiation damage. The signal behavior of the sensors is investigated during the development of amplification stages and prepared for a sub-experiment for dosimetry on a femto satellite in Low Earth Orbit (LEO).

For the sensor readout in the MVD, an ASIC named ToASt (Torino Amplifier for Silicon Strip Detectors) was developed at INFN Turin and was connected to the sensors for the first time via wire bonding. The ASIC offers the advantage of determining both the event time stamp and the energy deposited in the sensor using the Time-over-Threshold and Time-of-Arrival methods. Combining the ToASt-Sensor combination with the MDC (Module Data Concentrator) ASIC developed at KIT forms the first fully functional detector module. A combination of two of these modules was tested at the proton beam of the COSY facility in Jülich. Data obtained from beam tests and laboratory tests with sources are analyzed to demonstrate the functionality of the prototype and perform characterization. Important data have been collected to enable the development of the second prototype and to advance the construction and functionality of the MVD.

Zusammenfassung

Das Experiment $\overline{\text{P}}$ANDA (antiProton ANnihilation at DArmstadt) zielt darauf ab, die starke Wechselwirkung durch die Untersuchung von Annihilationsreaktionen mittels eines Antiprotonenstrahls und eines stationären Clusterstrahlziels zu erforschen. Der Mikro-Vertex-Detektor (MVD) ist der innerste Detektor im $\overline{\text{P}}$ANDA-Detektorsystem und befindet sich am nächsten zum Wechselwirkungspunkt. Er wurde für die präzise Bestimmung von Vertex- und Spurinformationen konzipiert und verwendet hierfür doppelseitige Siliziumstreifen- und Siliziumpixel-Detektoren. In Kombination mit anderen Subdetektoren ermöglicht $\overline{\text{P}}$ANDA die Teilchenspuren zu rekonstruieren, Teilchen zu identifizieren und deren Energie zu messen. Zusätzlich zum Einsatz im $\overline{\text{P}}$ANDA-Experiment werden weitere potenzielle Anwendungen des MVD sowie die Nutzung von Siliziumstreifensensoren in verschiedenen Konfigurationen diskutiert.

Die doppelseitigen Siliziumstreifendetektoren bieten eine hohe räumliche Auflösung, was jedoch eine strikte Einhaltung der Spezifikationen erfordert. Die Sensoren werden charakterisiert und einer detaillierten Qualitätsprüfung unterzogen, einschließlich einer Bestrahlung mit Protonen am Marburger Ionenstrahl-Therapiezentrum (MIT), um Strahlenschäden zu bewerten. Während der Entwicklung von Verstärkerstufen wird das Signalverhalten der Sensoren untersucht und für ein Subexperiment zur Dosimetrie an einem Femtosatelliten in niedriger Erdumlaufbahn (LEO) vorbereitet.

Für die Auslese der Sensoren im MVD wurde ein spezieller ASIC, der ToASt (Torino Amplifier for Silicon Strip Detectors), am INFN Turin entwickelt und erstmals mittels Drahtbonding mit den Sensoren verbunden. Der ASIC bietet den Vorteil, sowohl den Ereigniszeitstempel als auch die im Sensor deponierte Energie mithilfe der Time-over-Threshold- und Time-of-Arrival-Methoden zu bestimmen. Die Kombination des ToASt-Sensors mit dem am KIT entwickelten MDC (Module Data Concentrator)-ASIC bildet das erste vollständig funktionstüchtige Detektormodul. Zwei dieser Module wurden am Protonenstrahl der COSY-Anlage in Jülich getestet. Die bei Strahlentests und Labortests mit Strahlungsquellen gewonnenen Daten wurden analysiert, um die Funktionalität des Prototyps zu demonstrieren und eine eingehende Charakterisierung vorzunehmen. Diese wichtigen Daten bilden die Grundlage für die Entwicklung des zweiten Prototyps und den weiteren Fortschritt beim Bau und der Optimierung der Funktionalität des MVD.

Contents

1 Introduction **7**

2 The $\overline{\text{P}}$ANDA Experiment **9**
2.1 The $\overline{\text{P}}$ANDA Experiment at FAIR 9
2.2 Facility for Anti-Proton and Ion Research 10
2.2.1 The High Energy Storage Ring 11
2.3 The $\overline{\text{P}}$ANDA Detector 14
2.3.1 The Target Systems 14
2.4 Detector Systems at $\overline{\text{P}}$ANDA 16
2.4.1 Tracking System 16
2.4.2 Particle Identification Detector (PID) 17
2.4.3 Electromagnetic Calorimetry 18
2.4.4 The Magnet System 19

3 Further Possible Uses for the MVD **20**
3.1 The MVD at ELSA 20
3.1.1 BGO-Ball 21
3.1.2 Crystal Barrel and TAPS 22
3.2 Silicon Detectors for Ion Therapy 23

4 Micro Vertex Detector **24**
4.0.1 Silicon Strip Part 25
4.1 Theoretical Overview 28
4.1.1 The Standard Model of Particle Physics 28
4.1.2 The Strong Interaction 28
4.1.3 Charmonium 29
4.1.4 Glueballs 30
4.2 Introduction to Semiconductor Physics 31
4.2.1 Doping of Silicon 34
4.2.2 P-N Junction: Introduction and Basic Concepts 37
4.3 Interaction of Particle's with Matter 41
4.3.1 Energy Loss in $\overline{\text{P}}$ANDA-Sensors 43
4.3.2 Landau Distribution 44
4.4 Radiation Damage 45
4.4.1 The NIEL Theorem 47
4.4.2 Effects on Detector Properties 48

4.4.3 Thermal Annealing 49
4.4.4 Strontium-90 51
4.5 Surface Defects 52

5 Characterization of $\overline{\text{P}}$ANDA Double-Sided Silicon Strip Sensors 53
5.1 Measurement Setup 54
5.1.1 Diode Measurement Setup and Accuracy of Measurements . 58
5.1.2 Verification of Depletion Voltage 62
5.1.3 Setup of Sensor Measurements 64
5.1.4 $\overline{\text{P}}$ANDA MVD Silicon Strip Sensors 66
5.1.5 Structure of the $\overline{\text{P}}$ANDA Strip Sensors 68
5.1.6 Working Principle of Si-Strip-Sensors 70
5.2 Sensor Characteristics 71
5.2.1 Sensor/Diode Capacitance and Depletion Voltage 71
5.2.2 Leakage Current 74
5.3 Sensor Measurement Methods 76
5.4 Diode Measurements 78
5.4.1 Diode Series Measurements 78
5.5 Evaluation of Radiation Hardness of $\overline{\text{P}}$ANDA Wafer Test Diodes 88
5.5.1 Irradiation with Neutrons 89
5.5.2 Irradiation Setup with Neutrons - Upgraded Configuration . 91
5.5.3 MIT-Irradiation 96
5.5.4 MIT-Irradiation II 98
5.5.5 Thermal Annealing 104

6 Dosimetry with $\overline{\text{P}}$ANDA Diodes 108
6.1 Introduction and Ambasat 109
6.2 First Iteration 109
6.2.1 Transimpedance Amplifier 110
6.2.2 Setup 111
6.2.3 First Iteration Measurements 112
6.3 Second Iteration PCB 115
6.3.1 Second Iteration Measurements 118
6.3.2 Energy Calibration 120
6.4 Third Iteration all in one PCB 123
6.4.1 Conclusion Dosimetry with $\overline{\text{P}}$ANDA Diodes 128

7 MVD-Protoype 129
7.1 Mounting $\overline{\text{P}}$ANDA Sensors to the ToASt-ASIC 129
7.1.1 Torino Amplifier for Silicon Strip Detectors 129
7.1.2 First Mounting 130
7.2 Prototype Setup 139
7.2.1 Data Acquisition 139
7.2.2 Beam Time Setup 140

7.2.3 Hit Clustering . . . 143
7.2.4 Correlation of Clock Cycle Time . . . 146
7.3 COSY Beam Times . . . 152
7.3.1 Beam Time I . . . 152
7.3.2 Beam Time II . . . 153
7.3.3 Measurements Beam Time II . . . 153
7.3.4 Beam Time III . . . 157
7.3.5 Beam Time III Measurements . . . 158
7.3.6 Leakage Current during Beam Time . . . 167
7.3.7 Comparison of Beam times . . . 168
7.3.8 Change of ToASt Parameters . . . 169
7.3.9 Conclusion of Beam Time Measurements . . . 174
7.4 Prototype Testing under Controlled Conditions . . . 175
7.4.1 Measurement Setup . . . 175
7.4.2 Measurements . . . 176
7.4.3 Distribution of Strontium-90 Measurements . . . 185

8 Summary **192**

Bibliography **195**

A Detailed Tables of Series Measurements **216**

B S2 Sensor Properties **222**

C Additional Plots **224**

D Circuit Diagrams **227**

Chapter 1

Introduction

The Micro-Vertex-Detector (MVD) of the $\overline{\text{P}}$ANDA experiment aims to spatially resolve particle tracks resulting from antiproton-proton ($\overline{p}p$) collisions, thereby providing insights into the strong interaction within the energy range of quarks and hadrons. Planned for the future accelerator complex Facility for Anti-proton and Ion Research (FAIR), the $\overline{\text{P}}$ANDA detector complex will facilitate research on $\overline{p}p$ collisions with momenta ranging from 1.5 GeV/c to 15 GeV/c, at interaction rates of up to 20 MHz.

Operating at room temperature, the MVD is an independent detector capable of spatially identifying fast, charged particles and energetically classifying them through a magnetic field. Its compact design and high radiation tolerance enable a variety of applications beyond the main $\overline{\text{P}}$ANDA experiment, including beam profile analysis in medical accelerators or particle reconstructions in other accelerator experiments.
This thesis aims to verify the sensors for integration into the MVD and to integrate the sensors into the Slow Control system. To achieve this, the following milestones were established.

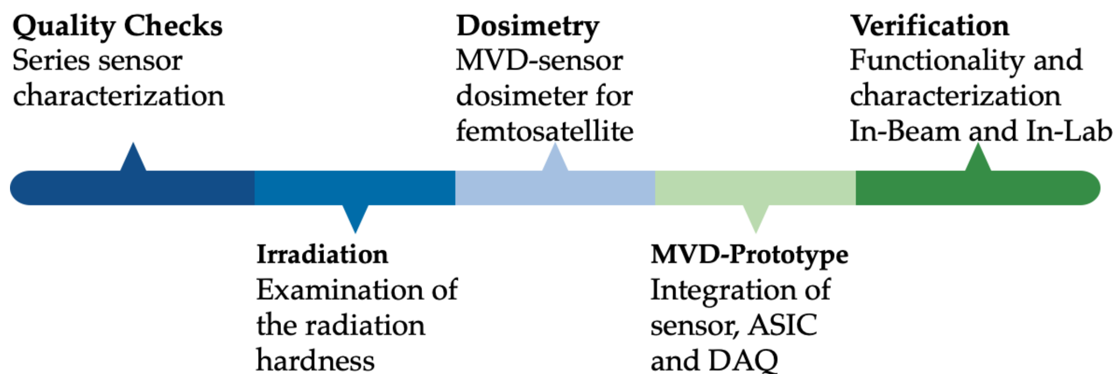

In this work, sensor test structures as well as full-size sensors are characterized based on their electrical properties. Measurement and fitting methods are developed to conduct series tests for verifying the sensor parameters. These quality checks are performed for all sensors, confirming the components for integration.

The radiation hardness of the test structures is investigated using neutron irradiation and at multiple beam times with proton beams. Additionally, the method of annealing is applied and verified.

In a sub-experiment, the test structures are used to establish a dosimetry concept, including understanding the signal behavior of the silicon detectors. Signals are read out by a micro controller after the sensor signals have been processed by amplifier stages and readout techniques. The final concept, based on a femto satellite, aims to conduct dosimetry in space in the future.

Sensors are connected for the first time with the Torino Amplifier for Silicon Strip Detectors (ToASt)-ASIC. Selected sensors are bonded with the ASIC developed for the MVD using wire bonding, demonstrating functionality through irradiation with a source.

An MVD-Prototype is developed with the Sensor-ToASt configuration and with the MVD-DAQ. The prototype is tested for functionality during three beam times at COSY in Jülich and in the laboratory with various sources. The obtained data is analyzed using various developed algorithms to characterize the prototype and identify issues for further iterations.

Chapter 2

The $\overline{\text{P}}$ANDA Experiment

The $\overline{\text{P}}$ANDA (antiProton ANnihilation at DArmstadt) experiment is one of the key projects of the future Facility for Antiproton and Ion Research (FAIR). The large-scale project, currently under construction in Darmstadt, is being built on the premises of the GSI Helmholtz Center for Heavy Ion Research.

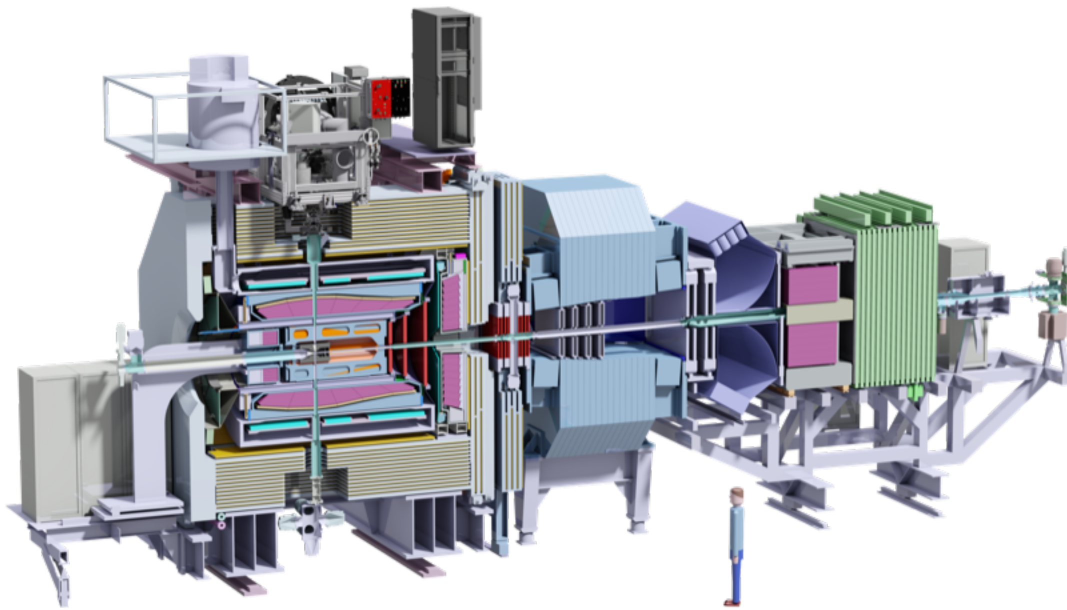

Figure 2.1: A schematic cross-section of the $\overline{\text{P}}$ANDA experiment with all subsystems highlighted [1].

2.1 The $\overline{\text{P}}$ANDA Experiment at FAIR

The existing structures at GSI accelerators are being upgraded and utilized for injection purposes. The $\overline{\text{P}}$ANDA experiment will be integrated into the High Energy Storage Ring (HESR), allowing research on charmonium states, the establishment of gluonic excitations, the study of modifications of meson properties in the nuclear medium, and precision gamma-ray spectroscopy of single and double hypernuclei using proton, antiproton, and ion beams.

2.2 Facility for Anti-Proton and Ion Research

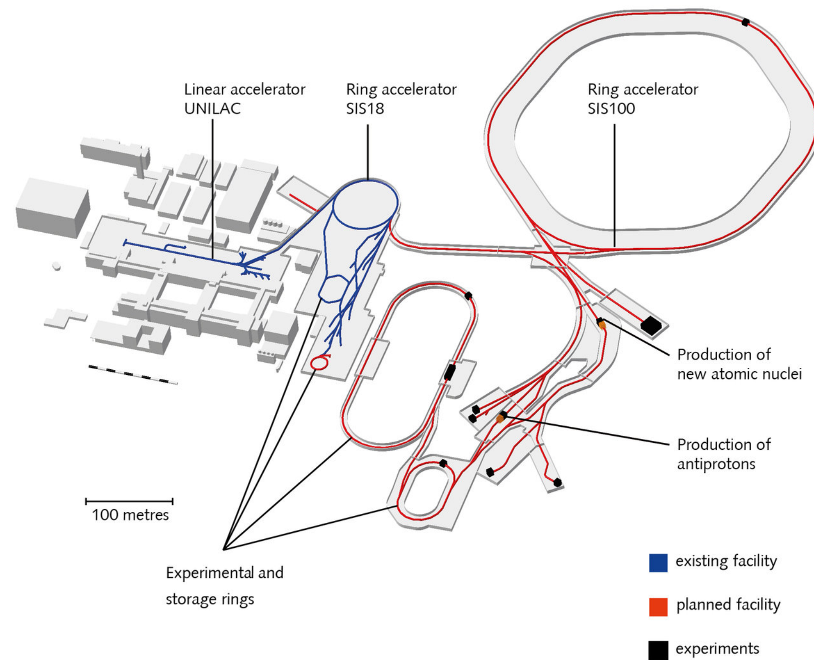

Figure 2.2: The FAIR accelerator facility in red with the existing GSI facility in blue [2].

As illustrated in Figure 2.2, the GSI facility comprises a linear accelerator and a heavy-ion synchrotron (UNILAC and SIS18). In the future, a proton accelerator (p-LINAC) will serve as an injector for the SIS18, which in turn injects particles into the SIS100.
At the heart of the future FAIR facility will be the SIS100 ring accelerator, with a circumference of 1100 meters [2]. The proton and heavy-ion synchrotron will accelerate protons, for example, up to 29 GeV with a maximum intensity of 2.5×10^{13} protons/cycle [3]. Antiprotons will be produced by colliding high-energy protons with a nuclear target [4].
The Collector Ring is planned for storing the beams, reducing the momentum spread through stochastic cooling. In addition, the High Energy Storage Ring (HESR) enables the experiment-specific acceleration of antiprotons. These facilities will serve the four main experiments:

- APPA: Atomic, Plasma Physics and Applications
- CBM: Compressed Baryonic Matter
- NuSTAR: Nuclear Structure, Astrophysics and Reactions
- $\overline{\text{P}}$ANDA: antiProton Annihilation at DArmstadt

The focus will now shift to the $\overline{\text{P}}$ANDA detector, which will conduct research using antiprotons.

2.2.1 The High Energy Storage Ring

The $\overline{\text{P}}$ANDA experiment will be located within the HESR. The HESR will provide the experiment with a highly intense and high-quality antiproton beam with a momentum ranging from 1.5 to 15 GeV/c. The storage ring has a circumference of 575 meters with two straight sections each of 132 meters length [5]. The $\overline{\text{P}}$ANDA experiment is situated in the middle of one of these two straight sections, as depicted in Figure 2.3.

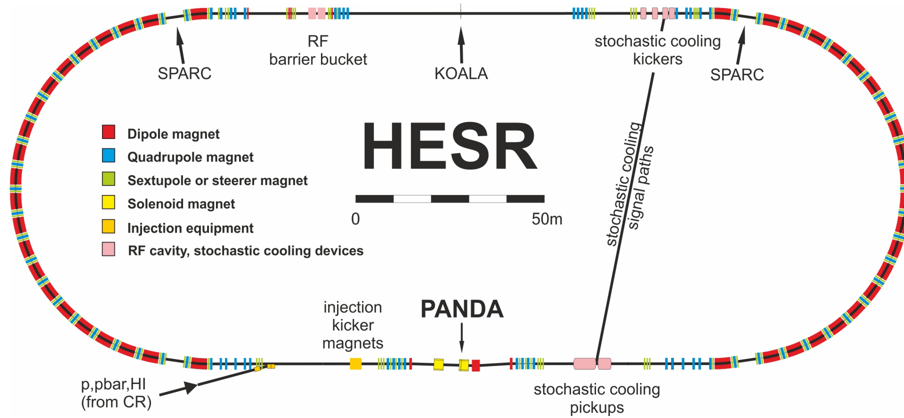

Figure 2.3: Schematic overview of the High Energy Storage Ring (HESR) at FAIR [6].

Opposite to the $\overline{\text{P}}$ANDA experiment lies the electron cooling facility, which can cool the beam to a small momentum spread σ_p/p below $4 \cdot 10^{-5}$ at momenta up to 8.9 GeV/c. Additionally, the beam can be further optimized through stochastic cooling.

The HESR operates in two different modes: high resolution and high luminosity. The high luminosity mode enables the generation of a beam with a luminosity of $2 \cdot 10^{32}\,\text{s}^{-1}\text{cm}^{-2}$ and a resolution of approximately $\sigma_p/p \sim 10^{-4}$. In the high-resolution mode, the beam spread is below $\sigma_p/p \leq 10^{-5}$ with a luminosity of $2 \cdot 10^{31}\,\text{s}^{-1}\text{cm}^{-2}$ [7].

$\overline{\text{P}}$ANDA Physics Program

The $\overline{\text{P}}$ANDA experiment will have unique opportunities during its run time due to the availability of high-intensity, cooled antiproton beams. This enables the investigation of questions in the field of QCD, comprehensive hadron structures, binding mechanisms of quarks in nuclei, and exotic particles. In particular, the realm of non-perturbative QCD can be explored, where quarks form hadrons. The following illustration 2.4 showcases the hadrons that can be generated through proton-antiproton annihilation.

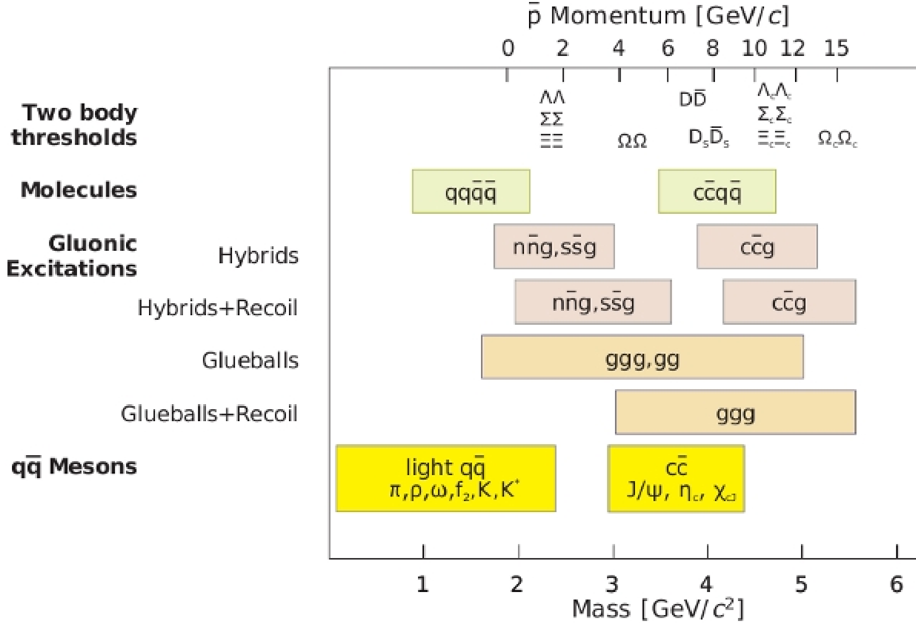

Figure 2.4: Hadrons which can be produced in the $\overline{\text{P}}$ANDA experiment by proton antiproton annihilation [8].

The main research objectives are listed below, to which a theoretical classification will be provided later in Chapter 4.1.

Charmonium Spectroscopy

The $\overline{\text{P}}$ANDA experiment plays a crucial role in researching the charmonium spectrum and surpasses all previous efforts. Charmonium, constituted by charm quarks and anti-charm quarks, provides insights into the non-perturbative and non-relativistic aspects of Quantum Chromodynamics (QCD). Theoretical frameworks such as effective field theories and Lattice QCD (LQCD) have been employed to calculate the charmonium spectrum.
So far, charmonium has primarily been observed in e^+e^- experiments, constrained by the limitations posed by the J^{PC} quantum numbers being restricted to 1^{--}. The broad energy range of $\bar{p}p$ annihilation in the $\overline{\text{P}}$ANDA experiment facilitates the direct generation of charmonium states [9].
The distinctive feature of the $\overline{\text{P}}$ANDA experiment lies in its high luminosity, enabling the measurement of thousands of $\bar{c}c$ states per day. This not only facilitates the measurement of rare states but, in conjunction with improved momentum resolution, also allows for a substantial enhancement in measurement accuracy. Consequently, this setup not only offers a significant improvement in precision but also opens avenues for novel insights. It enables a comprehensive examination of charmonium states based on their quantum mechanical properties, thereby deepening our understanding of non-perturbative QCD phenomena.

Gluonic Exitations

Another intriguing topic opened up by $\overline{\text{P}}$ANDA is the excitation of gluons, which is divided into two main categories. Glueballs are states composed solely of gluons as valence particles to describe the quantum numbers. Hybrids, on the other hand, consist of a quark-antiquark pair and excited gluons. These gluonic hadrons exhibit exotic quantum numbers J^{PC}, facilitating their experimental identification.

Antiproton-proton annihilations provide a favorable environment for the search for gluonic hadrons. In this process, gluonic states can emerge through the strong interaction of quarks and gluons, allowing insights into the structure of Quantum Chromodynamics (QCD).

Hadrons in Nuclear Matter and Hypernuclear Physics

Another research field is hadrons in nuclear matter, as modifications of the hadrons can be induced by the surrounding medium. These studies aim to understand the spontaneous chiral symmetry breaking in QCD and its partial restoration in a hadronic environment, with one effect being the change in hadron mass.

Previous experiments mainly focused on the light quark sector. With the $\overline{\text{P}}$ANDA experiment and its high-intensity (15 GeV/c) antiproton beam, this research can be expanded [10]. Predictions have been made for the modifications of open-charm and charmonium states in the medium, which will be experimentally accessible at the $\overline{\text{P}}$ANDA experiment. This will provide insights into the interactions of quarks and gluons in the dense nuclear medium [11].

Through the antiproton beam and the efficient production of hypernucleons, hypernuclear physics can be further researched, whereby a neutron or proton is replaced by a hyperon. A hyperon is a specific baryon particle that, in addition to the usual up and down quarks, contains a strange quark, distinguishing it from other baryons. This allows gaining insights into nuclear structure and the interaction between hyperons.

Nucleon Structure

The $\overline{\text{P}}$ANDA experiment is expected to play a crucial role in exploring nucleon structure. Particularly, the analysis of antiproton-proton collisions offers outstanding opportunities for $\overline{\text{P}}$ANDA to investigate various aspects such as structure functions and deep inelastic scattering (DIS). Through the examination of interactions and the resulting insights into the distribution of quarks and gluons within nucleons, the $\overline{\text{P}}$ANDA experiment can explore the theoretical framework of Generalized Parton Distributions (GPDs).

Furthermore, electromagnetic processes enable $\overline{\text{P}}$ANDA to gain insights into the structure of nucleons. Electromagnetic form factors, especially in processes like Deeply Virtual Compton Scattering and the antiproton-proton annihilation process $\overline{\text{p}}\text{p} \rightarrow e^+e^-$, can be determined.

2.3 The $\overline{\text{P}}$ANDA Detector

The $\overline{\text{P}}$ANDA experiment serves as a versatile detector, capable of identifying a diverse array of charged and neutral particles across nearly the entire solid angle, employing various subsystems. Key attributes of the detector system include high-resolution tracking and calorimetry for a variety of particles, at a broad momentum range and high average interaction rates of up to 20 MHz. In addition, the adaptability of the detector setup is of crucial importance in order to enable a wide range of physical experiments.

To fulfill these requirements, the experiment employs two distinctive magnetic spectrometers: one situated in the barrel section, referred to as the target spectrometer, and another in the forward section named the forward spectrometer. The target spectrometer emphasizes measurements of particles with large polar angles and relatively small momenta, employing a solenoid magnet to surround the interaction point.
In contrast, the forward spectrometer is tailored for measurements involving small polar angles and large momenta. To optimize particle measurements in this configuration, a superconducting dipole magnet is employed.

2.3.1 The Target Systems

The $\overline{\text{P}}$ANDA detector incorporates mainly two distinct target systems, tailored to specific experimental needs. A primary focus lies on collisions between the antiproton beam and protons. The choice of targets, and consequently the precise interaction point, is critical for achieving high measurement accuracy. The following briefly outlines the two systems, with a more in-depth examination available in [12] and [13].

The Cluster Target for $\overline{\text{P}}$ANDA

The cluster-jet target is composed of a convergent-divergent Laval-type nozzle with a micron-sized throat leading to the vacuum. In this technique, hydrogen gas is typically directed through the nozzle, resulting in the adiabatic cooling of the gas and the generation of a supersonic beam of clusters. The clusters form through the condensation of nano particles, depending on the gas used. There are extensive options for varying the cluster formation, e.g. through properties such as pressure or gas temperature, which can be adjusted as required. Typical cluster

sizes range from 10^3 to 10^5 atoms per cluster. This allows for achieving a target thickness of $>1 \cdot 10^{15}$ atoms/cm^2 in a continuous beam [13].

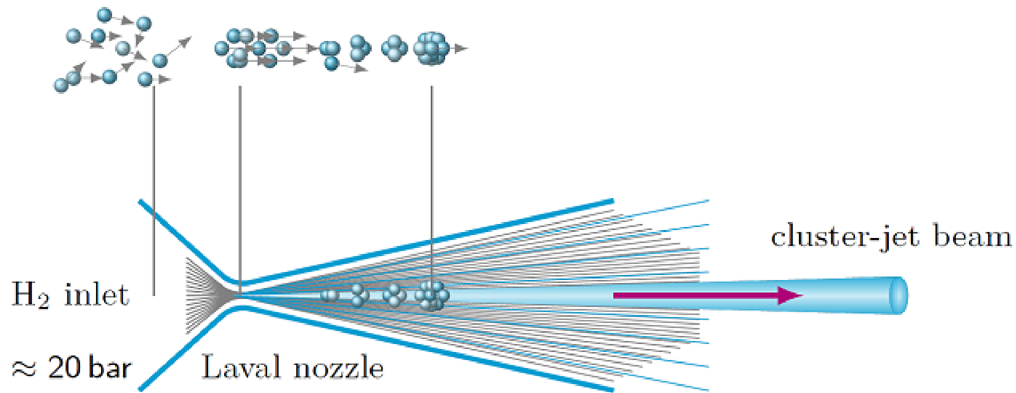

Figure 2.5: Sketch of the cluster-jet target production[14].

Crucial for a target is to possess a homogeneous volume density distribution, a sharp boundary, and a constant angular divergence. To achieve this, collimators are used to focus the cluster stream to a cluster size in nm to µm range. The main drawback of Cluster jets is their lateral spread, leading to uncertainty in the interaction points along the beam axis. The target stream diameter in the experiment is expected to be approximately 4 mm×12 mm [12].

The Pellet Target for $\overline{\text{P}}$ANDA

The Pellet Target system consists of a nozzle that injects a stream of frozen hydrogen micro spheres, referred to as pellets, vertically to the accelerator beam. Through a piezo element, the continuous stream is divided into small droplets. The pellet size depends on the nozzle diameter and can be adjusted accordingly, with typical sizes of 20 µm and 40 µm [15]. The pellets traverse the target within a thin tube, where the temperature of the stream further decreases until it forms frozen pellets. The trajectory of the pellets through the target system and the MVD, as well as the interaction point, can be observed in Figure 4.1. The stream exhibits low angular divergence, leading to a positional uncertainty at the interaction point of approximately ±1 mm [10]. The stream of pellets has a transverse size of less than 3 mm and an average distance between pellets of about 2-20 mm.

In comparison to the Cluster-jet, the Pellet Target System can achieve higher average areal densities of up to $5{\cdot}10^{15}$ atoms/cm^2 [13]. Additionally, the exact position of the pellets can be determined through optical systems, providing additional information about the interaction point.

2.4 Detector Systems at $\overline{\text{P}}$ANDA

2.4.1 Tracking System

The tracking system of the $\overline{\text{P}}$ANDA experiment will operate in two different magnetic fields, which will be further explained in section 2.4.4. To fulfill the complete solid angle with a high resolution, four different tracking systems and a luminosity detector are foreseen.

Micro Vertex Detector

The MVD will be the closest detector to the primary interaction vertex. Double-sided silicon strip detectors are arranged in two layers to track charged particles. The detector consists of a barrel section with rectangular sensors and a forward disk section with trapezoidal sensors. The MVD is explained in detail in Chapter 4.

Straw Tube Tracker (STT)

The STT consists of gas-filled cylindrical drift tubes with a length of 150 cm, arranged around the beam axis, as shown in Figure 2.6 [16]. When charged particles pass through the detector, the gas will be ionized. Due to the high voltage of several kV between the cathode wall and the anode wire, the free electrons are accelerated towards the anode and can be measured. From the drift time of the electrons, which is approximately 1000 times faster than that of the ions, the position of the particle can be determined.

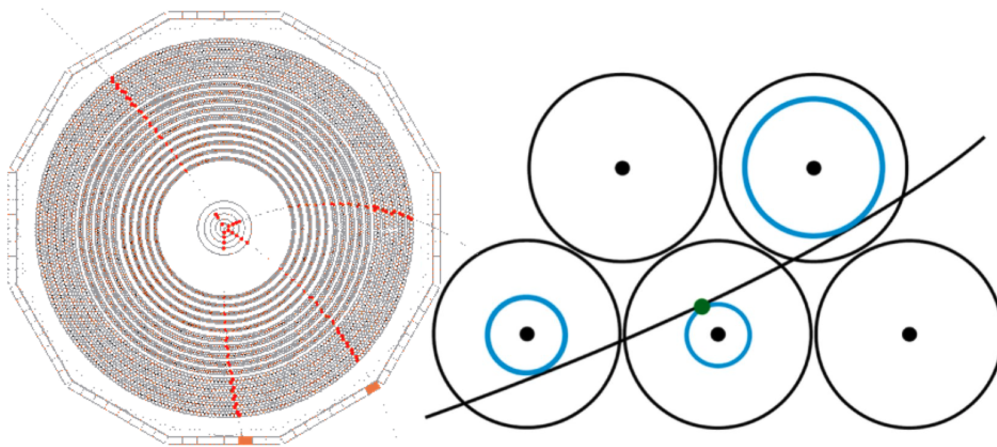

Figure 2.6: The $\overline{\text{P}}$ANDA Straw Tube Tracker is depicted on the left, with its operation principle outlined on the right [17],[18].

Gas Electron Multiplier Tracker (GEM)

The GEM tracker is utilized as the primary forward tracking detector and comprises multiple large-area planar gaseous electron multipliers. Due to the high

number of projections per detector layer, the position of the particle track can be determined.

Forward Tracker

Like the STT, the Forward Tracker consists of a composition of straw tubes. In total, six layers of different sizes are planned, each positioned between other subdetectors. This setup enables the determination of the particle trajectory, allowing for the measurement of the momentum of charged particles due to the magnetic field.

Luminosity Detector

The Luminosity Detector (LMD) is located approximately 11 m behind the interaction point (IP), making it the detector furthest downstream. The purpose of the LMD is to determine the interaction rate of antiprotons by employing elastic scattering of antiprotons with protons. High Voltage Monolithic Active Pixel Sensors (HV-MAPS) are used to determine both the absolute and relative luminosity.

2.4.2 Particle Identification Detector (PID)

As the name suggests, the PID is a detector complex designed to determine the nature of particles with high precision. This enables the experiment to distinguish between electrons, muons, pions, kaons, protons, and other charged particles by combining information from the detectors.

Detection of Internally Reflected Cherenkov light (DIRC)

The DIRC detector comprises a barrel section that surrounds the interaction point and an end-cap disk positioned downstream from the interaction point along the beam direction. A schematic illustration of these configurations is shown in Figure 2.7. This system is employed to measure light emissions generated by charged particles moving at velocities greater than the speed of light within the surrounding medium. The medium used consists of radiator bars or plates made of synthetic fused silica. Utilizing the characteristic Cherenkov light pattern, an analysis for particle identification can be conducted.

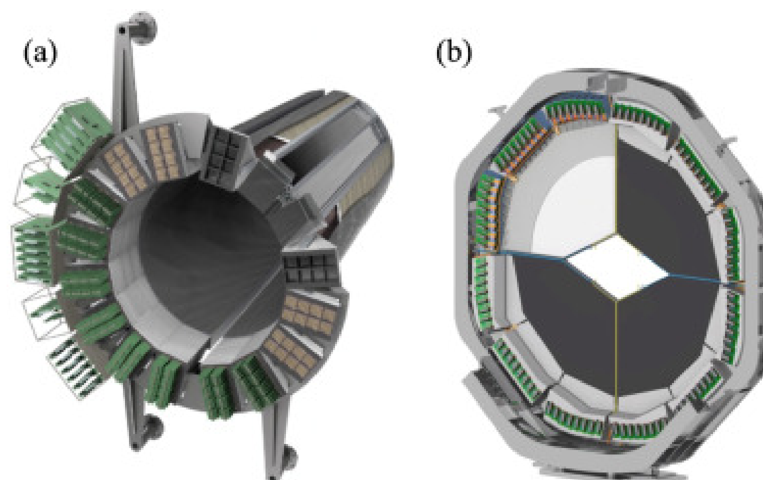

Figure 2.7: Schematic layout of the Barrel DIRC (a) and Endcap Disc DIRC (b) [19].

Time of Flight Detectors

Using the Time of Flight (TOF) method, slow particles with large polar angles can be identified. The setup relies on an arrangement of scintillators and is intended to be positioned directly in front of the DIRC endcap.

Muon Detection System

Muon detection is achieved using Mini Drift Tubes with wire readout and orthogonal cathode strips. Approximately 4200 tubes are planned, surrounded by the iron magnet yoke, to distinguish muons from pion backgrounds and to register neutrons [20].

Ring Imaging Cherenkov Counter

The forward RICH Detector performs particle identification (PID) similar to the DIRC detectors by utilizing the Cherenkov effect. In contrast to the DIRC, the RICH is a component of the Forward Spectrometer.

2.4.3 Electromagnetic Calorimetry

The Electromagnetic Calorimeter (EMC) is composed of second-generation lead tungstate (PWO II) crystals, which serve as scintillators. The arrangement enables almost hermetic coverage down to the beam pipe. This allows for the identification and reconstruction of multi-photon and lepton pairs. As depicted in Figure 2.8, the EMC consists of multiple subsystems, with only the Barrel EMC (blue) and the Forward Endcap EMC (green) shown in the Figure 2.8. The EMC is situated inside the solenoid magnet and encloses the Barrel DIRC, TOF sensors, and tracking systems such as the MVD.

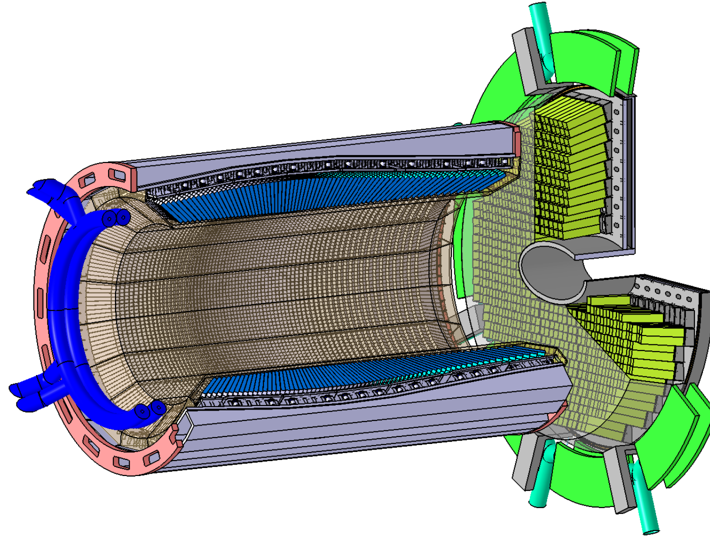

Figure 2.8: Schematic layout of the Barrel EMC in blue and the Backward Endcap EMC in green [21].

Barrel EMC

The Barrel EMC comprises a total of 11,360 crystals, arranged in 16 slices. All PWO II crystals are oriented towards the interaction point and are individually read out by large Avalanche Photodiodes (APDs).

Forward/Backward Endcap EMC

The Forward Endcap EMC is located in front of the IP with respect to the beam and consists of 3,856 crystals. Due to the dense arrangement of the crystals, they are partially read out using Vacuum Phototriodes (VPTTs).
The Backward Endcap EMC is located behind the IP region and consists of 524 crystals, which, like the Barrel, are read out using APDs [20].

2.4.4 The Magnet System

The magnet system of the $\overline{\text{P}}$ANDA experiment consists of two essential components: the solenoid magnet and the dipole magnet.

The superconducting solenoid magnet will provide a 2 T magnetic field, mainly for the inner volume of the cylinders and therefore also for the barrel detectors, although some shielding effects may occur. The magnet will ensure high homogeneity of $\pm 2\,\%$ in the beam direction.
The dipole magnet, located in front of the forward spectrometer, will exert a force of 2 Tm on particles emerging from the barrel part at low angles. Parts of the forward tracking detector systems will be situated within the dipole magnet.

Chapter 3

Further Possible Uses for the MVD

The Micro-Vertex Detector for $\overline{\text{P}}$ANDA, due to its relatively small size and the ability to operate at room temperature, is a versatile detector system. Thus, it is possible to use the MVD tracking system or parts of the MVD not only alongside $\overline{\text{P}}$ANDA but also exclusively at other locations outside of FAIR. Additionally, beyond fundamental research, it can also cover other fields such as medical physics or even practical applications in medicine. The following sections present several highly interesting possibilities for using the MVD or its sensors outside of FAIR.

3.1 The MVD at ELSA

One potential application for the MVD is at the ELSA (Electron Stretcher Accelerator) facility in Bonn. For instance, hadron physics experiments could be enhanced by incorporating the MVD silicon setup. This would elevate new possibilities for the detector system and take the research to a new level.

By arranging the Injector-LINAC, Booster Synchrotron, and Stretcher Ring, as shown in Figure 3.1, an electron beam with an energy of up to 3.2 GeV can be generated [22].

The accelerator system is currently serving two hadron physics experiments: the Crystal Barrel/TAPS, and the BGO Ball, which are explained in more detail below. It is important to note that both experiments lack a silicon detector tracking system. By expanding the systems with the MVD, the experimental portfolio can be broadened to address new research questions. Specifically, the experiments could better reconstruct the tracks of charged particles and study a wider range of reaction products.
The high resolution allows for more precise measurements of the paths, and thus the energies and momenta, of charged particles, which would enhance the accuracy of ELSA experiments. Adding silicon strip detectors could enable the identification and investigation of rare events with greater precision.

It is noteworthy that ELSA operates in a similar energy range as the Cooler Synchrotron (COSY) in Jülich, where the functionality of the strip detectors has already been demonstrated [23]. Furthermore, in this work, an MVD prototype was characterized and tested for functionality using COSY (Section 7.3). Therefore, it is reasonable to assume that the functionality at ELSA can be ensured.

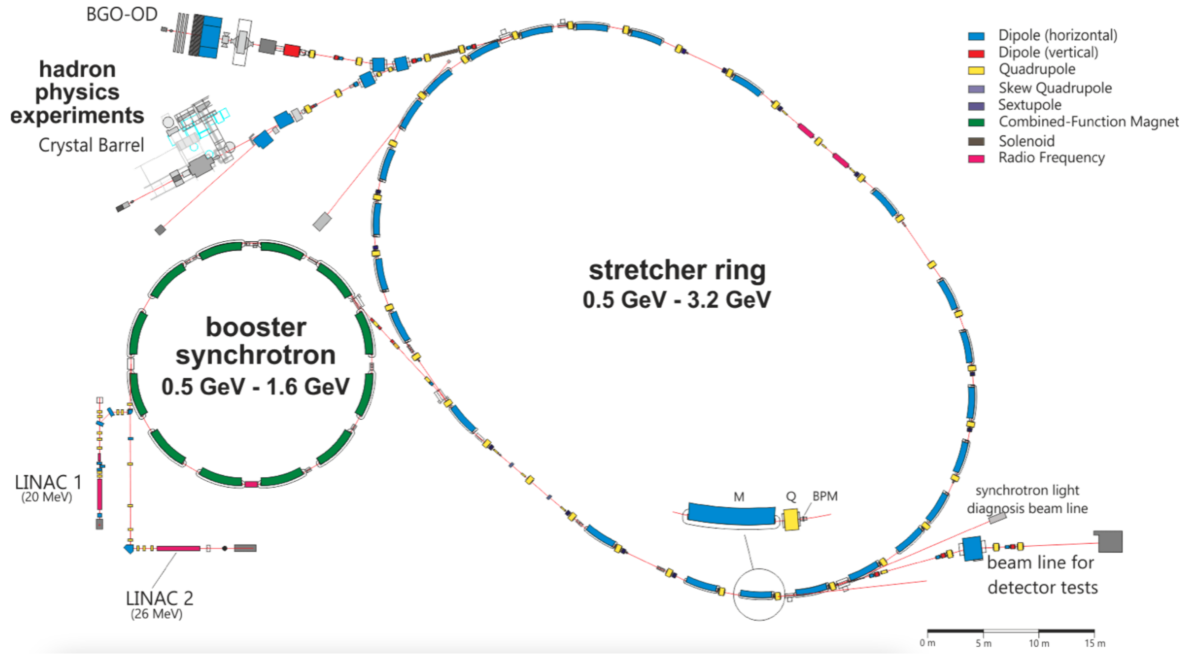

Figure 3.1: Schematic overview of the ELSA facility [24].

3.1.1 BGO-Ball

The BGO experiment comprises a crystal calorimeter and a forward magnetic spectrometer. This arrangement provides the capability to detect both charged and neutral particles. Measurements of non-strange and strange meson photo production reactions are conducted here. To date, baryonic and mesonic states in the strange quark sector have been investigated, with more detailed insights available in references [25], [26], and [27].
The core of the detector system is the "BGO Rugby Ball," as shown in Figure 3.2. This system also originates from a previous setup, the GRAAL experiment at ESRF [29]. The tracking system consists of a multi-wire proportional chamber (MWPC) inside the BGO, between the IP and the scintillators [30]. Here, the MVD could provide a major improvement, as the precision of the double-sided silicon detectors is significantly higher. Moreover, the tracking precision towards the forward spectrometer could be substantially increased by using the MVD-Strip Disc. Combined with the existing BGO scintillators, this would enable more accurate results, thereby elevating the research conducted with the BGO Ball to a new level.

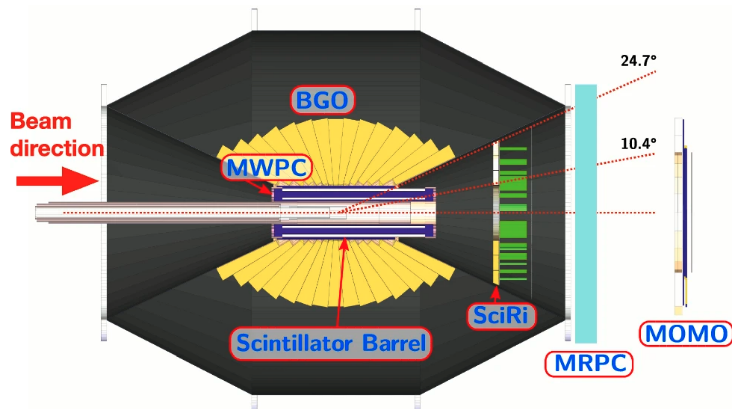

Figure 3.2: Schematic slice view of the BGO Ball Experiment [28].

3.1.2 Crystal Barrel and TAPS

The Crystal Barrel experiment consists of various scintillator arrangements. Similar to the BGO Ball, tracking is performed using MWPC detectors and particle identification through scintillator strips. The primary research areas are baryon spectroscopy and meson photo production to investigate baryonic excitations. As shown in Figure 3.3, the Crystal Barrel has been extended with 528 TAPS BaF2 detector modules, improving the solenoid angle. Together, the calorimeters cover almost the entire solid angle [31].

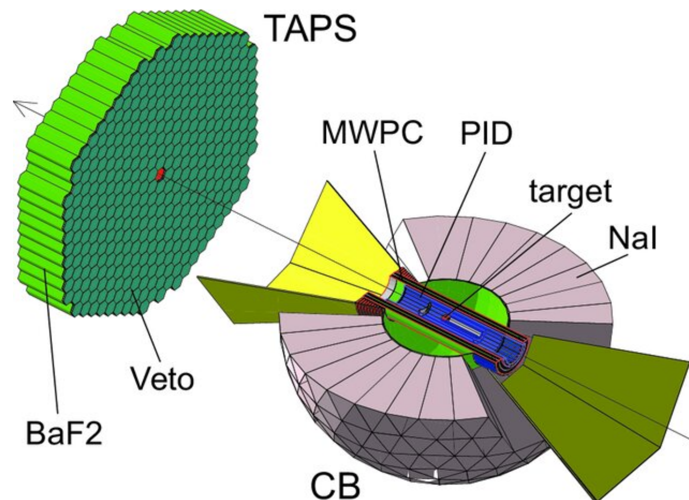

Figure 3.3: Schematic overview of the Crystal Ball/TAPS experiment [32].

Particle identification could be significantly improved using the MVD or MVD sensors, not only through enhanced accuracy but also due to a reduced material budget thanks to the thin silicon layers.

Overall, the incorporation of silicon detectors would greatly enhance the measurement accuracy in the ELSA experiments and significantly lower the material

budget. The MVD detectors would elevate the research conducted at the ELSA accelerator to a new level, thereby facilitating access to new physical insights.

3.2 Silicon Detectors for Ion Therapy

In addition to their applications in fundamental research, silicon detectors can be used as high-precision measuring instruments for ion therapy in medical applications. There are two possible uses. First, one or more arrays of MVD sensors can be used to verify the position and spread of the ion beam. Secondly, an arrangement of sensors can be used to verify the energy of the beam. Both options serve quality analysis for medical ion therapy, significantly increasing precision, especially for imaging.
Moreover, measurements can be conducted during the actual irradiation, allowing for adjustments to be made if necessary. Until now, beam quality has been determined before irradiation using photographic paper and verified with scanning procedures.
For a similar detector, Taylor, Waltham, Price, *et al.* [33] demonstrated the feasibility of the method using a 60 MeV proton beam. Although the protons are not minimally ionizing, the beam could be measured very precisely. In addition to the beam profile, the exciting new imaging method known as proton computed tomography (pCT) is also demonstrated.
An energy measurement for a 290 MeV/u ^{12}C ion beam was conducted by Debrot, Newall, Guatelli, *et al.* [34]. An array of silicon detectors allows the determination of the beam's energy for medical applications. By examining the deposited energy after a certain number of sensors and hence the silicon layer thickness, the Bragg peak and thus the initial energy can be determined.

Access to the "Marburg Ion Beam Therapy Center" and close collaboration could advance research in these areas. The energy range of the methods used in the aforementioned sources falls within the ranges of the MIT, with 48-221 MeV/u for protons and 86-430 MeV/u for carbon ions, making the results comparable. During a conducted beam time, an MVD prototype, explained in Chapter 7, was successfully tested. However, the presentation of the results of these tests is not intended for this work. Furthermore, the portfolio of the MIT and medical ion therapy can be expanded, improved, and secured through the integration of detectors.

For constructing such a measurement system, whether for imaging or energy verification, MVD strip sensors could be utilized. These sensors are available as by-products from the MVD development. For example, as shown in Chapter 5.4.1, the 58 remaining S2 sensors could be re-purposed for this application.

Chapter 4

Micro Vertex Detector

The Micro Vertex Detector (MVD) is one of the key experiments for $\overline{\text{P}}$ANDA, aimed at charged particle tracking. Being the closest detector to the interaction point (IP), the MVD will be the primary source of 3D hit information from primary and secondary vertices. MVDs are well-suited for precise timing measurements and particle tracking, enabling event reconstruction. Consequently, it can provide a time reference point for events even for the outer detectors. The sensors of the MVD are located within the solenoid magnet, allowing inferences on particle momentum and event topology. To meet these measurement conditions, various requirements have been set for the MVD.

Firstly, the MVD must have an optimal detector coverage to cover the entire IP as much as possible. This requires implementing as many detector layers per particle track as possible.

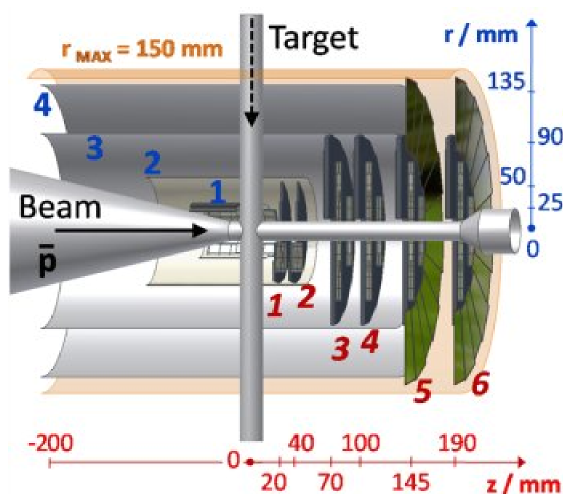

Figure 4.1: Basic layout of the MVD barrel with the pixel and strip detector parts [9].

In Figure 4.1, the original design consisting of four barrel layers and six forward discs is shown. As can be seen, the layers enclose both the antiproton-beam and the target. Not depicted is the Strip disc, which can be seen in Figure 4.2. It was planned that the inner two barrel layers and the forward discs would be equipped with silicon hybrid pixel sensors. However, due to numerous difficulties, the development of the silicon hybrid pixel sensors was abandoned.

Therefore, the further description focuses on the outer two layers of the barrels, which consist of square and rectangular double-sided silicon microstrip detectors,

and the forward disc, which is also of the same sensor type but trapezoidal in shape.
Secondly, the MVD must possess high spatial resolution. A precision of under 100 µm in z-direction (beam direction) and several 10 µm in the xy-plane is required. This precision can be achieved by using sensors with small pitch, which will be discussed later.
Thirdly, the particles to be measured should traverse the MVD with minimal disturbance to ensure the efficiency of the surrounding detectors is not compromised. Therefore, the generation of photons and multiple scattering must be minimized. The goal is to keep the total equivalent material budget of the whole MVD below 10 % of a radiation length in most regions.
Fourthly, a fast readout for high rates must be enabled. Due to the proximity to the IP, high rates are expected, which should be covered by a self-triggered readout. Continuous readout is expected to handle approximately 2×10^7 interactions/s, meaning rates of several kHz per strip and thus MHz per sensor are anticipated.
Fifthly, high radiation tolerance is required to ensure the functionality of the MVD throughout the entire lifetime of $\overline{\text{P}}$ANDA. Therefore, a maximum irradiation of approximately $10^{10}\,n_{eq}/cm^2$ and 100 kGy has been set as the limit for both the sensors and the readout electronics. This would imply a run time of approximately 10 years with a duty cycle of 50 %.

4.0.1 Silicon Strip Part

The following section will provide a detailed discussion of the Silicon Strip Detector part, as previously mentioned, without further elaboration on the Pixel Sensor part. As mentioned earlier, the MVD is divided into layers of silicon detectors, allowing the Barrel part to detect particles with a polar angle between 35 ° and approximately 140 °, depending on the azimuthal angle. The front disc can detect particles with a minimum polar angle of about 3 °. As shown in Figure 4.2, the barrel part, depicted in the left and middle sketches, consists of two layers of double-sided silicon strip sensors spaced 25 mm apart. Similarly, the disc part, illustrated in the right sketch, also comprises two layers.

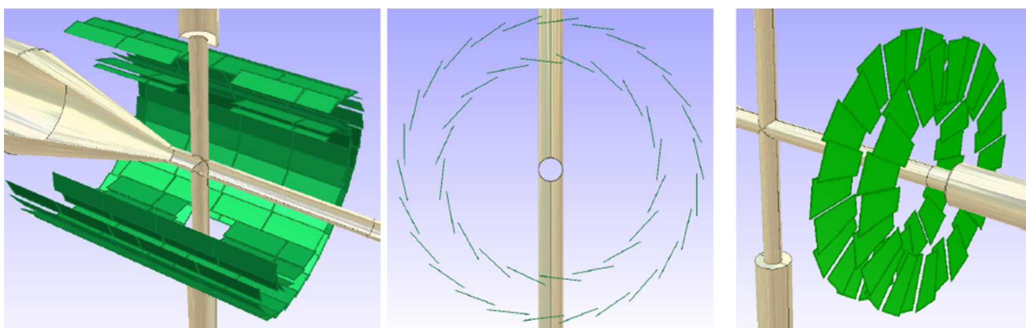

Figure 4.2: Schematic layout of the silicon strip sensors in the barrel part of the MVD from the side (left), from the front (middle), and the sensor arrangement of the strip disc (right) [35].

In total, the MVD will incorporate 248 double-sided silicon detectors in the barrel part and 48 in the disc part. These sensors will be mounted on staves made of carbon fiber, which are equipped with a cooling pipe since the Front-End chips will also be attached to the staves. The operating temperature has been set to room temperature, meaning the temperature of the cooling fluid will be approximately 16 °C. Each stave carries two square and four larger rectangular sensors, all of which are inclined at a certain angle towards the IP with their active surface. The trapezoidal sensors are held in pairs behind each other by a support frame. As a result, the readout chips must be attached to the frame at a 90 ° angle, which is made possible by using flex PCBs.

The sensors are read out using custom-designed front-end chips, the **To**rino **A**mplifier for silicon **St**rip detectors (ToASt) chips, which are further explained in Chapter 7.1.1. Each of these chips allows the readout of 64 strips. As depicted in Figure 4.3, eight ToASt chips are required for reading out both the front and back sides of the smallest sensor with 512×512 strips. This is due to the fact that only every second strip will be contacted in the final MVD, as explained in more detail in Subsection 4.0.1. As a result, 11 chips are needed for reading out the larger rectangular sensor, and 12 chips are required for the trapezoidal sensor.

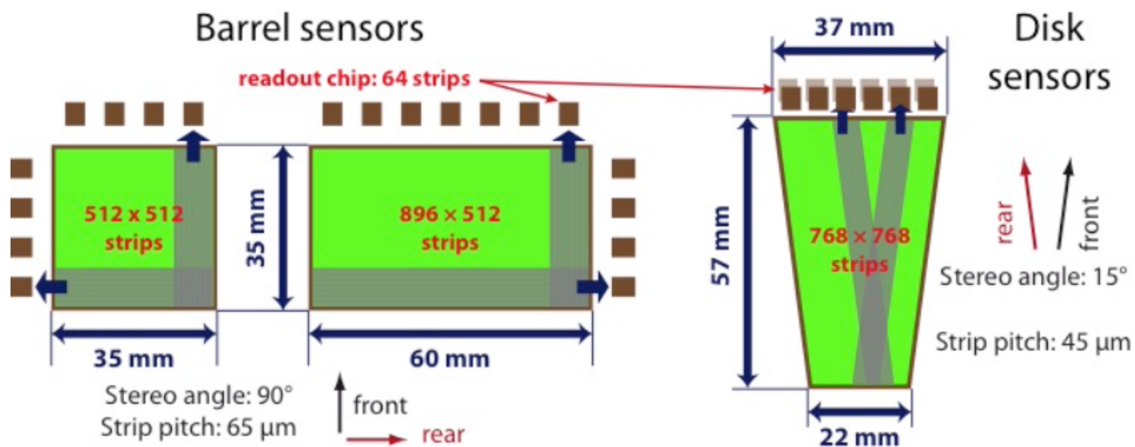

Figure 4.3: Schematic representation of the silicon strip sensors along with the readout chips.

As seen in the illustration, the rectangular sensors have a pitch of 65 µm with a stereo angle of 90 °. Chapter 5.1.4 provides a more detailed discussion of the sensor properties, with a focus on the rectangular sensors. The trapezoidal disk sensors feature 768 strips per side, with a stereo angle of 15 ° and a pitch of 45 µm. The sensors are fully depleted at approximately 100 V in the unirradiated state, with reverse bias voltage supplied to the sensors through the polysilicon resistor technique (further details in Chapter 5.1.5).

Spatial Resolution

In its simplest form, a silicon strip detector produces one-dimensional spatial information by being excited when a particle traverses a strip. The maximum resolution achievable is directly dependent on the distance between the strips, known as the pitch p. Assuming a uniform distribution of particles across the strips, this results in a resolution of $\sigma = p/\sqrt{12}$.

An increase in resolution, however, can be achieved by distributing the charge over multiple adjacent strips through charge sharing or an oblique angle of incidence, allowing the calculation of the center of gravity [36]. Investigations in the work of M. Kesselkaul [37] have revealed that a floating strip adjacent to the active one influences charge sharing and enhances resolution. As a result, in the MVD, only every second strip is contacted, resulting in a pitch of 130 µm or 90 µm. This is expected to yield a spatial resolution of a few 10 µm [38].

2D Spatial Information

For two-dimensional spatial information, two or more strips, with each providing the x and y coordinates respectively, need to intersect. This can be achieved with single-side readout by using two sensors placed one after the other, each with differently oriented strips. This method is discussed and utilized, for example, in Chapter 7.2. As depicted in Figure 4.3, the MVD sensors have strips with different orientations on the front and back sides. Thus, a single sensor can achieve two-dimensional resolution.

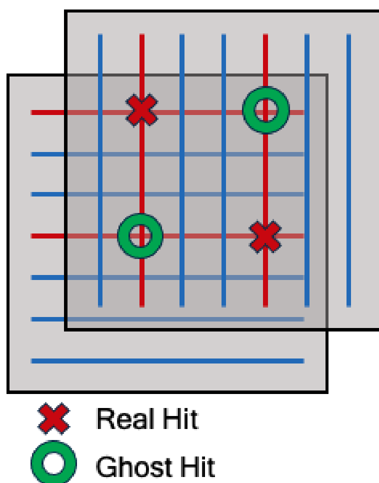

Figure 4.4: Illustration of two simultaneously measured particles in red and the resulting "fake" hits in green.

However, problems may arise at high rates due to so-called ghost hits. If more than one particle strikes a sensor during a readout cycle, it becomes difficult to directly distinguish where each particle was located. Additionally, the appearance of noise or, for example, scattered light can also cause these fake hits.With two particles there are a total of four spatial pieces of information and thus four potential locations for the particles, as depicted in Figure 4.4. As a result, two so-called "ghost" hits and two actual particles are registered. The actual hits can be filtered out, for example, through charge deposition, but with increasing rates, this becomes increasingly challenging.

4.1 Theoretical Overview

4.1.1 The Standard Model of Particle Physics

The Standard Model of particle physics is introduced in a shortened version below, with a focus on topics relevant to the $\overline{\text{P}}$ANDA experiment. The model describes fundamental particles and three of the four fundamental interactions: the Strong, Electromagnetic, and Weak (also known as the electroweak) interactions. The gravitational interaction is not covered. Interactions are described by gauge bosons with a spin of one, as outlined in Table 4.1. The graviton, which possesses a spin of 2, is excluded as it relies on theoretical data, as do the gluon, Z, and W bosons, which are also inferred through indirect observations.

Boson	Mass [GeV/c^2]	Charge (e)	Coupling	Spin
gluon	0	0	strong	1
photon (γ)	$<10^{-27}$	$<10^{-35}$	electromagnetic	1
Z	91.1876(21)	0	weak	1
W	80.377(12)	±1	weak	1
H	125.25(17)	0	-	0

Table 4.1: Overview of the elementary bosons (gauge bosons and the Higgs boson) and their properties within the standard model of particle physics [39].

4.1.2 The Strong Interaction

The strong interaction is responsible for binding quarks into hadrons, such as baryons (which consist of three quarks) or antibaryons (which consist of three antiquarks). The color charge of quarks is described by Quantum Chromodynamics (QCD), where quarks carry one of three distinct colors: Red, Green, or Blue. Their antimatter counterparts, antiquarks, carry the corresponding anticolors. To form a color-neutral particle, the three colors in baryons combine to result in a "white" or colorless state. Gluons, the mediators of the strong force, carry a combination of one color and one anticolor, which allows them to interact with both quarks and other gluons. This leads to eight possible gluon states with normalization constants $\sqrt{1/2}$ and $\sqrt{1/6}$ [40].

$$B\bar{R}, B\bar{G}, G\bar{B}, G\bar{R}, R\bar{G}, R\bar{B}, \sqrt{1/2}(R\bar{R} - G\bar{G}), \sqrt{1/6}(R\bar{R} + G\bar{G} - 2B\bar{B}) \qquad (4.1)$$

Even though baryons are overall color-neutral, there exists a slight interaction with a range of about 2.5 fm. Due to this strong interaction, protons and neutrons, which have a size of about 1 fm, can be bound into nuclei [41], [42].

These strongly interacting states can decay from more strongly bound states into less strongly bound, lighter particles, which can subsequently decay further into even lighter particles. However, mass alone does not dictate how strongly quarks

are bound in a hadron. The decay continues until a relatively stable particle, such as a proton or neutron, is produced. The decay products observed in particle physics experiments allow for the reconstruction of the original state and its properties.

Particle	Quark content	Mass [MeV/c^2]	Most probable decay
$\pi^{\pm}$	$u\bar{d}$, $d\bar{u}$	139.57039(18)	$\mu^{\pm}\,\nu/\bar{\nu}$
π^0	$(u\bar{u}$-$d\bar{d})/\sqrt{2}$	134.9768(5)	2γ
$K^{\pm}$	$u\bar{s}$, $\bar{u}s$	493.677(16)	$\mu^{\pm}\,\nu/\bar{\nu}$
K^0	$d\bar{s}$	497.611(13)	$\pi^+\pi^-, \pi^{\pm}e^{\pm}\nu_e$
p	uud	938.27208816(29)	-
n	udd	939.5654205(5)	pe$^-\nu_e$
ϕ	$s\bar{s}$	1019.461(16)	K^+K^-
J/Ψ	$c\bar{c}$	3096.900(6)	hadrons, virtual γ,ggg

Table 4.2: Overview of the properties and probable decay channels of some of the best known hadrons [39].

4.1.3 Charmonium

Charmonium is a bound system composed of a quark-antiquark pair, specifically a charm quark bound to a charm antiquark.
The $\overline{\text{P}}$ANDA experiment is designed to investigate the properties and excited states of charmonium. In electromagnetic interactions, a bound state can form between an electron and a positron, an analogy to various bound quark-antiquark states, including the J/Ψ state with quantum numbers J^{PC} = 1^{--}. Studies of the strong interaction potential are facilitated through the emission and absorption spectra of charmonium and its excited states, denoted as $\Psi^{'}$ and $\Psi^{''}$. The η_c represents the ground state of charmonium, characterized by spin 0. In analogy to QED dipole transitions, reaching the ground state requires a magnetic dipole transition. However, unlike in QED, only specific transitions are allowed, with total angular momentum (L) constant and spin (S) changing by 1 [43].
A characteristic feature of J/Ψ is the suppression of transitions to lower states via electromagnetic interactions, meaning that such decays by photon emission are highly unlikely and have not been observed. Like other quark-antiquark pairs, the charm quark (c) and its antiquark ($\bar{c}$) can mutually annihilate. As illustrated in Table 4.2, the predominant decay channel proceeds via strong interactions into gluons, although electromagnetic decays through a virtual photon can also occur.

The notably longer lifetime and narrower decay width of J/Ψ can be attributed to the Okubo-Zweig-Iizuka (OZI) rule, which suppresses decays where all gluon connections in a Feynman diagram can be "cut". This suppression increases the relative frequency of electromagnetic (EM) decays, enhancing the probability of leptonic final states. A Feynman diagram illustrates this suppressed hadronic

decay channel.
Most J/Ψ decays occur through strong or electromagnetic interactions. Strong interactions dominate, but electromagnetic processes contribute significantly, leading to both hadronic and leptonic final states. Due to color conservation, these transitions are of comparable magnitudes, as parity can only be transferred by three gluons. The probability of this process is proportional to α_s cubed, reflecting the contributions of the three gluons. The coupling constant α_s is relatively small at higher energies, as discussed by [44].
The most probable J/Ψ decay channels involve D-meson production, such as D^0 (charm and anti-down quarks) and D^+ (charm and anti-up quarks). Additionally, decays can produce an η(958)-meson with two pions, depending on the dynamics [45]. These decay modes provide insights into the strong interaction and meson quark structure.

Within the charmonium family, decays are also possible, for instance, χ_{cl} can decay into a J/Ψ particle. This particular decay is essential for studying charmonium-based particles in high-energy physics. As previously mentioned, electromagnetic decays are rare but yield distinct final states. Identifying the final states π^0 and η through photon detection helps reconstruct decays and determine quantum numbers. While such studies have primarily occurred in electron-positron colliders, the planned proton-antiproton collisions in $\overline{\text{P}}$ANDA offer more diverse opportunities to measure quantum numbers and ground states, allowing comprehensive analysis of the charmonium spectrum.

4.1.4 Glueballs

Glueballs are hypothetical configurations of subatomic particles consisting only of gluons. Configurations allowed by QCD for bound states of elementary particles responsible for the strong interaction include combinations of quarks and gluons. One possible configuration involves gluons interacting among themselves to form a glueball, which is a type of meson composed solely of gluons. However, like all baryons in the Standard Model except for the proton, this configuration is not a stable state under normal conditions due to the inherent confinement of color charge.
In the diverse decay process of J/Ψ, glueballs could be involved in one of the channels, such as the decay into two gluons with color charge and a photon. The gluons in this J/Ψ decay could then undergo hadronization, and properties like mass, lifetime, etc., could be determined from the secondary particles. Additionally, hybrids between quarks, antiquarks, and gluons within QCD are possible [46]. The $\overline{\text{P}}$ANDA experiment is well-positioned to contribute to this research by conducting measurements on charmonium and its decay products.

4.2 Introduction to Semiconductor Physics

The following section provides essential fundamentals to understand the properties and functionality of silicon (Si) detectors. While most topics are briefly discussed here, they can be explored in greater detail in references such as [36] and [47].
Semiconductor detectors play a crucial role in high-energy and nuclear physics. They are utilized for tasks such as gamma spectroscopy and as vertex detectors for tracking particle trajectories. These self-supporting solid-state detectors exhibit relatively high intrinsic radiation hardness. Achieving the desired signal behavior requires a compromise between a large signal, corresponding to a small band gap, and low noise, which demands a large band gap.
Silicon detectors are predominantly employed in MVDs and can be mass-produced in wafers of high purity. While for example gallium arsenide prototype detectors offer faster operation and greater radiation hardness, they are also more expensive to manufacture. Both materials are arranged in a diamond structure and are characterized by their adjustable conductivity. A suitable description of conductivity as a function of temperature is provided by the Fermi-Dirac distribution.

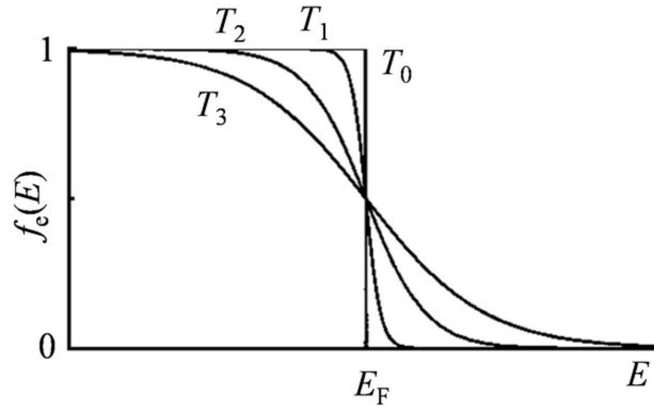

Figure 4.5: Fermi-Dirac distribution function for different temperatures $T_1 > T_2 > T_3 > T_0 = 0\,K$ [48].

$$f(E,T) = \frac{1}{e^{(E-E_F)/k_B T} + 1} \tag{4.2}$$

The Fermi level E_F describes the energy value at which the probability distribution of electrons in a solid at thermal equilibrium is situated. This allows for the determination of the state of electrons within the concept of the energy band diagram. The constant thermal excitation and recombination of electrons maintains the semiconductor in equilibrium. Intrinsic conduction occurs when an equal number of holes and electrons are continually formed, requiring the silicon to be pure (free of donors or acceptors).

Silicon, belonging to the 4th main group, exhibits typical semiconductor properties. with completely filled energy bands below the Fermi energy at temperature zero (T=0 K). Bands above the Fermi level are entirely empty as electrons occupy energy levels up to the Fermi level and no electrons are present in energy levels above it. According to the band model, the last fully occupied band is referred to as the valence band, while the conduction band is situated above it. Between these bands lies the band gap, which possesses a defined energy for an insulator, semiconductor, and conductor.

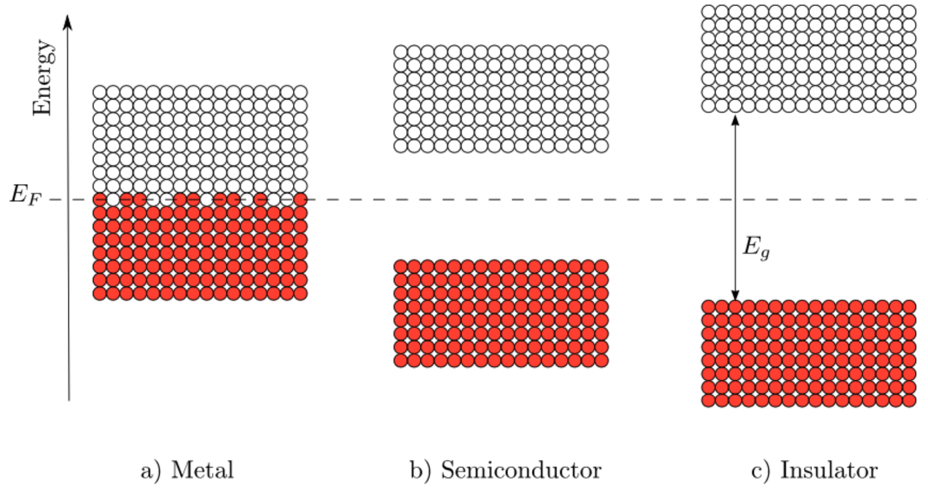

Figure 4.6: Schematic representation of the band diagram for a conductor (a), a semiconductor (b), and an insulator (c) [49].

The band gap between the valence and conduction bands for an insulator is typically large enough to prevent the promotion of electrons under normal conditions. In contrast, a semiconductor has a smaller band gap, allowing for electron promotion from the valence to the conduction band through thermal energy or external excitation, such as photons [50]. The released electron leaves a hole in the valence band, which then acts as a free charge carrier alongside the electron. This phenomenon is referred to as an intrinsic semiconductor, where the conductivity is highly dependent on the charge carrier density, i.e., on the temperature. Thus, the concentration values of the charge carriers n for electrons and holes are identical, which can be described using the Fermi function 4.2 (in the case of fermions) and the state density $N(E)$:

$$n = \int_0^\infty N(E) \cdot f(E,T) \cdot dE \tag{4.3}$$

Using both formulas, 4.2 and 4.3, the following illustration for intrinsic semiconductors can be created.

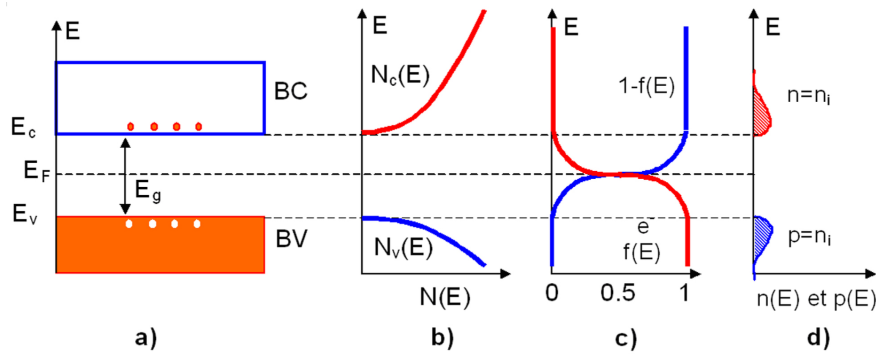

Figure 4.7: Illustration of band, energy, occupation probability, Fermi function, and charge carrier density of an intrinsic semiconductor [51]

In each part of Figure 4.7, the maximum energy of the valence band E_V, the minimum energy of the conduction band E_C, and the Fermi energy E_F are visible. In figure (a), the band-gap E_g between the bands and the electrons or holes can be observed. The density of states $N(E)$ is plotted in (b), while the Fermi energy is shown in (c). The charge carrier densities of electrons and holes are depicted in (d), demonstrating their equal distribution.

Additionally, semiconductors are classified into two categories, direct and indirect. In **direct semiconductors**, electrons can transition directly to the conduction band without requiring an exchange of momentum, provided their energy exceeds the band gap. This phenomenon occurs because the maximum of the valence band in momentum space aligns directly above the minimum of the conduction band, as depicted in the left illustration of Figure 4.8 for indium phosphide (InP).

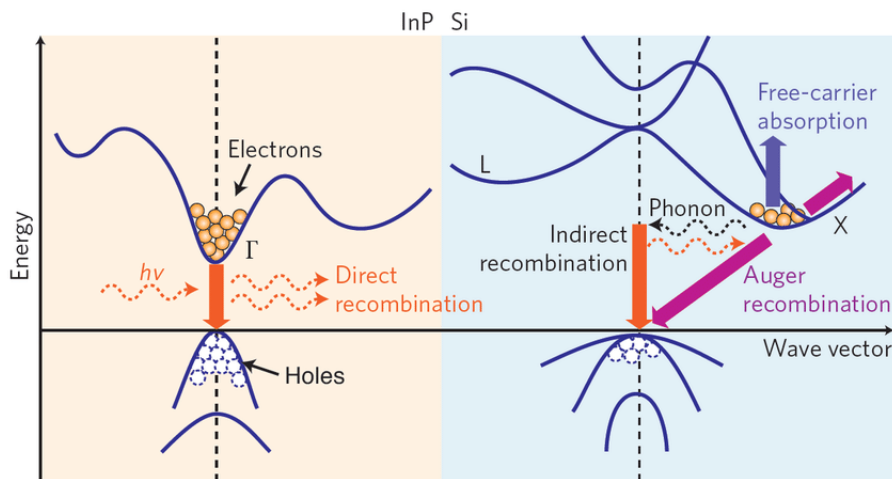

Figure 4.8: Schematic energy band diagram for a direct semiconductor with InP as an example on the left, and for an indirect semiconductor with Si as an example on the right [52].

In **indirect semiconductors**, electrons need to overcome a momentum gap to tran-

sition from the valence band to the conduction band. This can be achieved either by acquiring sufficient energy to jump directly into the band or by interacting with a phonon.
In the direct semiconductor case depicted on the left side of Figure 4.8, it can be observed that the conduction band's minimum aligns directly above the valence band's maximum. Conversely, in the right picture illustrating an indirect semiconductor, the electrons cannot directly transition to the potential minima because the maximum and minimum are shifted relative to each other.

Silicon, for instance, is an indirect semiconductor, indicating that an electron with a band gap energy of E_{gap}=1.12 eV requires an additional phonon to overcome the barrier [53]. For a direct transition, a minimum energy of E=3.62 eV is necessary to move an electron into the conduction band.

4.2.1 Doping of Silicon

However, when a semiconductor is contaminated with suitable atoms of other elements, it is called extrinsic. This contamination, known as doping, can alter the occupation probabilities, as illustrated in Figure 4.9.

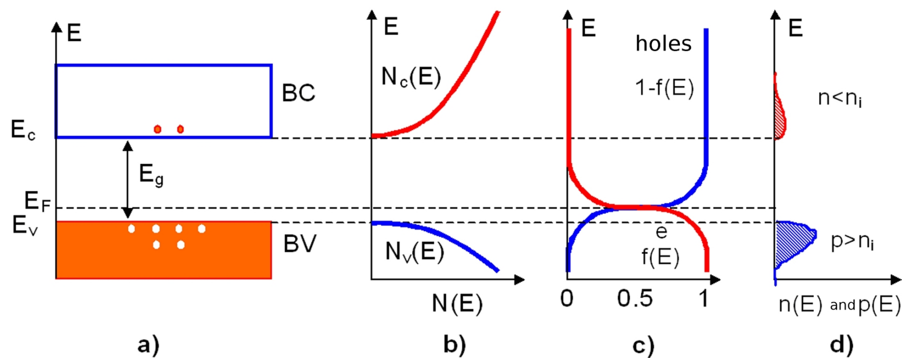

Figure 4.9: Illustration of band structure, energy levels, occupation probability, Fermi function, and charge carrier density in an extrinsic semiconductor [51].

In Figure 4.9, a lower Fermi energy E_F compared to Figure 4.7 is observed, which results from doping with acceptors. This type of doping with, for example, boron or indium, introduces holes (the absence of electrons), which is consequently referred to as p-doping. These acceptor atoms have three valence electrons and, upon bonding with the four-valent silicon, create a deficiency of one electron, resulting in a hole. Consequently, the occupation probability and Fermi levels are shifted towards the valence band.
Doping using donors such as phosphorus or arsenic, which have five valence electrons, forms covalent bonds with the four-valent silicon. This introduces extra electrons into the silicon lattice, increasing the number of free electrons available

for conduction, and is referred to as n-doping.

In part (d) of the figure, the higher density of holes compared to electrons is evident. Therefore, the densities of the charge carriers are not equal, attributed to the doping, a crucial characteristic of an extrinsic semiconductor. The donor or acceptor levels change the Fermi level and thus the conductivity.

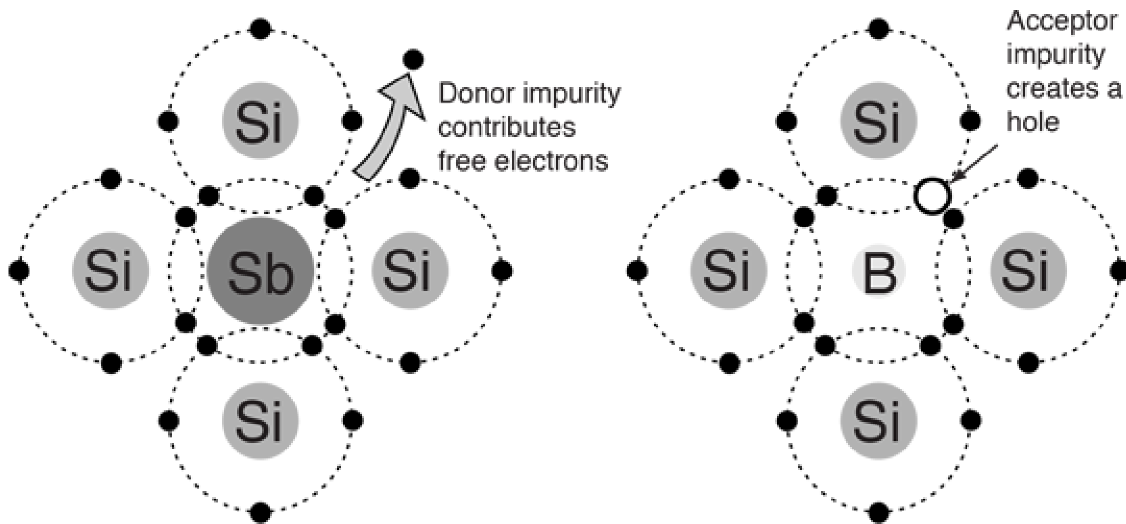

Figure 4.10: Schematic diagrams illustrating n-type and p-type doping of silicon with antimony and boron, respectively [54].

In Figure 4.10, on the left-hand side, one can see the free valence electron of the n-type doped semiconductor. On the right side, the hole created by the acceptor impurity is shown. The holes and free electrons affects the charge carrier density and thus the Fermi level, as shown in Figure 4.9. The behavior of the electron concentration as a function of temperature is illustrated in Figure 4.11 for doped (extrinsic) and undoped (intrinsic) silicon.

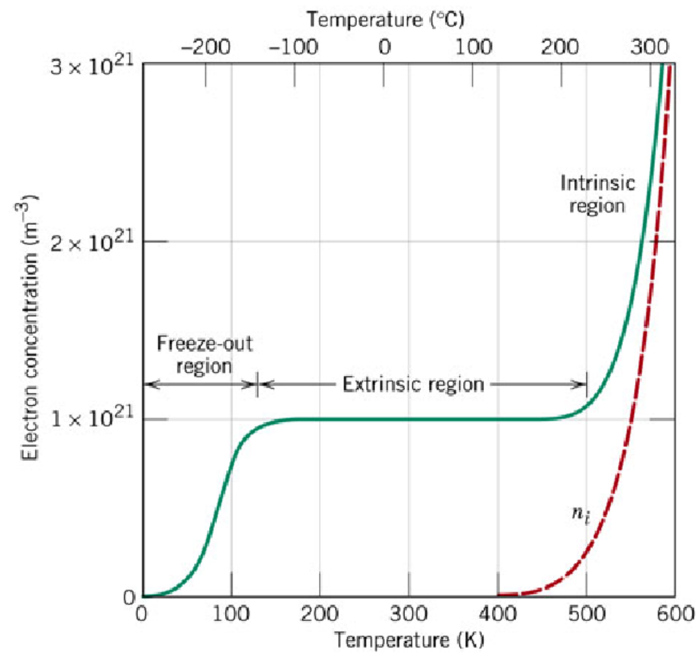

Figure 4.11: The electron concentration is plotted against temperature in Kelvin for doped silicon in green and intrinsic silicon in red [55].

In Figure 4.11, the electron concentration for doped silicon is depicted in green, while undoped silicon is shown in red for various temperatures. It is evident that throughout the entire range, the extrinsic semiconductor exhibits a higher electron concentration in the conduction band than the intrinsic semiconductor. As temperature increases, the concentration saturates for doped semiconductors once all available interference points (majority carriers for electrons and minority carriers for holes) are exhausted. With a further increase in temperature, electrons are facilitated to transition directly from the valence band to the conduction band. This behavior is attributed to the narrowing of the band gap due to temperature, known as intrinsic conduction, resulting in an increase in electron concentration for both semiconductors. In the case of doped silicon, electrons do not need to traverse the entire band gap, instead, they are already located at the donor level, which is closer to the conduction band. Similarly, for holes, the band gap is now situated between the conduction and the acceptor level.

The magnitude of the band gap can lead to increased sensor sensitivity, as a smaller band gap implies that less energy is required to move electrons from the valence band to the conduction band. This enables the detection of lower energy levels, enhancing sensitivity.
However, this consequently increases the noise levels. As illustrated in Figure 4.11, it can be observed that for the operational range of the MVD at approximately 290 K, the sensor is situated in the extrinsic region, thereby reducing the temperature dependence of measurements.

Typical doping concentrations for semiconductors range from 10^{14} to 10^{18} atoms/cm^3. Highly doped semiconductors, denoted by p^+ or n^+, have a doping concentration of approximately 10^{20} atoms/cm^3. Doping alters the electrical properties of the semiconductor, which is further explained in Section 4.4.2. Since majority charge carriers dominate, the conductivity in the extrinsic region is determined by the doping density. As a good approximation, the following relationship applies to the doping concentration.

$$\textit{n-type (for } N_D \gg N_A\textit{)}: \rho = \frac{1}{e\nu_n N_D} \tag{4.4}$$

$$\textit{p-type (for } N_A \gg N_D\textit{)}: \rho = \frac{1}{e\nu_p N_A} \tag{4.5}$$

$N_{D,A}$ represents the donor and acceptor levels, while $\nu_{n,p}$ denotes the mobility of electrons and holes, respectively. Contamination and damage from irradiation, for instance, have the potential to alter these levels.

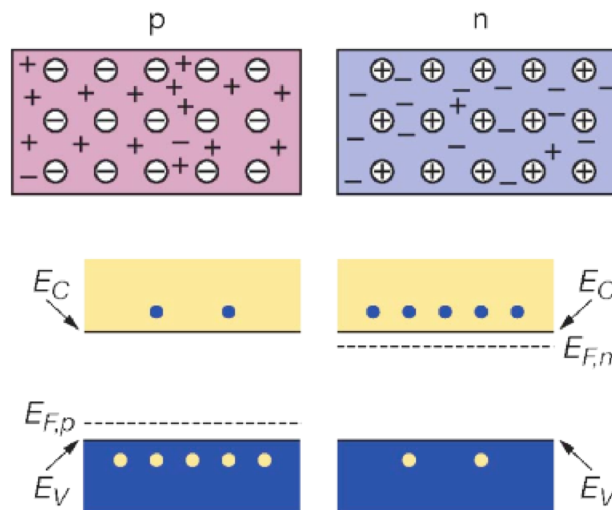

Figure 4.12: Diagram showing the effects of donation on the Fermi levels in silicon within the band model [56].

The principle of doping is depicted in Figure 4.12. In the illustration, $\oplus$ and $\ominus$ represent the donors and acceptors, while $+$ and $-$ denote the space charge (holes and electrons). It is evident that doping influences the Fermi energy. In comparison to an intrinsic semiconductor, the Fermi level in an n-type semiconductor is higher and closer to the conduction band. Conversely, in p-doped semiconductors, the Fermi level is closer to the valence band. Consequently, conductivity is contingent upon the doping level.

4.2.2 P-N Junction: Introduction and Basic Concepts

Combining extrinsic semiconductors with different doping levels results in the formation of a p-n junction. In thermal equilibrium, it is essential for the Fermi

levels of the adjoining regions to align. Consequently, electrons diffuse into the p-region while holes migrate into the n-region, giving rise to electron and hole currents, respectively.

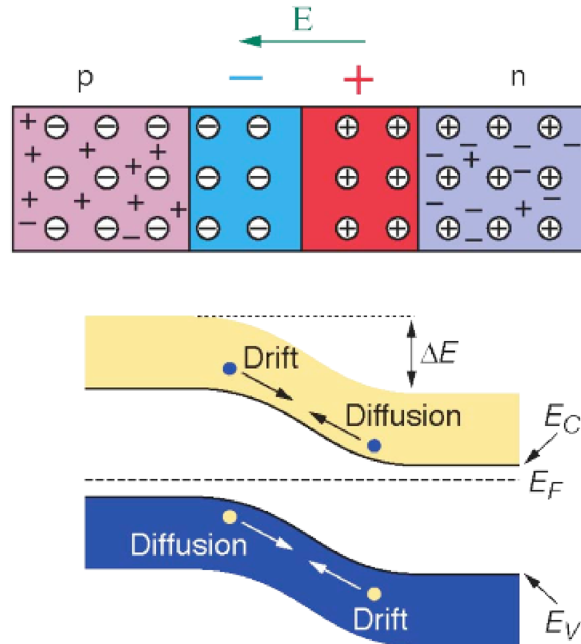

Figure 4.13: Schematic depicting energy levels and resulting diffusion in the pn-junction [56].

The ionization of donors and acceptors, along with the resulting electric field due to the voltage difference across the pn-junction, leads to the formation of a zone with fewer free charge carriers at the junction. This region, known as the depletion zone in the thermal equilibrium , is characterized by the depletion voltage V_D. This voltage opposes the current until equilibrium is achieved. At this juncture, the Fermi energy is equal in the p- and n-doped semiconductors. Assuming equal carrier density within the depletion region for both semiconductors, the potential profile can be calculated using the Poisson equation. During the process, there is continuous recombination of the ionization products.

$$\frac{\partial^2 V(x)}{\partial x^2} = -\frac{\rho(x)}{\epsilon_r \epsilon_0} \tag{4.6}$$

This gives the following equation for the dissipation voltage U_{diff}:

$$U_{\text{diff}} = \frac{e}{2\epsilon_r \epsilon_0}(N_D + N_A) d_n d_p \tag{4.7}$$

With d_p representing the thickness of the depletion region and N_D or N_A denoting the doping density (on the n-side and p-side respectively). Typical diffusion voltages are approximately 0.5 V, leading to a surplus of charge carriers in the respective opposite regions. The resulting electric field further transports the free

charge carriers and opposes diffusion. The extent of the depletion region in the p-region can be described as:

$$d_p = \sqrt{\frac{2\epsilon\epsilon_0}{e}\frac{1}{N_A(1+N_A/N_D)}U_{diff}} \tag{4.8}$$

The same applies to the n-region with:

$$d_n = \sqrt{\frac{2\epsilon\epsilon_0}{e}\frac{1}{N_D(1+N_D/N_A)}U_{diff}} \tag{4.9}$$

The depletion region is the sensitive area for ionizing particles, thus it should be made as large as possible in experiments. The electrical signal generated by the produced electron-hole pairs can be measured. To enlarge this region and reduce the probability of recombination, a voltage is applied in the reverse bias direction, which will be discussed in more detail in the next Chapter 4.2.2.

P-N Junction in Reverse Bias Configuration

The external voltage V applied in the reverse direction of the previously discussed pn junction is commonly referred to as reverse bias voltage. This gives the following expression for the thickness of the depletion region:

$$d = \sqrt{\frac{2\epsilon\epsilon_0}{e}\left(\frac{1}{N_d}+\frac{1}{N_a}\right)(U_{diff}-V)} \tag{4.10}$$

When the depletion region or the space charge zone occupies the entire semiconductor, the voltage is specifically termed the depletion voltage. This significant variable can be mathematically expressed using the formulas 4.8 and 4.9. It is noteworthy that an important limitation of the depletion voltage is the detector thickness D.

$$V_\mathrm{D} = \frac{e}{2\epsilon\epsilon_0|N_{eff}|D^2} \tag{4.11}$$

The decisive detector properties are still the doping densities, which are combined to obtain the effective doping density N_{eff}=N_D-N_A. The effective doping density can be measured, for instance, through the resistance ρ of the detector:

$$N_{eff} = \frac{1}{e\rho\mu} \tag{4.12}$$

A more detailed description of this relationship can be found in the chapter where a corresponding measurement was conducted 5.5.4.

Leakage Current in P-N Junction

Another important property of silicon detectors directly related to the material is the so-called leakage current. It arises from the thermal excitation in the crystal volume and flows through the contacts. As the recombination probability decreases

with increasing reverse bias voltage, I_{leak} reduces. Upon reaching the depletion voltage, the leakage current remains constant and only increases again at breakdown. This leads to a phenomenon known as Zener breakdown, where electrons are released from the covalent bonds due to the electric field, or avalanche breakdown, where there is an avalanche-like breakthrough due to the kinetic energy of the electrons. In this process, the semiconductor can be damaged. The leakage current, dependent on an external voltage V_B , can be described by the Shockley equation:

$$I = I_0 \cdot [exp(\frac{eV_B}{k_B T}) - 1] \quad (4.13)$$

I_0 is the reverse saturation current. In the forward direction ($V_B > 0$), the current increases exponentially with the applied voltage V_B. Under reverse bias direction, the exponential term can be neglected, and the current is limited by the saturation current. This estimation is only valid outside the breakdown voltage, as it is not taken into account.

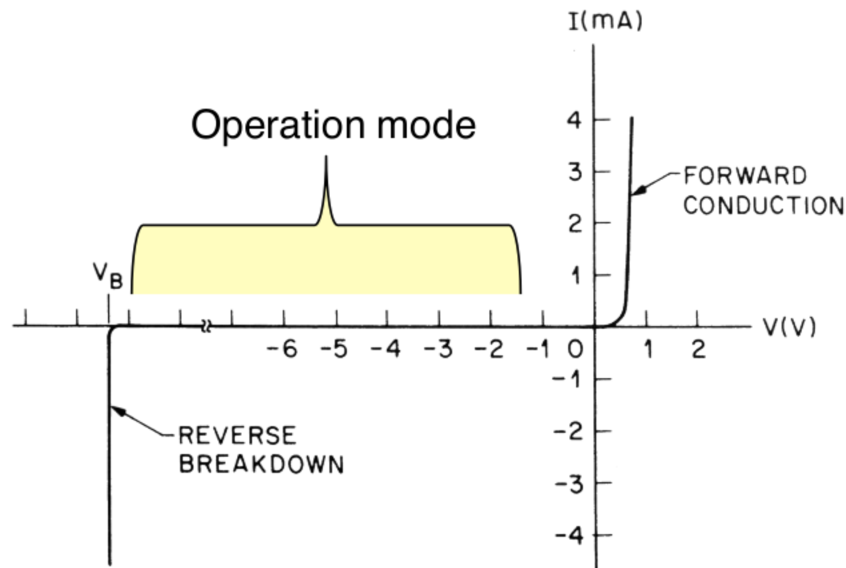

Figure 4.14: The I-V (current vs. voltage) characteristics of a p-n junction diode with the operating range for a silicon detector indicated [56].

In the illustration 4.14, the small saturation current in the reverse bias region for $V_B < 0$ can be seen. At a certain point, the current increases dramatically due to breakdown. In the forward bias direction, an exponential increase in current is depicted. The lowest possible leakage current is desirable, which comprises the crystal structure and the thermal generation from the diffusion and generation currents. This remains constant from the depletion voltage until breakdown.

Expansion of the Depletion Region

To increase the depletion region, as previously mentioned, a reverse bias voltage must be employed across the p-n junction. The reverse bias voltage is applied

with the anode connected to the n-side and the cathode to the p-side.

The reverse bias voltage attracts electrons to the n-side and holes to the p-side. As this voltage is increased, more and more free charge carriers are drawn to the sides, leading to an expansion of the depletion region until nearly all free charge carriers are depleted.
Upon reaching the full depletion voltage, the region has expanded across the entire active volume of the sensor. Verification of reaching the full depletion voltage is necessary for sensor installation and can be determined through capacitance measurements. The diode or sensor behaves in good approximation as a plate capacitor, as explained in sub Chapter 5.2. The expansion of the depletion region can be observed using the sketch of a silicon detector in Figure 4.15.

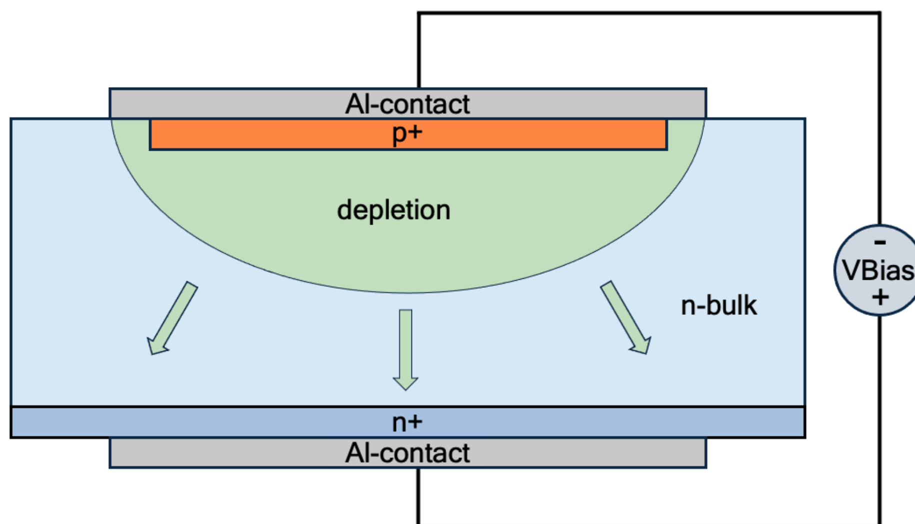

Figure 4.15: Illustration of the schematic enlargement of the depletion region in a diode while increasing the reverse bias voltage.

4.3 Interaction of Particle's with Matter

To detect a particle in a sensor, it must interact, and this chapter explains how a particle loses some of its kinetic energy along its track through the material by ionizing atoms. This interaction is well-described theoretically and experimentally by the Bethe-Bloch formula [57]. It describes statistically the loss of energy mostly due to ionization per path length for a charged particle traversing matter.

Important parameters for the Bethe-Bloch equation include the traversed path length of the particle through the material, x (in cm) and the constants
$2\pi N_0 r_e^2 m_e c^2 = 0.1535\,\mathrm{MeVc^2/g}$ with the classical electron radius ($r_e = \frac{q_{el}^2}{4\pi m_e c^2} = 2.817 \times 10^{-15}\,\mathrm{m}$), N_0 as Avogadro's number, and m_e as the electron mass, Z, A (atomic and mass number of the medium), ρ (density of the matter), the Lorentz

factors $\beta = \frac{v}{c}$ and $\gamma = \frac{1}{\sqrt{1-\beta^2}}$, the charge of the particle z, and corrections for density δ and shell C. I is the effective ionization potential averaged over all electrons, and $W_{\max}$ is the maximum energy transfer in a single collision.

$$\frac{dE}{dx} = 2\pi N_0 r_e^2 m_e c^2 \rho \frac{z^2}{\beta^2} \left[ln \left(\frac{2m_e \gamma^2 v^2 W_{max}}{I^2} \right) - 2\beta^2 - \delta - 2\frac{C}{Z} \right] \tag{4.14}$$

From $\beta\gamma > 1$ onwards, a relativistic increase can be observed, indicating that the particles become relativistic. This phenomenon can be explained by transverse field strengthening.
The equation is valid for a range between $\beta\gamma \leq 0.1$ to $\beta\gamma \leq 1000$ [45]. Beyond a particle energy of 10 MeV, the energy loss of electrons and positrons is dominated by bremsstrahlung and is hence no longer accurately described by the Bethe-Bloch formula.
In Figure 4.16, a graphical representation of the Bethe-Bloch equation can be seen. It is crucial for the generation of a signal to ionize the matter. The graph shows a minimum, which represents the point at which a particle experiences the least energy loss while ionizing atoms of the material, commonly referred to as a minimum ionizing particle (MIP). Often, the Lorentz factors $\beta\gamma$ are considered, and a particle is referred to as a MIP when $\beta\gamma \approx 3$.

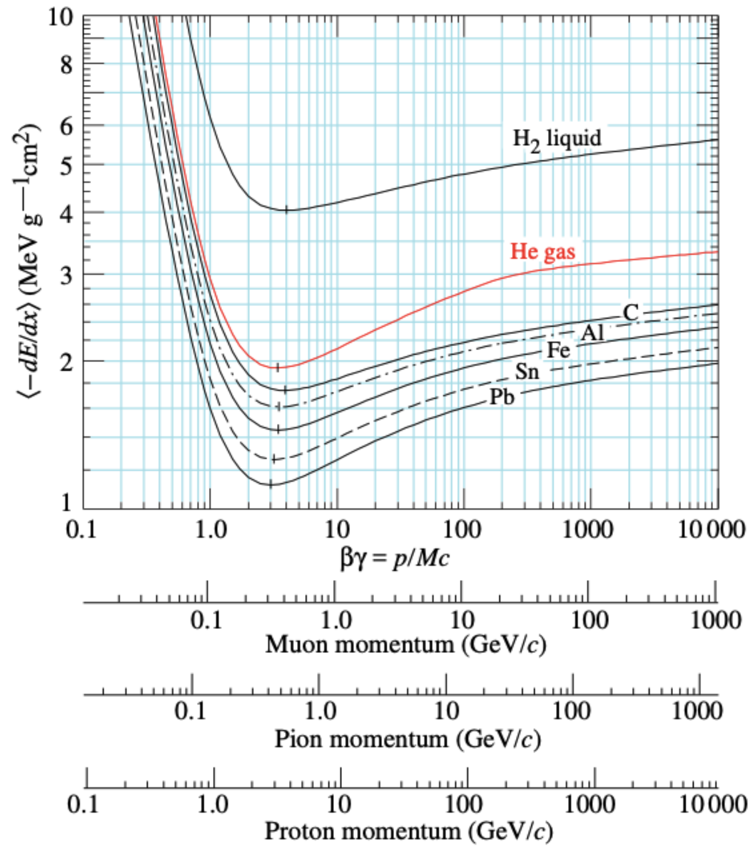

Figure 4.16: Specific energy loss rate for muons, pions and protons corresponding to different absorber materials [45].

In the energy range mentioned, the energy loss for particle types with the same charge remains approximately constant. This characteristic allows for the utilization of energy loss measurements for particle identification. Since this point is reached at different momenta for particles of varying masses, energy loss measurements offer the potential for precise particle identification.
Calculation of $\beta\gamma$ via the particle energy:

$$\gamma = \frac{E_{kin}}{E_0} + 1 \text{ and } \beta = \sqrt{1 - \frac{1}{\gamma^2}} \tag{4.15}$$

4.3.1 Energy Loss in $\overline{\text{P}}$ANDA-Sensors

Using the Bethe-Bloch formula, described in Section 4.3, one can calculate the average energy loss per distance traveled by an incident electron in silicon [58],[59]. It is assumed that the electron impacts the detector surface perpendicularly, covering a distance of 285 µm in silicon for $\overline{\text{P}}$ANDA sensors. As our primary irradiation involves ^{90}Sr, we will exemplify the stopping power calculation for an electron with the average energy $E_{\beta,\text{Avg}}$=0.3 MeV from the combined spectrum of ^{90}Sr and ^{90}Y.

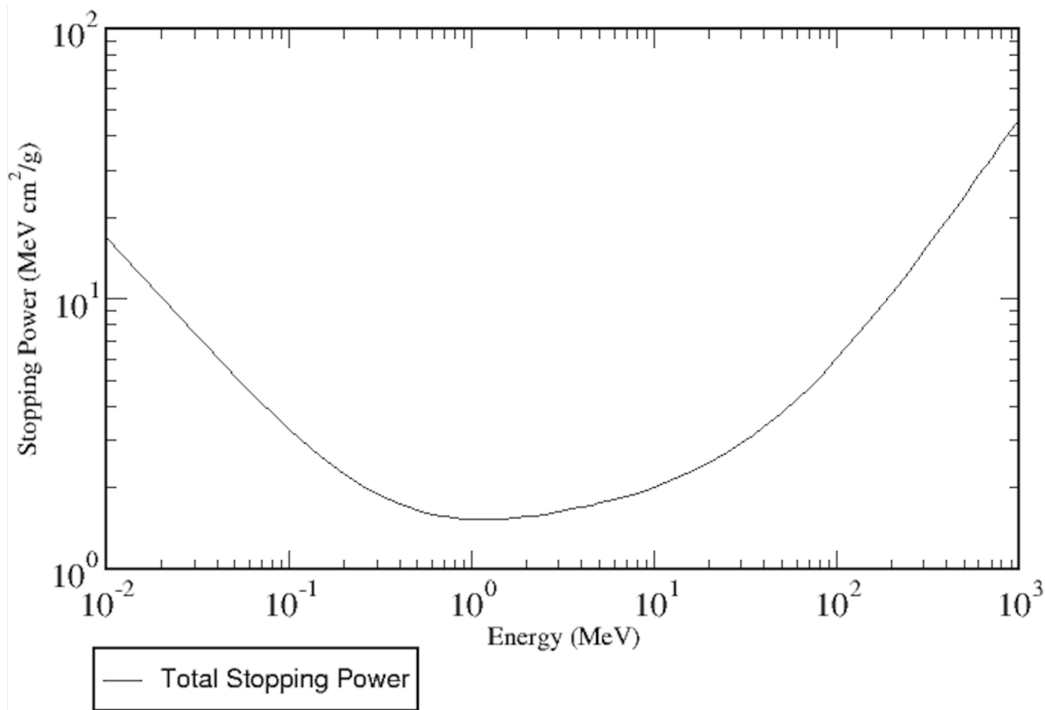

Figure 4.17: Total stopping power for electrons in silicon [60].

To do this, the energy-specific energy loss of electrons in silicon must first be determined, as shown in Figure 4.17, calculated to be S=1.903 $\frac{\text{MeVcm}^2}{\text{g}}$ using the NIST "ESTAR" program [60]. "ESTAR" calculates the stopping power S of electrons at specific energies for various materials.

With the density of silicon ρ=2.336 $\frac{\text{g}}{\text{cm}^3}$, the deposited energy of the electrons per distance traveled in the silicon-detector can be calculated:

$$-\frac{dE}{dx} = S \cdot \rho \tag{4.16}$$

$$-\frac{dE}{dx} = 1.903\,\frac{\text{MeV} \cdot \text{cm}^2}{\text{g}} \cdot 2.336\,\frac{\text{g}}{\text{cm}^3} \tag{4.17}$$

$$\frac{-dE}{dx} = 4.445\,\frac{\text{MeV}}{\text{cm}} \tag{4.18}$$

To calculate the total energy that the particle has lost while traversing through the sensor, the product of $\frac{dE}{dX}$ and the distance traveled must be considered. Assuming full depletion, the deposited energy ΔE can be calculated he distance of x=285 µm:

$$\Delta E = \int_0^x -\frac{dE}{dx}dx \tag{4.19}$$

$$\Delta E = -\frac{dE}{dx} \cdot x \tag{4.20}$$

$$\Delta E = 4.445\,\text{MeV}\,\text{cm}^{-1} \cdot 285\,\mu\text{m} \tag{4.21}$$

$$\Delta E = 126.694\,\text{keV} \tag{4.22}$$

4.3.2 Landau Distribution

For thin layers, where a limited number of collisions occur but with each depositing more energy than the ionization potential, the energy distribution becomes asymmetric and follows a Landau distribution [61], [62]. When minimum ionizing particles (MIPs) pass through a thin silicon layer, they continue to traverse the material without being stopped. The deposited energy fluctuates around the most probable value of the distribution, with a long tail allowing for occasional higher energy deposits [63]. For thinner layers, the fluctuations in energy deposition increase, making the distribution broader.

The asymmetry of the Landau distribution is mainly due to the so-called δ-electrons or knock-on electrons. These receive enough energy through the interaction to be able to ionize further themselves. This can create charge clouds that typically move in the perpendicular direction of the incident particle, which can worsen the spatial resolution [64]. The Landau distribution is typical for thin silicon detectors [65].

In a real silicon detector, such as the MVD, sensors with a thickness of about 285 µm are used. For thicker sensors, multiple collisions occur, resulting in a broader energy deposition distribution. While the Landau distribution still describes the

energy deposition due to ionization, additional scattering events smooth the distribution, but it remains asymmetric. In practice, noise from the detector electronics, which is often approximated by a Gaussian distribution, must also be considered. Therefore, the energy deposition in silicon detectors is typically modeled by a convolution of a Landau distribution (for the energy loss) and a Gaussian distribution (to account for electronic noise) [66].

In the following, a fitting method is used that involves a convolution of the two functions for the energy deposit in the sensors [67]. The Landau function is based on the estimations of [68]. The most probable value (MPV) of the function is determined through a simple Gaussian fit around the peak. This enables a more flexible and accurate determination of the MPV. The fit is intended to demonstrate the functionality of the sensors and identify potential differences in the distributions.

4.4 Radiation Damage

Due to the high velocity of charged particles, detectors within the particle accelerator are subjected to intense radiation. This exposure can lead to permanent damage, which cannot be reversed, although certain mitigation strategies may reduce its impact. Therefore, the sensors must have a high resistance to radiation and exhibit predictable behavior even after radiation damage, ensuring reliable operation over long periods of time.

Radiation effects are crucial parameters that limit the lifespan of experiments in high-energy physics. In the following, we briefly explore radiation damage in crystal structures; for a more in-depth understanding, refer to the work of [69].

Common radiation damages include the displacement of lattice atoms, nuclear interactions resulting from processes like neutron capture, and secondary processes. Initially, we will explore defects that may arise within the bulk, specifically inside the crystal structure, resulting in alterations to both the crystal lattice and doping. The introduction of impurities into the crystal has the potential to impact the electrical properties of the semiconductor, a consequence typically considered undesirable for semiconductor detectors.

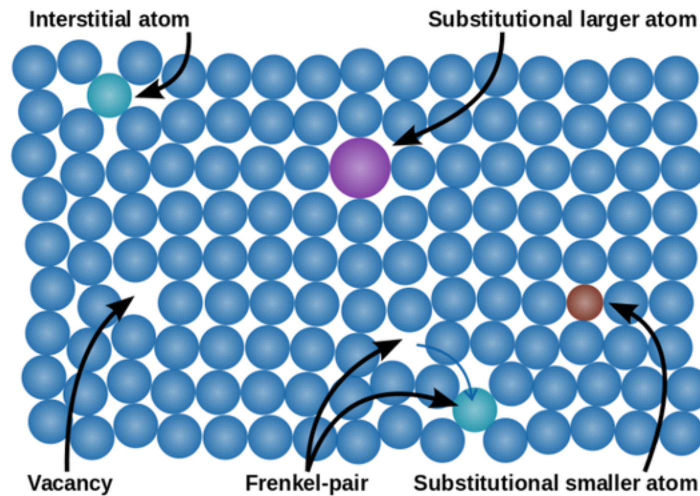

Figure 4.18: A schematic illustrates a silicon lattice after particle collisions, with atomic displacements representing typical point defects [70].

However, typical point defects, as depicted in Figure 4.18, include the "vacancy" at the bottom left, representing a missing atom in the lattice. Above, an "interstitial" atom is shown, denoting an additional atom of the same or a foreign nature located between regular lattice sites. Additionally, two "substitutional" atoms with different natures are illustrated between regular lattice sites. Another noteworthy defect is the "Frenkel defect", where interstitials appear next to vacancies, often referred to as a "Frenkel-Pair".

The formation of these defects can be attributed to particle interaction. This interactions occurs not only with the electron shell of the atoms, creating electron-hole pairs but also with the nucleus and, consequently, the lattice, leading to deformation, as illustrated in Figure 4.18. If the energy from an elastic collision exceeds the displacement energy in silicon (E_d of 25 eV), a lattice atom (primary knock-on atom, PKA) may be released [71]. The PKA can create vacancies in the lattice, while the displaced atoms may persist as interstitials.
For energies significantly surpassing E_d, the recoiling silicon atom itself can cause further damage [36]. A simulation of such a collision and its subsequent effects is shown in Figure 4.19.

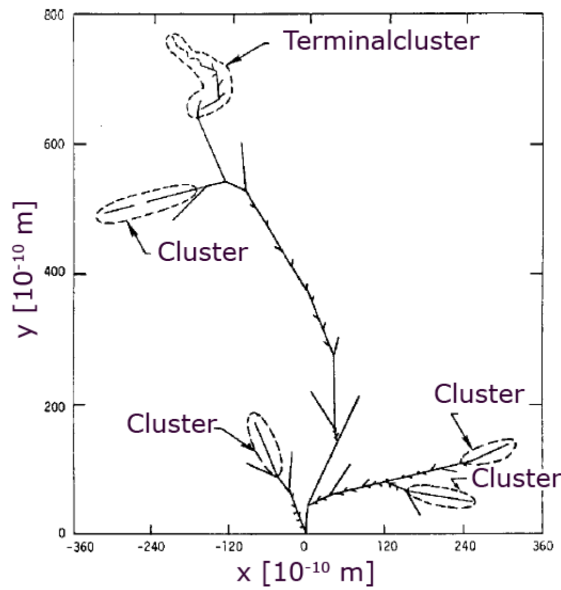

Figure 4.19: A Monte Carlo simulation was conducted to model the trajectory and defects resulting from a silicon atom knocked out with an initial energy of 50 keV. This initial energy is equivalent to the energy transfer of a 1 MeV neutron to the primary knock-on atom [72].

In Figure 4.19, the simulated trajectory of the PKA is depicted, showcasing the potential damage it can cause to the lattice with sufficient energy. Point defects may emerge along this trajectory, forming defect clusters when the energy of secondary particles is low enough to become immobilized. As a result, clusters tend to form at the end of the trajectories.

The distribution and clustering of defects are closely linked to the energy and type of the colliding atom. Therefore, the subsequent section introduces the common scaling method to facilitate the comparison of radiation damage caused by various particle types and energies.

4.4.1 The NIEL Theorem

The Non-Ionizing Energy Loss (NIEL) theory allows the comparison of radiation damage caused by hadrons or leptons by normalizing the damage relative to a 1-MeV neutron, as depicted in Figure 4.20 [73]. The induced material change through displacement is postulated to have a linear scaling with the transferred energy. Consequently, the actual particle fluence Φ_x can be scaled by the 1-MeV neutron equivalent fluence Φ_{eq}:

$$\Phi_{eq} = \kappa_x \cdot \Phi_x \tag{4.23}$$

Here, κ_x represents the hardness factor, which is dependent on the type of incident particle and has been experimentally determined by [69].

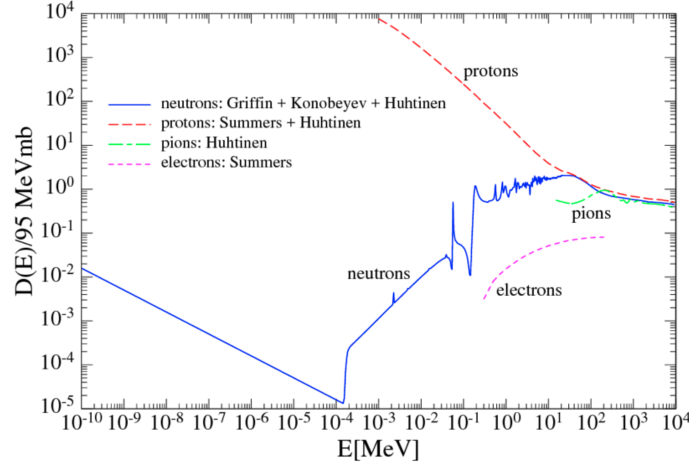

Figure 4.20: Displacement damage in silicon and hardness factor of different particles normalized to 95 MeV mb [73].

4.4.2 Effects on Detector Properties

The impact of radiation damage on sensor properties is of superior importance for this study. As the Micro-Vertex-Detector is designed to conduct research under exposure to a neutron equivalent fluence of $10^{14}\ \Phi_n\ \text{cm}^{-2}$ at 1 MeV, comprehending and verifying the alterations in its properties becomes crucial [10].

Full Depletion Voltage

An essential parameter directly affected by radiation damage is the full depletion voltage. This voltage, responsible for creating the active volume within the sensor, depends on the doping concentration of the silicon, specifically on the magnitude of the effective doping density N_{eff}.

$$V_{\text{dep}} = \frac{q_0}{2\epsilon\epsilon_0} \left| N_{eff} \right| d^2 \tag{4.24}$$

The effective doping density itself is highly influenced by the radiation, as reflected in the following formula:

$$N_{eff}(\Phi) = N_{D,0} \cdot e^{-c_D\Phi} - N_{A,0}e^{-c_A\Phi} + b_D\Phi - b_A\Phi \tag{4.25}$$

The concentrations of donors ($N_{D,0}$) and acceptors ($N_{A,0}$) before irradiation change due to irradiation, influenced by the factors for the generation (b_D and b_A) and annihilation (c_D and c_A) of dopants.The removal of donors and acceptors is induced by the formation of defect complexes, similar to the generation caused by the formation of defect complexes that assume positive/negative charge states in the space charge region [36].

However, in this process, donor removal dominates, resulting in a decrease in the full depletion voltage for an n-bulk silicon sensor at low neutron fluences

of approximately $10^{12}\,\Phi_n\,\text{cm}^{-2}$ while $N_D > N_A$. Beyond this turning point, the situation shifts, N_A becomes the dominating factor for the effective doping density. This behavior is referred to as type inversion, indicating a transition from n-type to p-type bulk sensor due to radiation damage. Subsequently, with increased irradiation levels, the full depletion voltage increases again due to its dependence on the absolute value of the effective doping concentration. This effect is examined and further explained in Section 5.5.4 [74], [75].

4.4.3 Thermal Annealing

Since the described radiation damages exhibit temperature dependency, their impact can be attenuated through heating. There are three observed regimes: stable damage, beneficial annealing, and reverse annealing. The beneficial annealing effect likely involves the creation of donors rather than the removal of acceptors. Consequently, this can lead to a partial reduction of radiation damage in the sensor, with the degradation primarily affecting donors. However, the combination of temperature and time can also introduce defects into the crystal lattice, contributing to the reverse annealing effect. If the annealing method is incorrectly applied or unintentionally triggered by incorrect ambient temperatures, reverse annealing can outweigh beneficial annealing, thus damaging the sensor properties.

The healing process was examined by the "Rose collaboration" [74], and it was determined that the optimal conditions for thermal healing are 60 °C for 80 minutes, as illustrated in Figure 4.21. The graph displays the dependence of the effective doping concentration on annealing time. Notably, there is a temporary reduction in concentration, which positively contributes to the recovery from radiation damage, particularly regarding the depletion voltage.

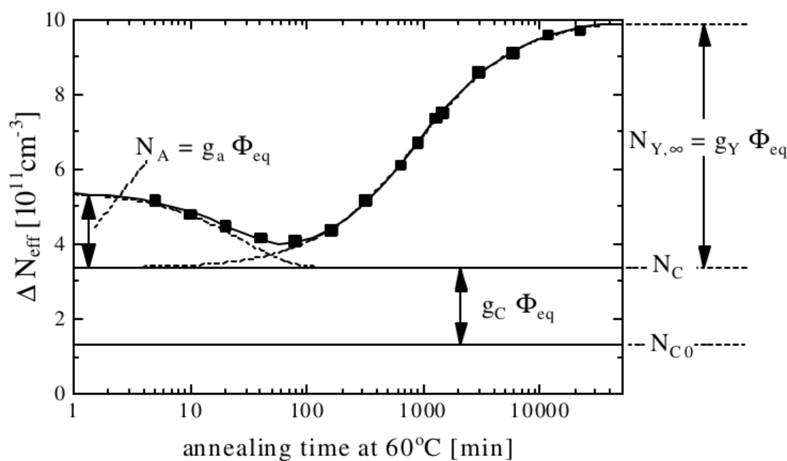

Figure 4.21: The change of the effective doping concentration ΔN_{eff} over time at an annealing temperature of 60 °C is illustrated in [74].

However, it must be noted that the annealing temperature is not precisely defined,

as annealing can occur above and below the sweet spot. Nevertheless, an exponential behavior of annealing with temperature and time is assumed [36].

Positive effects of annealing can also be observed for the leakage current. Taking beneficial annealing into account, the leakage current can be reduced, as experimentally shown in Figure 4.22.

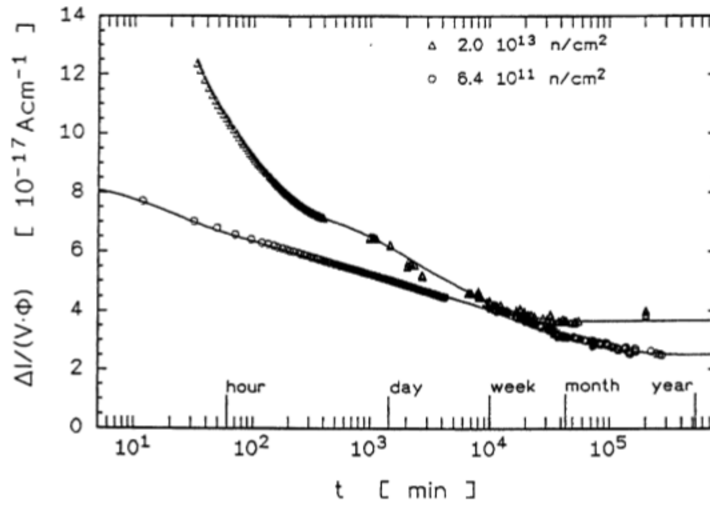

Figure 4.22: Change of the leakage current over time at 20 °C to investigate the annealing effect after irradiation with $2 \times 10^{13}\,\mathrm{n/cm^2}$ (upper curve) and with ($6.4 \times 10^{11}\,\mathrm{n/cm^2}$) (lower curve) [75].

The $\overline{\mathrm{P}}$ANDA test structures are also annealed after irradiation using temperature, and the effect is investigated in Section 5.5.5.

Reverse-Bias Current

The reverse-bias current, or leakage current, is also significantly influenced by radiation damage. However, its description is relatively straightforward since the change is solely caused by the generation of electron/hole pairs in the silicon bulk. The alteration in leakage current is directly proportional to the volume and the radiation exposure of the sensors and can be described by the following equation:

$$\frac{\Delta I}{V} = \alpha \Phi_{eq} \tag{4.26}$$

Where α represents the current-related damage rate. This factor does not appear to be dependent on detector properties such as p- or n-type sensors. Additionally, it seems to be identical for damage induced by protons, neutrons, or pions. However, α is influenced by the annealing method, which is explained in Section 4.4.3. For a standard annealing process at 60 °C for 80 minutes, the damage rate is:

$$\alpha_{80/60} = (3.99 \pm 0.03) \cdot 10^{-17}\mathrm{Acm}^{-1} \tag{4.27}$$

Consistent with the independence of the current-related damage rate from various sensor properties, the change in leakage current due to radiation exposure is also independent of these properties. This suggests that, regardless of the sensor type, the leakage current behaves similarly under radiation exposure. The relationship between leakage current and neutron fluence is clearly demonstrated, with each data point representing the response of an individual sensor to neutron irradiation, as shown in Figure 4.23.

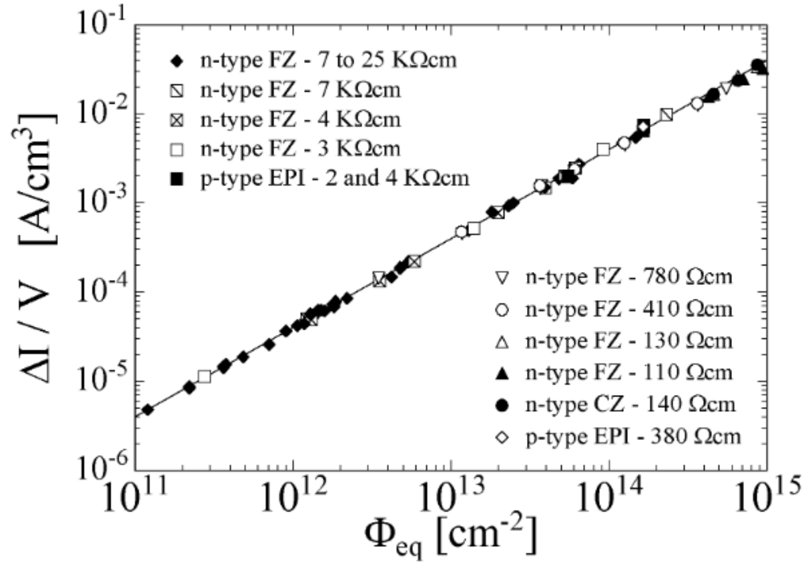

Figure 4.23: Dependence of the leakage current on the neutron fluence for various detector properties after annealing for 80 minutes at 60 °C [36].

The increase in leakage current with dose is examined for $\overline{\text{P}}$ANDA test structures in Section 5.5.4 and compared with the predictions.

4.4.4 Strontium-90

Strontium-90 ($^{90}_{38}$Sr) has a half-life of 28.8 years and undergoes beta decay [76]. In this process, a Strontium-90 isotope transforms into Yttrium ($^{90}_{39}$Y) by emitting an electron (β^-) and an antineutrino ($\bar{\nu}_e$), as shown in the decay series 4.28.

$$^{90}_{38}\text{Sr} \rightarrow ^{90}_{39}\text{Y} + \beta^- + \bar{\nu}_e \tag{4.28}$$

As seen in the decay series, beta decay involves the conversion of a neutron into a proton, emitting an electron (beta particle) and an antineutrino. The maximum energy of the ^{90}Sr β-particles is 545.9 keV.
Since the decay process also produces Yttrium, with its short half-life, it must be considered in the energy spectrum. Yttrium, in turn, has a half-life of 2.6684 days and also undergoes beta decay, transforming into Zirconium-90 (Zr-90) [76]. The decay results in β-particles with a maximum energy of 2,279.8 keV. The reaction equation is as follows:

$$^{90}_{39}\text{Y} \rightarrow ^{90}_{40}\text{Zr} + \beta^- + \bar{\nu}_e \tag{4.29}$$

In this process, an electron and an antineutrino are emitted once again. As the half-life of Zirconium-90 ($^{90}_{40}$Zr) is approximately 2.6 million years, its decay can be neglected during the irradiation with ^{90}Sr. Hence, during irradiation with ^{90}Sr, the overlap of electron energies from both ^{90}Sr and ^{90}Y decay must be considered, as investigated by Dixon, Rajan, Bohlemann, *et al.* [77] and illustrated in Figure 4.24.

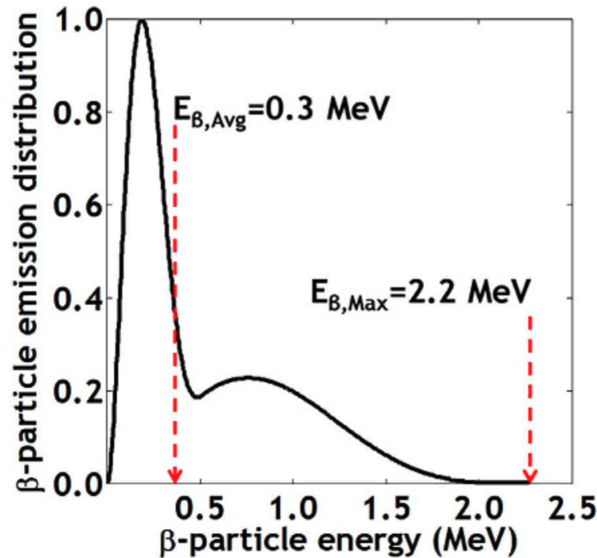

Figure 4.24: Normalized energy spectrum of β-particles emitted by the sequential decay of ^{90}Sr and ^{90}Y [77].

The figure indicates that the energy mean value of the overlay of beta decays is expected to be 0.3 MeV, with a maximum energy of approximately 2.2 MeV.

4.5 Surface Defects

The surface defects in a semiconductor occur through the open crystal lattice that has open bonds due to a cut or the end of the semiconductor. This effect can be minimized by implementing guard rings (Section 5.1.5) in the sensors. The surface of the active area, which is not excluded by the guard rings, has often a passivation layer applied. The insulation layer for silicon is often an oxide layer (SiO_2). This layer already has defects during manufacture, but these have no effect on the sensors. However, the ionization process, which also takes place in the oxide layer, is problematic. Due to the larger band gap of the insulator, the charge cannot flow off. Because of the different mobility of electrons and holes, positive charge carriers accumulate between the oxide layer and the silicon layer. The resulting electric fields can influence the fields of the sensor as well as the interstrip resistance and the interstrip capacitance.

Chapter 5

Characterization of $\overline{\text{P}}$ANDA Double-Sided Silicon Strip Sensors

The following section examines the properties of silicon strip sensors intended for the Micro-Vertex-Detector (MVD) of the $\overline{\text{P}}$ANDA experiment. However, the primary focus of this chapter is on the serial testing of the test structures, aimed at ensuring the quality of all sensors designated for installation in the MVD experiment. Additionally, irradiation tests are conducted to evaluate sensor performance over the lifetime of $\overline{\text{P}}$ANDA. Before delving into these tests, the measurement setups and methods are developed and discussed.

To characterize the sensors, standard methods for determining the properties of silicon detectors are employed, with a particular focus on capacitance and impedance measurements at various reverse bias voltages. These measurements are conducted in the probe station at University of Giessen (JLU), which facilitates precise contact with the sensors or diodes under controlled conditions. The specific measurement technique depends on the parameter being measured.

To determine the full depletion voltage, breakdown voltage, or leakage current, both the front and back sides of the diode or sensor must be contacted in order to apply the reverse bias. Once contact is successfully established, capacitance measurements can be used to assess the variation in capacitance as a function of voltage, providing insights into the depletion region. Simultaneously, monitoring the current enables the determination of leakage current and, if applicable, the breakdown voltage.
In addition, using needle probes within the probe station allows for precise contact with various components of the sensor, enabling the measurement of additional parameters, such as coupling capacitance or polysilicon resistances.

These different measurement methods serve to confirm the functionality of the sensors and determine key operational parameters. Therefore, it is essential to conduct these measurements with the highest level of precision.

5.1 Measurement Setup

The following sections provide a detailed overview of the methods used. This includes the development of a measurement program to ensure consistent measurement conditions, optimization of contact conditions, and data analysis using fitting methods. First, we examine the measurement program that enables the simultaneous variation of the voltage and the measurement of, for example, capacitance, voltage and leakage current.

The voltage is provided by a Keithley 2410 source meter with a maximum output voltage of 1100 V, while the current is measured continuously. Simultaneously, an impedance measurement is carried out using an LCR meter (Sourcetronic ST2826). To coordinate the two devices, a program in C++ was developed, facilitating serial commands transmission and receipt of measured data from the devices. This automation enables series measurements and minimizes measurement errors.

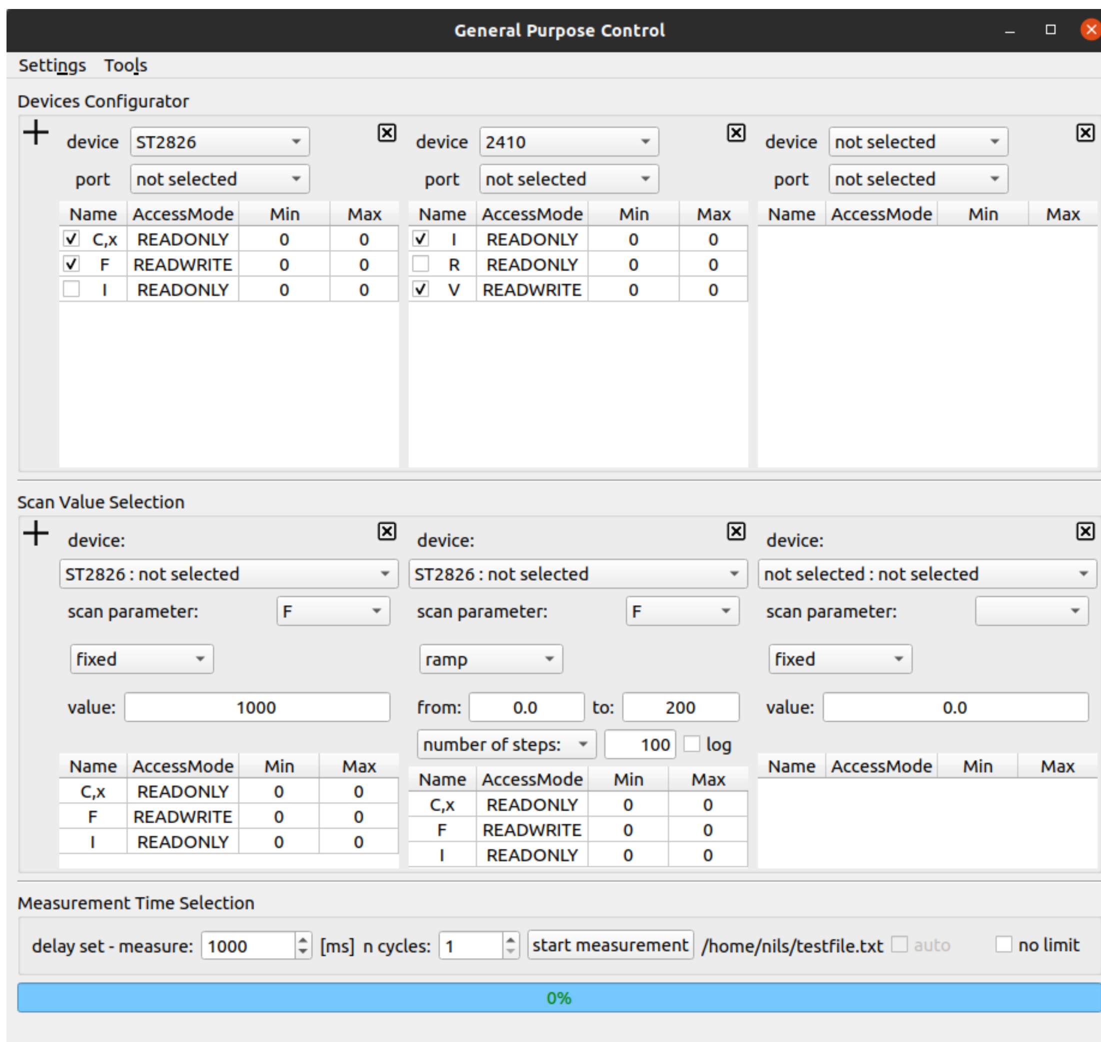

Figure 5.1: Interface of the General Purpose Device program, which is utilized for the subsequent measurements and operates on a Raspberry Pi.

The challenge lies in the disparate control commands and data output formats of the devices. The program addresses this by parsing and extracting the necessary information from each device's data string, which can then be saved in .csv format.
With this program, parameters can be ramped or held during measurements, and different parameters can be ramped simultaneously. An essential feature for sensor behavior is the implementation of a delay time between value setting and measurement, considering the pn-junction's operation similar to a capacitor, necessitating consideration of the charging and discharging processes.
Therefore, a customizable delay time was integrated to trigger the readout process. Additionally, the program offers easy integration of other devices, allowing multiple devices to be controlled simultaneously. Another notable function is the ability to query various parameters of a device.
For example, the Sourcetronic ST2826 LCR meter can operate in capacitance measurement mode, measuring capacitance C_P and quality factor D, or in resistance mode, measuring impedance $|Z|$ and phase angle φ. The program runs on Linux and Microsoft platforms and operates on a Raspberry Pi 4B 4Gb for the measurements.
In Figure 5.1, the graphical user interface of the program is shown, where both device control and measurement parameters can be configured. Since its completion, the program has been utilized for various other experiments, proving to be an extremely useful tool.

The LCR meter operates within a frequency range of 20 Hz to 5 MHz, with an accuracy of 0.1 %. Given the need to measure small capacitances precisely, it is vital to minimize any parasitic and stray capacitances. To achieve this, four-wire sensing was used, which separates the current and voltage electrodes to eliminate lead and contact resistance from the measurement. In this setup, the stimulus is applied to the outer contacts (H1 and L1), while the inner ones (H2 and L2) sample the voltage with high impedance at the Device Under Test (DUT). This configuration ensures that when measuring sensors with the probe card mentioned later, the measurements are highly accurate because sensing occurs precisely at the contacted DUT, minimizing all disturbances.
However, when dealing with diodes or unbonded sensors, parasitic/stray capacitance may arise due to contacting. Even in a clean room environment, there's a risk of dust or other disturbances between the contact and the DUT. To mitigate errors, all measurements are conducted with the probe station of the group at JLU. With this setup, the DUTs can be contacted with up to six needles, or the back side can be contacted with the chuck.

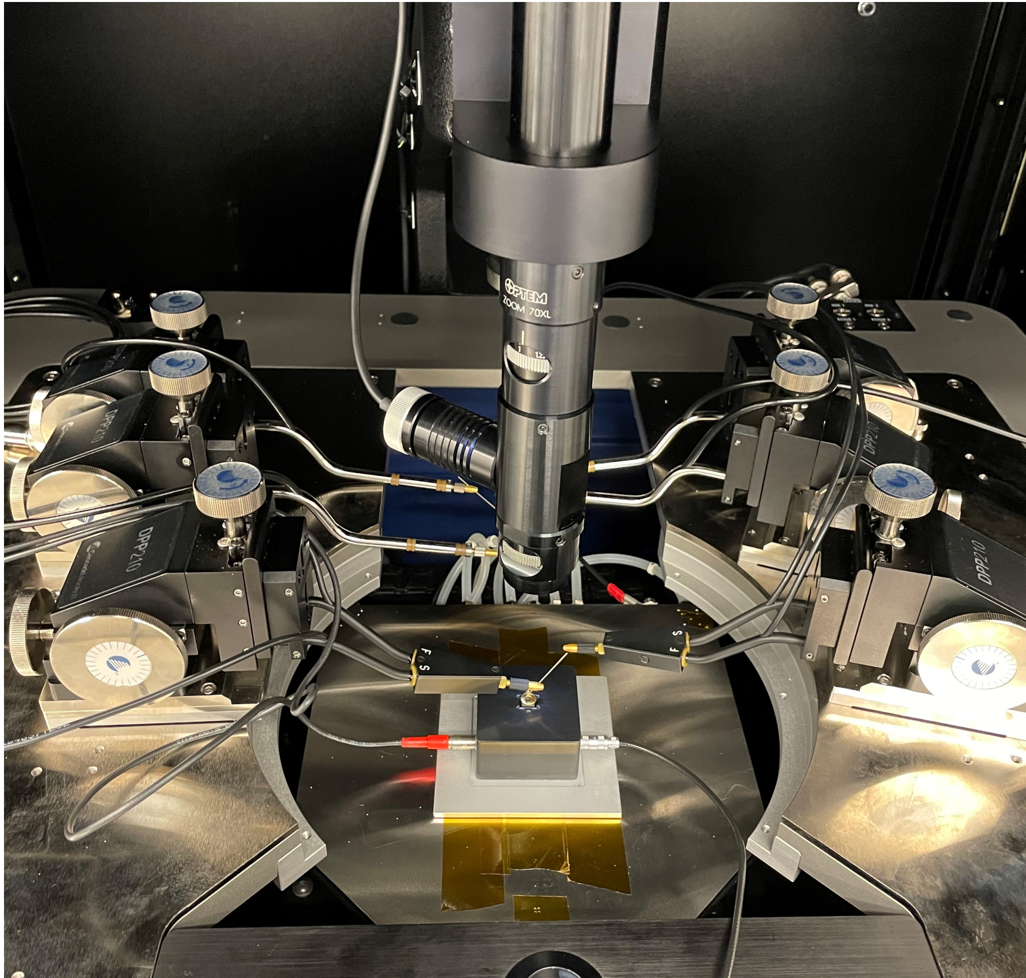

Figure 5.2: The probe station in the clean room consists of needles, the chuck positioned at the bottom, the diode measurement setup in the middle, and the observation system located on top.

The setup shown in Figure 5.2 is designed to ensure protection from light and electrical shielding, essential for conducting precise measurements. Equipped with a movable chuck, the probe station allows precise positioning of the DUT in all directions, with movements as small as a few microns. Notably, the chuck's positions, particularly its height, can be stored and reproduced, facilating the process of serial measurements. Additionally, each needle can be individually adjusted by hand using micrometer screws. The entire measurement process can be monitored via a camera and lens system, as well as through the previously mentioned program.

Another challenge arises from the precise connection of diodes, primarily due to passivated areas on the diode surface. Specialized measurement setups, as discussed in Chapter 5.1.1, are employed to tackle this issue. Additionally, safeguarding the LCR meter from the high voltages generated by the source meter is crucial. For this purpose, a bias box is utilized, which integrates four series capacitors (C_C), each with a capacitance of 100 nF and a rated voltage of 400 V.

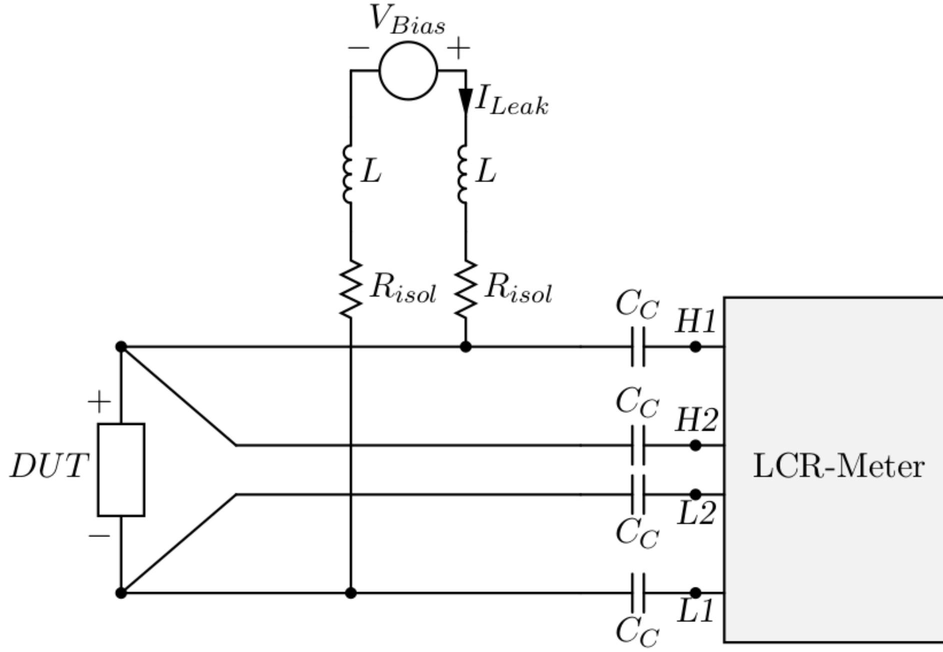

Figure 5.3: Diagram of the bias box designed to shield the measurement setup from over voltage, utilizing four series capacitors C_C for isolation [38].

In Figure 5.3, the schematic of four-wire sensing is depicted, illustrating how the LCR meter can measure parameters such as impedance, capacitance, or phase angles. The bias voltage supply V_{Bias} and the measurement of the leakage current I_{Leak}, managed by the source meter, are also visible.

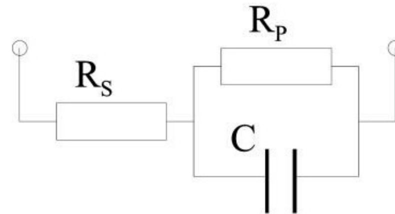

Figure 5.4: Scheme of the parallel two-port model [78].

Another important factor is the dissipation factor D or quality factor Q. Since the description of the diodes and sensors is best portrayed with the two-port model, where series resistance is negligible, the dissipation factor can be defined as:

$$D = \frac{1}{Q} = tan\sigma = \frac{Re}{Im} = \omega C_s R_s = \frac{1}{\omega C R_p} \tag{5.1}$$

The quality factor Q represents the ratio of reactance to resistance at a given frequency. A lower dissipation factor or a higher quality factor indicates that the pn-junction behaves more similar to an ideal capacitor. This behavior is favorable as it signifies a reduced energy loss rate and hence better accuracy. R_s denotes the

equivalent series resistance (ESR), which reflects the losses in the capacitor. R_p stands for the shunt resistance of the capacitor C under investigation. However, this relationship is only valid for sufficiently large values of R_p. Throughout the measurements, careful attention was paid to maintaining a small D factor, thereby resolving issues such as contact problems during the measurements.

5.1.1 Diode Measurement Setup and Accuracy of Measurements

The objective is to measure the depletion voltage with minimal systematic errors resulting from the setup. As previously mentioned, accuracy is crucial in determining the doping density and the resulting sensor properties. Common issues include weak electrical connections, temperature fluctuations, and physical pressure gradients at the probe. Additionally, it is important to highlight that the measurements are conducted in complete darkness. A typical test structure of a detector is a diode cut from the same wafer as the sensors.

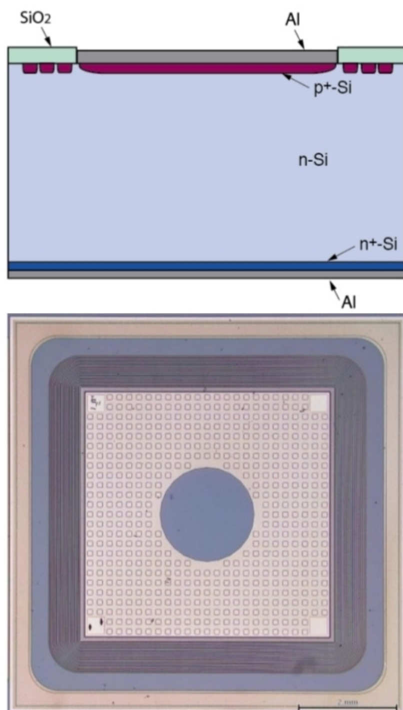

In Figure 5.5, the cross-section of a diode is compared to a photograph of the top view of an MVD diode. Aside from the round passivation layer of SiO_2 in the center of the diode, which is marked in dark, the two are nearly identical. A passivation layer on the back side of the diode has also been omitted in the sketch.
It is important to note that the thickness of the aluminum and SiO_2 layers may vary slightly. This variation can significantly affect the connection and, consequently, the measurement accuracy. For precise measurements, the aluminized layers of both the p- and n-sides must be contacted. The guard rings surrounding the active diode area are clearly visible, providing shielding against surface defects.

Figure 5.5: The top figure shows a sketch of the diode cross-section, while the bottom features a photograph of the top view of a $\overline{\text{P}}$ANDA MVD diode with an active area of approximately 25 mm^2[79].

As previously mentioned, the Sourcetronic ST2826 LCR meter and Keithley 2410 voltage source are utilized for the measurements. The low capacitance, ranging from 10-100 pF, demand significant measuring accuracy. However, traditional probing methods with needles have proven problematic, leading to physical stress and varying electrical connections depending on the needle's placement and contact force.

In particular, using the chuck as a counter electrode presents challenges. The SiO_2 layer interferes with effective contacting when the diode is placed solely on a flat surface. Moreover, conventional probing tips cannot contact the center of the diode due to the passivation layer, increasing the resultant pressure on the passivated outer layers.
In the following, capacitance measurements on diodes with reverse bias voltage for different setups are exemplified. C_b represents the capacitance of the depletion region of the diode, which varies as the reverse bias voltage increases, ultimately reaching full depletion. The dissipation factor D, which quantifies the energy loss in the dielectric material, is used to assess the accuracy and reliability of the capacitance measurement, ensuring minimal loss and high measurement quality.

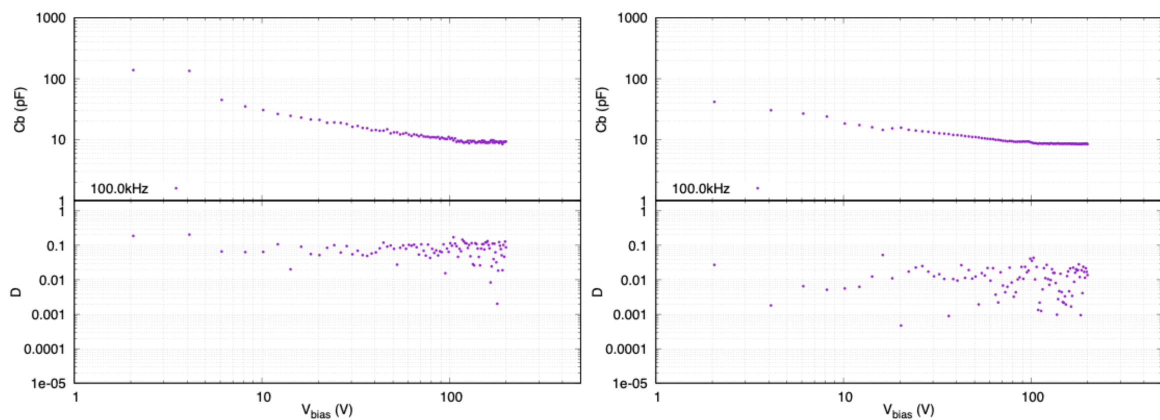

Figure 5.6: Needle-to-chuck connection measurements, with light and electric shielding on the right-hand side and without shielding on the left.

This involves a measurement conducted without electrical and light shielding. As expected, the left plot in Figure 5.6 shows insufficient accuracy in the measurement, resulting in a very high D-factor, and important key features such as the depletion voltage are not recognizable.
In the right plot of the figure, shielding was ensured in the probe station, and the measurement was conducted using a conventional probe. This time, the accuracy is significantly improved, and the full depletion voltage is clearly observable. However, the measurement remains too imprecise for an accurate determination.

After implementing light shielding, several connection options were tested to improve accuracy. Promising options, such as adhesive electrodes or electrodes with exact outer dimensions matching the diodes, showed improvement but were ultimately unsatisfactory. Replicated measurements revealed differences of up to 20 V in the depletion voltage, indicating a 20 % error.
The tests indicated that variationsin the contact force and different contact points, which led to different forces within the diode, resulted in inconsistencies when the measurement was repeated. It is possible that the passivated surface of the diode is disrupting the contact, contributing to the observed challenges.

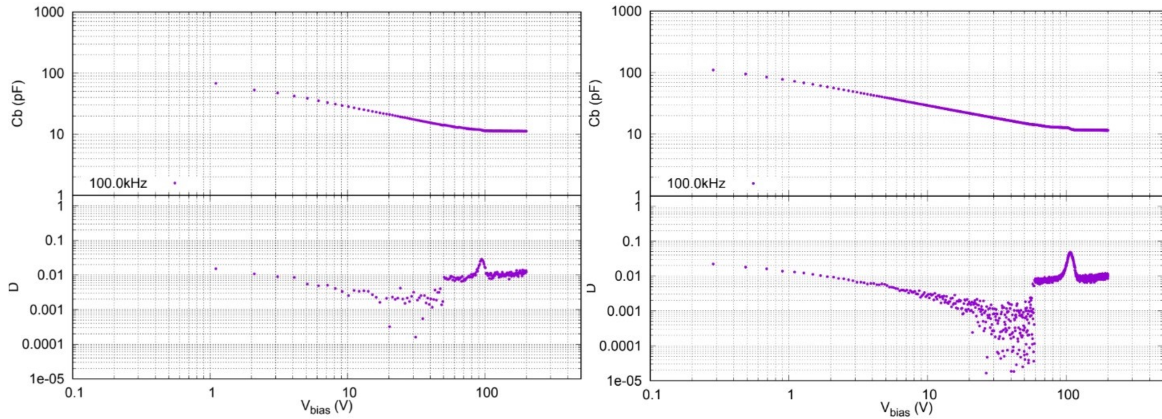

Figure 5.7: On the left-hand side, a diode measurement is shown, in which an aluminum block of the same size as the diode is used to make electrical contact with the entire diode area and ensure an evenly distributed contact force by placing it directly on the diode. On the right-hand side, the measurement was conducted using the final setup described below.

The accuracy is significantly improved, primarily attributable to the improved contacting method. In the left figure of 5.7, the depletion voltage is clearly discernible. Additionally, the peak corresponding to the very low D value is distinctly visible at the same position. However, a challenge with this method, as mentioned earlier, is reproducibility. This arises from the uneven distribution of contact pressure and the inability to entirely exclude the smallest edges of the otherwise flat electrode. Consequently, there could be a connection between the electrode and the passivated layer of the diode, leading to significant measurement errors.

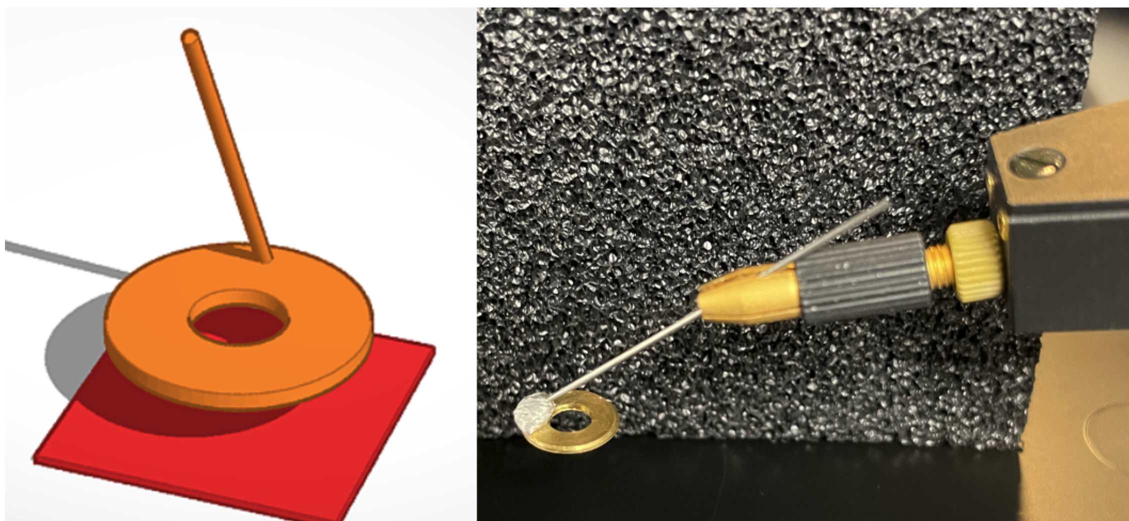

Figure 5.8: In the sketch on the left, the round electrode is shown above the square diode. The electrode consisting of a round surface similar in size to the active area of the diode. A circular hole in the center of the electrode excludes the passivated layer in the middle of the diode surface. This ensures both optimal electrical contact and an even distribution of the contact force. On the right, a photo of the final setup is shown.

The round electrode depicted in Figure 5.8 is directly connected to the bias box. Similarly, the counter electrode is also connected in this manner. The counter electrode is also circular, and the diodes are placed on it in such a way that no passivated layer comes into contact with the electrode. The measurement cycle is completed when the top electrode applies pressure to the diode (p-side). This configuration ensures contact only with the aluminum surface and not with the passivated parts of the diode. Special attention was paid to ensure that the contact pressure is applied to the center of the diode. Additionally, the circular electrode design ensures contact is made exclusively with the aluminum contact surface of the diode.

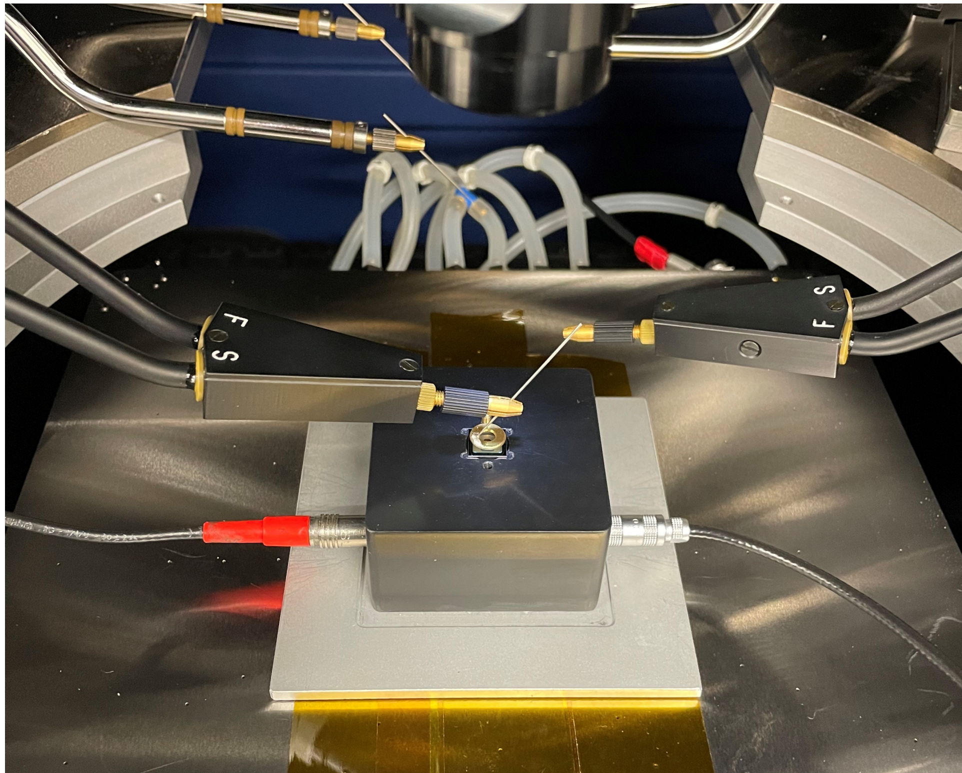

Figure 5.9: The back side (n-side) of the diode is connected using a circular beryllium copper electrode. Simultaneously, a circular needle exerts pressure on the front side (p-side) of the diode.

The setup depicted in Figure 5.9 shows the final measurement setup for the subsequent series measurements in Chapter 5.4.1. At the same time, the physical pressure of contact can be minimized with the help of the probe station and the micrometer screws.

In Figure 5.7, on the right, the results are displayed. The plateau of the depletion voltage and the peak at the D trail are clearly visible. Moreover, the D-factor is notably low, as discussed earlier, which is essential for precise measurements. Lastly, the measurements exhibit high reproducibility. Ten sets of measurements were conducted with a reverse bias voltage step size of 0.1 V, using a measurement

frequency of 100 kHz. Following each test, the same diode was disengaged from the setup and reconnected. The results, depicted in Figure 5.10, for the clipped section of the beginning of the depletion voltage, reveal a maximum error of 0.3 V and a standard deviation of 0.108 V within the 10 measurements. The depletion voltages are highlighted in red, with one measurement curve represented in dark blue, and the associated error depicted in light blue.

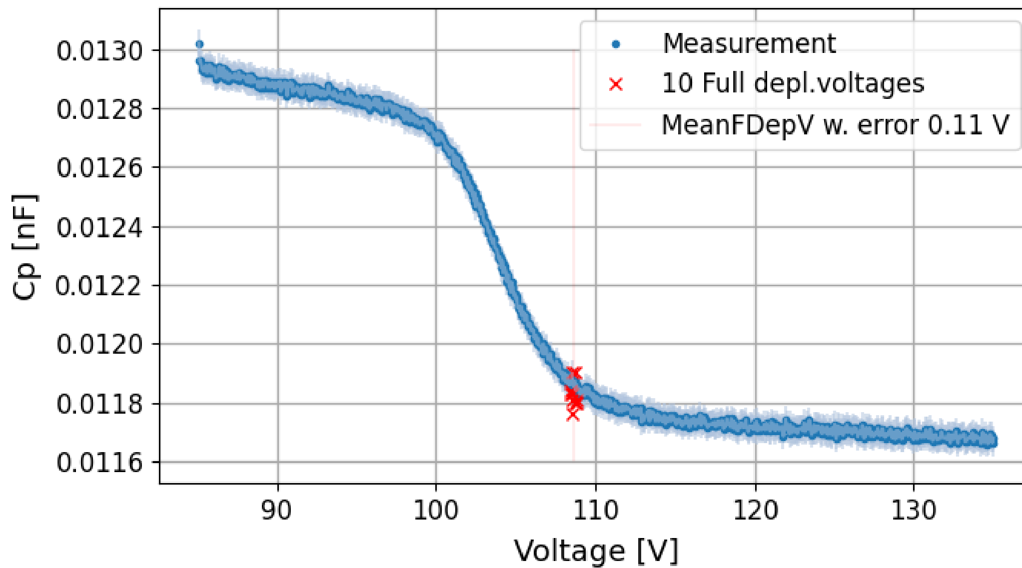

Figure 5.10: Accuracy measurement with the standard deviation error of ten measurements with the same diode. In red, the estimated depletion voltages, calculated with a fit (description in Chapter 5.1.2) of every series.

5.1.2 Verification of Depletion Voltage

In order to determine the most important parameters such as depletion voltage and the associated capacitance and current from the data, two fitting methods were developed to ensure accuracy.

The first method utilizes a cutout of the measurement data. In the vicinity of the depletion voltage, the capacitance experiences a significant drop over a few volts, as depicted in Figure 5.10. This dip is utilized to create a linear model and a step model. These models are then combined to achieve a precise fit to determine the onset of the depletion plateau. It is important to note that this model is applicable only for highly accurate measurements. If the measurement accuracy exceeds 5 V, the dip becomes less distinct, rendering the fit unreliable. Moreover, poor contacting or frequency-dependent jumps in the measurement can cause the dip to shift. Nonetheless, with precise measurement data, this method yields highly accurate results.

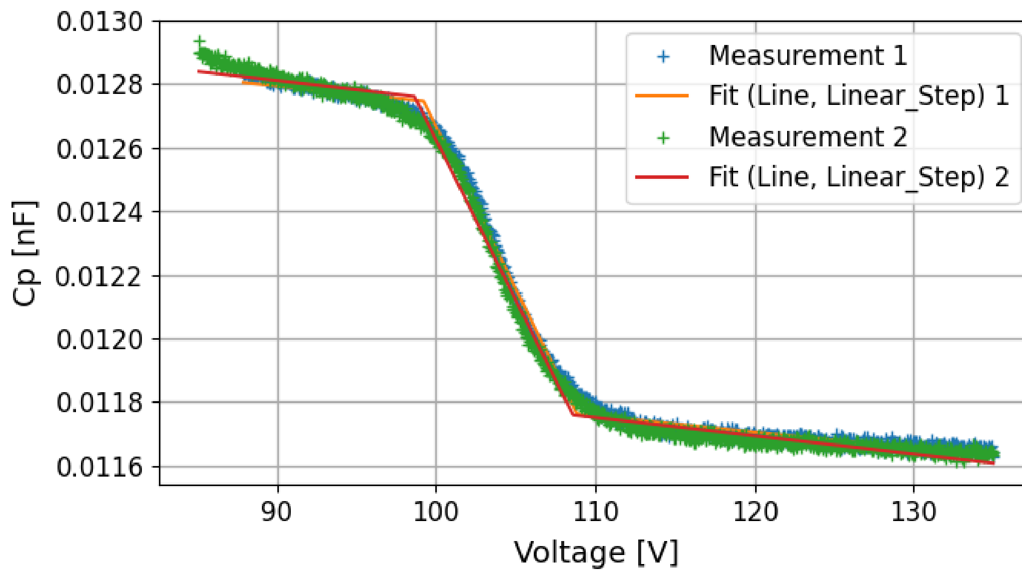

Figure 5.11: Two excerpts from two series measurements (cross) of the same diode were applied and evaluated with a fit method (lines).

In Figure 5.11, the fit of the measurement is depicted by colored lines, while the data points are marked with crosses. The linear model was chosen due to the linear shape of the curve after reaching the depletion voltage, as well as the linear drop upon reaching the depletion voltage. The model is defined as follows:

$$f(x; m, b) = mx + b \tag{5.2}$$

The step model was selected due to the distinct steps observed in Figure 5.11. To fit the curve, at least two steps are required to fit the step sections using linear fits. The first step occurs just before the "depletion dip", while the end of the dip marks the second step. Between these steps, the linear fit is applied. Firstly, the region before the dip, then the dip itself, and lastly, the depletion plateau. The depletion voltage can be determined by finding the zero of the second derivative of the combined fit function. In literature, the depletion voltage is often determined by the intersection point of the linear fit of the "depletion dip" and the plateau, which is equivalent to the described method. The fit functions perform well, as evidenced visually in Figure 5.11 and supported by the fit report. This method was also utilized in Figure 5.1.1, where the same diode was measured ten times. The fit results indicated a mean error of 0.108 V between the measurements. Hence, it is reasonable to assume that the fit model can accurately determine the depletion voltage with more precise measurements.

A second fit model was employed to facilitate enhancements in the fit when encountering jumps in the measurement or less precise measurements. These jumps are sporadic and dependent on frequency. Thus, a fit resembling models found in literature ([80], [81], and [82]) was utilized, which has proven to be

effective. This method was also applied to analyze the series measurements conducted by the company CiS GmbH in Erfurt (CiS).

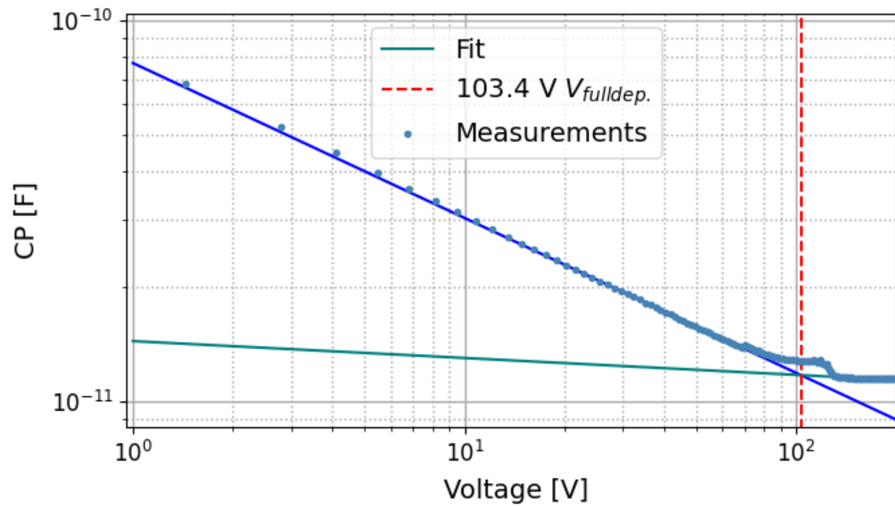

Figure 5.12: The capacitance as a function of reverse bias voltage measured for a $\overline{\text{P}}$ANDA diode (marked as a cross). Two fitted lines are shown in color, and the dotted line in red indicating the full depletion voltage is marked at the intersection of the lines.

In the fit example 5.12 of a measured diode, the use of two fitted lines can be observed. The turquoise line represents the extended depletion plateau obtained by averaging all its values and determining the slope. Crossed with it is the blue line, which depicts the extended linear curve in the double logarithmic scale. For the fit of the blue line, the slope of the measurement data between 10 V and 80 V was utilized. The crossing point of the two lines, marked in red, represents the full depletion voltage.
It has been demonstrated that both methods work very effectively. For highly accurate measurements, which can be ensured by bonded contacts, the first method described is utilized. For instance, for serial tests or less precise measurements, the second method is employed.

5.1.3 Setup of Sensor Measurements

The measurement of the Silicon Sensors is clearly more complex due to the structures on both sides. Unlike diodes, where only the capacitance and the current of the entire DUT can be measured, sensors allow for the measurement of additional parameters such as strip capacitance, strip leakage current, interstrip capacitance, coupling capacitance, resistance between the strips, resistance between the strip and the bias line, and more for both sides.
However, due to the double-sided layout, establishing a connection to the back side is very challenging. It has been found that the only feasible option for the probe station measurements is to connect the sensors with bonding wires. This

ensures that each strip is connected correctly and that the entire sensor can be measured. To facilitate this, a so-called probe card was utilized, allowing for easy connection of every $\overline{\text{P}}$ANDA sensor to the measuring setup.

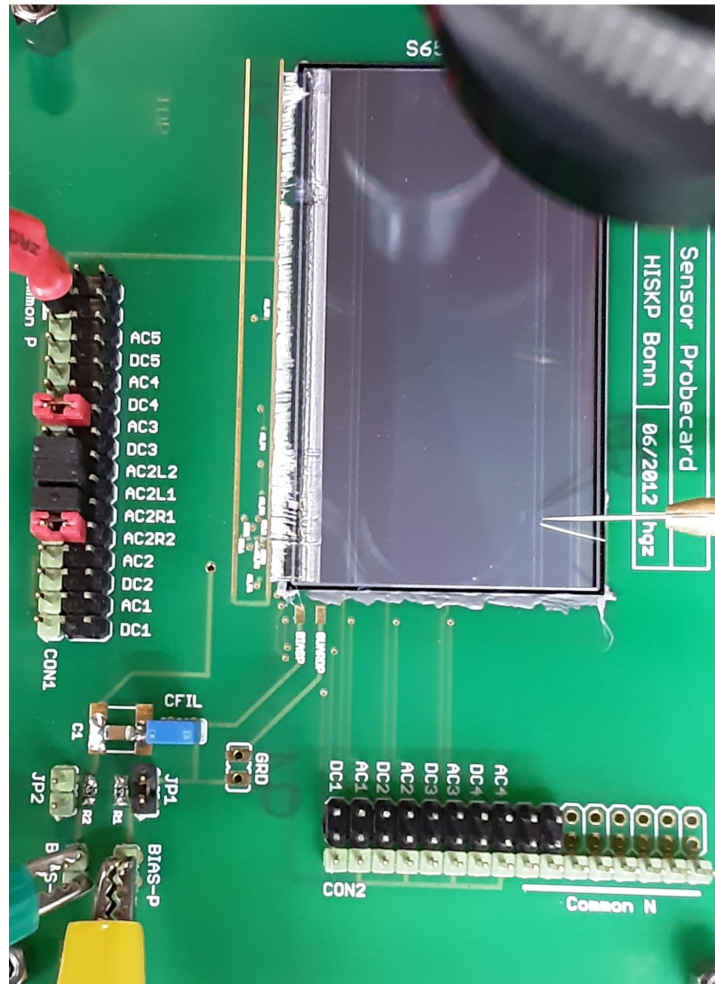

Figure 5.13: Probe card with bonded sensor and needle setup in the probe station with observation system on the top right. The reverse bias voltage is applied on the bottom left.

In Figure 5.13, an S1 sensor is bonded to a probe card. This image illustrates the measurement between a needle and the probe card. It is also possible to conduct measurements with up to 6 needles or without any needle. Most importantly, the reverse bias voltage can be separately applied due to bonding wires connected to the bias pads of the sensor. Not shown in the picture is the connection with the back side, like the front side, every strip is connected to the probe card.
Using a probe card is necessary to determine the characteristics of the sensors with our possibilities. However, it must also be mentioned that every sensor bonded to the device can't be used for the detector. Therefore, only some sensors are sacrificed, representative of all sensors in the same production lot. As a result, only exemplary measurements of the sensor properties will be shown later. The main serial testing will be performed with the diodes, which have no tasks other than for testing purposes.

5.1.4 $\overline{\text{P}}$ANDA MVD Silicon Strip Sensors

In the following, the basic properties of the silicon strip component of the MVD are discussed. The double-sided silicon strip detectors are radiation-hard sensors with a target thickness ranging from 200 to 300 µm. The working principle will be outlined in Section 5.1.6. These detectors are commonly used as tracking detectors in particle physics. Due to the mesh formed by the double-sided layout with orthogonal strips, the position of the particles can be detected with high accuracy. The $\overline{\text{P}}$ANDA sensors are manufactured by the company CiS GmbH in Erfurt (CiS), Germany. In Figure 5.14, a 4"-inch wafer cut in $\langle 111 \rangle$ orientation can be seen, which is then cut into the sensors and test structures. The properties of these structures are listed in Table 5.15.

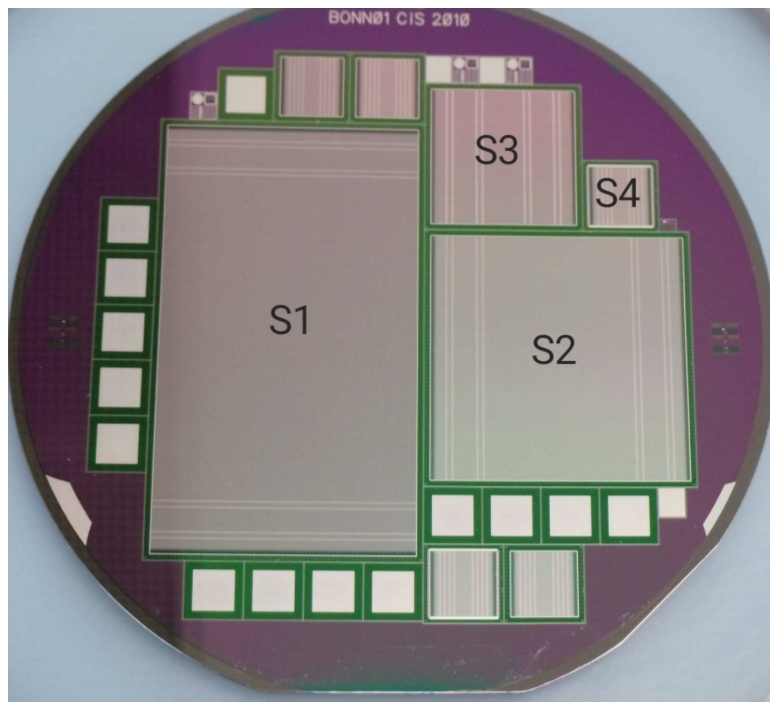

Figure 5.14: 4"-Wafer with the $\overline{\text{P}}$ANDA sensors and test structures.

The wafer material consists of mono crystalline floating zone silicon, with the front side strips implemented as p+ implants in an n-doped substrate. On the back side, n+ implants form the strips embedded in an n-substrate. Eight guard rings are incorporated to ensure a stable electric field by delimiting the active area from the cutting edges.

general	
wafer material	FZ Si, 4", n/P
thickness	285 ± 10 µm
resistivity	2.3-5.0 kΩ·cm
n-side isolation	p-spray
guard rings	8
stereo angle	90°
passive rim	860 µm
S1	
n-side strips	512
p-side strips	896
pitch	65 µm
active area	$58.275 \times 33.315\,\mathrm{mm}^2$
S2	
n-side strips	512
p-side strips	512
pitch	65 µm
active area	$33.315 \times 33.315\,\mathrm{mm}^2$
S3	
n-side strips	384
p-side strips	384
pitch	50 µm
active area	$19.230 \times 19.230\,\mathrm{mm}^2$
S4	
n-side strips	128
p-side strips	128
pitch	65 µm
active area	$8.355 \times 8.355\,\mathrm{mm}^2$

Figure 5.15: Specifications of the silicon strip sensors [10].

Figure 5.14 illustrates the cutting of a wafer into S1, S2, S3, S4 sensors, and test structures. The largest sensors, S1 and S2, are full-size sensors, with one of each being cut from a wafer and which will be used for the final MVD setup. Additionally, each wafer yields one S3 sensor, five S4 ("Baby Sensor") sensors, and fourteen test structures, referred to as diodes hereafter. These diodes are tested as representatives of the sensors, as the properties of the entire wafer should be consistent. Consequently, destructive radiation tests can be performed without compromising sensors. Only sensors that meet defined limits are used in the $\overline{\text{P}}$ANDA detector to ensure error-free operation.
The first limitation concerns the global leakage current, which must not exceed 10 µA below the breakdown voltage. Secondly, the breakdown voltage must be at least 50 V higher than the maximum anticipated bias voltage of 200 V. Lastly, the capacitance of the entire sensor must exhibit full depletion above the depletion voltage.

The methods for determining the parameters of the sensors are described in Chapter 5.1.6. The manufacturer of the sensors also conducted measurements for each sensor, including full depletion voltage, leakage current, and broken strips. These results will be compared and evaluated in Chapter 5.4.1, which serves as a representative analysis for the sensors alongside the diodes discussed in Chapter 5.4.

5.1.5 Structure of the $\overline{\text{P}}$ANDA Strip Sensors

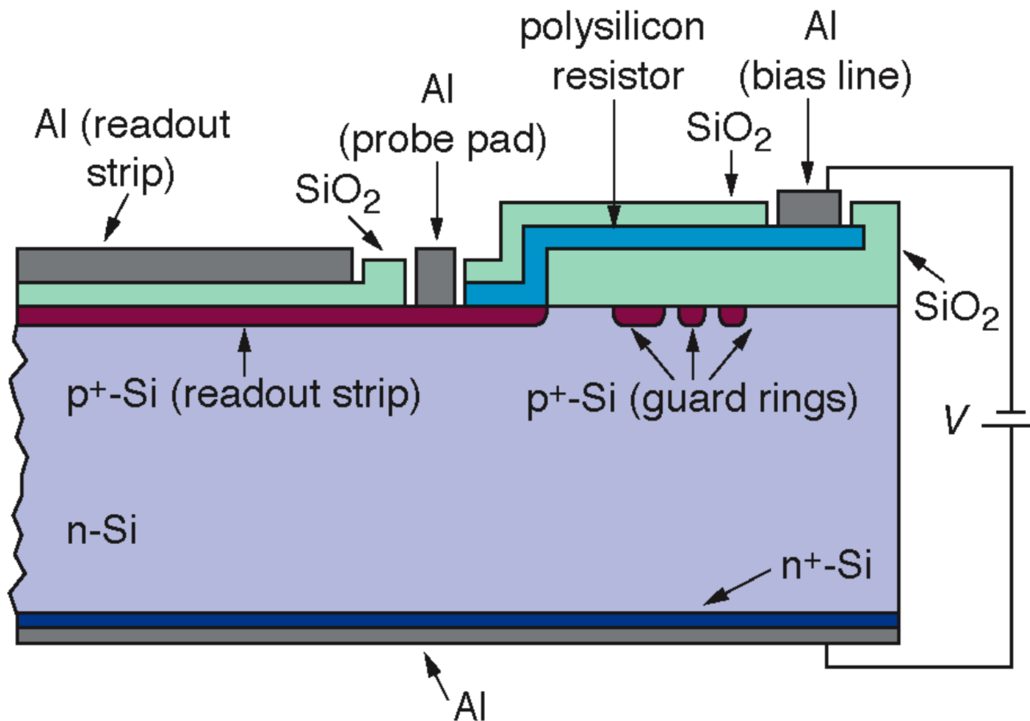

Figure 5.16: The schematic illustrates a cross-section of a Si-sensor, with the p-side at the top and the n-side at the bottom [83].

The complex sensor structure is depicted in Figure 5.16. In the following, the different features will be explained.

Guard Ring
: Guard rings are positioned near the detector border to minimize leakage currents caused by crystal defects in the cut edges. These rings serve to protect the detector from voltage flash overs on the back side. Inside the rings, the active area of the sensor is enclosed by at least one guard. Guard rings are typically p+ implants at the same potential as the active p+ implants.

Bias Ring
: For proper operation, the entire active surface must be biased to the reverse potential. This is achieved through a bias ring made of aluminum, which supplies the applied voltage to every strip via special resistors. Another method for biasing the strips is the so-called punch-through method, which, however, is not used for the $\overline{\text{P}}$ANDA sensors and can be referenced in the source [83].

Polysilicon Resistors
: The mentioned resistors supply the strips with the applied voltage without disturbing signal extraction. With resistances as high as 20 MΩ, the resistors

provide sufficient isolation of the signals collected at the strips electrode from the low impedance of the bias supply.

Silicon Readout Strips

Readout strips are highly p-doped silicon implants designed to collect the space charge generated by events. Test measurements can be conducted using the so-called DC or probe pad, which is an aluminum pad positioned directly above the strip. However, due to the electrical resistance of the implant, signal readout must be facilitated by an additional system. The Si-Readout Strips are directly connected to the reverse bias voltage using the polysilicon resistors.

Aluminum Readout Strips and AC Pad

Signals can be read out by the AC pad, which is a bonding pad connecting an aluminum strip with the readout electronics. Positioned directly above the entire readout strip, the strip picks up the signal capacitively (through capacitive coupling capacitance). An SiO_2 layer separates the two strips, allowing the sensor to be measured without interference from the measuring instruments. With a thickness of 100-200 nm, typical capacitance range from 8-32 pF/cm. However, pinholes in the dielectric, which allow the strips to be connected, can potentially lead to strip failure.

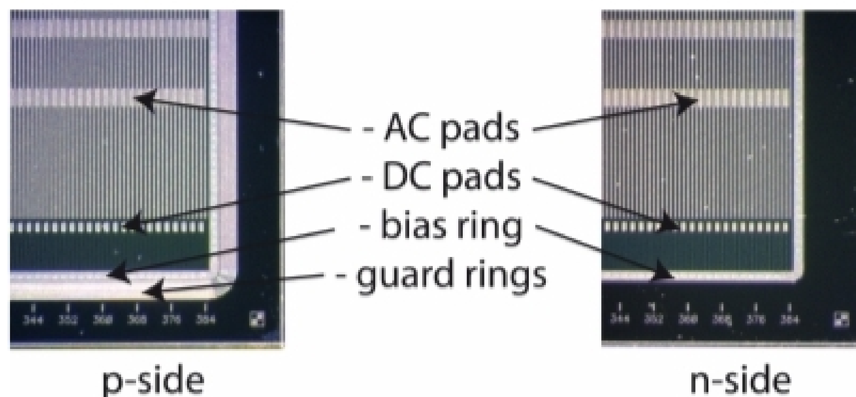

Figure 5.17: The p- and n-side of a double-sided silicon strip detector.

The back side of the detector (n-side) is not depicted in illustration 5.16. It mirrors the front side, with the readout strips made of n+ implants, while only the p-side features guard rings. Figure 5.17 displays a typical structure of a double-sided silicon detector, highlighting the most important components for measurements. The aluminum-coated pads are connected with bond wires for testing or operation. Regardless, the voltage must be supplied by the bias ring. Hence, the bias ring is also equipped with bonding pads on the p- and n-sides. The generation of this signal is explained in the following Chapter 5.1.6.

5.1.6 Working Principle of Si-Strip-Sensors

Fast charged particles can ionize silicon atoms, generating free charge carriers in the n-bulk-silicon. Ideally, there are no other electrons or holes in the depletion zone of the sensor, allowing the charges to be measured at the electrodes.

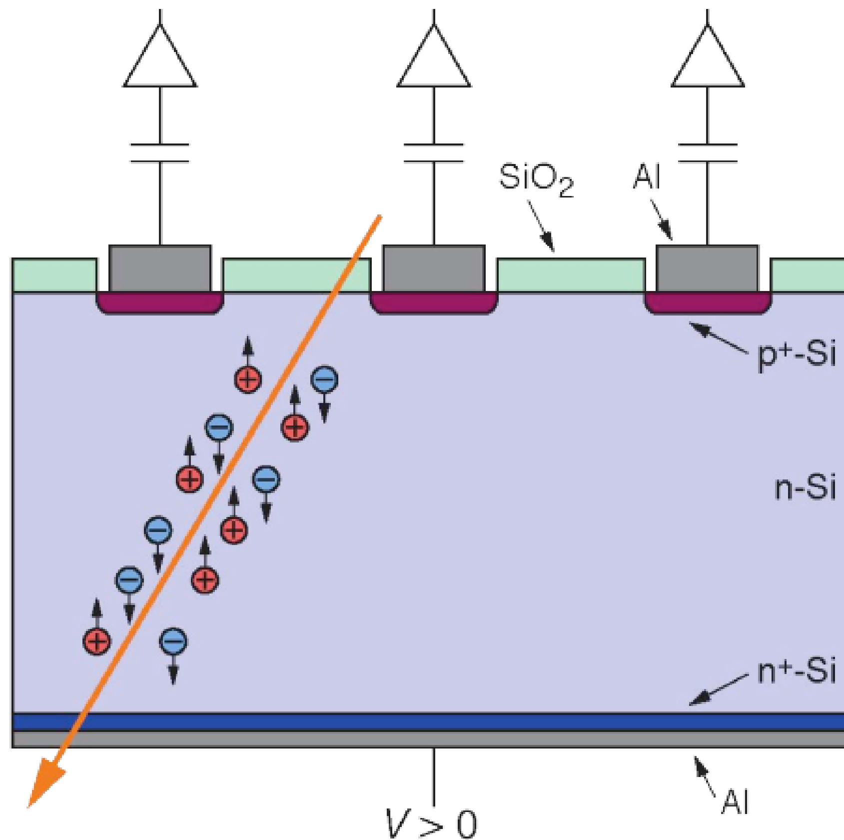

Figure 5.18: Simple schematic representation illustrating the sensor's function, depicted with an impinging minimal ionizing particle [83].

In Figure 5.18, the drift direction of the holes and electrons generated by a particle can be observed. The electric field causes electrons to be attracted to the n^+ strip and holes to the p^+ strip (readout strips). This drift of the charge carriers leads to charge separation, which can be measured. Although both electrons and holes experience the same electric field, electrons move faster because they have a significantly higher mobility in silicon, which is due to their lower effective mass in the crystal lattice. This concept will be further explained in Chapter 7.2.3.

The electric signal, averaging approximately 30,000 electrons, can be read out by the strips using low-noise electronics. The small current is amplified, shaped, and processed in ASICs (Application-Specific Integrated Circuits). In a DC-coupled setup (connection to the DC-pad), the dark current, caused by thermally generated electron-hole pairs, can introduce additional noise in the amplifier circuit.

To reduce noise from dark current and other sources, the strips are electrically decoupled from the amplifiers by a thin SiO_2 insulation layer, which helps to minimize the interference of dark current, especially in the presence of reverse bias. This process, known as AC coupling, involves connecting the AC pads to transmit the signal without linking the amplifiers to the bias voltage. However, the readout strips still require the necessary reverse bias voltage, which is provided through connections with the polysilicon detectors. To prevent shorting of the strips, the voltage supply must be electrically separated, facilitated by the polysilicon resistors and the SiO_2 layer. Pinholes, or shorted strips, can damage the readout and render the strip non-functional.

Since the strips are orthogonal to each other, the signal can be assigned coordinates in the x- and y- planes, enabling the determination of the particle's passage location. Complete depletion is crucial for low noise and the largest possible signal, as the electric field will remove free charge from the active volume.

5.2 Sensor Characteristics

The following section presents examples and explanations of the crucial parameters for the $\overline{\text{P}}$ANDA double-sided silicon strip sensors. Conducting a series of measurements on the sensors is impractical due to the irreversible nature of wire-bond contacts. Contacting with needles has proven to be inaccurate and challenging due to the sensor structures. Therefore, we will employ the measurement methods with the probe card described earlier and utilize the general-purpose program for analysis.

5.2.1 Sensor/Diode Capacitance and Depletion Voltage

In Chapter 4.2.2, the behavior of the pn-junction under reverse bias was explained. The space charge zone mentioned therein is a crucial factor in determining the sensor characteristics. Full depletion voltage can be assessed through capacitance measurements. When depleted, the sensors or diodes behave approximately like a plate capacitor. The depletion region reflects the distance between the plates, which in this case are the p- and n-implants. The relationship between the increase in charge (dQ) on both electrodes, the reduction in the size of the zone (dW), and the change in reverse bias (dV) can be described as follows:

$$C = \frac{dQ}{dV} \cdot \frac{dW}{dV} \tag{5.3}$$

With the active sensor area A and assuming complete depletion, the capacitance can be calculated using the sensor thickness w:

$$C = \frac{\epsilon\epsilon_0 A}{w} \tag{5.4}$$

The expansion of the depletion region leads to a larger distance between the plates, resulting in a decrease in capacitance. This behavior can be described using equation 5.4 as follows:

$$C = \sqrt{\frac{\epsilon\epsilon_0 \cdot e \cdot A^2 \cdot N_{eff}}{2|V|}} \tag{5.5}$$

Where $N_{D,A}$ has been replaced by the effective doping concentration N_{eff} ($N_{eff} = \frac{N_A \cdot N_D}{N_A + N_D}$). Typically, for a pn-detector, $N_A \gg N_D \gg n_i$ (intrinsic charge carrier concentration), which simplifies the equation to:

$$C = \sqrt{\frac{\epsilon_0 \epsilon_\gamma A^2}{2\mu\rho|V|}} \tag{5.6}$$

The depletion voltage is reached when the space charge zone occupies the entire volume of the sensor. Until this point, the capacitance decreases as the voltage increases. Here, ρ represents the bulk resistivity, and μ denotes the charge carrier mobility [56].

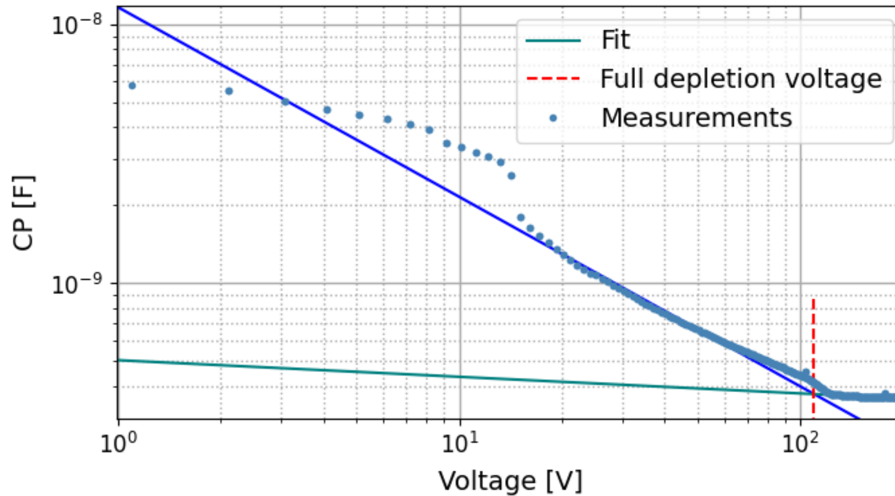

Figure 5.19: Capacitance measurement of a $\overline{\text{P}}$ANDA silicon S2 sensor as a function of the increasing reverse bias voltage.

The graph in 5.19 illustrates an example of the change in capacitance as the reverse bias voltage is varied, providing insight into the electrical properties of the sensor. The curve depicts the typical CV behavior for a pn-junction under increasing reverse bias voltage. The capacitance reaches its minimum, falling into the pF range, at around 110 V, indicating complete expansion of the space charge zone at this voltage. Therefore, capacitance measurements serve as an effective method for determining the depletion voltage.

Type	Capacitance calculated [pF]	Capacitance measured [pF]
S1	717.75 ± 24.33	678.30
S2	410.33 ± 13.91	369.65
S3	136.71 ± 4.56	-
S4	25.81 ± 0.88	24.05
Diode	9.24 ± 0.31	12.15

Table 5.1: Capacitances of the $\overline{\text{P}}$ANDA double-sided silicon strip sensors at full depletion, calculated and measured.

The capacitances for each $\overline{\text{P}}$ANDA sensor configuration and diode in Table 5.1 are calculated using equation 5.4 and the data provided in Table 5.15. Additionally, one sensor of each type, except the S3 sensor, was measured exemplary, and the full depletion voltage was determined using the method described in Chapter 5.1.2. The S3 sensor was not measured due to its different pitch, resulting in different properties than the $\overline{\text{P}}$ANDA MVD sensors. Hence, the high effort of bonding for this sensor was omitted.
In comparison with Table 5.1 and Figure 5.19, it can be observed that the measured and calculated values are almost identical. The slight difference may be attributed to a systematic error resulting from calibration or the sensor connection mentioned in Chapter 5.1.1.

To conduct the measurements, the bias rings on both the front and back side need to be contacted. Due to the various passivation layers, contacting with probe needles is difficult. Therefore, measurements were performed using the probe card, as shown in Figure 5.13. This allows the measurement of the sensor capacitance $C_{backplane}^{p-side}$ from Figure 5.22.

Furthermore, it's important to consider the measurement frequency as it significantly impacts the capacitances. For instance, measurements of the S1 sensor revealed a capacitance of 678 pF at a frequency of 100 kHz and 747 pF at 1 MHz. Hence, both the calculations and the measurements exhibit a high level of comparability, indicating that the measured diode and sensor possess the required thickness.

Sensor Strip Capacitance

To determine the single strip capacitance, the measured or calculated capacitance can simply be divided by the number of strips on the p- or n-side.

$$C_{Strip} = \frac{1}{N} \cdot C \tag{5.7}$$

For the square-shaped sensors, this calculation remains the same for both sides since the strips have the same dimensions. However, for the S1 sensor, there are

differences because the longer strips on the n-side also result in a larger capacitance. Thus, for an S2 sensor with the calculated values, the strip capacitance is C_{Strip}=0.801±0.027 pF, while for the S1 sensor, C_{Strip}=1.402±0.046 pF for the n-side and C_{Strip}=0.801±0.027 pF for the p-side.

To measure the single-strip capacitance, more effort is required. Therefore, it was performed exemplary for a strip of the S2 sensor. For this measurement, one side of the sensor must be fully contacted, while a strip on the other side is contacted via the AC pad with a probing needle. However, for the reverse bias voltage, both sides must be contacted through the bias ring.

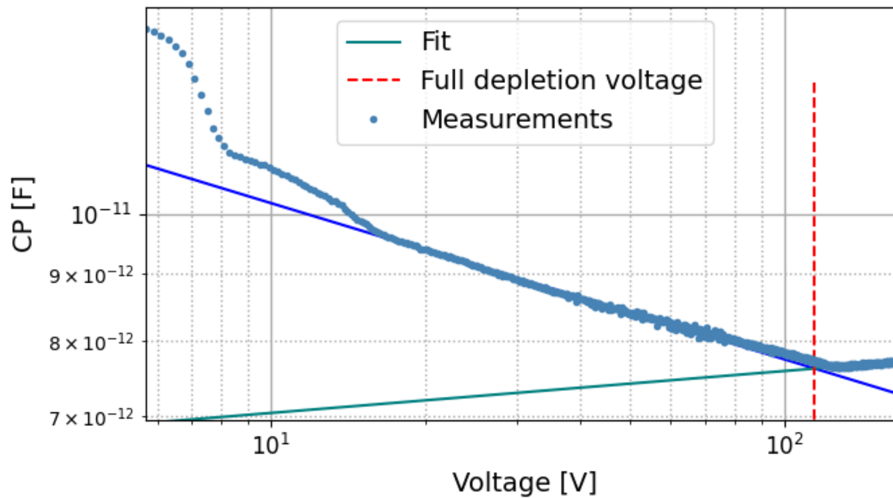

Figure 5.20: Single-strip capacitance measurement of a $\overline{\text{P}}$ANDA silicon S2 sensor as a function of increasing reverse bias voltage

In Figure 5.20, the point of full depletion is marked in red at 115.375 V with a capacitance of 7.614 pF. It is evident that the measurement exhibits high uncertainty, likely due to the probe contact. The capacitance is also higher than expected but falls within the anticipated range.

5.2.2 Leakage Current

The leakage or dark current, as mentioned earlier, results from thermally generated electrons and holes. This current, which also contributes to noise, occurs due to the separation of free charges by the electric field, hindering recombination and affecting measurements. Efforts are made to minimize this current as much as possible, for instance through the use of guard rings. Minimizing the leakage current is critical for two main reasons:

Firstly, the power consumed by the sensor is given by P=$U*I$, where I is the leakage current and U is the applied voltage. If the leakage current becomes

too high, the power dissipation increases, leading to excessive heating. This can initiate a thermal runaway effect, where the increased temperature further raises the leakage current. This effect is particularly critical in uncooled sensors, as it can exacerbate heating and potentially damage the sensor.
Secondly, if the leakage current becomes too high, the resulting voltage drop across the sensor can prevent it from being fully depleted. The performance of the sensor heavily depends on the depletion zone, which defines the sensitive volume for charge collection.

The current is particularly important because it is strongly influenced by radiation exposure, making it a key parameter for estimating the sensor's operational lifetime.
The leakage current can be divided into diffusion current and generation current. In a fully depleted sensor, the diffusion current is negligible as it is generated at the edges of the depletion region. With little or no electric field across the guard rings, charges can easily recombine. Of particular importance for sensors is the generation current, which is thermally produced within the depletion region. Therefore, the reverse saturation current in equation 4.13 is highly temperature-dependent and can be described as:

$$j_{gen} = \frac{1}{2} q \frac{n_i}{\tau_0} W \tag{5.8}$$

$$I_0 \propto T^2 e^{\frac{E_g}{2kT}} \tag{5.9}$$

A doubling of the leakage current is indicated for a positive temperature change of ΔT of 7 K [56]. This current can be mitigated by employing pure, defect-free materials and is particularly influenced by the expansion of the depleted volume. Clearly, lower temperatures in a controlled environment result in reduced leakage current. For measuring the leakage current, the depletion voltage measurements can be utilized since the general-purpose program enables simultaneous measurement.

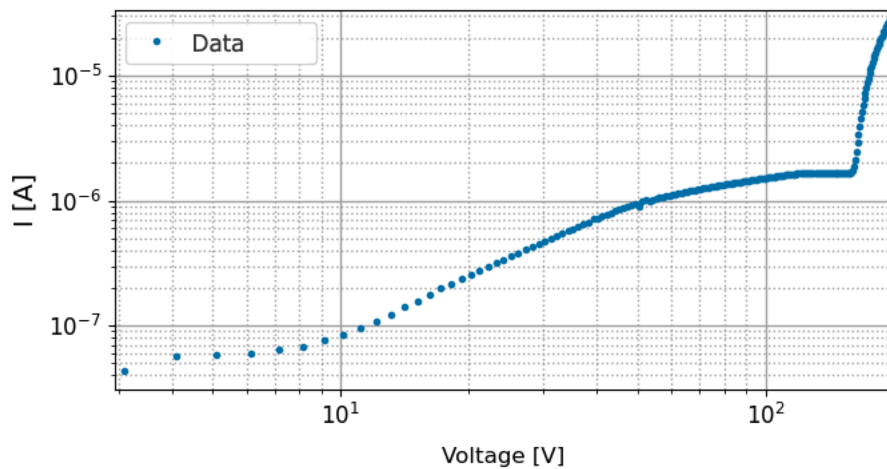

Figure 5.21: Current-voltage curve measured for an S2 sensor with increasing reverse bias voltage.

Figure 5.21 illustrates a representative IV curve for a measured S2 sensor. The curve displays a typical behavior for diodes, with current saturation observed at full depletion around 120 V, indicated by the steady current beyond this voltage. Beyond approximately 170 V, the current sharply increases, characteristic of breakdown.

Sensor Strip Leakage Current

The leakage current of a single strip is relevant primarily in terms of shot noise, as only individual strips are read out in the MVD. Due to the AC coupling, the leakage current of a strip does not flow directly into the preamplifier but still contributes to noise. As mentioned earlier, the total current of the sensor can be divided by the number of strips to estimate the current per strip:

$$I_{strip} = \frac{1}{N} \cdot I_{leak} \tag{5.10}$$

The resulting table for the measured leakage currents at full depletion is as follows:

Type	Sensor Leakage Current [μA]	Strip Leakage Current [nA]
S1	2.886	5.637(n-side), 3.221(p-side)
S2	1.546	3.019
S3	-	-
S4	0.188	1.469
Diode	0.052	-

Table 5.2: Leakage currents of the $\overline{\text{P}}$ANDA sensors at complete depletion, measured for full sensors and divided by the number of strips for strip leakage currents.

The leakage current measurements provide insights into the proper contacting of the sensors and the occurrence of pinholes, which is important for the trouble-free operation of the sensor.

5.3 Sensor Measurement Methods

For the functionality of the sensors, it is not only necessary to consider the general sensor properties as previously discussed, but also the characteristics of the applied structures. In the schematic representation in Figure 5.22 of the capacitances on a double-sided silicon strip detector, the most important capacitances due to the structures are illustrated. Capacitance like the coupling capacitance $C_{coupling}$ is essential to probe the functionality of the sensors, while the interstrip capacitance $C^{int}_{AC/DC}$ plays a crucial role in determining signal separation and minimizing noise, thus significantly influencing the sensor's precision and resolution.

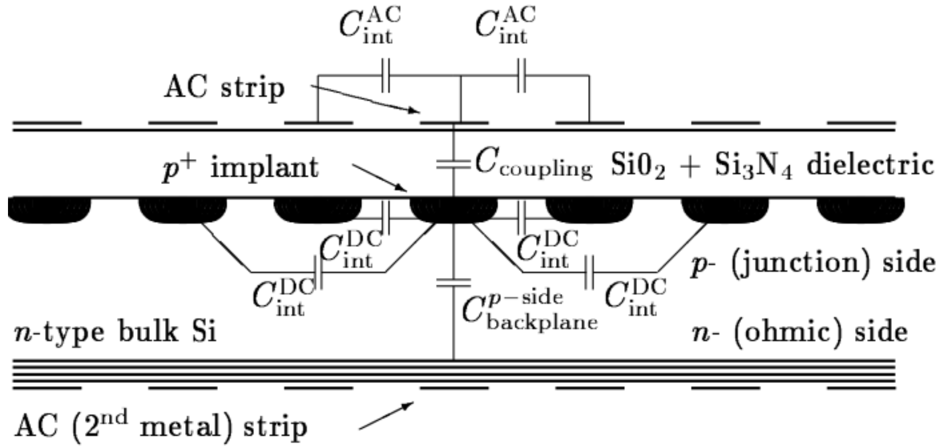

Figure 5.22: Schematic capacitance of a silicon strip sensor (not to scale) [84].

An important structure, the polysilicon resistor, is not depicted in Figure 5.22. Since these parameters play a minor role in the course of the work, the exemplary measurements for the S2 sensor can be found in the appendix B. Additionally, the prototype of the $\overline{\text{P}}$ANDA sensors was already characterized in the work by H.-G. Zaunick [38].

Coupling Capacitance

The SiO_2 layer between the AC-readout strip and the DC-readout strip is responsible for the coupling capacitance $C_{coupling}$. It is very important that this layer is not damaged, to isolate the bias voltage and the leakage current from the readout electronics. The capacitance is frequency-dependent, therefore measurements are carried out at depletion voltage of different frequencies. It is important to understand the capacitance as it directly affects the readout chain and therefore the signal-to-noise ratio.

Interstrip Capacitance

The interstrip capacitance C_{int}^{AC} characterizes the coupling between adjacent metal strips. The dominant component of the total capacitance relative to the ground comes from this capacitance. The readout signal can be reduced by coupling with the other strips, so the interstrip capacitance must be kept as small as possible to minimize noise. A higher capacitance, however, can lead to increased noise due to enhanced capacitive coupling between strips, which affects the signal quality. The measurement of this capacitance provides insight into the balance between noise minimization and signal preservation during charge collection processes.

5.4 Diode Measurements

The measurement of diodes is a crucial step in testing the quality of the sensors. Multiple sensors and diodes can be fabricated from each semiconductor wafer. It is assumed that the diodes exhibit the same quality and properties as the sensors since they are cut from the same wafers. This approach allows for the measurement of important parameters without damaging the sensors. Due to the complex structures of the sensors, measuring their properties would only be possible with the risk of damage, or by using a probe card, which would destroy the sensor.
These parameters can be measured before, during, and after radiation exposure, as well as before and after the thermal annealing process described in Chapter 5.5 and 4.4.3.
While all sensors have already been measured by CiS, the CV measurements lacked sufficient accuracy. However, CiS had the capability to inspect the sensors for pinholes, ensuring that all associated sensors with the diodes being measured here already comply with the rejection limits regarding pinholes.

5.4.1 Diode Series Measurements

In this section, the measurement methods outlined in Chapter 5.1.1 and the data processing techniques described in Chapter 5.1.2 are utilized to analyze lots 341776, 352154, 352155, 352156, 352157, 342563, 341772, 341773, 341774, 341775, 410535, 410536, 410537, 413017, 413018 and 413019 of the $\overline{\text{P}}$anda MVD-Project. These lots contain all the sensors required for the complete assembly of the barrel strip part. Each lot consists of up to 25 wafers, with 14 diodes on each wafer. At least one diode on each wafer is measured for capacitance, leakage current, and full depletion voltage through series measurements.

The depletion voltage measurements are then compared to the data obtained by CiS. This comparison enables the detection of any damage or errors in the production, shipping, or storing of the diodes and, consequently, the wafers, revealing important parameters for the smooth operation of the sensors. Moreover, the initial parameters for the experiment are determined.

The measurements conducted at JLU have a step size of 0.5 V, providing a finer resolution for accurate estimation of the full depletion voltage when combined with the fit method. Additionally, the diodes were tested up to a voltage of 200 V to minimize the risk of breakdown during the experiment. In contrast, CiS used steps of 5 V, requiring three steps for measurement and resulting in a potential error of around 15 V in finding the full depletion voltage. Moreover, the wafers were only checked up to a voltage of 150 V at CiS. Below, the accuracy of the measurements is compared using two example measurements, one from CiS and one from the JLU, both conducted on the same wafer.
In Figure 5.23, the measured data from CiS is evaluated using the fit method

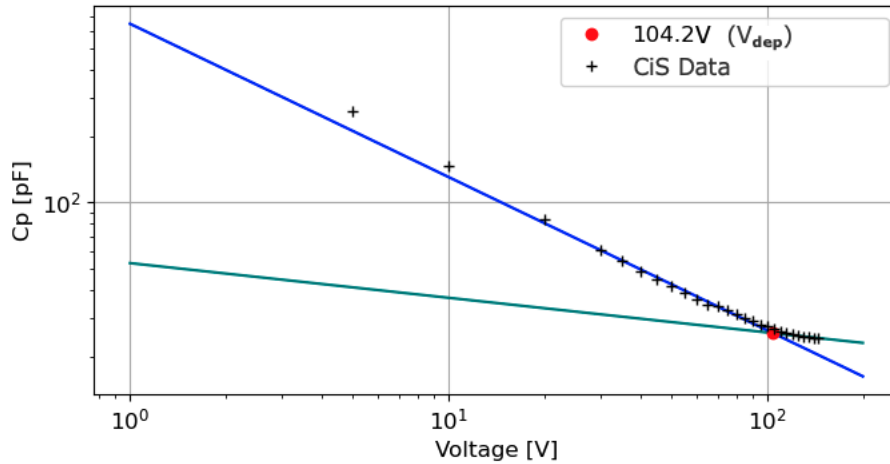

Figure 5.23: CV-measurement carried out by CiS for a diode from lot 341772 wafer 15.

described in Section 5.1.2. The imprecise measurement obscures the transition to the depletion plateau, making the detection of the voltage less accurate but sufficient for estimation. CiS estimated the full depletion voltage of the sensor to be 127.01 V. However, the fit method yielded a full depletion voltage of 105.23 V at a capacitance of 25.52 pF, showing a significant difference from the value provided by CiS. Furthermore, the comparison of the measured capacitance, which was more than twice as large as calculated (see Table 5.1), further confirms the inaccuracy of the measurement underscores the need for precise measurements. A similar measurement conducted for the same wafer using our method is plotted in Figure 5.24.

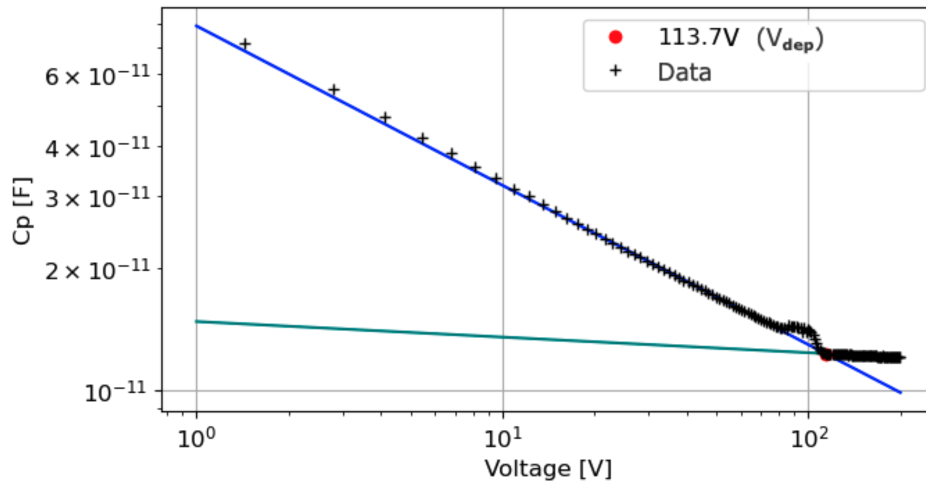

Figure 5.24: CV-measurement carried out at the probe station of the JLU for a diode from lot 341772 wafer 15.

The depletion plateau is clearly visible, indicating a constant capacitance value after reaching the full depletion voltage. Consequently, the determination of the characteristics becomes much more precise. The full depletion voltage of the diode was determined to be 113.74 V. The full dataset provides a leakage current

of $3.97 \cdot 10^{-8}$ A (leakage current data is not provided by CiS). With a measured capacitance of 12.12 pF, a comparable value was determined as calculated in Table 5.1, with 9.24 pF.

During the series of measurements, it was consistently observed that the measured capacitance values were slightly elevated compared to the calculated value, suggesting the presence of a systematic measurement error.
To ascertain the actual accuracy, measurements were conducted on a lot of 10 wafers, each containing 3 diodes. The average capacitance for the resulting 30 diodes was found to be 11.59 pF, with a maximum deviation from the mean value of 0.43 pF. This indicates that the actual measurement error is much smaller than the difference between the measurement and the calculated values. Thus, the measurements are highly suitable for monitoring the diodes and, consequently, the wafers.

In the following section, the most relevant data from all measured lots will be presented. Particular attention is given to anomalous diodes or wafers, which are reassessed, if necessary, through additional measurements in Section 5.4.1. For a better overview, the corresponding tables detailing individual lots can be found in the appendix A. These tables provide the mean values for the depletion voltage, leakage current, and capacitance at full depletion, along with the associated maximum deviation for each lot. Additionally, wafers exhibiting anomalies are identified, and a comparison with the data provided by CiS is conducted.

For Lot 341776 (see Appendix A.1), it is noteworthy that the average depletion voltage of the measured data differs by 11 V from the CiS data. This variance can be attributed to the imprecision of the CiS data and a resulting systematic error in the evaluation process. Upon comparison of the individual wafers, no systematic differences in the depletion voltages are observed. This suggests that if the locally measured data indicate a high depletion voltage, the corresponding CiS data do not consistently reflect a high voltage as well.
Furthermore, several diodes from a single wafer were measured and compared. This analysis revealed that diodes on the same wafer exhibit similar depletion voltages. Although the full depletion voltages of different wafers vary by up to 18 V. Hence, it can be inferred that the measurements are consistent and reliable.
In lot 341776, issues were observed with three diodes on wafers 01, 16, and 18. Given that the problems occurred with only one out of three diodes on each wafer, it is reasonable to assume that the overall sensor properties remain unaffected. The most probable cause of these abnormalities could be attributed to minor scratches or faulty contacting of the diodes. The presence of these three damaged diodes significantly raises the average leakage current ($I_{leak}\varnothing$), which typically falls within the mid $10 \cdot 10^{-8}$ A range for most other diodes. Therefore, all wafers from this lot have passed the quality check.

Lot 352157 (see Appendix A.6) exhibits no issues, indicating that all wafers passed the test successfully. The lot is characterized by a low mean leakage current of $3.255 \cdot 10^{-8}$ and a full depletion voltage of around 100 V. Additionally, the lot is characterized by minimal variation between diodes in terms of full depletion voltage, leakage current, and capacitance.

Wafer 20 of lot 352156 (see Appendix A.2) exhibited anomalies in the capacitance measurement. The capacitance of the diodes and sensors, depending on the reverse bias voltage, may exhibit shifts influenced by the sampling rate. The frequency introduces this uncertainty, causing variations in the voltage at which anomalies occur for a diode depending on the frequency.

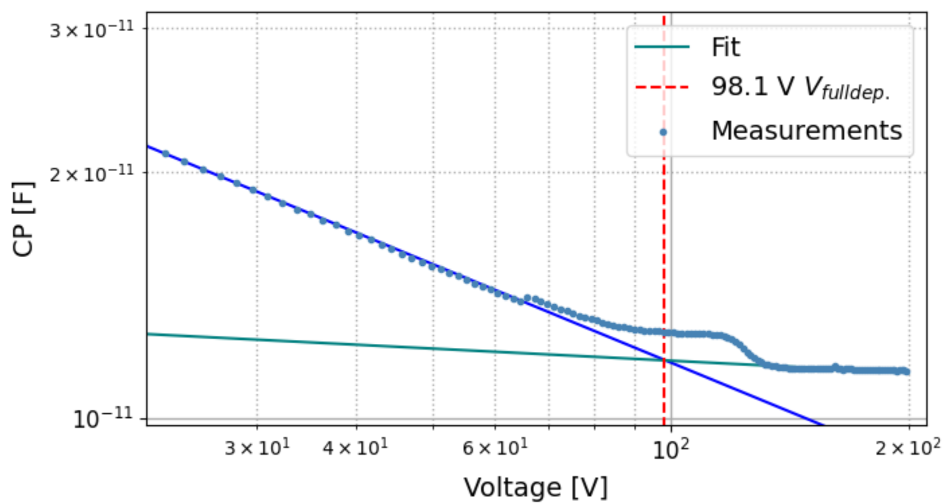

Figure 5.25: Section of the capacitance measurement of wafer 20 with the mentioned shift at around 80 V for 100 kHz.

The jump in capacitance is evident in Figure 5.25. It's crucial to recognize that this also affects the determination of the full depletion voltage. Hence, determining the minimum voltage for complete depletion must consider different frequencies. At 1000 kHz, the depletion voltage shifts from 99.22 V to 112.94 V. Since the uncertainty remains below the depletion voltage, the wafer can be safely operated above a voltage of 112.94 V without encountering issues. Lot 352156 has thus passed the quality check.

The full depletion voltage of lot number 352155 (see Appendix A.3) shows a slight increase, with the maximum deviation from the mean also being higher. Upon examining all measured wafers of the lot, a higher depletion voltage is noticeable for wafers 12 and 16. Both are fully depleted above 120 V, which is not problematic but contributes to the observed deviation.
Wafer 05 exhibits a significant shift in capacitance near the depletion voltage, which requires further investigation.

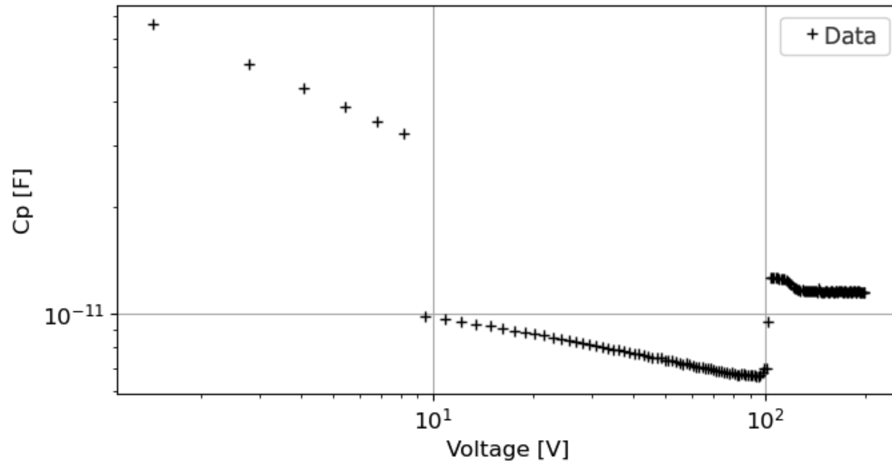

Figure 5.26: Section of the capacitance measurement of wafer 05 showing a jump around the depletion voltage for 100 kHz (see text).

Considering the capacitance measurement of wafer 05 in Figure 5.26 and the leakage current in Figure 5.27, it can be confirmed that this is not a breakdown.

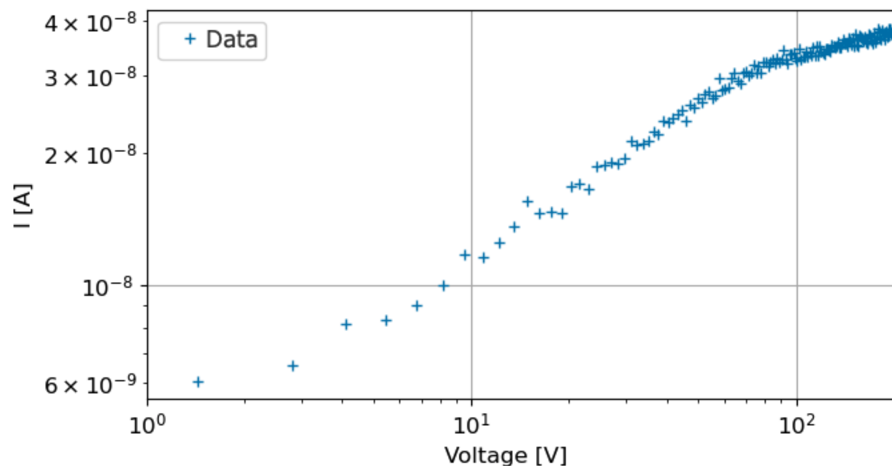

Figure 5.27: Leakage current vs. reverse-bias voltage measurement of wafer 05 for 100 kHz.

Therefore, it is simply a jump in capacitance occurring around a voltage of approximately 100 V. However, to ensure the smooth operation of the sensor, it is necessary to determine the extent to which this jump affects its functionality. For this purpose, further diodes of wafer 05, as well as sensors, need to be characterized. Additionally, the effect of radiation on the depletion voltage needs to be considered. Since the dark current, measured for operational purposes, shows no abnormalities, it can be assumed that wafer 05 is operational.

Lot 352154 (see Appendix A.4) comprised only one wafer, hence no error calculation was performed. The results of the measurement indicate that the lot meets the expected criteria.

The significant deviation in the full depletion voltage of lot 342563 (see Appendix A.5) in the data from CiS can be attributed to a specific wafer, wafer 14, which exhibited a notably low full depletion voltage of 70 V. Unfortunately, this particular wafer was not sent to the JLU for verification, indicating that it may have been rejected by CiS due to not meeting the required standards.
Wafer number 17 exhibited an unusual increase in capacitance at around 180 V. Examination of the leakage current indicates that breakdown initiates around 130 V. If other diodes from wafer 17 exhibit similar characteristics, they should be excluded from use. However, if this issue is isolated to individual diodes, it may be attributed to factors such as transport or contamination, and the wafer can still be considered usable. A retest of wafer 17 will be conducted in Chapter 5.4.1 as part of additional measurements. The rest of the lot 342563 passed the quality check.

In lot 341772 (see Appendix A.10), wafer number 19 is under investigation. Figure 5.28 depicts a dip in the depletion plateau around 160 V, which could be critical for the sensor's operation.

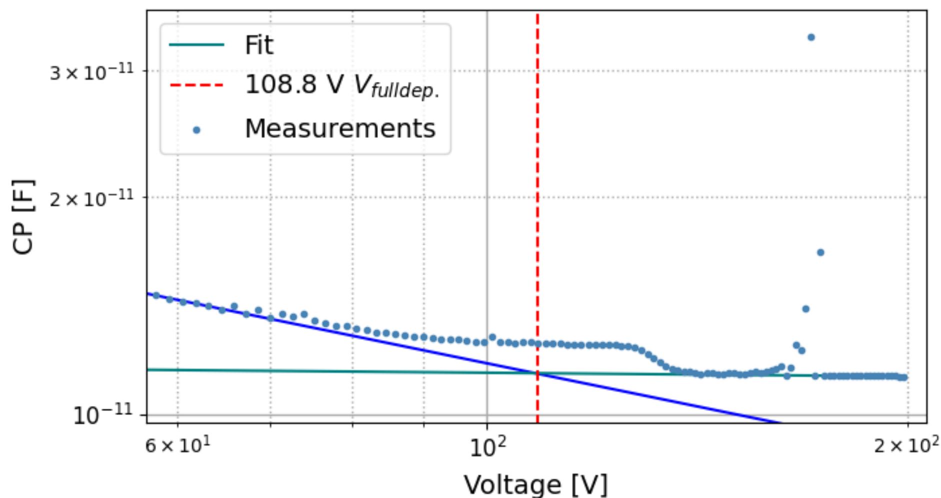

Figure 5.28: Section of the capacitance measurement against reverse-bias voltage of wafer 19 for 100 kHz.

By examining the dark current in Figure 5.29, it's evident that a simple jump can be ruled out. The characteristic rise indicates that the breakdown occurs around 115 V.

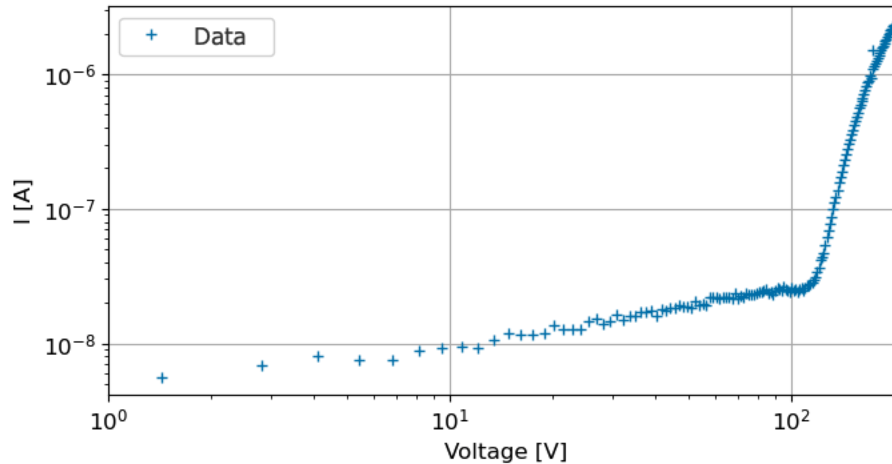

Figure 5.29: Leakage current against reverse-bias voltage measurement of wafer 19 for 100 kHz.

Therefore, the other diodes of wafer 19 must be tested. As described in lot 342563, it can then be determined whether the wafer is functional or not, as discussed in Section 5.4.1. All other wafers of lot 341772 meet the requirements.

Each wafer from lots 341773, 341774, and 341775 (see Appendix A) exhibits the required characteristics for use in the MVD.

Overall, the measurements of the lots delivered before 2023, starting with the lot number 3, showed an average full depletion voltage of 106.297 V, with a capacitance of $1.164 \cdot 10^{-11}$ F. The average leakage current at depletion voltage is $8.123 \cdot 10^{-8}$ A. These values, along with the average maximum error of the full depletion voltage at 8.886 V, indicate that the lots were delivered in sufficient quality. Only five wafers showed problems, which are being investigated.

Next, we will examine the lots delivered to Giessen from 2023 onwards. These lots, starting with the lot number 4, mainly include S1 sensors, as they are needed in higher quantities. In the series tests, none of the wafers showed any abnormalities. This, along with the increased number of sensors delivered per lot, indicates an improved quality in production. Overall, these lots have an average full depletion voltage of 104.83 V. The average leakage current and capacitance of the lots at the depletion voltage are $5.21 \cdot 10^{-8}$ A and $1.15 \cdot 10^{-11}$ F, respectively. This means that all sensors from the lots 413017, 413018, 413019, 410535, 410536, 410537 (tables of all lots in Appendix A) are verified for use in the MVD.

Further Investigations and Conclusion

As previously mentioned, wafers with anomalies are being re-evaluated. This time, different diodes from the same wafer are being investigated. To avoid errors caused by scratches from previous measurements, the diodes are being measured

for the first time.
The most investigated CiS-lot of the MVD project is 341776. An optical inspection with the microscope and measurements of other diodes from the wafers have shown that the higher leakage currents of wafers number 16 and 18 are caused by scratches. Diodes from the same wafers showed leakage currents at around 10 nA. Wafer 03 showed a breakdown at around 190 V. However, the measurement of two other diodes from Wafer 03 did not confirm this observation. The capacitance-to-voltage and the leakage current-to-voltage measurement showed no issues. Therefore, it can be assumed that the diode has been damaged, but the wafer remains fully functional. Hence every wafer of lot 341776 is qualified for the MVD.

Wafer 20 of lot 352156 exhibits a shift at approximately 80 V, as depicted in Figure 5.25. Importantly, this shift does not encroach into the depletion zone, thus ensuring it does not alter the sensor's functionality. Another diode from wafer 20 displayed only a minor shift, which is unlikely to impact functionality. Moreover, even at different frequencies, there is no risk of the sensors on the wafer being compromised. Consequently, all wafers from lot 352156 meet the qualification criteria.

In lot 352155, an unusual jump in capacitance was observed in a specific region of interest for wafer 05. Subsequently, two additional diodes from the same wafer were measured. However, no jumps or abnormalities in capacitance or leakage current were detected in these measurements. It appears that the initial observation was likely due to damage to the first diode measured, possibly caused by a scratch or weak connection. Further measurements confirmed that lot 352155 meets all qualification criteria for installation.

Another breakdown was observed in a diode from wafer 17 of lot 342563. However, subsequent measurements of two other diodes from the same wafer confirmed that it remains functional. No breakdown occurred even at a voltage of 200 V, indicating that the faulty diode likely experienced a premature breakdown due to scratches.

Similarly, in lot 341772, a shift in capacitance along with a breakdown in one diode from wafer 19 was investigated. However, subsequent measurements of the same wafer did not reveal any further errors.

Overall, all wafers from each lot successfully passed the secondary quality control at JLU, following the initial assessment at CiS. This confirms that the thickness, doping levels, and leakage current of the wafers are within the specified parameters. Therefore, the functionality of the sensors has been verified, even after transport and storage.
In preparation for the university measurements, the sensors were initially characterized by the manufacturer CiS These measurements primarily focused on

Accepted DATA@Giessen/ fully functional SENSORS@Giessen				
File	**LOT**	**S1**	**S2**	**comment**
2019-01.29_Daten_Uni_G	381921, 381922	25	25	plus dummys
Bonn01_Overwiew_UniGi	341772,341773,341774,341775,341776,342563,352154,352155,352156,352157	82	86	plus dummys
Bonn-02Lieferung2	410535,410536,410537	22	12	
Bonn-02-Lieferung 3b	413017,413018,413019	60	0	plus 16 sensors with slight overlap
Total		189	123	
Needed		184	64	

Figure 5.30: Audit of all available sensors after all requirements are passed.

pinholes. Only sensors meeting the criteria of a maximum of 50 strip failures on the p-side and 2 on the n-side were released and shipped. All sensors measured above adhere to these requirements. This results in the compiled table, as shown in Table 5.30. It includes all available S1 and S2 sensors located in Giessen that passed both tests. In green, it can be observed that there are a sufficient number of both S1 and S2 sensors for the assembly of the MVD. Additionally, almost half of the S2 sensors remain available for alternative experiments. There are also functional dummy sensors and approximately 16 sensors that narrowly missed meeting the requirements.
For the deployment of the sensors in the MVD, the key properties of the lots determined during the series measurements are summarized in Table 5.3. The voltage, leakage current, and capacitance are reported for achieving full depletion, with the measured values averaged across the different wafers within each lot. The deviation was determined using the sample standard deviation.
It should be noted that no diodes were delivered for lots 381921 and 381922, meaning that no series measurements could be performed. Therefore, only the full depletion voltage as measured by CiS is provided for these lots.
In Figures 5.31, 5.32, 5.33 for an overview, the voltage, leakage current, and capacitance at full depletion from Table 5.3 are presented. It is evident that the measured values for voltage and capacitance show only minor deviations between the lots. However, for the leakage current at full depletion, it is noticeable that the value for lot 341776 is nearly increased by a factor of 10. Further measurements, as discussed in Chapter 5.4.1, confirmed that this is due to damaged diodes, while the sensors themselves remain intact. The increased leakage current can be attributed to scratches on the diodes of two wafers. All other diodes from these wafers showed no irregularities, suggesting that the leakage current for the undamaged sensors is consistent with the other lots, qualifying them for integration.

Lot	Dep. Voltage [V]	Dep. Current [A]	Dep. Capacitance [F]	# S1	# S2
341772	109.39 (4.09)	$4.26\,(1.98) \cdot 10^{-8}$	$1.166\,(0.033) \cdot 10^{-11}$	5	6
341773	102.91 (5.97)	$5.84\,(2.35) \cdot 10^{-8}$	$1.170\,(0.019) \cdot 10^{-11}$	5	4
341774	104.97 (6.98)	$5.25\,(2.17) \cdot 10^{-8}$	$1.160\,(0.014) \cdot 10^{-11}$	5	10
341775	112.84 (3.81)	$4.71\,(0.87) \cdot 10^{-8}$	$1.149\,(0.006) \cdot 10^{-11}$	1	3
341776	102.82 (9.43)	$4.10\,(13.30) \cdot 10^{-7}$	$1.159\,(0.015) \cdot 10^{-11}$	7	9
342563	105.78 (6.60)	$4.11\,(3.21) \cdot 10^{-8}$	$1.141\,(0.006) \cdot 10^{-11}$	8	4
352154*	108.79	$5.40 \cdot 10^{-8}$	$1.183 \cdot 10^{-11}$	1	0
352155	107.79 (6.91)	$3.91\,(2.78) \cdot 10^{-8}$	$1.181\,(0.021) \cdot 10^{-11}$	20	20
352156	102.71 (3.40)	$3.55\,(1.91) \cdot 10^{-8}$	$1.160\,(0.010) \cdot 10^{-11}$	14	14
352157	104.97 (3.42)	$3.26\,(1.38) \cdot 10^{-8}$	$1.173\,(0.012) \cdot 10^{-11}$	16	16
413017	110.56 (13.23)	$4.97\,(0.69) \cdot 10^{-8}$	$1.100\,(0.089) \cdot 10^{-11}$	20	-
413018	106.06 (11.85)	$5.06\,(1.20) \cdot 10^{-8}$	$1.100\,(0.066) \cdot 10^{-11}$	21	-
413019	103.50 (10.86)	$4.12\,(1.10) \cdot 10^{-8}$	$1.111\,(0.039) \cdot 10^{-11}$	19	-
410535*	113.61	$2.19 \cdot 10^{-8}$	$1.189 \cdot 10^{-11}$	1	0
410536	97.61 (6.40)	$7.28\,(2.56) \cdot 10^{-8}$	$1.210\,(0.038) \cdot 10^{-11}$	10	6
410537	97.64 (2.68)	$7.61\,(1.22) \cdot 10^{-8}$	$1.200\,(0.016) \cdot 10^{-11}$	11	6
381921**	97.5 (4.9)	-	-	18	20
381922**	97.5 (6.2)	-	-	7	5

Table 5.3: Table of lots showing the voltage, leakage current, and capacitance at full depletion, along with the corresponding deviations, as well as the number of sensors S1 and S2.
* Lot includes only one wafer, therefore no deviation is measurable.
** No diodes were delivered from CiS; checks were performed by CiS, which did not include measurements of Dep. Current and Dep. Capacitance.

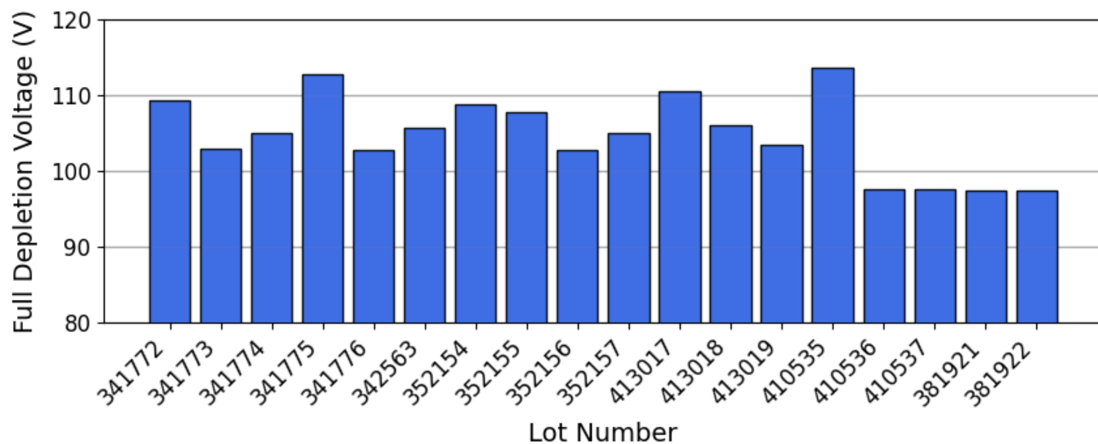

Figure 5.31: Overview of the averaged full depletion voltage for each measured lot.

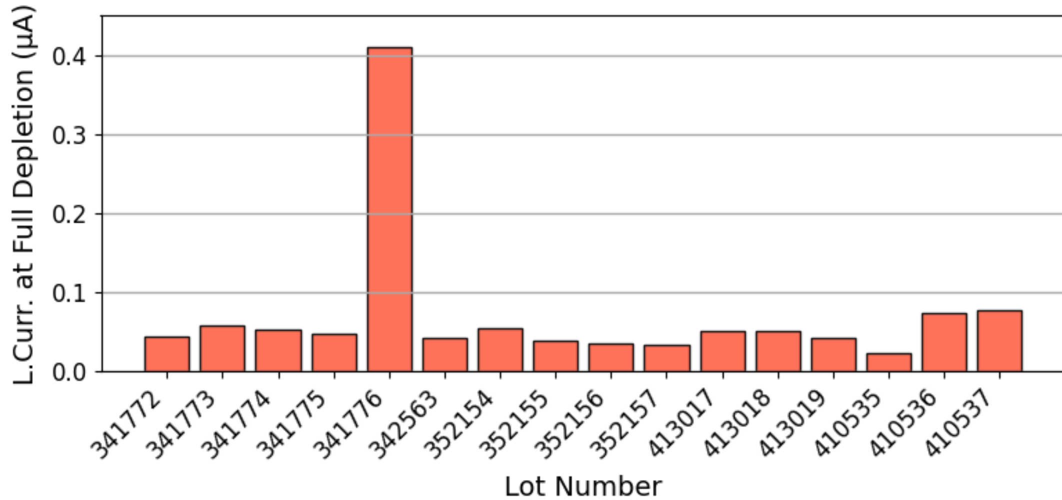

Figure 5.32: Overview of the averaged leakage current at full depletion for each measured lot.

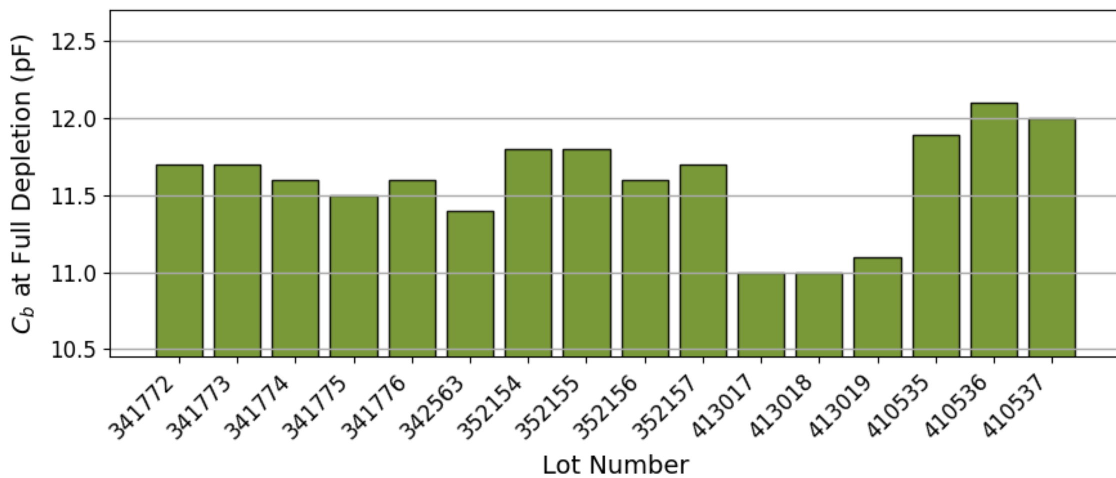

Figure 5.33: Overview of the averaged capacitance C_b at full depletion for each measured lot.

5.5 Evaluation of Radiation Hardness of $\overline{\text{P}}$ANDA Wafer Test Diodes

In this chapter, we assess the radiation hardness of the $\overline{\text{P}}$ANDA MVD test structures, which are diode-based. As discussed in Chapter 4.4, radiation hardness is a crucial criterion for semiconductor components. The irradiation process involves four intervals, two utilizing a neutron source and two employing the proton beam from the Marburg Ion Beam Therapy Center (MIT). Similar to previous assessments, diodes representative of the sensors undergo examination after adjusting depletion voltage and leakage current to determine experiment-specific properties.

5.5.1 Irradiation with Neutrons

At JLU, irradiation is conducted using an Americium-241/Beryllium (AmBe) neutron source. This method offers significant advantages, as the resulting irradiation damage can be directly compared to the predictions of the NIEL theory (see Chapter 4.4.1 for a detailed explanation) for neutron irradiation.

To initiate the assessment, it is essential to calculate the radiation dose experienced by the diodes per unit of time from the source. Considering the distance dependence and assuming a spherical distribution of radiation, the flux is determined using the following formula:

$$\phi_n(d) = \frac{A}{4\pi d^2} \tag{5.11}$$

The source possesses an initial neutron activity, A_n=$(1.3 \pm 0.26)\cdot 10^7$ neutrons/s. As the container housing the diodes horizontally fits at the bottom of the sample container in the irradiation setup, the distance d from each diode to the source remains nearly constant. The distance from the bottom of the container to the source is d=(7 ± 0.5) cm. Consequently, the diodes are subjected to a neutron flux of:

$$\phi(7cm) = (21.1 \pm 7.2) \cdot 10^3 \frac{n}{cm^2 s} \tag{5.12}$$

Hence, the irradiation time becomes the primary determinant of the dose. Consequently, various diodes were exposed to different irradiation durations. The chosen diodes are sourced from a single lot. Given that we measure ten time intervals and, consequently, exposure levels, multiple wafers need to be utilized. Specifically, three diodes were selected from each of the 10 wafers. This arrangement permitted the irradiation of two diodes from each wafer, with one diode serving as a reference for subsequent measurements.

Lot	Interval time	Integrated time	Integrated fluence
Wafer	**time [h]**	**time [h]**	**$\varnothing$ [$10^8 \frac{n}{cm^2}$]**
3	1	1	0.759
7	2	3	2.279
9	3	6	4.558
14	6	12	9.115
16	24	36	27.346
17	48	84	63.806
18	99	183	139.007
19	200	383	290.927
22	400	783	594.766
23	800	1583	1202.447

Table 5.4: Radiation exposure from neutron irradiation on diodes from different wafers of the MVD lot 352157.

The measurements have revealed no dependence of the depletion voltage on radiation. This lack of dependence is attributed to the low exposure, where the measurement error surpasses the observed change in value. Consequently, a new setup is employed, as detailed in Section 5.5.2. However, a distinct dependence on irradiation is evident in the leakage current. Figure 5.34 illustrates the plotted fluence for both measurements and the calculated eq. neutron fluence against the exposure time. The fluence from the measurements was determined using the leakage current and the following formula:

$$\phi_{eq} = \frac{\Delta I}{\alpha V} \tag{5.13}$$

ΔI represents the difference in leakage current before and after radiation.The volume V of the active region was calculated to be $7.125 \cdot 10^{-3}$ cm^3. The current related damage rate is represented by $\alpha_{80/60}(3.99 \pm 0.03) \cdot 10^{-17}$Acm^{-1} [74].

In Figure 5.34, measurements and a calculation of the applied neutron fluence are presented. Reference diodes, shown in green, originate from the same wafers and have not been exposed to radiation. Measurements were taken before and after the irradiation period, concurrently with the irradiated diodes. The negligible influence of ambient radiation on reference diodes is confirmed. The calculated values closely align with zero, as anticipated. However, a noticeable deviation, particularly at the beginning of the measurements, persists from the theoretical value.

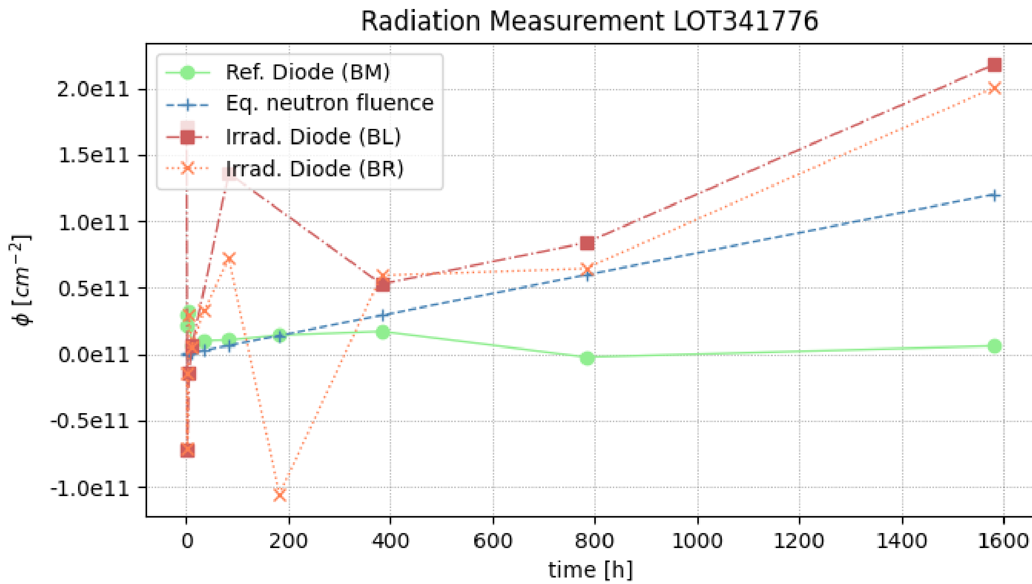

Figure 5.34: The irradiation of the diodes for up to 1600 hours with neutrons is depicted in red and orange, while the unirradiated reference diodes are shown in green. The abbreviations "BM," "BL," and "BR" indicate the original positions of the diodes on the wafer.

In the subsequent measurement series, the focus is on not only maximizing the number of samples but also compiling a comprehensive data set. Consequently, a detailed error analysis, as discussed in Section 5.5.2, will be conducted.
In blue, the linear trend of the calculated value is illustrated. The orange and red curves represent the measured values for the irradiated diodes. Up to the integrated time of 383 h, the values exhibit significant fluctuations. However, a clear correlation becomes evident when comparing the measured values with the calculated ones. While the results fall within the expected range, they are notably influenced by measurement inaccuracies. Consequently, the measurement method will be adjusted in the following to not only achieve more precise leakage current measurements but also to observe any influence on the depletion voltage.

5.5.2 Irradiation Setup with Neutrons - Upgraded Configuration

Given that the leakage current of the diodes under investigation is approximately 10 nA, precise measurements are essential. Chapter 5.5 deepens into the significance of current concerning irradiation. To ensure consistent and accurate results in each measurement, reliable electrical contact is essential. This can only be achieved through wire-bond contacts. Consequently, the main factors influencing leakage current are limited to temperature, light, and the radiation exposure along with its associated physical effects. As the measurements take place in the probe station of the climate-controlled cleanroom at the JLU, only the experienced neutron fluence can impact the parameters. To address this issue, a Printed Circuit Board (PCB) was designed to serve as a diode carrier.

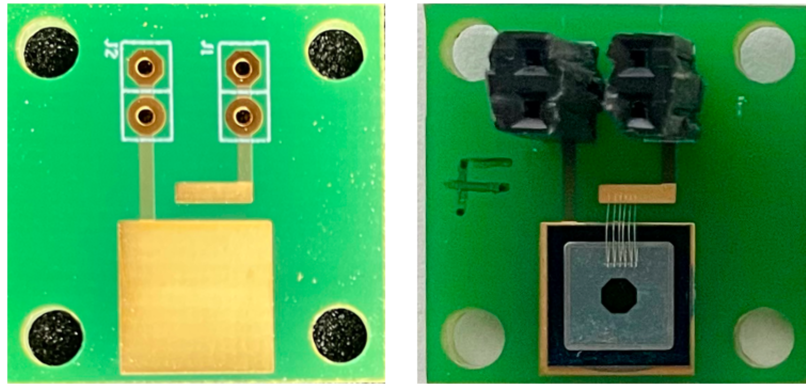

Figure 5.35: On the left, the PCB displays pads for back side contacting and bonding wires, while on the right, the PCB features a diode glued, bonded, and soldered with contacts.

The selected diodes are glued to the board using conductive adhesive. This is feasible due to the metallized back side of the diode. The contact areas on the front (p-side) are bonded with aluminum wires to a bonding pad. The PCB is connected to the measuring instruments with plugs.
It should be noted, that wire-bonds and the PCB consumes more space, increasing the distance between each diode during irradiation. This can potentially lead to errors due to the radial emission of the source. Therefore, the decision was made to irradiate only 5 diodes simultaneously, with 4 of them undergoing the same irradiation time to estimate potential errors. Despite the improved contact and measurement quality achieved through bonding, systematic errors, as described in Chapter 5.4.1, may still occur. However, since our focus is primarily on observing changes using two identical measurement methods, this error can be considered negligible.

Irradiation Measurements with Neutrons

For the measurements using the diode carrier board as described in 5.5.2 combined with the diodes from lot 352157, one diode from each of wafers 2, 3, 4, 5, and 6 was selected. Notably, these diodes have never been utilized before, minimizing structural damage due to scratching. However, it is essential to acknowledge that production errors can still influence the measurements. As demonstrated in the series tests (see Section 5.4), no abnormalities were found in this lot. After bonding, the diodes underwent comprehensive measurements before being placed in the irradiation chamber, following the established procedure.
As mentioned earlier, to estimate potential errors, the irradiation for four out of the five diodes was conducted over the same duration of 3795 hours, with diode number 5 receiving a slightly shorter irradiation time, totaling 3600 hours. The subsequent analysis focuses on the changes in leakage current and depletion voltage at full depletion induced by the irradiation.

Lot 352157	**Measurement**	**3795 h irrad.**	
Wafer	**Δ V$_{Depletion}$$\varnothing$ [V]**	**Δ I$_{leak}$$\varnothing$ [A]**	**Exp. fluence $\left[\frac{n}{cm^2}\right]$**
2	-4.277	$9.962 \cdot 10^{-8}$	$3.504 \cdot 10^{11}$
3	-7.325	$1.029 \cdot 10^{-7}$	$3.618 \cdot 10^{11}$
4	-6.293	$1.474 \cdot 10^{-7}$	$5.186 \cdot 10^{11}$
6	-6.273	$1.178 \cdot 10^{-7}$	$4.143 \cdot 10^{11}$

Table 5.5: Changes in the properties of silicon diodes after 3795 hours of neutron irradiation with the exp. fluence calculated with the change in the leakage current.

In Table 5.5, the changes in the diodes after irradiation with approximately $(2882.682\pm983.664)\cdot10^{8}$ neutrons/cm^2 are presented. The deviation originates from the estimated error of the source, as described above, at 34 %. On average, the depletion voltage changed by (6.042 ± 1.765) V, considering the maximum deviation from the mean, and the leakage current changed by $(1.169\pm0.305)\cdot10^{-7}$ A due to irradiation.
Using the leakage current, the neutron fluence can be calculated with the formula in 5.12 to be $(4.113\pm1.073)\cdot10^{11}$ neutrons/cm^2. The relatively large deviation of approximately 26 % is mainly attributed to the measurement of one of the diodes, which exhibited an elevated leakage current, indicating a measurement-related issue. However, as observed previously, the measured fluence is significantly higher compared to the calculated fluence. This suggests that the distance of the diodes to the source might be less than 7 cm. The distance is an estimate from previous measurements.
For visualization, Figure 5.36 displays the fluences measured using the leakage current and the calculated fluences from the source data with the source deviations. The plot includes the mean value of the four measured diodes and the error derived from the deviation from the mean.

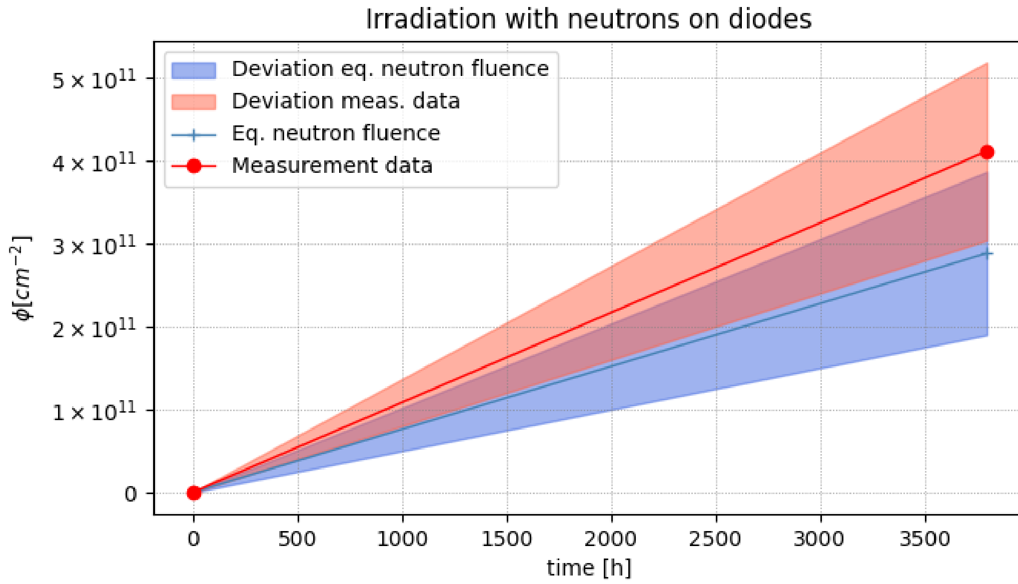

Figure 5.36: Comparison of the measured fluences in red, derived from the change in leakage current with irradiation and the calculated fluences in blue, from the activity of the neutron source.

Clearly, it can be seen that the measured fluences are significantly higher than the calculated ones. Overall, none of the four measured diodes indicate a fluence lower than the calculated one, despite the large deviation. Most likely, the distance between the diodes and the source is indeed less than 7 cm, which is, however, challenging to verify. To obtain more precise results, irradiations will be conducted at MIT, where a very accurate particle count can be applied to the diodes.
First, the diodes irradiated with neutrons will be examined in more detail. For all diodes of this wafer, a shift in the capacitance measurement at about 50 V was observed. This shift was taken into account when determining the values and can be exemplary seen for diode # 5 in Figure 5.37
As mentioned earlier, diode # 5 was removed earlier, and therefore, it was irradiated with $(2734.560 \pm 0.933) \cdot 10^8 \, \frac{n}{cm^2}$. Considering the neutron fluence dependence on the change in leakage current of equation 5.13, theoretically, a total fluence of $3088.508 \cdot 10^8 \, \frac{n}{cm^2}$ was applied in the first radiation session, corresponding to a deviation of 13 % from the expected value. In Table 5.6, the properties of diode # 5 from lot 352157 before irradiation are exemplary presented, and in Table 5.7, the changes due to irradiation are shown.

Lot 352157	**Measurement**	**no radiation**		
Wafer	**$V_{Depletion}$ [V]**	**I_{leak} [A]**	**C [F]**	**time [h]**
5	75.501	$1.379 \cdot 10^{-7}$	$1.177 \cdot 10^{-11}$	3528

Table 5.6: Bonded diode properties before exposure to the neutron source for 3600 hours.

It can be observed that the irradiation has no effect on the capacitance C, as

expected.

Lot 352157	Measurement	3600 h irrad.		
Wafer	**$\Delta V_{Depletion}$ [V]**	**ΔI_{leak} [A]**	**ΔC [F]**	**Exp.flu $\left[\frac{n}{cm^2}\right]$**
5	-7.273	$9.267 \cdot 10^{-8}$	$5.56 \cdot 10^{-14}$	$3.089 \cdot 10^{11}$

Table 5.7: Changes in main properties of the diode #5 before and after 3600 hours of radiation exposure.

However, the expected steady increase in current with the experienced flux was observed. This well-known effect is attributed to semiconductor damage which is explained in Chapter 4.4.3. The onset of type inversion is also evident in the depletion voltage decreasing by 7.273 V. While high-precision measurements were mentioned earlier, for a more accurate assessment of errors and a detailed analysis of the cause, a precise calibration of the source or an exact dosage application is required. This will be achieved in the next chapter through irradiation with protons.

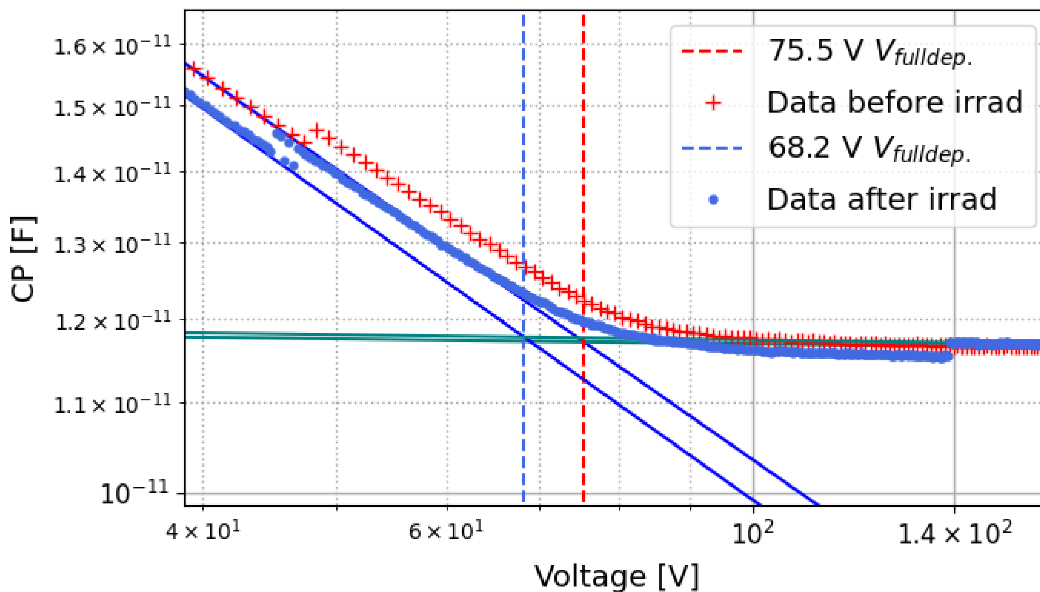

Figure 5.37: Capacitance-to-reverse-bias voltage curve for bonded diode number 5 before and after irradiation.

In Figure 5.37, the impact of irradiation on the depletion voltage is evident, with an additional shift appearing around 140 V, in contrast to the previously known shift around 50 V. This second shift is likely induced by radiation, a behavior that requires validation through ongoing measurements of other diodes.
However, no abrupt change is noticeable in the leakage current, as depicted in Figure 5.38. The diode exhibits the expected behavior with the increase in leakage current during irradiation, consistent with the description provided by

equation 5.13.
Plotted is the leakage current as a function of the reverse bias voltage for the same diode before irradiation in blue and after irradiation in orange.

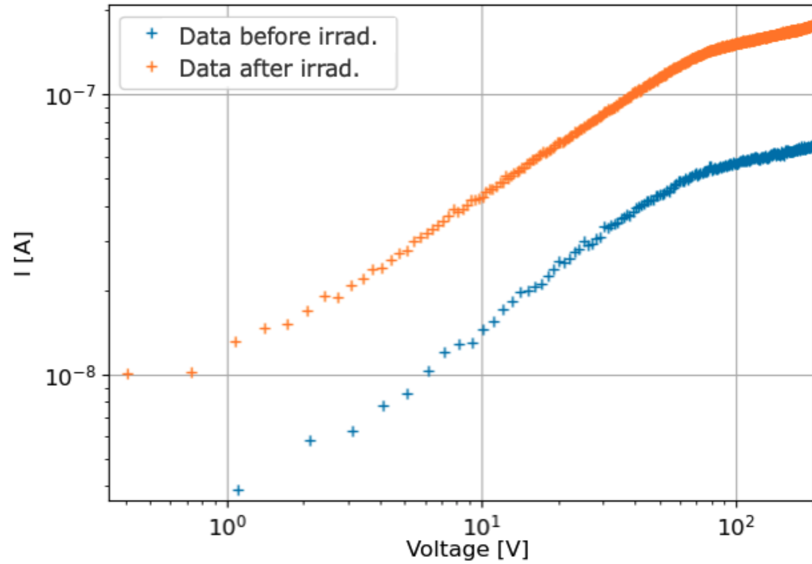

Figure 5.38: Leakage current of diode # 5 before and after neutron radiation.

5.5.3 MIT-Irradiation

After the preliminary measurements with the source, additional irradiations were conducted at the Ion Beam Therapy Center Marburg (MIT). The MIT is one of two accelerator centers in Germany where medical irradiation with protons and heavy ions, such as carbon, can be performed. The system consists of a linear accelerator and a synchrotron.
Medical approval ensures a stable and well defined beam, allowing for the precise determination of the particles actually impacted. The MIT can provide protons in an energy range of 48 to 221 MeV with up to $1.9{\cdot}10^{9}$ particles/s. The Gaussian beam dimensions depend on the intensity and energy [85].
Since the irradiation is performed with protons, the equivalent flux for neutrons, Φ_{eq}, must be calculated for comparison. This is necessary because the deposited energy is not the same, as illustrated in the damage function Figure 4.20.

$$\Phi_{eq} = \kappa_x * \Phi_x \tag{5.14}$$

The hardness factor κ_x for protons is determined by the NIEL equation and is approximately 1.907 for 50 MeV protons [86], [87]. For lower energies, this conversion factor is larger for the energy deposition of protons. Therefore, the irradiation was conducted with the minimum proton energy of 48.1 MeV. Together with the highest intensity, the full width at half maximum (FWHM) of the beam's intensity distribution is 31.5 mm. The beam dimensions and the size of the active diode area, approximately 5 mm in length, can be observed in Figure 5.39. The actual radiated

area of the square diode was calculated through integration. The beam distribution is based on the geometry determined by MIT. A subsequent determination of the geometry using photo films was not possible due to overexposure caused by the high radiation intensity.

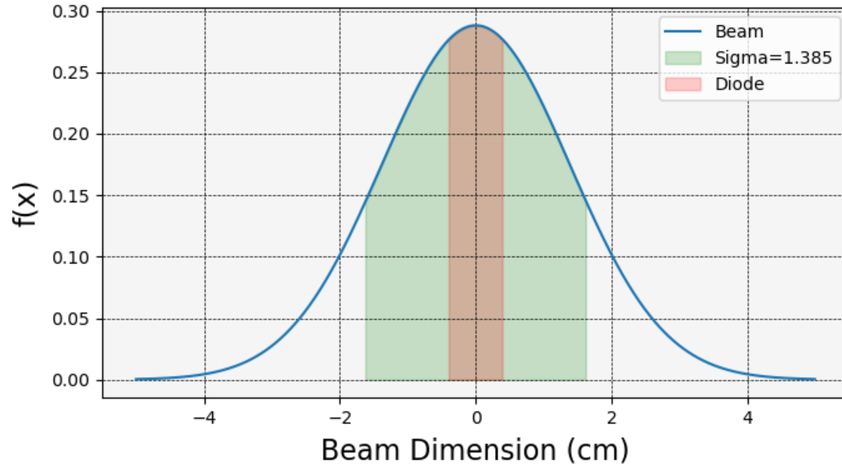

Figure 5.39: Gaussian beam distribution of the proton beam, with the diode dimensions at the center, similar to Beam Time I. The distribution has been calculated based on the beam geometry previously determined by MIT.

In total, four diodes were exposed to different fluxes. These diodes were bonded to a special PCB, as explained in Section 5.5.2. The properties, leakage current, voltage, and capacitance, were measured at full depletion both before and after irradiation. It is important to note that the diodes were stored for a few days to allow the radiation to decay before measurement, in accordance with radiation safety protocols.
The radiation was administered in multiple sessions, which were then combined and calculated to determine the neutron equivalent flux Φ_n. The flux calculation was designed to count only the particles that actually impacted the active surface of the diode. The results of the radiation are presented in the following Table 5.8.

Wafer	**Neutron flux**	**Full depletion voltage**	**Leakage current**
Number	$\Phi_n [cm^{-2}]$	$\Delta\ V_{Depletion}\ [V]$	$\Delta\ I_{leak}\ [A]$
1	4.57E+09	0.49	2.31E-09
2	2.97E+10	-0.99	1.07E-08
3	6.47E+10	-0.499	1.24E-08
4	4.02E+11	-5.01	4.88E-08

Table 5.8: Changes of the $\overline{\text{P}}$ANDA diodes properties after irradiation with protons.

In Table 5.8, the changes in the most critical properties of silicon detectors due to irradiation are presented. It is essential to note that the measurement accuracy

was 0.5 V. The changes in leakage current and full depletion voltage are observable with the applied radiation.
The results of the irradiations at MIT are combined and discussed for both beam times since the second beam time involves an extension of the first, with the same diodes being further irradiated.

5.5.4 MIT-Irradiation II

In a subsequent beam time at MIT, adjustments were made to the beam diameter, and a series of diodes were irradiated under the same irradiation conditions. The same diodes that were irradiated in MIT Beam Time I were used to further expand the accumulated radiation exposure.
To maintain maximum beam intensity, it was necessary to increase the energy. Consequently, the hardness factor κ_x, which is approximately 0.9516 at a beam energy of 221.07 MeV protons, also underwent changes. These changes are explained in detail in Section 5.5.3 [86], [87]. The increased energy also resulted in a more focused beam, with a FWHM of approximately 8.1 mm. This adjustment meant that a greater number of the accelerated protons would impact the diode compared to Beam Time I.

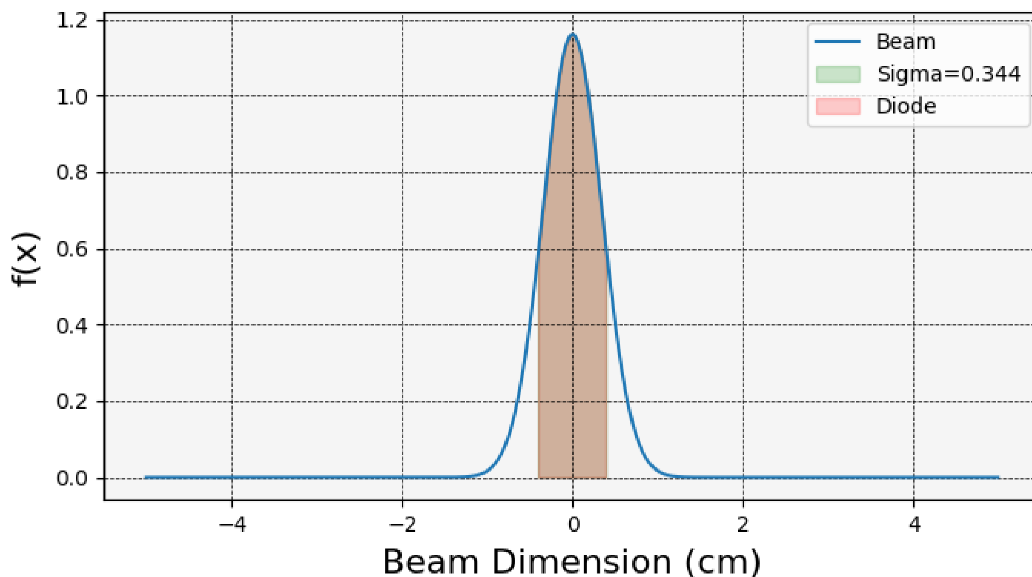

Figure 5.40: Gaussian beam distribution of the proton beam, with the diode dimensions at the center, similar to Beam Time II. The distribution has been calculated based on the beam geometry previously determined by MIT.

As depicted in Figure 5.40, the beam, with a full width at half maximum (FWHM) of approximately 8.1 mm, has dimensions similar to the active area of the diodes, measuring approximately 8 mm on each side. A total of 10^{12} protons with an energy of 221.07 MeV were applied for irradiation during MIT Beam Time II.
In Figure 5.41, the alignment of the diodes in MIT is depicted using a pilot laser.

The intersection point denotes the beam focus. The right image displays the exposed dosimeter film after irradiation, positioned behind the first diode, as indicated by the white area in the left image.

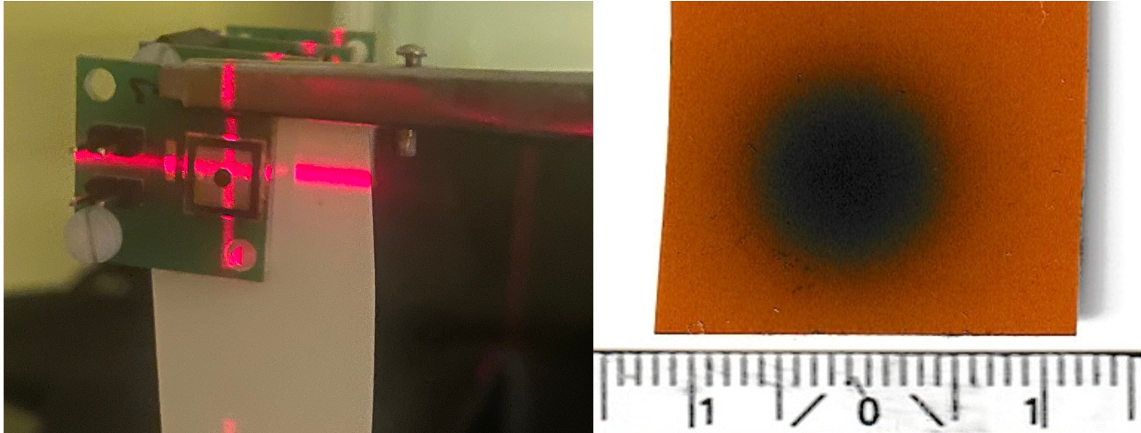

Figure 5.41: Diodes on PCBs are situated in the alignment laser system at MIT, accompanied by an unexposed radiographic dosimeter film on the left and an exposed radiographic dosimeter film on the right.

In the following table, the equivalent neutron flux on the active area of the diode is presented. Additionally, the changes in full depletion voltage and leakage current induced by radiation are depicted. It should be noted that these measurements were conducted prior to thermal annealing.

Wafer	**Neutron flux**	**Full depletion voltage**	**Leakage current**
Number	$\Phi_n [cm^{-2}]$	$\Delta V_{Depletion}$ $[V]$	ΔI_{leak} $[A]$
1	$7.19 \cdot 10^{11}$	-4.04	$1.75 \cdot 10^{-7}$
2	$7.19 \cdot 10^{11}$	-5.05	$1.92 \cdot 10^{-7}$
3	$7.19 \cdot 10^{11}$	-6.00	$1.90 \cdot 10^{-7}$
4	$7.19 \cdot 10^{11}$	-5.04	$1.92 \cdot 10^{-7}$

Table 5.9: Changes of the $\overline{\text{P}}$ANDA diodes properties after irradiation with protons in MIT Beam Time II.

Diodes 1, 2, 3, and 4 are the same as those used in MIT Beam Time I, as illustrated in Table 5.8. All diodes were additionally irradiated with an equivalent neutron flux of $7.19 \cdot 10^{11}$ $n_{1MeV,eq}$ cm^{-2}.
Table 5.9 indicates that the full depletion voltage has decreased by an average of (5.03 ± 0.99) V, with a measurement accuracy of approximately 0.5 V. Conversely, the leakage current at the full depletion voltage has increased by an average of $(1.87 \pm 0.12) \cdot 10^{-7}$ A, as expected.

Radiation and Leakage Current

As mentioned earlier, the changes in leakage current after both MIT beam times are considered in the following. In Chapter 4.4, the dependency of leakage current and fluence was explained by equation 5.13. This behavior can be clearly seen in Figure 5.42. As expected, with a higher radiation load, the leakage current also increases.

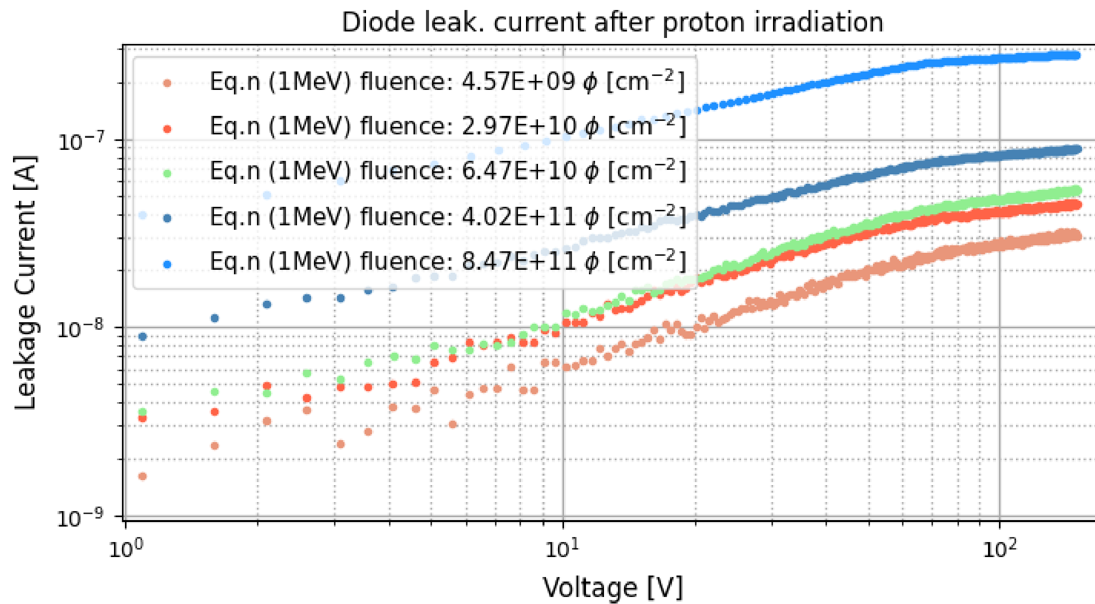

Figure 5.42: Leakage current for diodes after irradiation with different proton fluences at MIT; for comparability, the equivalent neutron fluence for 1 MeV neutrons was calculated and plotted.

In Figure 5.42, all irradiated diodes from the first MIT beam time, as shown in Table 5.8, are plotted along with one diode from beam time two, as shown in 5.9. The experienced fluence was calculated considering the leakage current using equation 5.13 and the corresponding hardness factor from equation 5.14. However, an equivalent neutron fluence of $11.21 \cdot 10^{11}\, n_{1MeV,eq}\, cm^{-2}$ was used for the irradiation overall, indicating that the diodes were not precisely aligned at the exact beam center for every measurement. This alignment issue is further explored in Figure 5.43. No unirradiated reference diode is shown, as the diode with a fluence of
$4.57 \cdot 10^{9}\, _{1MeV,eq}\, cm^{-2}$ does not exhibit any measurable damage due to the low irradiation.
The measurement in light blue represents the leakage current of the diode irradiated in both beam times, experiencing the highest equivalent neutron fluence of $8.47 \cdot 10^{11}\, n_{1MeV,eq}\, cm^{-2}$.
Given the linearity between the experienced radiation and the change in current, a comparison between the expected formula and the actual measurements can be conducted. For this purpose, the expected leakage current after irradiation

with $11.21 \cdot 10^{11}$ $n_{1MeV,eq}$ cm^{-2} was calculated using equation 5.13, and the actually measured leakage current for the different irradiation intervals was plotted.

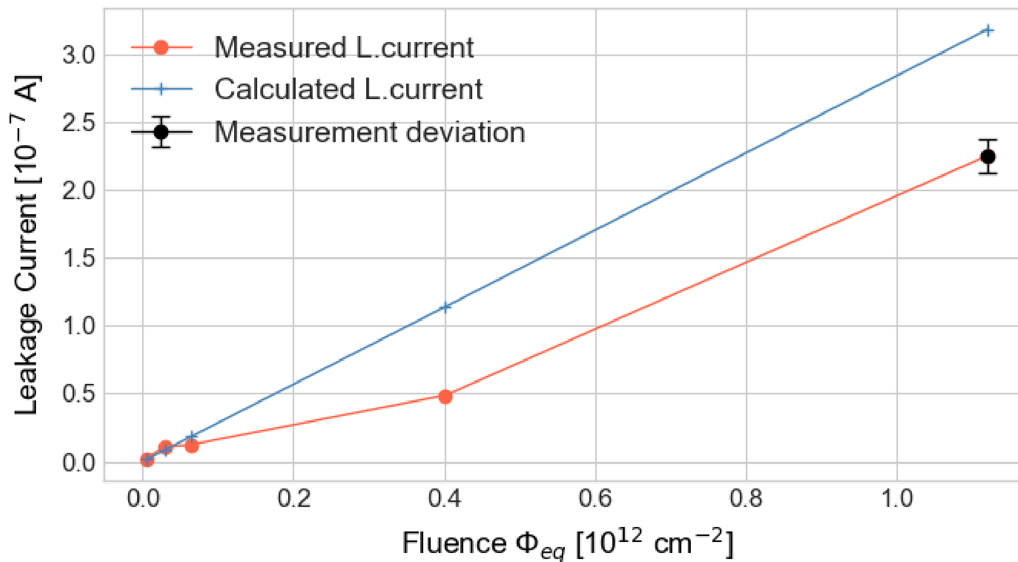

Figure 5.43: Measured and calculated change of the leakage current at full depletion to the experienced equivalent neutron fluence.

The linear relationship is evident for both the calculated values in blue and the measured values in red. However, the measurement at $4.02 \cdot 10^{11}$ $n_{1MeV,eq}$ cm^{-2} shows a shallower value than expected. As a result, the measurement between 4.02 and $0.65 \cdot 10^{11}$ $n_{1MeV,eq}$ cm^{-2} has a lower slope than anticipated. Before and after this interval, the slope is nearly the same as the calculated curve in blue. This suggests that during the irradiation, the diode was likely slightly off center relative to the beam center.This interpretation is supported by the low measurement error, which is plotted for the last measurement. In that case, four diodes were irradiated with the same total fluence, and the deviation from the mean of the changed leakage current after irradiation provides the error. This error is significantly smaller than the separation between the curves. This comparison, along with the neutron measurements in Figure 5.36, indicates that the measurement method is suitable.
The good agreement between the calculated and measured values indicates the reliability of the applied radiation model and the properties of the test structures.

Radiation and Full Depletion Voltage

The MIT irradiation in tables 5.8 and 5.9 for MIT Beam Times I and II shows a reduction in the full depletion voltage as the radiation increases. To assess whether the silicon wafers possess the correct properties and radiation hardness, the measured values will be compared with theoretical expectations.

The reduction in voltage is expected because the irradiation changes the effective doping concentration N_{eff}, which is correlated with the depletion voltage.

$$V_{\text{dep}} = \frac{e \cdot d^2}{\epsilon \epsilon_0} \cdot |N_{eff}| \tag{5.15}$$

Both the donor and acceptor concentrations are affected by radiation, primarily through crystal defects explained in Section 4.4. However, the donor degradation dominates, leading to a decreasing in N_{eff}. The n-type semiconductor undergoes a conversion to p-type when $N_D < N_A$. Due to the absolute value of N_{eff} in equation 5.15, the full depletion voltage starts to rise again at this point. This phenomenon is known as type inversion. A simplified representation of the effective doping concentration, as proposed by R. Wunstorf [75], is employed for the calculated depletion voltage (blue line) in Figure 5.44.

$$N_{eff}(\Phi) = N_{D,0} \cdot exp(-c\Phi) - N_{A,0} - b\Phi \tag{5.16}$$

It has been found, that the initial doping concentration for the donors $N_{D,0}$ is proportional to the donor removal, leading to the donor removal rate:

$$c = a/N_{D,0} \tag{5.17}$$

With a typical value of a=0.1, the removal rate of donors (c) can be calculated [88]. The increase in acceptors due to irradiation can be determined using the known value of approximately b=0.024 cm^{-2} [89], [90].
The concentration of the donors and acceptors before the radiation is described by $N_{D,0}$ and $N_{A,0}$ respectively, within the given context:

$$N_{eff,0} = N_{D,0} - N_{A,0} \tag{5.18}$$

When these values are incorporated into the equation alongside the specific properties of the sensor, the theoretical behavior of the depletion voltage can be calculated. This calculation is depicted in Figure 5.44 and is referred to as the "Theoretical Function", represented by the blue curve.
To determine the effective donor doping density $N_{D,0}$ for an n-type bulk semiconductor the following formula is used:

$$N_{D,0} = \frac{1}{q \cdot \mu_n \cdot r} \tag{5.19}$$

In the process, μ_n represents the electron mobility, which is approximately 1500 cm^2/Vs, and r denotes the specific resistivity of the sensor. The resistivity of the sensors ranges from 2.3 to 5.0 $\text{k}\Omega \cdot \text{cm}$, as indicated in Table 5.15. Additionally, a resistance of 4.304 $\text{k}\Omega \cdot \text{cm}$ was measured.
This allows for the calculation of the donor doping density $N_{D,0}$ for an n-type bulk material as follows [36]:

$$N_{D,0} = \frac{1}{e \cdot 1500\,\text{cm}^2/\text{Vs} \cdot 4.304\,\text{k}\Omega \cdot \text{cm}} = 9.668 \cdot 10^{11}\,\text{cm}^{-3} \tag{5.20}$$

The calculation of the effective donor doping density $N_{D,0}$ involves the relative permittivity ϵ for silicon, which is 11.68. Using the measured full depletion voltage V_{dep}=80 V, $N_{eff,0}$ can be determined [91].
It should be noted that the effective doping density is calculated for one of the diodes. Prior to irradiation, there were maximum differences of 5 V in the full depletion voltages among all used diodes, and this is considered in the error analysis.

$$N_{eff,0} = \frac{V_{\text{depl}} \cdot 2\epsilon\epsilon_0}{D^2 \cdot e} = \frac{80\,\text{V} \cdot 2 \cdot 11.68}{(285\,\mu\text{m})^2 \cdot e} = 1.272 \cdot 10^{12}\,\text{cm}^{-3} \tag{5.21}$$

The calculated values are substituted into equation 5.16, allowing the theoretical calculation of the behavior of the full depletion voltage in relation to the neutron fluence Φ. Additionally, the actually measured changes in the full depletion voltage, obtained during MIT Beam Times I and II, are plotted in red. The error of 2.64 V in the measured values results from the maximum deviation occurring due to repeated measurements.

For error consideration of the theoretical function in blue, the method of error propagation was applied. As demonstrated in the serial measurements in Section 5.4.1, the full depletion voltage can vary significantly within a lot, with a maximum value of 25.212 V. This variation is related to the doping density and, consequently, directly to the resistance. To estimate the error sensibly, it was assumed that only the parameters N_A and N_D change due to irradiation. Given the substantial discrepancy in the theoretical resistance and the associated calculation of $N_{D,0}$, the error was determined by the 24 % deviation of the measured value from the mean of the theoretical values.

For $N_{eff,0}$, derived from measured values, the error was calculated based on the largest deviation from the full depletion voltage ΔV_{dep}=5 V among the used diodes. This results in an error $\Delta N_{eff,0}$= $0.079 \cdot 10^{12}\,\text{cm}^{-3}$, corresponding to an error of 6.21 %. Since, as mentioned earlier, $N_{A,0}$ is calculated from both values, the overall error is calculated through error propagation. This yields an error for the theoretical function of V_{dep} of 18.257 %, corresponding to a starting value of the function of (79.927±14.592) V. This error seems reasonable considering the observed discrepancies in the measured serial measurements from Chapter 5.4.1, where differences of up to 25.212 V were measured within a wafer, falling within the deviation range of the calculated values of 29.184 V.

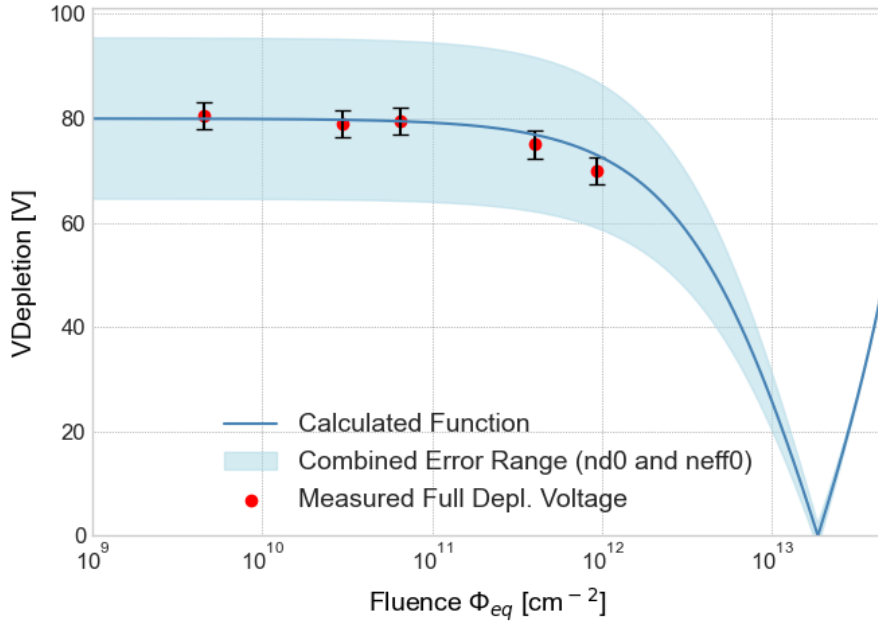

Figure 5.44: Comparison of the measured and calculated changes in the full depletion voltage of silicon test structures after irradiation with protons at MIT, converted into 1 MeV equivalent neutron fluence.

The comparison reveals that the measured changes align well with the calculated values. The error range of the measured values falls within the calculated curve. By estimating the error range of the calculated curve, it can be inferred for $\overline{\text{P}}$ANDA sensors that type inversion is highly likely to occur after an irradiation of $(1.859 \pm 0.102) \cdot 10^{13}\, n_{1\text{MeV,eq}}\, \text{cm}^{-2}$. The required lifetime limit of $10^{14}\, n_{1\text{MeV,eq}}\, \text{cm}^{-2}$, which is surpassed at approximately 131.7 V, allows the sensors to operate within the lifetime limit below the specified 200 V depletion voltage.

The error also accounts for those diodes having a full depletion voltage lower or higher than 80 V, as explained earlier. The value falls within the range of expected radiation damage, confirming the requirements for the sensors [10]. It should be noted that this is an estimated lifetime, derived from both calculated and measured values. A clear assessment would require irradiation up to $10^{14}\, n_{1\text{MeV,eq}}\, \text{cm}^{-2}$.

5.5.5 Thermal Annealing

A well-known method for healing radiation damage in silicon is thermal annealing, as explained in more detail in Chapter 4.4.3. In this method, the irradiated diodes or sensors are heated for precisely 80 minutes at 60 °C [74].
In Table 5.10, the changes in full depletion voltage and leakage current at the full depletion voltage are presented after irradiation and subsequent treatment with thermal annealing. This means that the values of $\Delta V_{\text{Depletion}}$ and ΔI_{Anneal} indicate the difference between the unirradiated diodes and the irradiated and thermally

annealed diodes.
Additionally, the $\Delta I_{\text{Leakanneal}}$ value represents the difference in leakage current between post-irradiation and post-thermal annealing, aiming to clarify the influence of annealing on irradiated diodes.

Wafer	**Neutron fluence**	**Change in f.depletion voltage**	**Change in leakage current**	**Change in l. current post anneal**
Number	$\Phi_n[cm^{-2}]$	$\Delta V_{\textbf{Depletion}}\ [V]$	$\Delta I_{\textbf{Anneal}}\ [A]$	$\Delta I_{\textbf{Leakanneal}}\ [A]$
1	$7.19 \cdot 10^{11}$	-3.04	$1.09 \cdot 10^{-7}$	$6.55 \cdot 10^{-8}$
2	$7.19 \cdot 10^{11}$	-6.05	$1.09 \cdot 10^{-7}$	$8.33 \cdot 10^{-8}$
3	$7.19 \cdot 10^{11}$	-8.06	$1.27 \cdot 10^{-7}$	$6.33 \cdot 10^{-8}$
4	$7.19 \cdot 10^{11}$	-4.05	$1.20 \cdot 10^{-7}$	$7.16 \cdot 10^{-8}$

Table 5.10: Changes in $\overline{\text{P}}$ANDA diode properties at full depletion after irradiation with protons and after additional thermal annealing.

It can be observed that, on average, the change in the full depletion voltage remains around (5.30±2.26) V after annealing. Due to the relatively large measurement error, no significant impact of thermal annealing on the full depletion voltage could be identified.
Meanwhile, as shown in Table 5.10, a clear reduction in leakage current is evident, especially when comparing the measurement results with Table 5.9 before thermal annealing. The differences in the leakage current measurements are shown in Figure 5.45, where the leakage current versus voltage is plotted before and after irradiation with $7.19 \cdot 10^{11}\ \text{n}_{\text{1MeV,eq}}\,\text{cm}^{-2}$, as well as after annealing.
Before thermal annealing, the diode's average leakage current at full depletion was $(2.32\pm0.22)\cdot10^{-7}$ A, and after annealing, it decreased to $(1.61\pm0.21)\cdot10^{-7}$ A. This indicates a reduction in leakage current by $(0.71\pm0.30)\cdot10^{-7}$ A, which can be utilized to extend the experiment's lifespan. The proper annealing procedure positively influences $\overline{\text{P}}$ANDA sensors, manifesting a decrease in leakage current by (30.60±13.93) %.

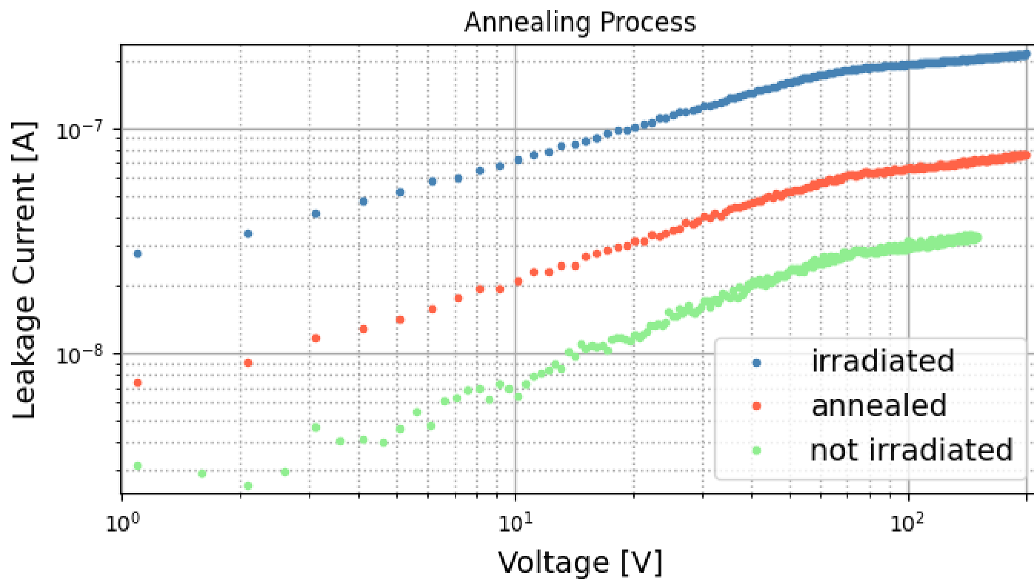

Figure 5.45: Leakage current versus reverse bias voltage for an unirradiated silicon diode in green, a proton-irradiated one in blue, and one irradiated and thermally annealed in red.

Hadronic Irradition Damage Conclusion

The irradiation of the test structures of $\overline{\text{P}}$ANDA silicon sensors was examined using a neutron source and a proton beam at MIT. For neutron irradiation, it was observed that slightly higher radiation damage occurred than anticipated. Particularly, the leakage current is slightly elevated compared to the irradiation level. This is most likely attributed to a statistical error in irradiation, as the diodes were evidently closer to the source than expected, resulting in a greater neutron flux than anticipated.

The significant uncertainty in measurements is likely due to variations in measurement timing. In some instances, months passed between measurements due to the low activity of the source, leading to potential errors. Thermal annealing, even at room temperature, can alter damages over time, emphasizing the crucial role of the measurement timing.

Nevertheless, irradiation with up to $4.113 \cdot 10^{11}\ \text{n} \cdot \text{cm}^{-2}$ demonstrated the linear relationship between leakage current and experienced neutron fluence, as well as a reduction in the full depletion voltage.

Using a designed setup for more precise measurements of the test structures, two proton beam sessions were conducted at MIT. In total, the diodes were irradiated with up to $1.121 \cdot 10^{12}\ \text{n}_{\text{1MeV,eq}}\ \text{cm}^{-2}$. The linearity of the leakage current and fluence was demonstrated and it was verified that the leakage current remains within

the predictable range and is confirmed by the theory to behave as expected. The error introduced by the measurement method and proton irradiation is significantly reduced.

The variation in the full depletion voltage, a crucial factor for the experiment's lifespan, was investigated. It was found that the full depletion voltage decreases, as expected. By comparing the measured values with theoretical considerations, it was demonstrated that the sensors will remain operational even beyond the specified lifetime fluence of $10^{14}\,\mathrm{n_{1MeV,eq}\,cm^{-2}}$.

Furthermore, various parameters were determined and confirmed, such as effective doping density, resistance, donor density, and acceptor density. Thermal annealing has shown that radiation damage can be partially reversed with only the healing of leakage current demonstrated.

The tests indicate that, concerning radiation hardness and fundamental properties, the sensors are prepared for operation in the $\overline{\mathrm{P}}$ANDA experiment.

Chapter 6

Dosimetry with $\overline{\text{P}}$ANDA Diodes

In the following section, the test structures of the $\overline{\text{P}}$ANDA MVD, referred to as diodes, are employed for a dosimetry concept.The aim of this project is to comprehend the signal behavior of the silicon diodes, which can be extrapolated to the sensors of the MVD due to similar diode characteristics. This knowledge is employed to connect the sensors with the ToASt ASIC (Section 7.1.1) and the MVDs DAQ for signal readout.
Furthermore, the goal is to perform dosimetry in space environment. Thus, the entire dosimeter setup must be space-ready and compatible with the AmbaSat company's femto satellite (refer to Section 6.1). This satellite was chosen for its cost-effectiveness and suitability for our application.
Since only about 30,000 electron-hole pairs are generated by a MIP in 300 µm of silicon, signal amplification is necessary [92] . Additionally, signal readout is intended to be conducted through a micro controller with a clock frequency of 4 MHz, requiring the signal to be temporally extended. The following outlines the construction of such a circuit in three iterations which also comply with the regulations of the AmbaSat project and are suitable for space operations.

6.1 Introduction and Ambasat

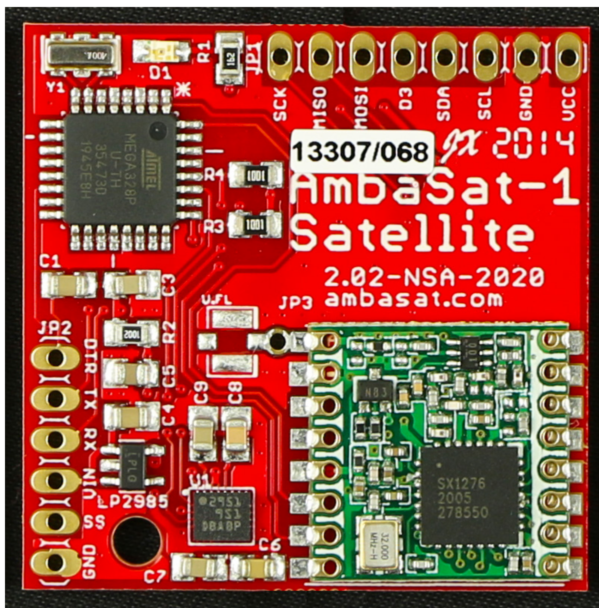

Figure 6.1: AmbaSat-1 femto-satellite [93].

The AmbaSat Space Satellite kit is designed for educational purposes to transport an individual payload on a specified satellite. The kit includes a 35×35 mm and 10 g femto satellite controlled by an ATmega328P micro controller. A sensor board can be attached to the main board, allowing experimenters to design their own sensor configurations within specified limits. In the third iteration (see Section 6.4), the entire AmbaSat PCB was redesigned to integrate the sensor unit onto the satellite's main board. The satellite is solar-powered and, due to its limited surface area and power consumption, must be developed with optimal efficiency.

However, within the package, there is also a rocket launch that propels the femto satellite into Low Earth Orbit (LEO), at an altitude of approximately 300-500 km for a duration of about one month. Communication is facilitated through the LoRa transceiver (RFM95) and the Long Range Wide Area Network (LoRaWan).

Long Range Wide Area Network

While the communication system of the satellite is briefly mentioned, it was not the primary focus of the research, yet it remains crucial for AmbaSat. Long Range Wide Area Network (LoRaWAN) is a low-power wireless network protocol designed for transmitting small amounts of data over extensive distances. The signal is relayed through a network of transmitting and receiving gates via the Internet, enabling a range of approximately 1000 km for minimal data transfer [94].

6.2 First Iteration

In the first iteration, a minimalist approach is chosen to demonstrate the feasibility of such a dosimeter and to outline the basic procedure of the overall project. For this purpose, an amplification stage based on a trans impedance amplifier was developed to amplify the signals to a level suitable for readout. The supply voltage, as well as the biasing of the diode, was initially achieved through external

power sources. In this chapter, details such as the circuit diagram are only briefly outlined, a more detailed description can be found in a project work about the first iteration.

6.2.1 Transimpedance Amplifier

A trans impedance amplifier (TIA) is a circuit consisting of an operational amplifier based on the standard inverting amplifier configuration. The TIA is characterized by its ability to convert current pulses into a voltage. It amplifies the input voltage U_E through a feedback resistor R_F between the output and the inverting input, which sets the amplification factor. In an ideal operational amplifier, it is assumed that the current pulse from the diode flows entirely into the feedback loop, where the resistor R_F and the capacitance C_F are illustrated in Figure 6.2. The output voltage V_{out} can be calculated using Formula 6.1 :

$$V_{OUT} = -I_{PD} \cdot R_F \tag{6.1}$$

The capacitance C_F alters the pole frequency t_f of the circuit by the factor $\tau = R_F C_F$, which affects the amplification in the input frequency range above t_f:

$$f_p = \frac{1}{2\pi\tau} = \frac{1}{2\pi C_F R_F} \tag{6.2}$$

This creates a high-pass filter that dampens frequencies above f_p. Consequently, for very large values of $C_F R_F$, signals may be significantly dampened or even completely filtered out. Furthermore, the capacitance stabilizes the circuit by compensating the diode capacitance and establishing a working point for the OpAmp [95]. With a diode capacitance of approximately 12 pF at a bias voltage of 100 V, the amplification factor is constrained by the sensitive volume, which is approximately 285 µm multiplied by the active area achieved at the specified bias voltage. This characteristic makes $\overline{\text{P}}$ANDA-diodes highly suitable.

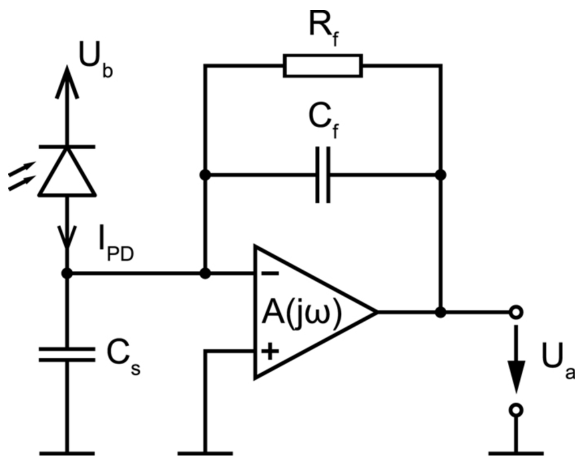

Figure 6.2: Transimpedance amplifier circuit [95].

It is important to note whether the diodes are read out on the cathode or anode side, as this determines whether holes or electrons are detected, thereby establishing the polarity of the pulse. In our case, both cathode-side and anode-side readouts were tested. However, in the following, only the cathode-side (with respect to the diode) readout is considered, resulting in negative voltage pulses.

Operational Amplifier (OpAmp)

The characteristics of the OpAmp also determine the properties of the amplification, hence the choice of the OpAmp and its tuning with the diode is crucial. An important limitation in the choice of a suitable OpAmp is the bandwidth, with a rise time of the current pulse from the diode of about 20 ns, a bandwidth of over 17.5 MHz is required [10], [96].
As very low signal amplitudes are expected, attention must be paid to the noise behavior to maintain the **signal-to-noise ratio (SNR)** within an acceptable range. Moreover, the **voltage noise density** should not exceed the nano-volt per square root hertz ($nV/\sqrt{Hz}$) range, and the **current noise density** should be less than pico-amperes per square root hertz ($pA/\sqrt{Hz}$). Another challenge is the low signal input of the diode, which is at around 150 nA for minimal ionizing particles at a fully depleted sensor [10]. The OpAmp must be able to amplify nano-ampere **Input Currents** and therefore the input current has to be magnitudes smaller. Finally, the OpAmp should feature a low total input capacitance (common-mode plus differential), ideally lower than the capacitance C_F or that of the diode, to prevent the introduction of significant parasitic capacitance without compromising the stability of the circuit. A high slew rate is also required to ensure fast operation.
There are many potential candidates, but ultimately, we chose the OPA354 (Texas Instruments) for its suitability with these requirements. It is important to mention that it is operated with a supply voltage of ± 2.5 V or can be operated in single supply mode, thereby setting the amplification boundaries to $\pm V_{CC}$ [97]. The input bias current I_{PD} is at a low value of (3 ± 50) pA with a bandwidth of 100 MHz and a slew rate of 150 V/µs.

6.2.2 Setup

The $\overline{\text{P}}$ANDA-diode with an active area of around 25 mm^2 and 285 µm thickness is glued with a conductive adhesive to a PCB which can be easily attached to the circuit. Both cathode and anode readouts are possible depending on which diode side is introduced to the OpAmp input with a capacitor (C_3 for cathode and C_4 for anode readout in the prototype board configuration as indicated in attachment D).

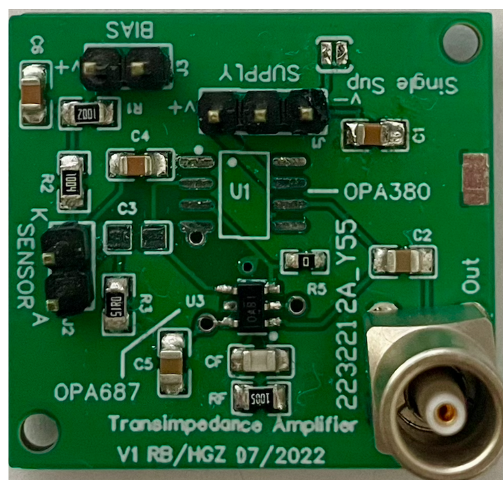

Figure 6.3: PCB of the first iteration dosimeter without attached $\overline{\text{P}}$ANDA-diode.

In the following measurements, only the cathode side of the diode is connected, resulting in negative pulses. However, the anode side was also tested. With an external power supply the diode is biased to full depletion at around 72 V, which was measured previously. The OpAmp can be powered in single- or dual-supply configurations using jumpers, but we consistently used a dual supply with a voltage of $\pm$ 2.5 V. V_{ref} is maintained at GND throughout the entire duration. In this iteration, a single amplification stage is tested, and the resistances for amplification ($R_{\mathbf{F}}$) were varied for 1 MΩ and 10 MΩ, with a constant capacitance C_{F} of 2.2 pF. Since the negative pulses go to the inverting input of the OpAmp, an amplified positive signal is expected.

6.2.3 First Iteration Measurements

The measurements are conducted in the two described configurations under the variation of the bias voltage to draw conclusions about the noise behavior. This serves as preparation for the final AmbaSat design, as voltages around full depletion are challenging to achieve. Both the maximum amplitude of the signals V_{max} and the root mean square of the noise V_{RMS}, also known as the effective value of the noise, are considered. The signals are generated by irradiation with a strontium-90 beta-emitter (description of the source in Section 4.4.4). The maximum signal V_{max} in the following tables is determined by averaging extreme values over a specific time period. In Table 6.1, only the absolute maximum measured amplitudes are considered for bias voltages of 30 V and 100 V.

V_{RBias}	V_{RMS}	V_{max}	SNR
0 V	2 mV	9 mV	4.50
5 V	2 mV	13 mV	6.50
10 V	2 mV	15 mV	7.50
15 V	2 mV	17 mV	8.50
30 V	2 mV	27 mV	13.50
100 V	2 mV	27 mV	13.50

Table 6.1: R_F = 1 MΩ

V_{RBias}	V_{RMS}	V_{max}	SNR
0 V	0.8 mV	9 mV	11.50
5 V	0.8 mV	16 mV	20.00
10 V	0.8 mV	18 mV	22.50
15 V	0.8 mV	20 mV	25.00
30 V	0.8 mV	22 mV	27.50
100 V	0.8 mV	30 mV	37.50

Table 6.2: R_F = 10 MΩ

In Tables 6.1 and 6.2, it is evident that the noise does not change with the increase in reverse bias voltage for both circuits. For a silicon detector, this behavior is expected, indicating that the dominant noise factor is not the diode but is related to the circuit layout and the noise behavior of the used components. Therefore, in the upcoming iterations, decoupling capacitors will be employed, and the PCB will be kept as small as possible to avoid "long" paths.
More importantly, the transfer function of the system exhibits a single-pole roll off at a frequency f_n=1/(2πRC). Therefore, employing a high R_F minimizes the output noise, and C_F is chosen in a way that f_n is kept as small as possible while still allowing the system to respond to the desired signal frequency while the signal amplitudes significantly increase.
This results in a higher Signal-to-Noise Ratio (SNR) and, consequently, a clearer signal. To gain a better understanding of the signal behavior, oscillograms of both circuits for an ^{90}Sr- signal at a reverse bias voltage of 100 V are presented in the following Figures 6.4 and 6.5.

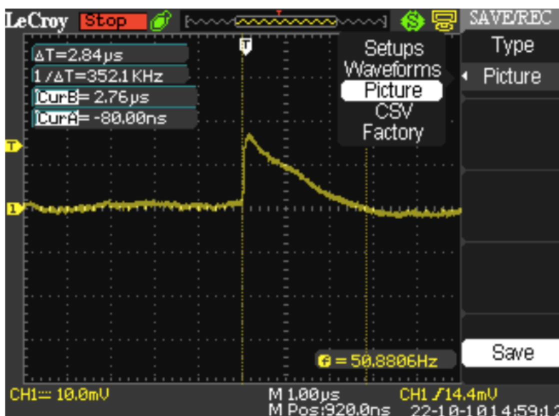

Figure 6.4: Signal for R_F=1 MΩ

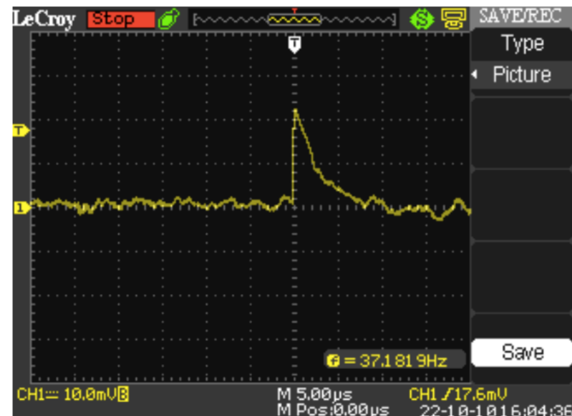

Figure 6.5: Signal for R_F=10 MΩ

The signals are clearly distinguishable from the noise. Furthermore, as previously verified in the tables, it is noticeable that the signal amplitude for 10 MΩ is higher than for 1 MΩ. It's important to note that this is a snapshot, and during the measurements, signal amplitudes exceeding 30 mV were measured at regular intervals. The rise time of the peaks remains consistent for both, approximately

200 ns. However, the signal duration has doubled from approximately 2 µs to over 5 µs due to the larger R_F. Considering the histogram in Figure 6.6, obtained using an ESP32 micro controller, the energy spectrum of ^{90}Sr can be visualized.

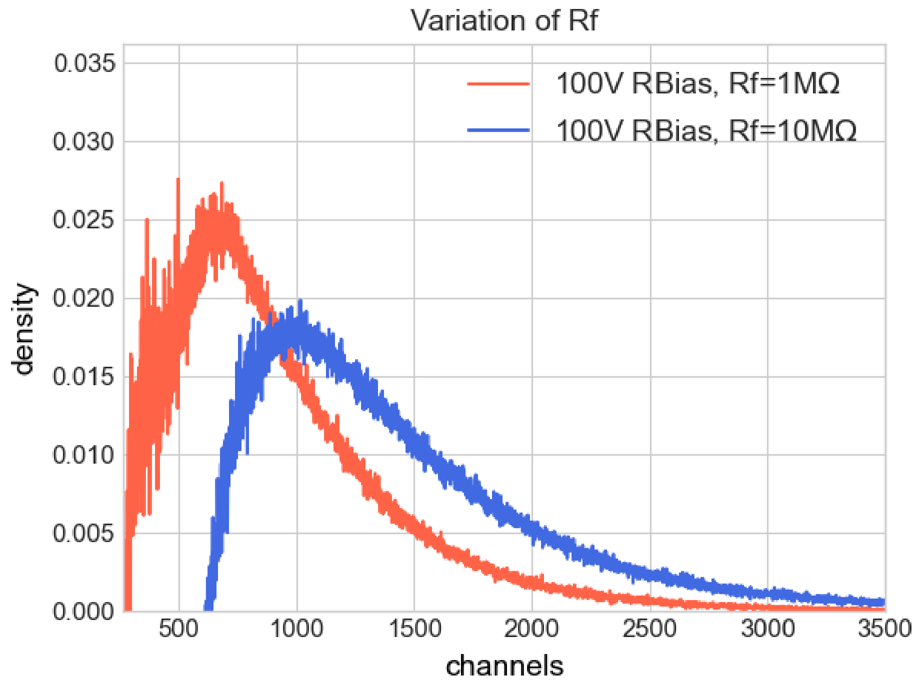

Figure 6.6: Histogrammed measurement of ^{90}Sr for R_F = 1 MΩ and 10 MΩ.

What can be observed is characteristic of the beta emitter in a thin silicon layer, namely, the Landau distribution or the superposition of several Landau distributions. On the x-axis, the channels are plotted, each corresponding to an ADC value and thus reflecting the energy. In the blue plot representing the 10 MΩ circuit, it is evident that higher channels were recorded, indicative of a higher energy measurement. This corresponds to the higher signals for the resistance R_F=10 MΩ in the tables 6.1 and 6.2

In Figure 6.7, the histogrammed measurement from Table 6.1 is visualized. The purpose of this plot is to determine whether the reverse bias voltage needs to reach full depletion, a challenging task for a stand alone design without laboratory voltage supplies.

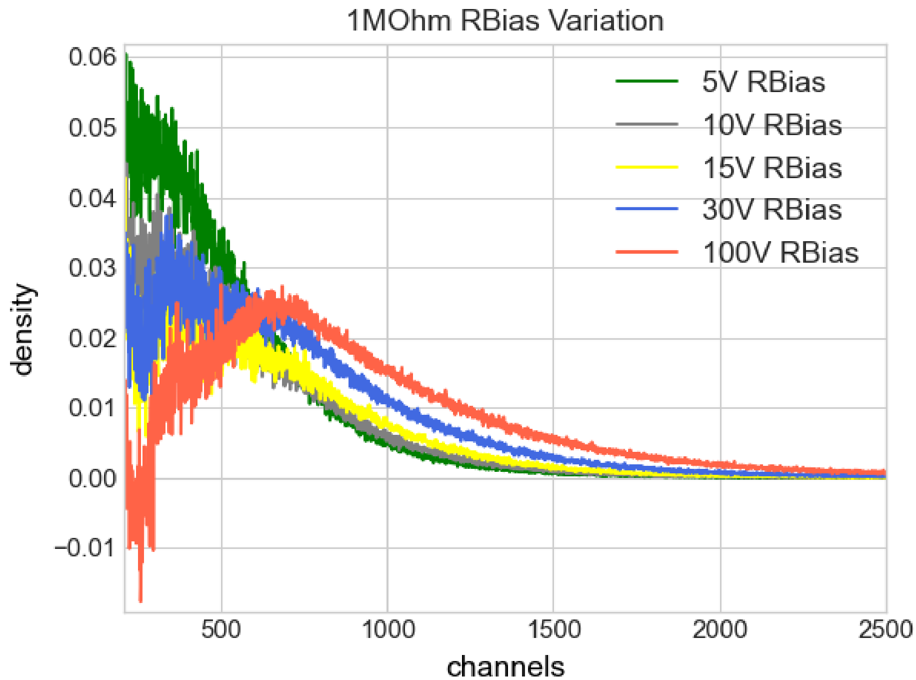

Figure 6.7: Histogrammed measurement of ^{90}Sr for different reverse bias voltages.

It is obvious that the variation is significant for voltages up to 15 V. In contrast, the curves for 30 and 100 V exhibit minimal differences and are positioned, as expected, in a higher energy range. This aligns with expectations, as the capacitance and thus the depletion zone of the diode undergo substantial changes for lower voltages, whereas for higher voltages, the changes are minimal. This phenomenon is clearly illustrated in Figure 6.16. Overall, it is apparent that larger voltages correspond to higher sensitive volume thickness and so a higher energy deposit is expected.

Findings of 1. iteration

It is clearly evident that a larger R_{F} improves the signal behavior. Since a cut-off is set for the high frequency of the signal spectrum, a significant portion of the signal could be cut off for a large τ=RC. To measure signals, the diode does not need to be fully depleted. Although, a higher depletion results in stronger signals. Since this depends on the length a particle can travel through the depleted zone and the zone decreases exponentially with voltage, the difference is minimal for voltages above 15 V. Therefore, the dosimeter can be operated with a reverse bias voltage of 30 V.

6.3 Second Iteration PCB

In the second iteration, the circuit undergoes significant adjustments. Given that the sensor will not be fully depleted and dosimetry involves considering not only

maximum values, it is necessary to amplify the signal and extend its duration, since a micro controller readout is targeted. In this section we will not explain the circuit (circuit diagram in the appendix D.2) in detail, which was done in the study by Erik Euler.

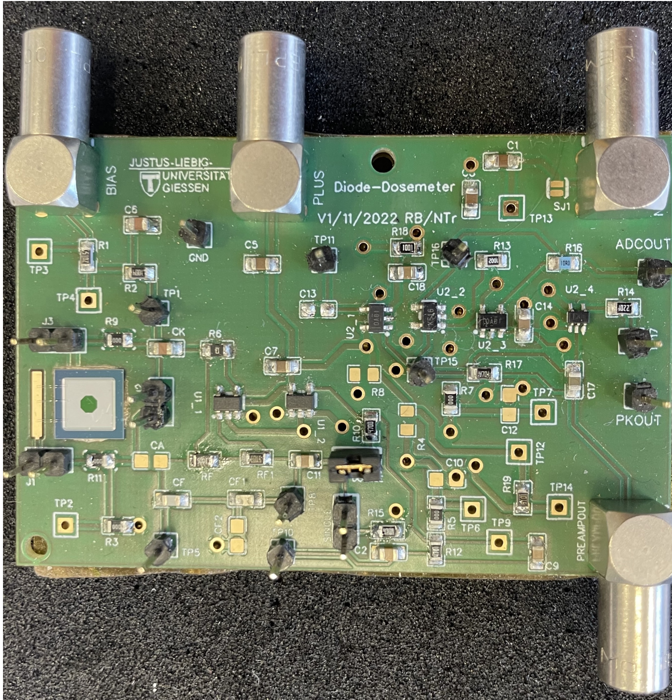

Figure 6.8: Image of the 2nd Iteration Dosimeter with the $\overline{\text{P}}$ANDA Diode.

Furthermore, several improvements have been implemented to reduce noise. For instance, the diode has been directly glued with conductive adhesive to the circuit's printed circuit board (PCB), where it is connected to the circuit through wire bonding, ensuring optimal contact. The traces were kept small, feedback capacitances were incorporated, and the contacting was enhanced. As before, the dosimeter can be read out in cathodes or anodes by attaching jumpers.

In addition, contacts have been fitted before and after each stage in order to understand the circuit. This leads us to the two major changes. In this iteration, three amplification stages, following the same scheme as explained in iteration one (Section 6.2.1), have been implemented, with the corresponding PCB shown in Figure 6.8. This results in the amplification and extension of the signal, as shown in Table 6.3. Furthermore, in this iteration, a peak detection stage has been introduced to ensure the determination of the signal's maximum value, which is detailed in Section 6.3. For the circuit readout, an ESP32 micro controller was used, as in iteration one. This choice was made to test the performance of the circuit in this iteration, and the ESP32 allows for more accurate data recording compared to the Atmega328p.

Peak-Detect Stage

The Peak-Detect stage was inspired by the **AIRDOS**-project, which is based on a comparator [98]. To ensure pulse detection, the Peak-Detect stage is designed to maintain the pulse at its maximum for a defined time which is mainly dependent on the ADC readout speed and the amount of samples one want to measure per peak. In the case of very short pulses, there is a risk that the signal may already

be flattened before the Analog-to-Digital Converter (ADC) can capture it, either due to insufficient ADC clock frequency or capturing the signal before or after its maximum. To prevent the same pulse from being read multiple times, the peak-detect stage is reset after each reading operation. The highest pulse generated between two reading cycles is held until a reset occurs. Additionally, a threshold can be set so that pulses are only recorded if they surpass a certain amplitude, effectively filtering out noise.

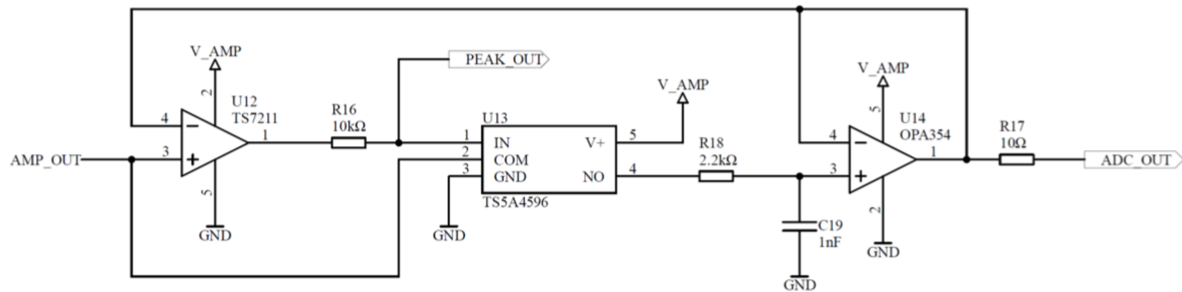

Figure 6.9: Circut of the peak-detect stage.

At the beginning of a readout operation, all capacitors are discharged, and all lines processing signals are grounded. When a pulse from the voltage amplifier is introduced into the non-inverting input of U_{12}, its output is elevated to the supply voltage V_AMP. Following, the analog switch U_{13} is activated, directing the incoming signal at the Peak-Detect stage AMP_OUT from COM to the analog switch (U_{13} in Figure 6.9). At this point, capacitor C_{19} is rapidly charged through resistor R_{18}. The signal is then passed to the OpAmp U_{14} configured as an impedance converter. As a result, capacitor C_{19} discharges very slowly, enhancing the Peak-Detect stage's resilience without a decline in voltage. The unamplified voltage level is then transmitted to the analog-to-digital converter (ADC).

To complete the feedback loop, the outgoing signal is continuously compared with the input signal by the comparator U_{12}. If the voltage of the input signal decreases, the output of U_{12} drops to ground, consequently closing the analog switch. Capacitor C_{19} maintains its voltage level and continues to transmit it to the output

In the loaded state, if a larger signal is introduced, either due to another particle or because the particle's peak has not yet been reached, U_{12} and therefore U_{13} are activated as before. This action raises the potential of capacitor C_{19} to the higher signal level, which, as previously described, is then transmitted to the ADC.

When a readout cycle concludes, determined by the micro controller, the analog switch is pulled to ground via PEAK_OUT, which is connected to a port of the micro controller. It is crucial to ensure that this condition persists until C_{19} is completely discharged. The peak-detect stage is now reset, and all signal lines are grounded. The micro controller can initiate the readout process again by releasing PEAK_OUT.

The behavior is evident in the oscillogram shown in Figure 6.11. It is clear that

the output of the Peak-Detect stage in yellow holds the voltage following the incoming signal in blue. The input signal shows slight distortion due to the use of the measurement probe.

6.3.1 Second Iteration Measurements

As in the first iteration (see Section 6.2), the behavior of the amplification stages is examined. Signals were probed after each of the three amplification stages using measurement probes. To further understand the influence of the bias voltage, each stage was tested for bias voltages of 5, 10, 20, and 90 V. Additionally, the signal length was estimated. Similar to previous tests, the signals were generated by irradiating the diode with ^{90}Sr.

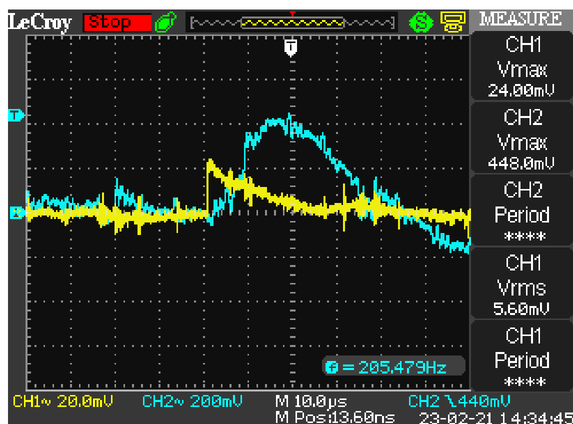

Figure 6.10: ^{90}Sr-signal after amplification stage one in yellow and three in blue.

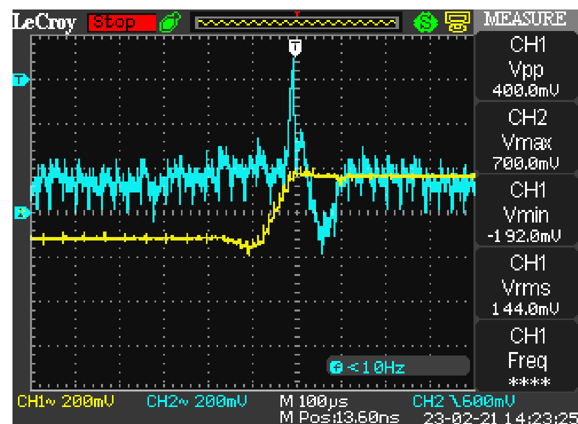

Figure 6.11: ^{90}Sr-signal after amplification stage three in blue and after peak detection in yellow.

In Figure 6.10, a measured pulse is exemplary plotted in yellow after stage one and in blue after stage three. Considering the scale, it is evident that the signal has almost twenty folded after the third stage compared to the first. The signal length has increased. Additionally, a signal overshoot is observed after the third stage, indicating a need for adjustments to coupling capacitors in the next iteration. All results from the measurements are presented in Table 6.3.

Stage	V_{RBias} [V]	V_{max} [mV]	Signal length [µs]	V_{RMS} [mV]	SNR
1	5	26.4	16.8	0.6	44
	10	29.6	15.4	0.6	49.3
	20	30.4	14.8	0.6	50.7
	90	32.8	22.8	0.6	54.7
2	5	-45.6	39.6	0.4	114
	10	-64.8	40.4	0.4	162
	20	-57.6	35.2	0.4	144
	90	-88	40.8	0.4	220
3	5	312	38.4	1.6	195
	10	416	36.8	1.6	260
	20	384	34.8	1.6	240
	90	544	37.6	1.6	340

Table 6.3: Measurements of ^{90}Sr signals after the three amplification stages for various reverse bias voltages.

An immediate observation in Table 6.3 is that stage two outputs negative signals. This is expected considering the circuitry for the trans impedance amplifier (see Section 6.2.1), as the positive signal from stage one is amplified and inverted by the inverting input of stage two. The same behavior occurs in stage three, with the signal being inverted back to positive. As before, the signal amplitude is dependent on the reverse bias voltage, but the noise is not. Consequently, the Signal-to-Noise Ratio (SNR) is directly influenced by the depletion of the diode. At a bias voltage of 5 V, the amplitude of the signal increased by a factor of approximately 11.8 between the first and third stages, and the signal length extended by a factor of 2.3. At a bias voltage of 90 V, the amplitude increased by a factor of 16.4, but the signal length only extended by about 1.7 times. The seemingly lesser extension of the signal could be attributed to an overshoot observed in the signal waveform, making it challenging to determine the signal length. The SNR also improves significantly through the amplification stages, for example, increasing from 54.7 to 340 at 90 V.

Time Resolution

As mentioned in Section 6.1, in the final setup, the analog signal is read out using an ATmega328p. Therefore, the signal properties of the sensor will be compared to those of the ATmega, even though the measurements are carried out with an ESP32. The micro controller's Analog-to-Digital Converter (ADC) is utilized for this purpose. However, with a maximum sampling rate of 15 kSps (thousand samples per second), there are significant limitations in signal length. The minimum duration t_{min} of a readout process can be calculated as follows:

$$T = \frac{1}{f} \quad \text{with} \quad f \leq 15\,\text{kHz} \tag{6.3}$$

$$T \geq \frac{1}{15\,\text{kHz}} \tag{6.4}$$

$$t_{\text{min}} \geq 66.7\,\mu\text{s} \tag{6.5}$$

So, the readout process takes a minimum of 66.7 µs. When comparing this with the signal lengths from Table 6.3, with a maximum length of 40.8 µs, it becomes apparent that the ADC of the ATmega328p is significantly too slow. The peak-detect stage is, therefore, essential. It determines the highest signal coming from the amplification stages in 66.7 µs, reads it, and then resets. In this process, it may happen that smaller signals are not captured since the peak-detect already holds a maximum.

ADC Resolution

The Analog-to-Digital Converter (ADC) of the ATmega covers a range of 1.1 V across 10 bits [99]. This results in a resolution of:

$$\frac{1.1\,\text{V}}{1024} = 1.07\,\text{mV} \tag{6.6}$$

This resolution is sufficient to sensibly capture the signal. Considering the pure signal height, it may be feasible to read out stages one and two as well.

6.3.2 Energy Calibration

In the calibration process, an estimation is sought between the energy deposit in the detector and the ADC channels. This allows the detector to provide an approximation of the deposited energy of a particle. For calibration, a Strontium-90 source was employed, the decay of the source is described in Chapter 4.4.4. A total of 4096 ADC channels were utilized, corresponding to the maximum capability of the ESP32 [100].

For the calibration, three points are selected: the Most Probable Value (MPV), corresponding to the peak of the distribution, the mean value, representing the average, and the maximum value. The maximum value is assumed to be reached when, with sufficient statistical data, an electron with the maximum energy of the Yttrium decay, approximately 2.2 MeV, deposits all its kinetic energy in the sensor.

During the measurement, a plastic scintillator detector was positioned beneath the sensor for conducting a coincidence measurement. This implies that signals are only recorded by the dosimeter when the second detector simultaneously detects a particle. To achieve this, the readout times of the detectors were synchronized.

As the particle's energy must be sufficient to generate signals in both detectors, it can be reasonably assumed that these are minimally ionizing particles. Particles of lower energy, such as photons, would only leave a signal in one of the two sensors. This minimizes noise from background radiation and fulfills the requirement for comparing the mean value and MPV value, a comparison valid only for Minimum Ionizing Particles (MIPs).

Hence, it is assumed that Yttrium is primarily responsible for the spectrum observed in Figure 6.12. This is because the β-energy of the ^{90}Sr decay is significantly lower than that of ^{90}Y and is, therefore, largely absorbed in the first detector. This estimation is made considering $\beta\gamma$, where a $\beta\gamma \geq 3$ corresponds to a minimum ionizing particle [45]. Using the formulas in 4.15, with the rest energy of electrons E_0=0.511 MeV and the maximum kinetic energy from Yttrium decay E_{Ykin}=2.279 MeV, $\beta\gamma$ can be determined to be 5.37. For the maximum energy of the ^{90}Sr decay E_{Srkin}=0.546 MeV, this results in only $\beta\gamma = 1.81$.

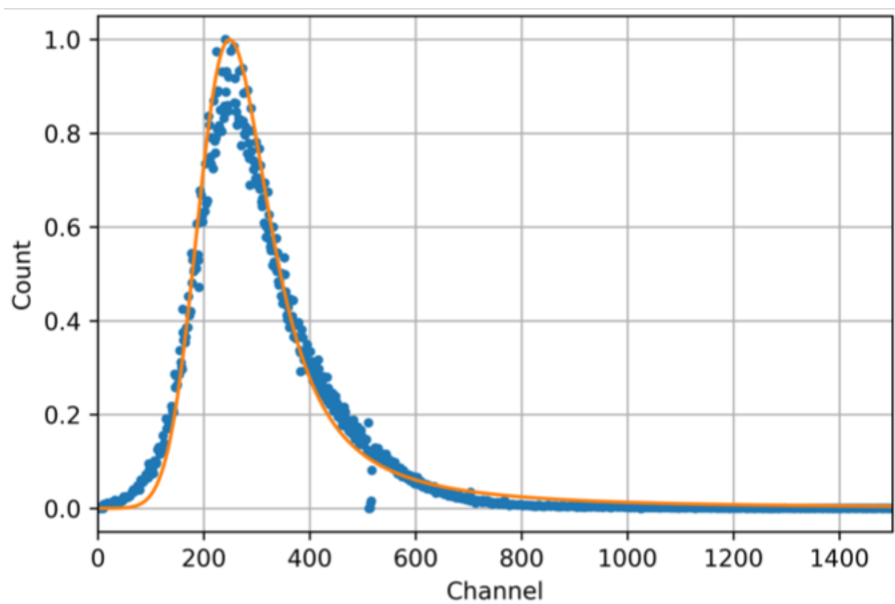

Figure 6.12: Distribution of the deposited energy in the dosimeter due to irradiation with ^{90}Sr.

The distribution conforms to the typical Landau distribution for the energy deposited by electrons in a semiconductor. To illustrate this, a Landau fit (explained in Section 4.3.2) in yellow has been overlaid on the data.
The Most Probable Value (MPV) for the measurement can be established at channel 249, as explained earlier, representing the most likely energy resulting from the Yttrium decay.

For energy calibration, as detailed in Section 4.3.1, the Bethe-Bloch formula was utilized to calculate the deposited energy of ^{90}Sr-radiation when traversing through

the fully depleted sensor.
Using the stopping power formula in 4.16, for the average energy of the ^{90}Y, β-particles of approximately 0.8 MeV, a deposited energy of 107.9 keV can be computed. The conversion factor for the Landau function from MPV to mean is 0.675 MeV, corresponding to channel 368 and an energy of 159.9 keV. This conversion factor depends on $\beta\gamma$ and the absorber thickness, as described in source [45].

For the maximum energy, as explained earlier, the maximum energy from Yttrium decay is chosen as 2.2 MeV, and the highest measured channel at 2272 is selected. With these three points, a linear fit can be performed for calibration, as shown in Figure 6.13.

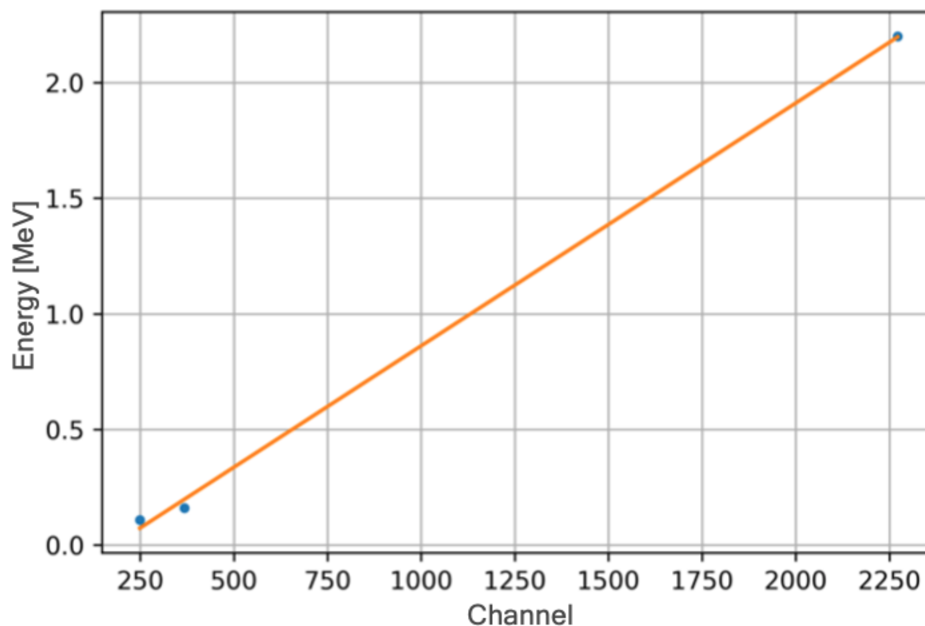

Figure 6.13: In blue, the data points from the Yttrium measurement, and in orange, the linear fit.

As evident, the points align very well with the linear fit. This is further supported by the low error in the slope a, which simultaneously represents the sought value for the ratio of ADC channel to deposited energy:

$$a = (1.051 \pm 0.039)\,\frac{\text{keV}}{\text{channel}} \tag{6.7}$$

Energy calibration is provisional, as it was based on the assumption of Minimum Ionizing Particles (MIPs). This assumption is valid for the coincidence measurement but may not hold for the entire spectrum of Strontium. Additionally, choosing the highest measured value assumes that a particle of the highest energy indeed caused a signal, depositing only minimal energy in the veto detector and the rest in the dosimeter. Given the lack of alternative sources for calibration in this iteration, these assumptions were necessary.

In future iterations, it is essential to perform a precise calibration using methods such as simulations or exact energies. Nonetheless, with a slope error of 3.72%, it can be considered a good approximation.

Findings of the 2. Iteration

The investigations of the 2nd iteration primarily focused on making preparations to finalize the circuit diagram for the Ambasat PCB. It became evident that the Peak-Detect stage is necessary due to the low readout speed of the micro controller. To address this, a Peak-Detect stage that can be controlled by the micro controller was successfully tested. In addition, it has been determined that signals from a non-fully depleted $\overline{\text{P}}$ANDA sensor can be meaningfully measured even with just one or two amplifier stages.

6.4 Third Iteration all in one PCB

In the third iteration, the insights gained with the first two iterations were applied to integrate the dosimeter circuit with the AmbaSat femto satellite. For this purpose, Nico Krug and I collaboratively redesigned the AmbaSat PCB (see Figure 6.14), with significant portions of the work presented in his bachelor thesis. The circuit diagram can be found in the appendix (D.4). Technical details will be briefly touched upon in this chapter, while a comprehensive explanation of the circuit and additional information on its construction can be found in the aforementioned thesis. Since the femto satellite operates at a voltage of 3.3 V, a voltage transformation was incorporated to generate a voltage of 35 V [93]. As demonstrated in the first iteration (6.2), it was shown that 30 V is sufficient for signal readout. Nevertheless, in this iteration, a $\overline{\text{P}}$ANDA test diode was employed, which is fully depleted at around 50 V resulting in the same sensitive volume of 285 µm. This is expected to result in larger pulses even at lower reverse bias voltages. The number of amplifier stages was reduced from three to two. Additionally, initial tests for operation in space, such as vacuum and light tightness, were conducted. The concept was also tested with ^{90}Sr and at the MIT using a proton beam.

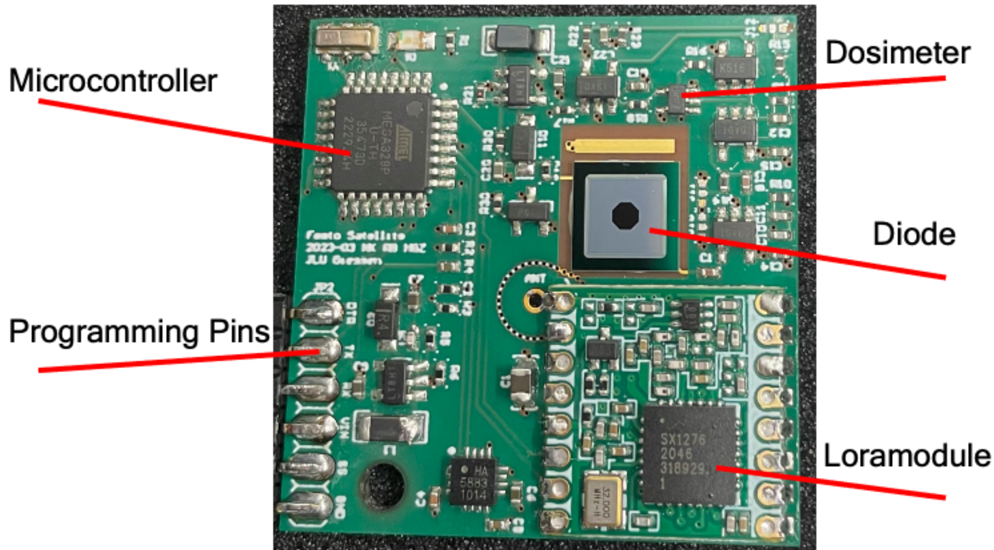

Figure 6.14: Dosimeter integrated with the AmbaSat hardware and the $\overline{\text{P}}$ANDA diode.

The first amplification stage is implemented using the same approach discussed in Section 6.2.1 as a current-voltage converter. The second stage is constructed as a voltage amplifier. The distinction between the first and second stages lies in the utilization of the non-inverting input of the OpAmp.

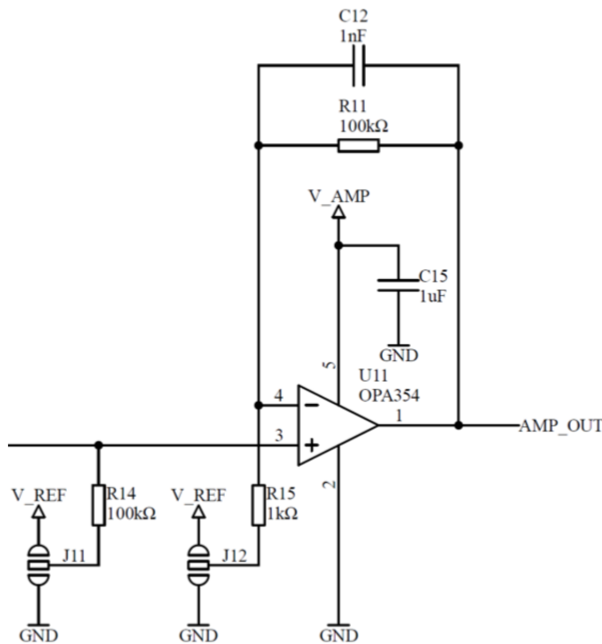

Figure 6.15: Third iteration voltage amplifier stage.

The stage is supposed to amplify the signal from the first stage to approximately 1 V. To achieve this, an amplification factor A of around 100 is necessary, as explained by Formula 6.9 and the resistor R_{15} and feedback resistor R_{11}.

$$A = 1 + \frac{R_{11}}{R_{15}} \tag{6.8}$$

$$A = 1 + \frac{100\,\text{k}\Omega}{1\,\text{k}\Omega} \tag{6.9}$$

$$A = 101 \tag{6.10}$$

In addition, C_{12} is reduced to 1 nF to adjust the pulse lengths to approximately $\tau = \text{R}_F \cdot \text{C}_F$=100 µs, ensuring a stable working point for the OpAmp. The peak-detect stage worked as expected in iteration two (Section 6.3), therefore no changes are needed. The reference voltage (V_{ref}) is set through a voltage divider to

$V_{\mathrm{ref}} = \frac{1}{10} \cdot V_{\mathrm{amp}}$ to define the working level of the OpAmp which is due to single voltage between $+VCC$ and GND.This allows pulses both above and below V_{ref} to be amplified. Due to the limited power availability on the femto satellite, which is entirely allocated for transmitting data via LoRaWAN 6.1, a transistor circuit has been implemented. This circuit enables the complete powering on and off of the detector. A significant challenge involves the voltage transformation for the reverse bias voltage of the diode. This transformation was achieved using an LT1615 DC/DC converter, which transforms the voltage from V_{amp}=3.3 V to approximately V_{bias}=35 V. As a result, the bias voltage has been stably set to slightly above 30 V so far.
However, there is a peaking of the bias voltage by approximately 50 mV. Since this fluctuation is directly capacitively coupled to the amplification stages, it renders measurements impossible. This issue is more precisely described in a project work and will be addressed in the next iteration. The rest of the circuit could be tested using an external bias voltage of either 5 or 30 V.

$\overline{\mathrm{P}}$ANDA-Diode with Full Depletion at 50 V

As already mentioned, an older model of the $\overline{\mathrm{P}}$ANDA sensors is used for the third iteration. As before, the sensors are 285 µm thick and therefore have the same capacitance, but they have a lower depletion voltage of V_{dep}=50 V. This has disadvantages for extremely high radiation doses like in the $\overline{\mathrm{P}}$ANDA experiment with more than 10 MRad, but this is not a problem for our application, where a dose of 2 to 10 kRad at the low earh orbit for around one year is expected [10], [101].

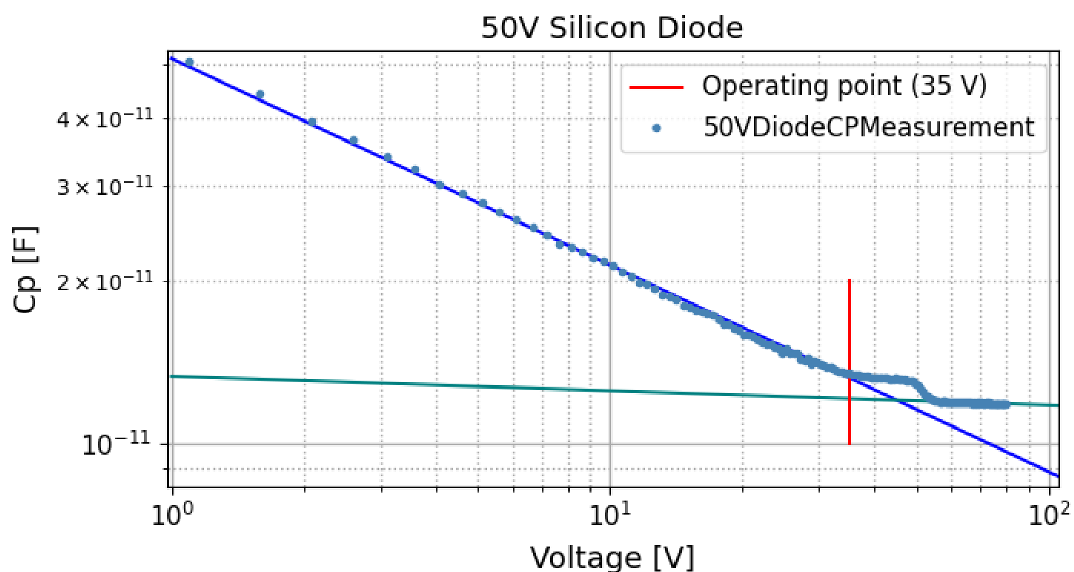

Figure 6.16: The capacitance measurement against the reverse bias voltage of the 50 V $\overline{\mathrm{P}}$ANDA diode.

The depletion plateau is clearly visible and was measured to be 44.82 V ± 1 V through the two linear fits. For full depletion, a capacitance of 12.0 pF was measured, and for the operating point of the diode at 35 V, a capacitance of 13.43 pF was measured. With the capacitance of the undepleted diode being 103.62 pF, it can be inferred that the diode is 98.45 % depleted at 35 V.
This makes it clear that sufficiently high signals can be expected even at 35 V. The precisely measured diode was attached to the PCB using conductive adhesive and contacted with several bonding wires.

Signal Testing

The signal was tested again using a ^{90}Sr-source and with an external power supply for the bias voltage of 5 V. However, it was observed that even without the source, a high number of pulses could be detected. Consequently, it is not entirely clear whether these signals can be attributed to the source or, for example, to ambient photons. Therefore, efforts are being made in Section 6.4 to make the diode light-tight, aiming to minimize unintended interference signals. Nonetheless, the functionality of the dosimeter can be demonstrated.

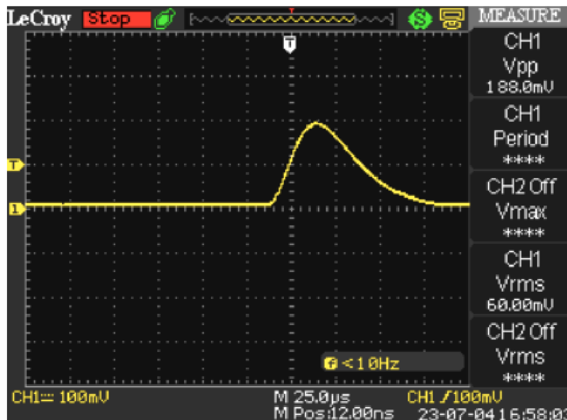

Figure 6.17: ^{90}Sr-signal after amplification stage two in yellow.

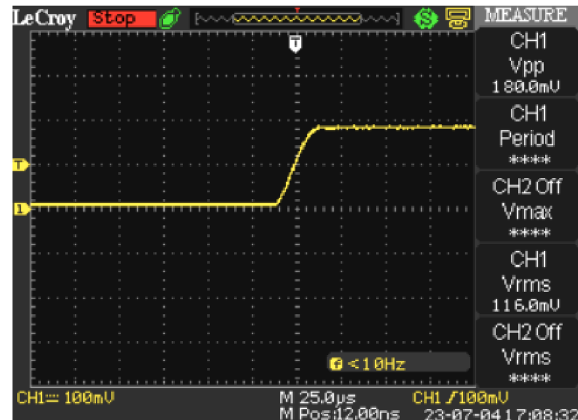

Figure 6.18: ^{90}Sr-signal after Peak-Detection stage in yellow.

The pulse after the amplification stages can be observed in Figure 6.17. In comparison to iteration two, the undershoot has been successfully corrected. Additionally, the Peak-Detect stage in Figure 6.18 is operational, maintaining the signal at the same level throughout the required readout time.

Vacuum and Light Tightness Tests

To prepare for deployment in low earth orbit, several properties were tested, one of which is the light tightness of the diode. This is of fundamental importance since photons hitting the sensor would also generate an electrical signal, potentially overlaying measurements of cosmic radiation. For this purpose, diodes were bonded to PCBs and tested for functionality under illumination using an LCR

meter. The tests were conducted in the probe station in the clean room of the JLU, which provides optimal conditions.

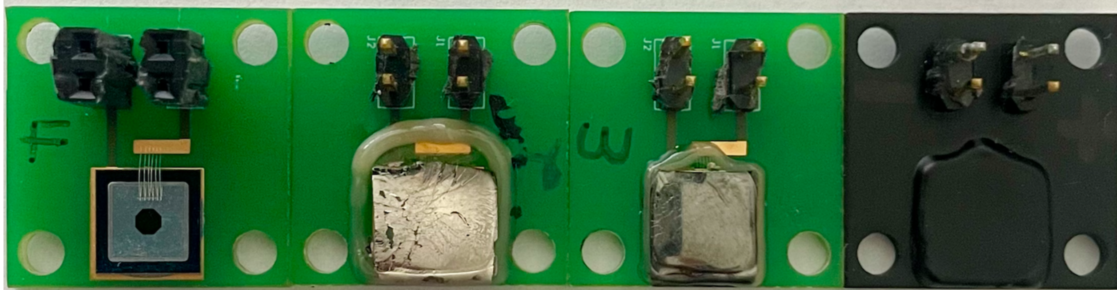

Figure 6.19: Bonded diodes, without glob top (left), with glob top and sputter coating (both in the middle), and with glob top and paint coating (right).

Initially, the diodes and bonding wires were sealed with a glob top to protect the connections. This did not affect the measured parameters of capacitance, leakage current, and depletion voltage. To achieve light tightness for the diode, several sputtering tests were undertaken, where a thin layer of aluminum was applied to the glob top through various methods of plasma sputtering. However, this rendered the diode unusable. The simplest and most light-tight method was achieved through painting. A thin layer of black paint was applied using spray paint, which, considering Figure 6.20, prevents light from reaching the diode. Every tested method can be seen in Figure 6.19.

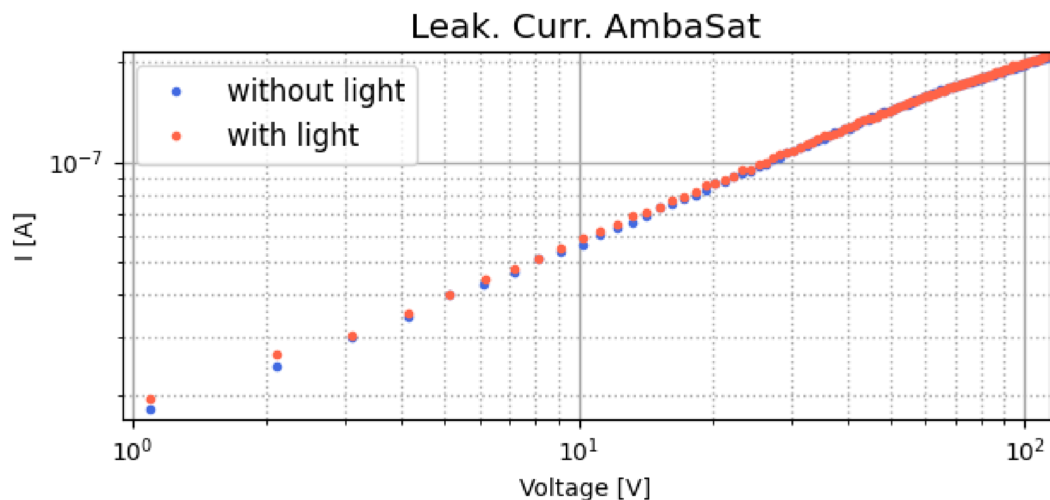

Figure 6.20: Leakage current against reverse bias voltage of a painted diode with illumination in red and without illumination in blue.

It is clearly visible that the leakage currents with and without illumination of the diode do not differ. Additionally, the diodes were placed in a vacuum for several weeks to simulate conditions in space and to check for issues with the glob top, i.e. trapped air bubbles. It has been demonstrated that the properties have not

changed. This is the desired outcome, and painted glob tops can be used for the final dosimeter.

6.4.1 Conclusion Dosimetry with $\overline{\text{P}}$ANDA Diodes

This chapter has examined the development and performance of a novel dosimeter concept based on $\overline{\text{P}}$ANDA diodes. The results demonstrate that these diodes can be successfully utilized for dosimetry. Furthermore, comprehensive knowledge about the energy deposition of fast charged particles in silicon has been acquired, which is crucial for the precise detection and analysis of radiation doses.

The primary focus was on characterizing the signal behavior of the diodes and their amplification, which is essential for the development of reliable dosimetry systems. These findings are now being integrated into the ongoing development of MVD prototypes, as described in Section 7.
For the dosimeter concept itself, only suitable voltage transformation, energy calibration, and a launch date for space transport are required. For energy calibration, beam time at the Marburg Ion Beam Therapy Center is planned, as well as a new circuit design for voltage transformation. The signal acquisition and processing, as successfully demonstrated in this section, will be maintained.

Chapter 7

MVD-Protoype

7.1 Mounting $\overline{\text{P}}$ANDA Sensors to the ToASt-ASIC

One of the main task of this work is the adaption of the $\overline{\text{P}}$ANDA Sensors to the ToASt (**To**rino **A**mplifier for silicon **St**rip detectors) chip. With the ToASt front-ends the signals generated by the silicon strip detectors can be read out, digitized and processed further.

7.1.1 Torino Amplifier for Silicon Strip Detectors

Input capacitance	2/17 pF
Max rate per strip	50 kHz
Input charge range	1/40 fC
Max noise	1500 e^-
Peaking time	50-100 ns (prog)
Channels per chip	64
Channel pitch	66 µm
Reference clock	160 MHz
Charge resolution	8 bits
Time resolution	6.25 ns (pk-pk) 1.8 ns rms
Output drivers	2×160 MS/s
Max output rate	2×4.9 Mevents/s
Max power consumption (estimated, full TMR) (estimated, no TMR)	 360 mW (5.6 mW/ch) 257 mW (4 mW/ch)
Die size	3.24×4.41 mm^2
Pads position	On two sides only

Table 7.1: Characteristics and possibilities of the ToASt.

The ToASt-ASIC is a 64-channel integrated circuit design that offers information about the position, time, and deposited energy of particles passing through a silicon strip detector.
A key feature of the ToASt is the absence of a trigger signal, providing great flexibility in data selection algorithms. Timing and energy information are obtained from two time stamps, which correspond to the times at which the signal crosses two predefined thresholds. These are acquired by storing the value of a global counter [102].

In the following, the sides of the sensors are distinguished by their doping: the side with n-doping is referred to as the n-side, and accordingly, the strips with p-doping are referred to as the p-side.
The ToASt is implemented in a commercial 110 nm CMOS technology and nominally operates with a 160 MHz clock. It provides two serial 160 Mb/s links to connect the higher level data concentrator [103]. A global unit manages configuration information for all regions. With standard settings, the Time-over-Threshold gain for p-type sensors or p-side readout is 40 ns/fC, and for the n-side, it is 30 ns/fC. Using a test pulse, a test charge can be injected for functional tests and a preliminary energy calibration of the chip. The thresholds and the ToT current can be tuned at a coarse level on the chip (referred to as global) and with finer resolution on the channel level. The global time and energy thresholds have a tuning range of 494 mV with an LSB of 15 mV. The fine tuning has a range of 84 mV with 1.3 mV LSB.
The ToT current can be adjusted from 2.1 nA to 488 nA with an LSB resolution of 15.2 nA. For the channels, the current can be set with an LSB of 28.3 nA, ranging from 27 nA to 906 nA.
In normal operation, the ToASt records both the rising and falling edges, from which the deposited energy of a particle can be calculated using the Time-over-Threshold method, as explained in Chapter 7.1.2.

However, if information about energy is not needed but a high rate is desired, the ToASt can also operate in **le_only** mode, where only the rising edge is recorded. The resolution of the time information is 6.25 ns with a maximum rate of 50 kHz per strip.
The data output is organized in 32 bit words containing the region and channel address, leading and trailing edge time stamps. Data corresponding to the same time stamp counter cycle is encapsulated in frames, distinguished by a frame header and a frame trailer. The frame header includes the chip address and the frame number, whereas the frame trailer contains the count of data words. In cases where no data is received, the ToASt sends a synchronization packet. The ToASt can be configured by external input signals by 16 bit commands.

7.1.2 First Mounting

The initial mounting of a sensor onto a ToASt chip was accompanied by test measurements to identify potential sources of errors. For testing purposes, sensors not intended for the final $\overline{\text{P}}$ANDA detector were connected to a test board containing a ToASt chip, as illustrated in Figure 7.2.

The sensors S3 and S4 from the $\overline{\text{P}}$ANDA-Wafers are well-suited for initial tests. The smaller sensors are easier to handle but exhibit nearly identical characteristics to the full-size sensors (S1 and S2) since they originate from the same wafer. It is noteworthy that the S3 sensor (see Table 5.15) has a different pitch than the other

sensors, a factor that has been taken care of. Prior to mounting, the properties of the wafers from which the sensors are sourced are examined for leakage current and full depletion voltage. This ensures the overall functionality of the sensors. Nonetheless, it should be acknowledged that the structures on the sensors may incur damage, which could be attributed to bonding, transportation, or production.

In the following figure, the schematic of the bonding pads for each side of the sensor is presented. The bias pads are marked in blue, the DC test pads in yellow, and the AC readout pads in red.

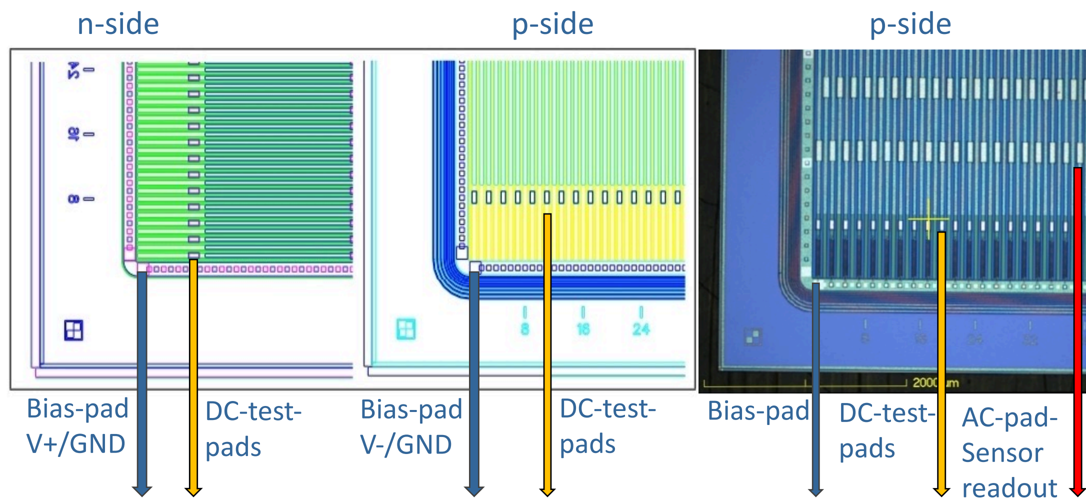

Figure 7.1: Sensor bonding pads for p- and n-side [10].

The following lists which sensor pads need to be connected to the ToASt test board pads to enable functionality:

- n-side bias pad to HV+
- p-side bias pad to AGND
- AC pads to ToASt channels

At first a S4 "Baby Sensor" was mounted to the # 5-ToASt-Board. The sensor was attached to the board with double-sided adhesive tape so that both sides could be contacted by wire-bonding. The n-side was connected to the positive high voltage and the p-side to the AGND contact of the board. Therefore the sensor is connected to the reverse bias-voltage.

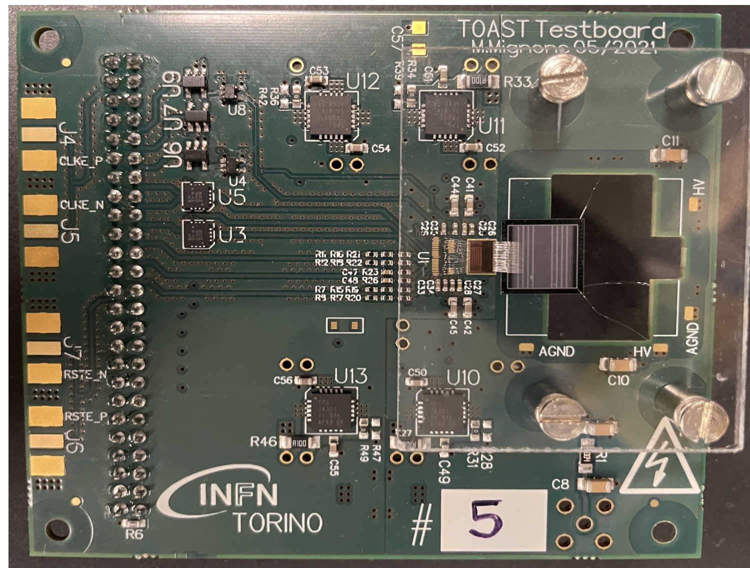

Figure 7.2: S3 sensor connected to the reverse-bias voltage pads and the 64 readout channels of the ToASt Testboard.

At first, the sensor underwent testing by incrementally increasing the voltage and measuring the leakage current. In this preliminary test, the board was not connected to the FPGA, and the supply voltage was not applied. Additionally, the AC pads were not bonded to the readout pads of the ToASt. In these measurements, values in the nano-ampere range are anticipated and measured as illustrated in Figure 7.3 (green line, "Only Bias"). This expectation is based on previous results in Section 5.4.1, where test structures with a comparable active area size are measured.

After the successful test, the board was also fully connected and the test was repeated. As before, the current is in the expected range, but significantly increased due to the connection to the board (blue line "Bias and ToASt"). In the third test, each of the 64 channels of the ToASt is connected to a strip of the sensor by bonding the AC pads of the sensor. In this configuration, the AC pads of the n-side of the sensor are connected to the readout pads of the board. The test was stopped at 50 V this time because the current unexpectedly increased, as illustrated in Figure 7.3 (red line, "Bias AC-Pads and ToASt"). Simultaneously, one of the ToASt-Board channels experienced a failure. The channel failure and the rise in leakage current suggest that one of the strips of the sensor has failed. This can occur when the oxide layer between the aluminum strip (readout strip) and the highly doped Si-strip is damaged, resulting in a phenomenon known as a pinhole. The pinhole breaks the capacitance between both strips, causing direct contact of the channel with the bias voltage and ultimately leading to channel failure. This unintentional contact can induce currents that impact the leakage current.
As a result, it was decided to remove the bonding wire from the faulty channel and strip. Subsequently, the same measurement was conducted, and the leakage current behaved as expected until a voltage of 15 V. At this point, the current

abruptly spiked to an unacceptable value, similar to the previous measurement, and another channel became compromised. Even after reducing the voltage below 15 V, the current remained high. This behavior indicates that the oxide layer of a strip was damaged, likely thinner than planned at one point due to bonding or faulty manufacturing. This thinner layer has a lower breakdown voltage, in this case, 15 V, and is consequently completely destroyed.

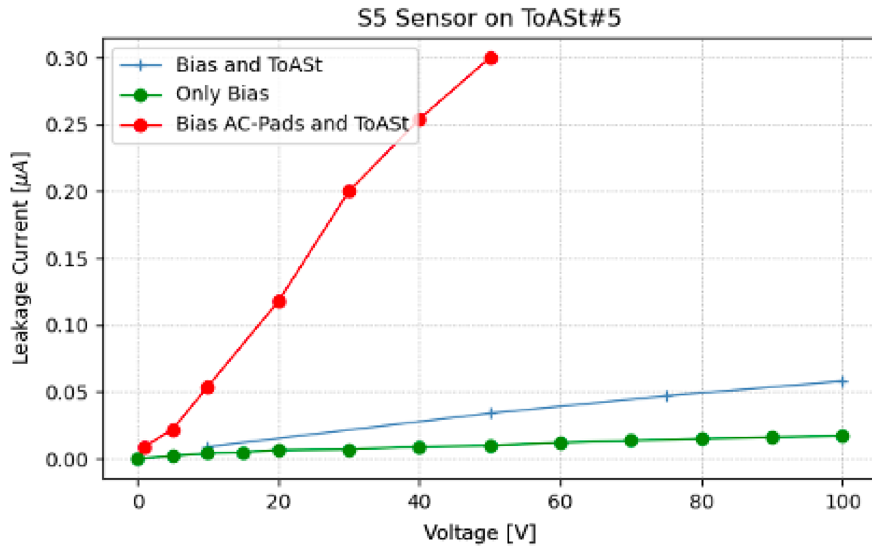

Figure 7.3: Leakage current to bias voltage for a S4 sensor bonded to a ToASt-Board in different configurations.

To ensure that neither the ToASt nor the sensor has incurred further damage, new components are being used. This time, the # 2-ToASt-Board was mounted with an S4 sensor. It was observed that, once again, one of the strips malfunctioned. However, after removing one bonding wire, every test was successfully passed. A noise measurement indicated a decrease in noise between 90 and 100 V, as expected for the n-side. The depletion region initiates at the border between the n and p-doped silicon, located on the p-side. As the depletion region extends, it reaches the n-side at a depletion voltage of around 100 V. Consequently, the noise at this voltage decreases significantly since, at this point, there are hardly any free charge carriers around the strips of the n-side responsible for the noise. The same behavior can be observed when measuring the capacitance of the n-side.

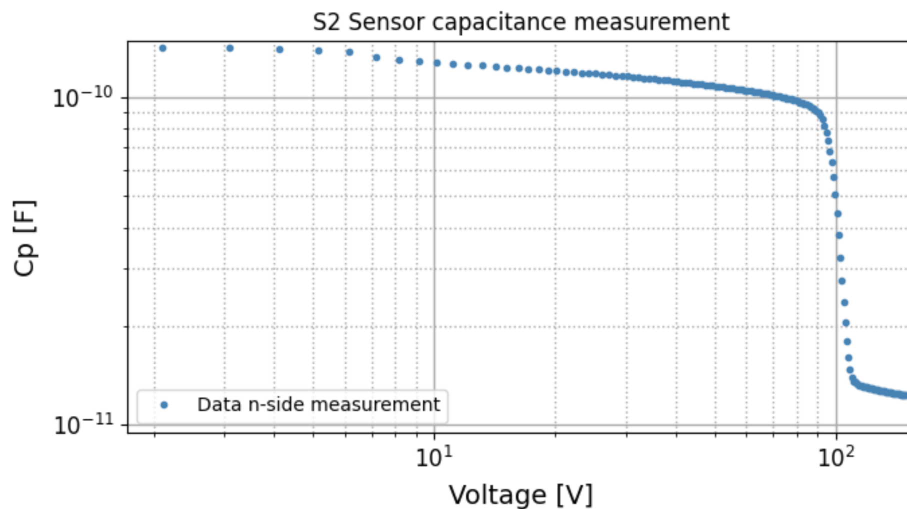

Figure 7.4: Capacitance measurement of a single n-side strip against the entire p-side of an S2 sensor.

In Figure 7.4, a capacitance measurement of a bonded S2 sensor is displayed. A strip on the n-side was measured in relation to the p-side with an increasing bias voltage. The decline in capacitance after full depletion is attributed to the absence of charge carriers, and the entire dependency is described by the formula 5.4.
After the initial successful mounting, a ^{90}Sr beta-source was used to generate events on the sensor. Series of measurements were conducted both with and without the source over the same time. It was demonstrated that the number of events with the source was significantly higher than without, aligning with expectations. This serves as confirmation that the sensor can effectively collaborate with the board.
Following two additional unsuccessful attempts to mount the # 5-ToASt-Board (resulting in damaged strips on the sensor and bond pads on the board), the decision was made to connect the p-side of the sensor to the channels of the board. On this side, the depletion and also signals can be measured without pushing the sensor to its full depletion voltage. This behavior can be well explained by examining the capacitance measurement in Figure 7.5.

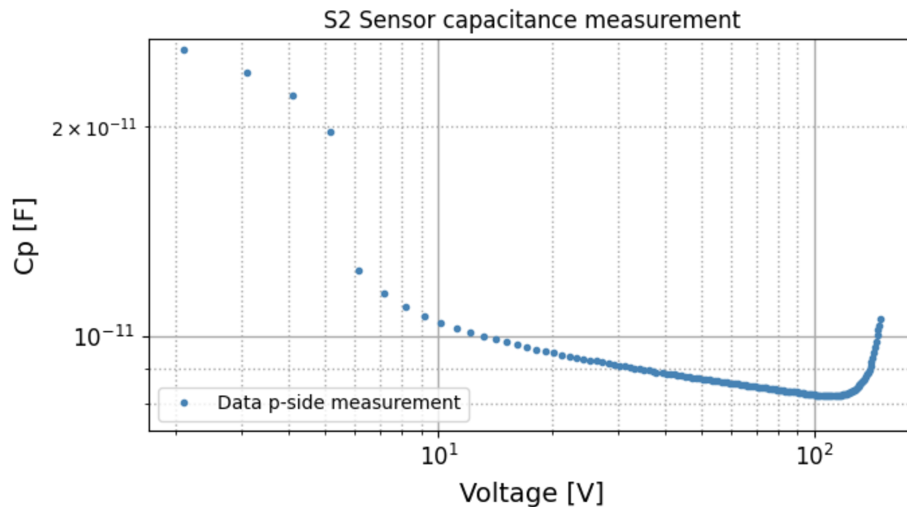

Figure 7.5: Capacitance measurement of a single p-side strip against the entire n-side of an S2 sensor.

As soon as a voltage in reverse bias direction is applied, the free charge carriers become attracted by the electric field. Subsequently, a reverse bias voltage is applied, leading to the depletion zone spreading from the p-side towards the n-side as the voltage increases. It can be observed that the p-side (Figure 7.5) senses this change even with small voltages, whereas the n-side (Figure 7.4) is still surrounded by charge carriers until the depletion voltage is reached.
The sensor is already more than half depleted from 10 V at the p-side, allowing the measurement of events below the full depletion voltage of around 100 V. This provides the best possible protection for the potentially damaged oxide layer and minimizes the likelihood of strip failures. The decision was made not to set the reverse bias voltage above 50 V at this point, striking a compromise between depletion and protection. Another advantage of connecting the p-side, which is grounded (AGND), is that if an oxide-layer fails, the readout components of the ToASt-board are not connected to the HV. Consequently, the board and channels are more protected.
In this manner, an S4 sensor was mounted to the # 5-ToASt-Board. Every test, including those with the radiation source, showed the expected results, which confirms successful contacting. It was observed that the noise decreases even at low voltages, as expected. Notably, the leakage current remained high with this configuration. However, all channels worked, although it does not exclude the possibility that a strip is broken in this case. Since the side connected to ground is now linked to the channels, the high voltage cannot cause any damage to the board. Therefore, events in the individual strips must be measured in an additional test, which was not possible at that time. This would enable the removal of damaged strips. It should also be noted that the signal is now received with reversed polarity. The n-side of the sensors produces negative signals, conversely the p-side produces positive signals. Similarly, an S3 sensor was mounted to a

ToASt-Board and passed every functional test.

Signal Testing

As mentioned earlier, measurements were conducted with a β-source to confirm functionality. In this initial series of functional tests, hits on the connected strips and the time over threshold were measured. The subsequent measurements showcase an S4 sensor where 64 strips are connected to the readout system of the ToASt.

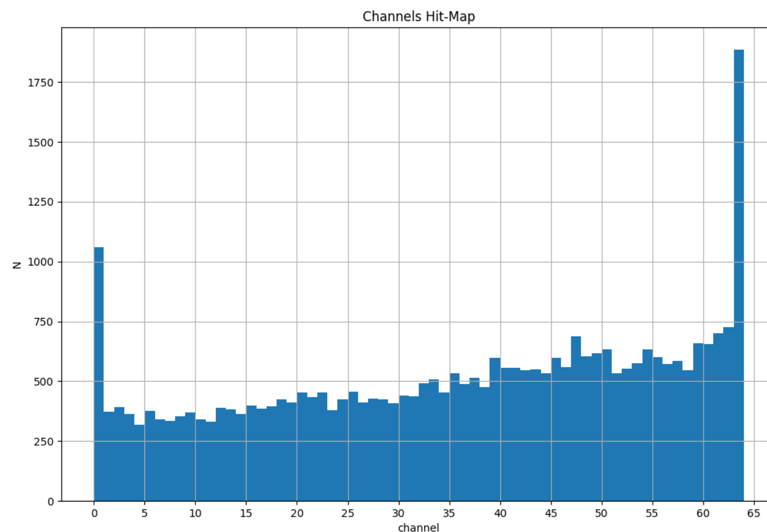

Figure 7.6: Distribution of ^{90}Sr-events on a double-sided $\overline{\text{P}}$ANDA S4 strip sensor, readout from a ToASt chip, for each of the 64 channels.

Figure 7.6 illustrates the typical behavior of a connected silicon strip sensor. Each channel of the ToASt represents one strip of the sensor and displays a comprehensible number of hits on the strips. The uneven distribution of events may be attributed to the source's location or the absence of calibration. As these tests are solely employed to verify functionality, the measurement's accuracy is not considered.
The higher value of the outer channels is clearly recognizable, which can be explained by the presence of floating strips neighboring to the connected ones.

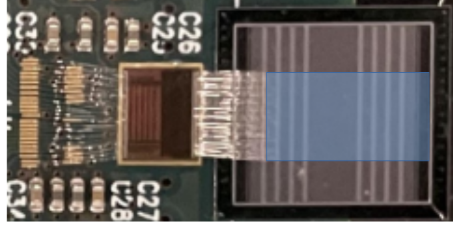

Figure 7.7: Photograph showing the sensor-front-end assembly with 64 wire-bonded strips of an S4 sensor and the placement of the ToASt-FE on the PCB.

In Figure 7.7, the 64 connected strips in the middle of the sensor are visible, while every other strip of the sensor is not connected. These floating strips accumulate the charge from the hits. This charge collected on the unconnected floating strips overflows to the next connected strips, which are the two outer ones, thereby generating the increased signal.

Time-over-Threshold (ToT)

Time-over-Threshold is a common method for calculating the time and energy of a signal. Essentially, the time duration of a signal is measured above a threshold value. Generally, only the deposited energy (dE) can be determined from the duration of the signal, which may give some indication about the type of particle.

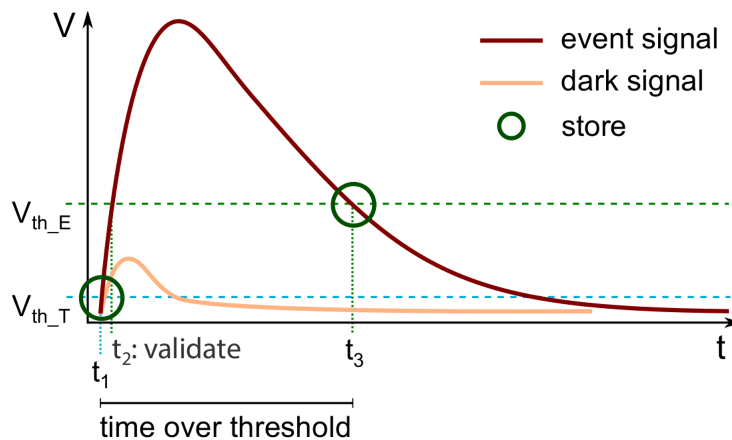

Figure 7.8: Dual-threshold method employed on the ToASt Chip [102].

Typically, Time-over-Threshold (ToT) consists of two time stamps, one for the beginning and one for the end of an event. Since the ToASt utilizes the dual threshold concept, a third time is measured. The first time is t_1, which is when the signal voltage exceeds the first threshold V_{th_T}. If the signal also breaks through the second threshold at V_{th_E}, the second time t_2 is measured.
V_{th_T} represents the start of the time threshold and specifies the minimum duration that an event must last in order to be counted as an event, whereby the end of the time threshold is reached at the point in time at which V_{th_E} is cut for the second

time. The second threshold V_{th_E} refers to the energy, signifying the minimum signal height required to be considered an event.
Only if the signal surpasses both thresholds is it considered valid. This provides a more precise time measurement and minimizes time walk effects (explained in Section 7.2.3), which refer to the difference in time delay between large and small signals. The last time signal t_3 is measured when the signal drops again below the threshold V_{th_E}. The difference between t_1 and t_3 is the Time-over-Threshold.

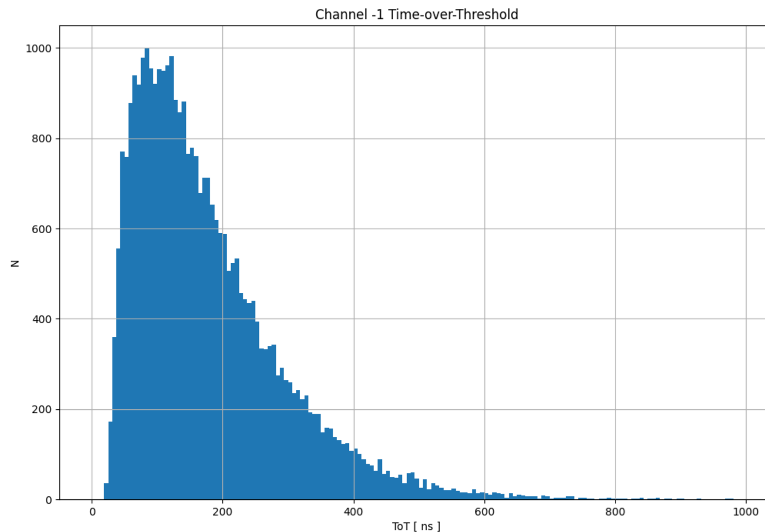

Figure 7.9: ToT distribution of a single sensor channel.

In Figure 7.9, the Time-over-Threshold of one channel is depicted. To a good approximation, a Landau-Gaussian convoluted distribution can be recognized, describing the energy loss of charged particles in a thin layer of silicon. Therefore, the Langau-like distribution in Figure 7.9 represents the energy loss of particles in the 285 µm silicon layer of the sensors, as expected and described in Section 4.3.2. Hence, all measurements clearly demonstrate that the ToASt chip functions in conjunction with the sensors. The signals from the CiS sensors can be read out for the first time.
Additionally, a preliminary calibration was performed for both detectors, which is likely to be very inaccurate as only the built-in pulser was used, and no sources or particle beams of exact energies were employed. Nevertheless, calibrating to 60 ns/fC provides a reference for later results.

7.2 Prototype Setup

7.2.1 Data Acquisition

The data acquisition (DAQ) of the $\overline{\text{P}}$ANDA-MVD is tested for the first time in combination with a $\overline{\text{P}}$ANDA sensor and a ToASt-board in the beam times described below. The requirements for the DAQ include that each sub detector can detect hits without an external trigger, and these hits can subsequently be differentiated into noise and actual hits by the front-end electronics. In this process, digital transmission of hit information, along with an accurate time stamp, must occur for up to 20 million antiproton-proton annihilation's per second. As illustrated in Figure 7.10, sensor data undergoes processing through the ToASt front-ends (see Section 7.1.1) and is subsequently organized and formatted by the Module Data Concentrator (MDC) application-specific integrated circuit (ASIC).

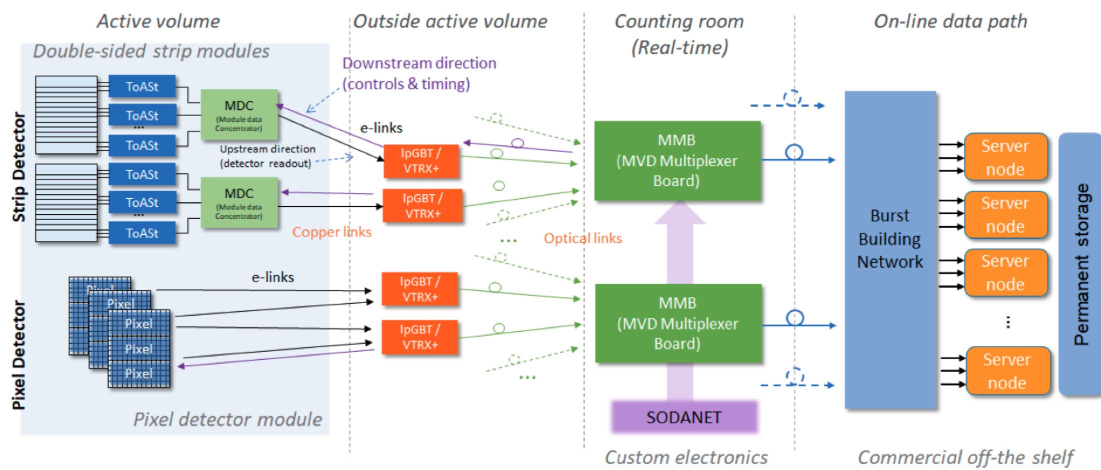

Figure 7.10: Data acquisition architecture of the PANDA-MVD detector [104].

The MDC is designed to readout up to 12 ToASts. One additional task is to handle the processing of commands, configurations, clock signals, and the slow control of the system. It also serves as a digital controller for the detector module, enabling the configuration of the ToASt front ends. Additionally, it is responsible for temporally sorting the received data, as the ToASt does not align it according to event time. One MDC for each sensor side is foreseen due to the polarity. However, in the MVD prototype, where the sensors are read out single sided, one MDC per sensor handles the readout. The data is then transmitted from the MDCs outside the active measurement range through optical Low Power GigaBit Transceiver (lpGBT) links [105]. The data is then processed on the multiplexer board (MMB) specially designed for the MVD. For accurate temporal storage of data, an exact time stamp is assigned to the detector data through the synchronization information provided by the Synchronization Of Data Acquisition (SODANET) with the MMB. The data is reduced to include only relevant physical signals and is then transmitted at a maximum data rate of 580 Mbit/s to the burst building network, where the data can be stored.

7.2.2 Beam Time Setup

The entire setup was designed to be as flexible as possible. This is because the MVD prototype was the second user of the beam during the beam times, which means that the proton beam could not be actively changed. In addition, some of the primary experiments were placed in front of the MVD in terms of beam direction. Therefore, the entire structure was assembled and secured using item profiles, attached to a three-legged stand. The adjustable tripod allowed movement of the setup, particularly the sensors, in all spatial directions, enabling variation in intensity by approaching the beam center.

The Sensor-ToASt combination, previously explained and utilized in Section 7.1, could be directly fastened to the item profiles. This allowed sensor alignment without relocating the entire structure. The sensors were positioned so that the rear sensor was placed ideally in the beam shadow of the front sensor, facilitating coincidence measurements and extended clustering. However, with an approximate 4 cm spacing, the sensors were relatively distant in the first two beam times, as evident in Figure 7.11.

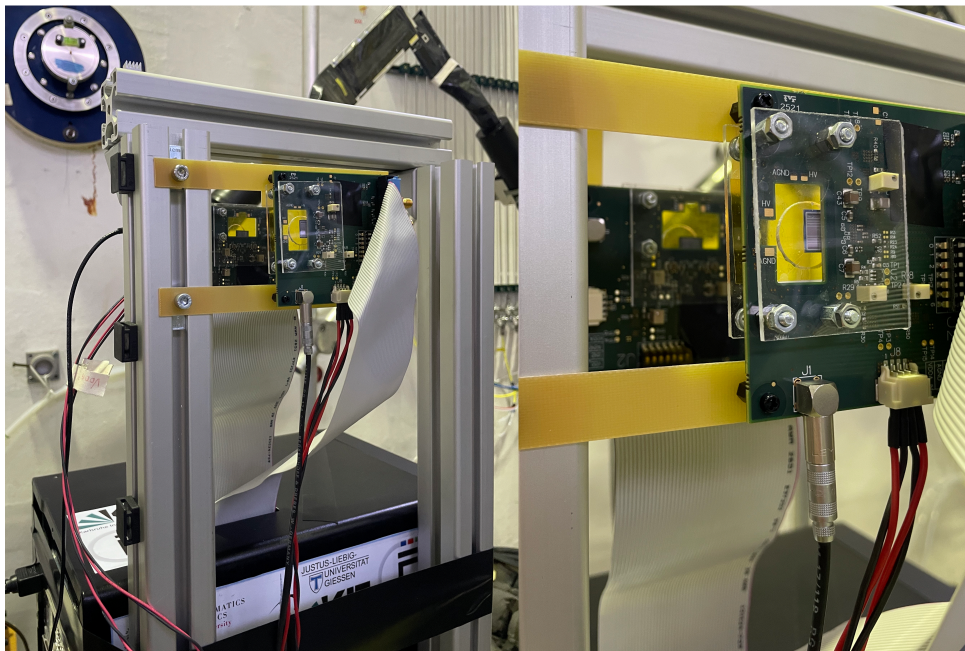

Figure 7.11: MVD prototype setup from the COSY08 beam time, mounted on top of a tripod in COSY's TOF Hall.

Upon closer inspection, the left image reveals the beam dump in the upper left, corresponding to the center of the proton particle beam. The sensors were laser-aligned accordingly, and the intensity on the sensors was regulated through the height adjust ability of the tripod. The entire setup is situated behind several primary experiments, indicating an extensively spread-out beam. After alignment,

the sensors were made as light-tight as possible by covering them with several layers of black fabric.

The prototype DAQ is built upon a HighFlex card [106], with the MDC described in Section 7.2.1 being utilized as FPGA version. This ensures maximum flexibility while maintaining full functionality. The entire DAQ was connected to a PC beneath the sensors using the HighFlex cable, as depicted in the left image of Figure 7.11.
The control of the system, including the PC, was carried out from outside the cave, allowing parameters to be adjusted during beam operation. A graphical user interface (GUI) was developed for the control, and further details were discussed in the conference contribution [107].

The sensors were individually powered with a voltage supply, applying the reverse bias voltage. Leakage currents were monitored throughout the entire beam time. The ToASts were operated with a power supply during which both ToASts were provided with a negative voltage of -3 V at 0.166 A and a positive voltage of 4.5 V at 0.533 A. It is noteworthy that currents may vary when the ToASts are in configuration mode.
In the following, the two sensor-readout combinations will be referred to as T01 and T02. T02 is the p-side readout sensor located on ToASt # 5, while T01 is the n-side readout combination on the ToASt # 2 test board.

Simple Functional Tests

By conducting a simple functional test of the data readout, it can be demonstrated that it accurately stores events with the correct timing. The leading and trailing edges were histogrammed for this purpose. To obtain the most comprehensive statistics, the measurement with the highest number of data points across all beam times was used as an example. The data set is analyzed without preprocessing, such as clustering. During the tests, both sensors were fully depleted using a reverse bias voltage of 100 V, and the ToASt sensors were calibrated with the standard beam time calibration (ToASt1: **2023-08-11T17-37-27-p-type** and ToASt2: **2023-08-11T18-01-33-n-type**). As evident in the Figure 7.12, the mean of both values is approximately half of the 4096 bits, as expected for a properly functioning readout.
The same data set was utilized to test the functionality and calibration of the strips. It is noteworthy that in T01, one strip malfunctioned, the strip seems to be floating evidenced by the increased hits on the adjacent strips. This behavior can be attributed to charge sharing (refer to Section 7.2.3), similar to what is observed in the outermost channels.

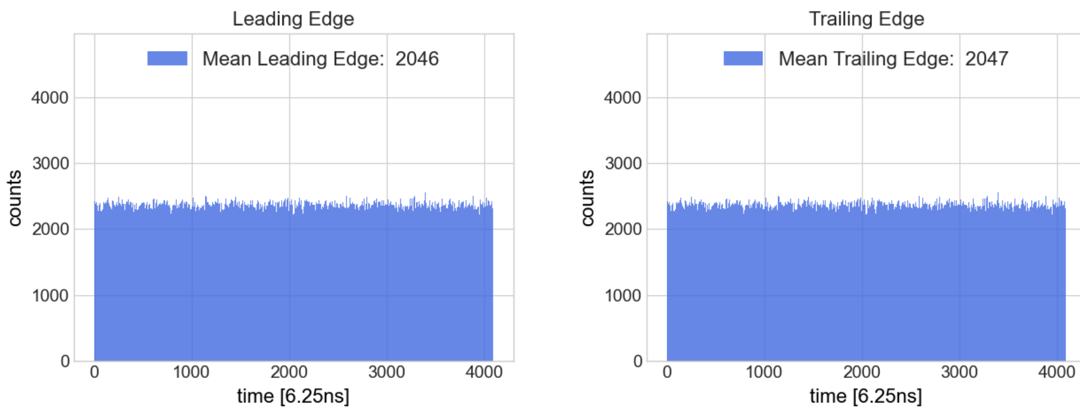

Figure 7.12: Leading and trailing edge times for a raw beam time data set with 6.25 ns per time step.

The adjacent strips of these channels are also not contacted, preventing the generated charge from dissipating and instead transferring it to the next contacted channel.

The malfunctioned strip in the measurement of figure 7.13 seems to be damaged between the aluminum-coated readout strip and the implant (coupling capacitance, as depicted in Figure 5.22). This results in a so-called pinhole, establishing an electrical connection from the readout strip to the bias line. A closer examination of the schematic structure of the sensor in Figure 5.16 supports this explanation. Nevertheless, the ToASt still functions despite the bias voltage, as the pinhole was detected before the bias voltage was applied. The malfunction was identified through the analysis of channel leakage current and noise. To save the sensor-readout combination, the bonding wire was removed, rendering data readout impossible for the malfunctioned channel but protecting the ToASt. The absence of the bonding wire prevents the charge from flowing anywhere except interfering with the neighboring channels, as can be observed.

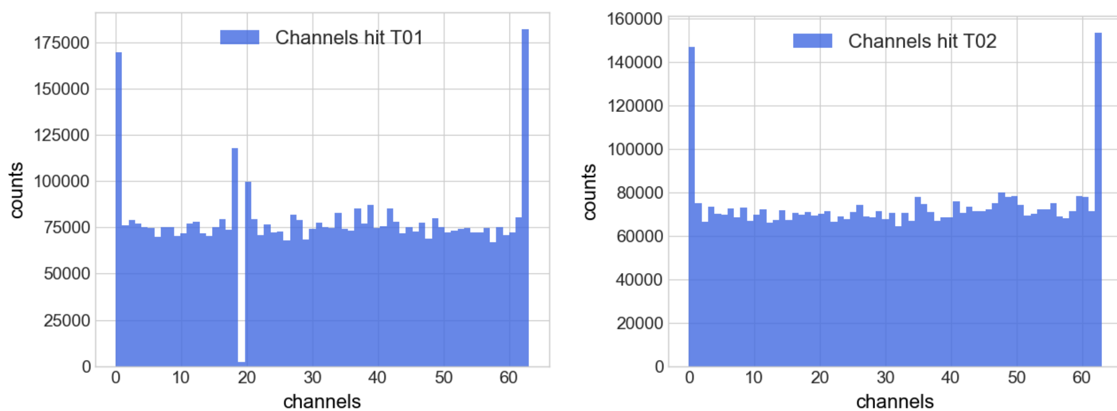

Figure 7.13: Hit channels of T01/02 for a raw beam time data set.

Overall, it can be observed that the calibration appears to have been successful, as all channels, except those affected by the damages, are at a similar counting level. This suggests that the thresholds have been well chosen for the individual channels. However, it cannot be ruled out that one side of the sensors may have experienced a higher intensity than the other. Nevertheless, it can be assumed that due to the widely spread beam, the intensities are approximately equal.

7.2.3 Hit Clustering

A cluster event occurs when multiple strips of one or multiple sensors are hit by a fast charged particle. The strips share the deposited energy through charge sharing, as explained in Section 7.2.3. To increase the cluster size and, consequently, the resolution, sensors are typically slightly tilted by an angle θ_i, as shown in Figure 7.14. This statistical tilting increases the likelihood of particles entering the sensor at an angle, thereby exciting more strips and enlarging the cluster.

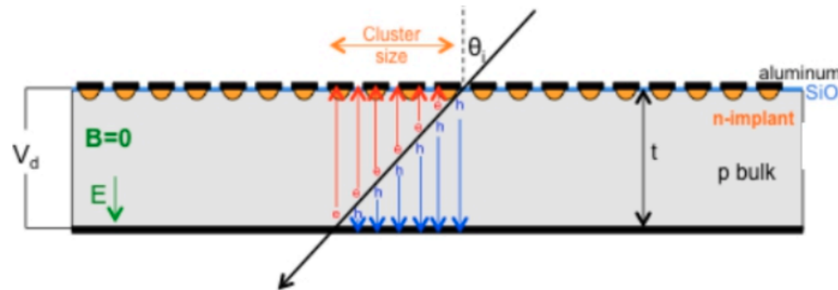

Figure 7.14: Schematic representation of a cluster in a silicon strip sensor [108].

For the definition of a cluster, it is essential to establish a time period during which events are read out by the ASIC. It is crucial to acknowledge that each event has a certain duration, which can be understood as Time-over-Threshold (ToT) (see Section 7.1.2). Additionally, each event takes a certain amount of time due to the mobility of the charge carriers, which differs for electrons and holes, leading to time walk. Moreover, at high rates, it is essential to ensure that signals from only one particle are accurately counted as a cluster. Therefore, the readout time of a cluster is limited upwards and downwards, as investigated in the following Section 7.2.4 for the MVD-prototype.

Multiplicity

The multiplicity indicates how many strips are excited by an event. This can be observed as the cluster size in Figure 7.14. Accordingly, each cluster has a multiplicity greater than one; otherwise, it would be considered a single hit. The multiplicity is calculated separately for each sensor, meaning that each sensor calculates its own multiplicity independently, even in cases of synchronous events.

However, a special case is considered in the analysis, where synchronous clusters in both sensors are counted together, resulting in an aggregated multiplicity. For synchronous single hits, however, the multiplicity is assigned a value of one, rather than adding up to two, allowing these events to be analyzed separately. This approach provides an additional perspective that becomes informative when the sensors are no longer positioned precisely one behind the other due to a change in the angle of incidence. In this way, discrepancies between the sensors that arise from the particle angle of incidence can be observed.

The multiplicity can be influenced, for example, by the angle of incidence of the charged particles or by a magnetic field. This causes the deposited energy to be distributed across multiple strips, thereby increasing spatial resolution, as explained in Chapter 4.0.1.

Drift Velocity and Mobility

The drift velocity of electrons is significantly higher than that of holes due to their lower effective mass, which results in greater mobility under the same electric field, despite collisions with lattice defects, as shown in Figure 7.15.

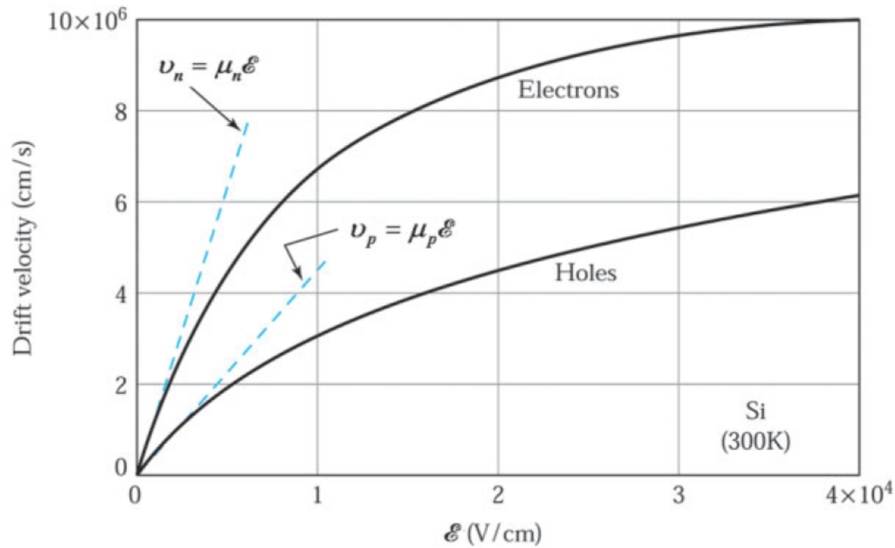

Figure 7.15: Drift velocity of electrons and holes versus electric field in Silicon [47].

To get an estimation of the electron mobility in the $\overline{\text{P}}$ANDA silicon detectors, Formula 7.1 which is valid for small fields is taken into account [36].

$$v_n = \mu_n \cdot E \tag{7.1}$$

Estimating the signal length involves considering the mobility of the electrons ($\mu_n = 1500\,\text{cm}^2/\text{Vs}$) and holes ($\mu_p = 450\,\text{cm}^2/\text{Vs}$) [36]. By incorporating this information along with knowledge of the full depletion voltage at around 100 V

and sensor thickness of 285 µm the drift time of holes and electrons across the entire sensor can be calculated with the Formula 7.2 to $t_{\text{electrons}}$=2.708 ns and t_{holes}=9.025 ns.

$$t_{drift} = \frac{d^2}{2\mu_n V_{\text{dep}}} \tag{7.2}$$

Therefore, with the knowledge that a clock cycle of the ToASt (Chapter 7.1.1) takes 6.25 ns, the readout time for a cluster must be at least 2 clock cycles.

Time Walk

Time Walk occurs because signals of different amplitudes require different times to exceed a defined threshold. Stronger signals reach this threshold faster, while weaker signals need more time to reach the same point. This leads to a temporal distortion of the measurement, even though the events actually occurred at the same time.

Charge Sharing

Charge sharing refers to the distribution of the signal charge from an event across multiple sensor strips, enhancing spatial resolution by representing the event in clusters rather than on individual strips. This effect occurs when the charge from the event spreads naturally over an area, causing neighboring strips to detect a portion of it. Additionally, due to capacitive coupling, charge can be shared between adjacent strips, even if the primary charge is not directly deposited on those strips.

The extent of charge sharing depends on factors such as whether neighboring strips are contacted and the interstrip capacitance (see Chapter 5.3). In microvertex detectors, charge sharing can often be enhanced by rotating the sensors or applying a magnetic field, as described in Section 7.2.3 on cluster formation.

Cross Talk

Cross talk refers to the transfer of signals between neighboring strips, leading to unwanted signals in the readout channels that do not originate from the primary event. This occurs when the charge or signal on one strip induces a signal on neighboring strips through capacitive coupling or induction. These induced signals can distort measurements, as they do not represent actual charge events. To minimize cross talk, the interstrip capacitance (see Section 5.3) should be optimized, for example by only contacting every other strip.

7.2.4 Correlation of Clock Cycle Time

To identify a cluster, the distance between clock cycles of the leading edges of events is analyzed in the following section. We examine measurement data obtained from proton irradiation at the COSY accelerator in Jülich; this chapter serves as a preparation for accurate data collection. For this purpose, measurements taken with the prototype discussed in Section 7.2.2 during three separate beam times are used. A detailed analysis of these beam times will be provided in the following chapters, incorporating the insights gained here.

Correlation of Clock Cycle Time on Multiplicity

Specifically, at first we examine the normalized events against the multiplicity, as explained in Section 7.2.3. In Figure 7.16a, the maximum distance between the leading edges of signals in one cluster is two clock cycles which is equal to 12.5 ns. In the logarithmic representation, it is noticeable that despite the large data set of over 2.5 million clusters, only a few events are displayed that reach high multiplicities, exceeding 45.

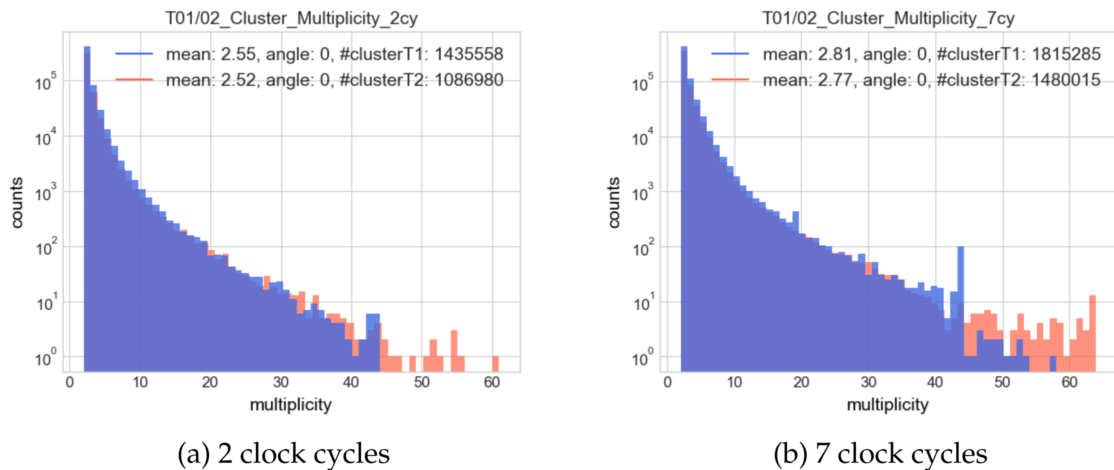

(a) 2 clock cycles

(b) 7 clock cycles

Figure 7.16: Strips per cluster multiplicity for different signal time intervals within an event.

Given that the proton beam, being relatively broad for secondary users, surely encountered some collision products on the sensor, we can also expect high multiplicities.

The impact becomes even more pronounced when considering the total number of clusters. In comparison to a separation of 7 clock cycles, as shown in Figure 7.16b, it is noticeable that over 30 % fewer clusters are identified for a 2-clock cycle separation. This indicates that a significant portion of clusters is filtered out due to drift time and time walk when the separation between leading edges is less than 7 clock cycles. The determination of drift time and time walk is discussed in Section 7.2.3.

However, it is observed that for 7 clock cycles, there is an increase in multiplicities of 44 and 19. This occurs only for Detector T01, and there is a noticeable reduction in the distribution from Multiplicity 44 on wards. For T02, an expected curve is apparent, with Multiplicity 63, where all strips are excited, being slightly increased. This increase is explainable on the sensor side, potentially due to common noise. Regarding the two increases for T01, these are also caused by common noise. For T01, Strip 19 is not connected, as explained in Chapter 7.1.2. Upon examining the data, it is evident that for most multiplicities of 44 and 19, this channel still generated a signal in the ToASt, but with a larger separation in clock cycles than 7. This can be attributed to cross talk in the ToASt, indicated by the significantly lower signal height for channel 19 compared to adjacent channels. Consequently, a cluster with Multiplicity 63 is split into two clusters with 44 and 19. This leads to the truncation of many clusters in higher multiplicities.

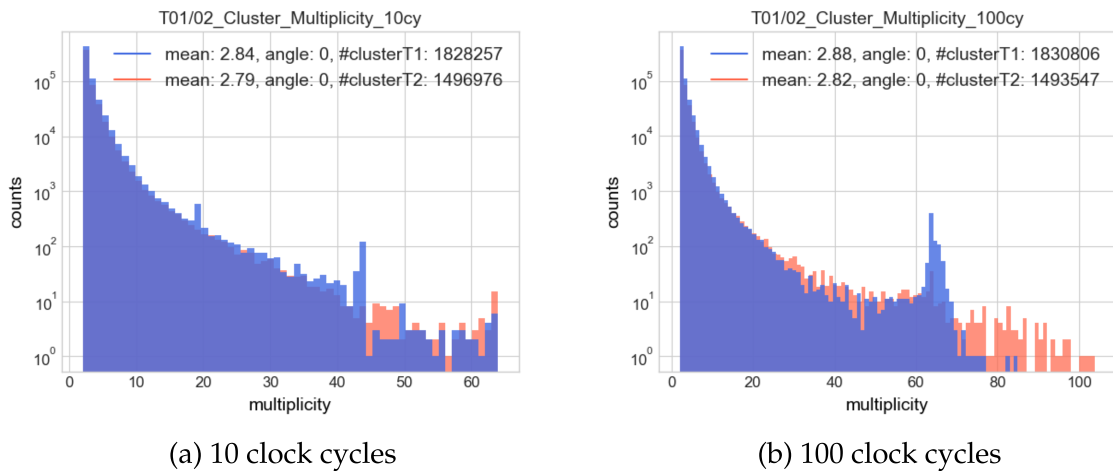

(a) 10 clock cycles

(b) 100 clock cycles

Figure 7.17: Strips per cluster multiplicity for different signal time intervals within an event.

Examining Figure 7.17a, with a maximum leading edge separation of 10 clock cycles, the observations for 7 clock cycles become even more pronounced. This time, T01 also penetrates more into higher multiplicity ranges. When looking at the increases in Multiplicities 19, 44, and 63 for T01, it becomes evident that this detector is significantly more influenced by common noise compared to T02. When considering a separation of 100 clock cycles, as shown in Figure 7.17b, the behavior becomes evident. T01 now exhibits a distinct peak around multiplicity 63, while for T02, only multiplicity 63 is increased, although significantly less than for T01.

Both detectors now show multiplicities beyond 63, which is non-physical, as it would require a particle to excite more than all the strips. Hence, it becomes clear that the dead time of the sensors has been exceeded, and additional events in a cluster have been counted together. Dead time is the duration a strip needs to

be ready again to receive a new signal after excitation. This behavior is clearly observable for T02.
For T01, it can be seen that multiplicities between 20 and 60 contribute to the peak around 64. Upon closer inspection of the data, it is noticeable that these clusters are mainly filled with random hits, which can be noise or individual events. Due to the dead time, there is an increased filling up to multiplicity 64, particularly extending the higher multiplicities, as a coherent cluster with bordering strips needs to be filled within the clock cycle time.

This effect is also observable for T02 but to a significantly lesser extent, attributed to a lower intensity of approximately 12.5 %. Additionally, when examining the data for T02, it is apparent that clusters of larger multiplicities are extended with random events, even beyond 63. This suggests that T02 has a shorter dead time than T01.

As the clock cycles are increased to multiples of the dead time, the distribution remains unchanged. One would expect the peak to disappear as more events are added, and significantly more higher multiplicities are found. To explain this phenomenon, distributions recorded under controlled conditions in Figures 7.53a and 7.53b must be considered.

In those Figures, the peak and multiplicities beyond 63 are not present, even for high clock cycle times. This indicates that cyclic signals were causing clusters to be filled during the COSY beam times, possibly due to uncovered LEDs or stray light from fluorescent lamps or COSY spill structure. Therefore, the ToASt and the sensor are not affected by common noise, which does not consist of real signals.

This interference makes it challenging to analyze multiplicities, so a consideration in multiplicity with clock cycles between 2 and 5 is recommended, corresponding to 12.5 ns and 31.25 ns. Moreover, insights into the dead times, which depend on the Time-over-Threshold, were obtained, with a minimum of approximately 50 cycles for T01 and 20 cycles for T02, corresponding to 312.5 ns and 125 ns, respectively. This corresponds to maximum rates between 3.20 MHz and 8 MHz, i.e., 50 kHz and 125 kHz per strip, fulfilling the requirement of approximately 10 kHz per strip [10].

Correlation of Clock Cycle Time on Synchronous Hits

The following examines the impact of the distance of the leading edge within a cluster on the deposited energy, using measurements from the COSY-Beam Time III (detailed evaluation of the measurements in Chapter 7.3.4). For this, synchronous hits are plotted for 2 and 7 clock cycles as a function of their deposited energy of both sensors. The x-axis represents the Time-over-Threshold of T01, while the y-axis represents that of T02. As described in Section 7.1.1, one clock cycle

corresponds to 6.25 ns. When observing the distributions in 7.18, it is immediately apparent that hits near the x- and y-axes decrease significantly with the clock cycles.
These events can have various causes. On the one hand, they can be caused by particles that pass through one sensor with a small loss of energy (as explained in Chapter 4.3.1) and get stuck in the second sensor. As a result, the deposited energy in the second sensor is significantly higher, as all the kinetic energy is absorbed by the sensor.
On the other hand, such events can be caused by particles that cannot penetrate the sensor, such as photons from scattered light. However, for a synchronous hit to occur at the both sensors, an event must also be measured within the synchronicity time window at the second sensor, which may be the case in setups lacking light proofing.
As observed in the distributions, reducing the synchronicity time mainly filters out distributions of these asymmetrical energy deposits, suggesting that a significant number of photons from scattered light were measured.
However, as evident in Figure 7.18, the distribution along the diagonal, likely caused by fast charged particles, decreases. Despite this, the reduction in the distributions along the x- and y-axes is notably greater than that of the events along the diagonal. Therefore, by reducing the synchronization time window from 7 to 2 cycles, noise can be filtered out.

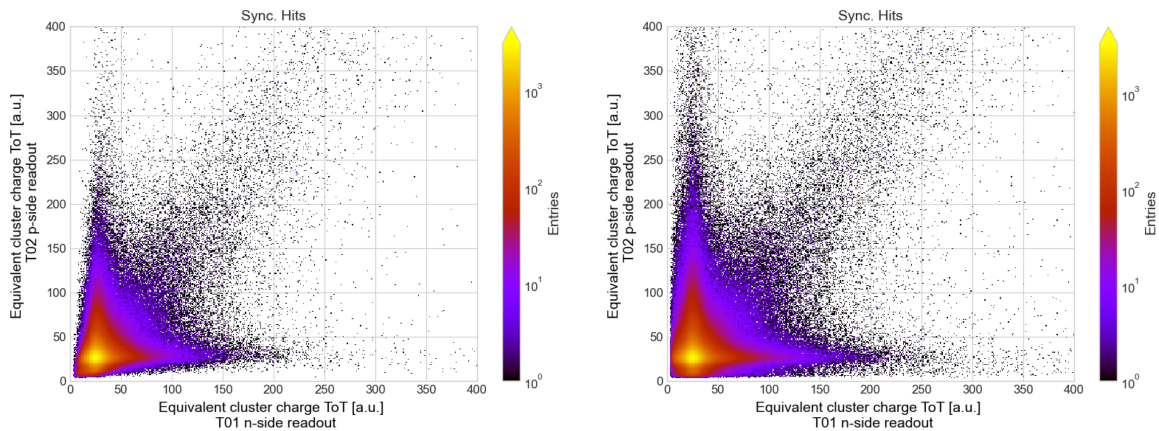

Figure 7.18: Correlation of deposited energy with different signal time intervals within an event of 2 clock cycles on the left and 7 on the right for the same measurement.

Examining the number of excited strips in both distributions reveals that the count has changed significantly by adjusting the different signal time intervals within an event from 7 to 2 clock cycles. For 2 clock cycles, 37.15 % fewer hits were recorded on both sides. Which is roughly the same as in the multiplicity consideration. To demonstrate that predominantly asymmetric events were filtered out, the absolute values resulting from the subtraction of the Time-over-Threshold of T01 and T02 were calculated for each hit, described as T_D.

$$T_D = |T01_{tot} - T02_{tot}| \tag{7.3}$$

From this, the average distance $\overline{T}_D$ from the diagonal can then be calculated:

$$\overline{T}_D = \frac{\sum_{i=1}^{n} T_{Di}}{n} \tag{7.4}$$

This results in a deviation of all hits by 22.55 ToT for 7 clock cycles and by 15.11 ToT for 2 clock cycles. Assuming only MIPs are being registered and the ToASts are precisely calibrated, this deviation should approach zero [65]. The reduction by 32.99 % clearly indicates that the reduction in clock cycles particularly filtered out noise hits. Thus, when considering only synchronous events, a reduction in cluster time to 2 clock cycles, equivalent to 12.5 ns, is beneficial.

Correlation on Signal Time Intervals within an Event on Channel Hits

Another consideration for verifying the cluster duration involves examining the excited channels of all clusters. That means, in the following, the count of how often each channel was excited during a measurement run is plotted for various 2 and 7 clock cycle distances within a cluster of the leading edge. For this, every channel that was excited within a cluster is plotted. Initially, T01 and T02 for 7 clock cycles are considered.

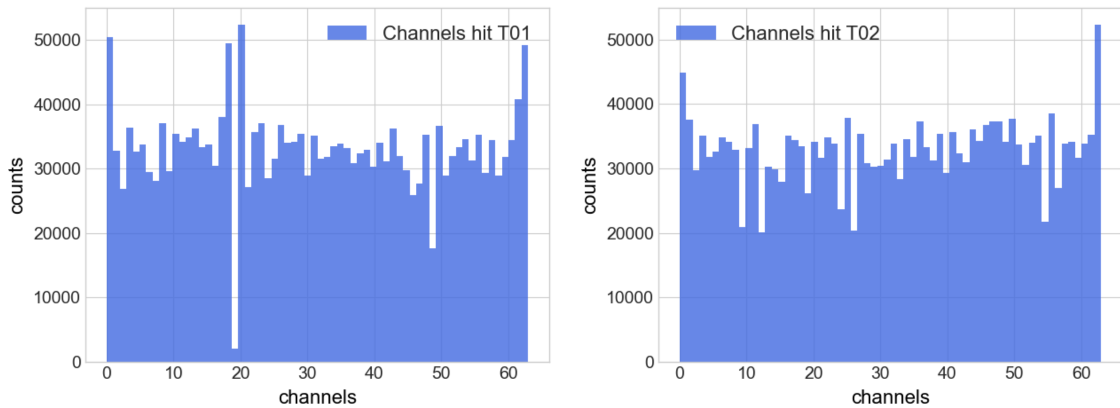

Figure 7.19: Hit cluster channels of T01/02 for 7 clock cycles leding edge difference.

Comparing Figure 7.19 and Figure 7.13, where raw data, i.e., non-clustered data, is plotted, the first observation is a noticeable reduction in counts. More strikingly, the two outer channels, heavily influenced by charge sharing as neighboring channels are not connected, have significantly decreased compared to the remaining counts. This suggests that clustering has at least partially filtered out charge-sharing signals. A slight increase is still visible for a 7 clock cycle distance.
In total, 4.72 and 5.01 million events were recorded for T01 and T02 in the raw data. On average, this means 78.22 and 73.67 thousand events per channel. For the raw data, the two outer channels for T01 are increased by 124.89 % compared

to the mean, and for T02 by 104.23 %. For the clustered channels with a 7 clock cycle distance, the number of events is reduced to 2.12 and 2.10 million events with a channel mean of 33.16 and 32.88 thousand events, resulting in a difference of the outer channels to the mean of 50.08 % for T01 and 47.67 % for T02. In total, 130.56 % fewer events were recorded. It is clear that clustering can significantly filter out charge-sharing signals. However, not only charge sharing signals but also other noise and real events are filtered. To emphasize this, considering Figure 7.20, where noise is evidently filtered for 2 clock cycles, the same is examined for the channel observation.
For T01, a total of 1.65 million events were recorded for 2 clock cycles, and for T02, 1.71 million events, belonging to a cluster. This also means an average of 25.78 and 26.64 thousand events per channel.

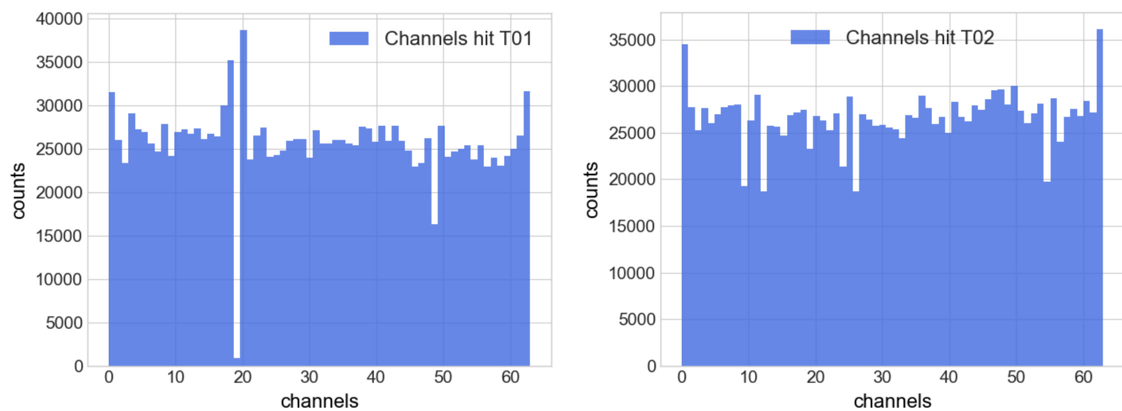

Figure 7.20: Hit cluster channels of T01/02 for 2 clock cycles leding edge difference.

In comparison with the raw data and the data clustered with 7 clock cycles from Figures 7.13 and 7.20, there is again a reduction in total events and a decrease in the outermost channels. In numbers, this means an increase for T01 of 22.69 % for the two outer channels compared to the mean and 32.48 % for T02. Compared to the raw data, 189.58 % of the data was discarded, and compared to the 7 clock cycles, 25.59 %. It is noticeable that the total events between clock cycle distances 2 and 7 have decreased almost equally, as have events on the outermost strips. This is mainly explained by the reduction in charge sharing. However, it must be noted that real events are also filtered out due to the short cluster length, as explained in Sections 7.2.4 and 7.2.4.

In conclusion, it can be stated that reducing the clock cycles, which corresponds to shortening the allowed signal time intervals within an event, effectively filters out noise and non-cluster signals. The primary cause for the exclusion of some signals was identified as charge sharing, which can result in signals that are not correctly associated with a cluster. However, this reduction in time intervals may also lead to the loss of valid events.

Conclusion

In considering all methods for verifying the clock cycle time, two things must be particularly noted. Firstly, the time should not exceed 7 clock cycles, corresponding to a time of 43.75 ns. Beyond this, common noise is recorded as signals by the ToASt, and clusters are no longer properly distinguished. Secondly, at least two 2 clock cycles (e.g. 12.5 ns) should be considered for verifying clusters, as below this, real events can be sorted out due to the drift time of electrons and holes, as shown in Section 7.2.3. However, it has also been clearly shown that reducing the clock cycles reduces signals not corresponding to clusters. The main cause identified was charge sharing. It must be noted, that below 7 clock cycles, actual events are also sorted out. Charge sharing will be reduced in the actual MVD setup, as the plan is to contact every second strip. In the prototype, on the other hand, every strip was contacted. Therefore, it can be assumed that in the final setup, the minimum limit does not need to be pushed to the extreme due to noise and charge sharing.

7.3 COSY Beam Times

A total of three beam times were conducted at the COoler SYnchrotron (COSY) with the MVD prototype. During each beam time, the sensor configuration was slightly modified, as explained in the respective sections. The setup consistently served as a secondary experiment, meaning that other experiments were in the direct beam path, and the prototype received a widely spread beam as a result of the preceding experiments. This included not only protons but also a diverse array of particle products.

COSY has the capability to accelerate protons with a maximum momentum of 3500 MeV/c [109]. The last of the mentioned beam times also marked the conclusion of COSY's operational period.

7.3.1 Beam Time I

In the first beam time, the setup described in Section 7.2.2 was utilized, with only one sensor. It marked the initial combination of Sensor-ToASt and DAQ outside the laboratory, representing the first opportunity to detect radiation. Therefore, efforts were made to simplify the setup as much as possible. The beam time was affected by beam failures and challenges in interpreting detector behavior. Despite these issues, valuable information was gathered, including the correct polarity configurations of the ToASt. The ToASt is programmed such that, in its configuration, the p-side readout expects a negative pulse, and correspondingly, the n-side expects a positive one. However, when considering the sensor-side readout, connecting to the AC pads on the p-side results in positive signals being

transmitted to the ToASt, and on the n-side, negative pulses are expected. These insights and others allowed to observe plausible signals after the beam time.

7.3.2 Beam Time II

In the second beam time, the setup was exactly as described in Section 7.2.2. Two sensors with strips orthogonal to each other were positioned at a distance of around 4 cm. Throughout the beam time, efforts were made to maintain the COSY proton beam relatively constant at an momentum of around 2740 MeV/c, owing to a long-time measurement by a first user. During this period, the intensity was adjusted by changing the tripod height. Nevertheless, the sensors were positioned quite far away from the beam center due to concerns about radiation damage to the PC.

In Beam Time II, general functional tests were being conducted, which included modifying ToASt parameters and performing calibrations. Additionally, the reverse-bias voltage was altered, with the plotted measurements reflecting only the fully depleted sensor.

7.3.3 Measurements Beam Time II

To illustrate the functionality of the detectors firstly, the measurement from Beam Time II with the highest statistics are examined. Figure 7.21 displays the data from T01 on the left and T02 on the right without any processing. In this analysis, all channels have been summed, resulting in histograms that include data from all 64 channels of the ToASts. A detailed representation of individual channels for T01 can be found in Appendix Figure D.5, and for T02 in Figure D.6. Notably, the unconnected Channel 19 in T01 is once again apparent.

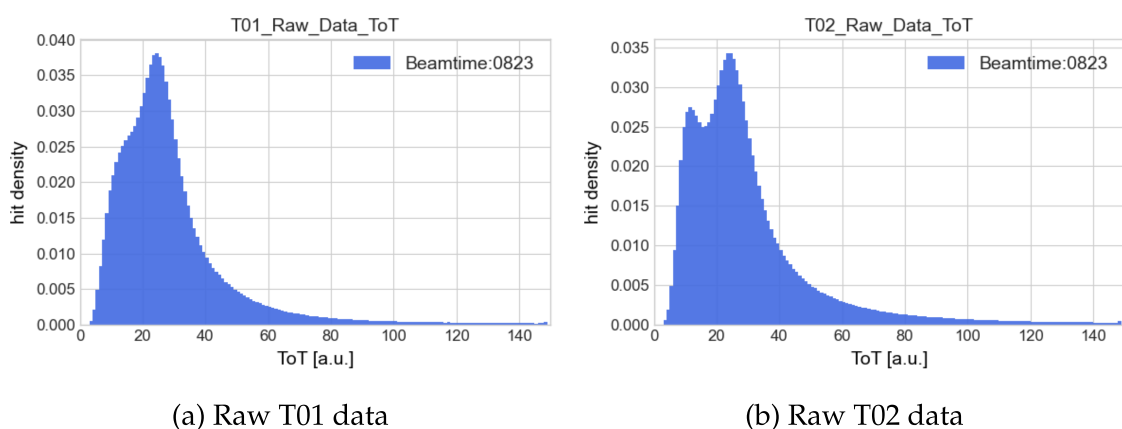

(a) Raw T01 data

(b) Raw T02 data

Figure 7.21: Measurement with the MVD prototype using a proton beam at COSY, with T01 (a) and T02 (b), based on unclustered raw data.

The examination of the raw data in Figure 7.21 reveals a slightly shifted Landau distribution or a combination of Landau and Gaussian distributions, as explained

in Chapter 4.3.2. However, especially for T02, an additional peak is noticeable before the main peak. To ensure that this is not caused by the summation of different gains and thresholds of the channels, the analysis is extended to the raw data of an individual channel.
The double-peak structure is also evident for individual channels in Figure 7.22, more pronounced for T02 than for T01, possibly due to the global threshold setting. However, it is also noticeable that the Landau distribution has a slightly steeper decline, indicating a less perfect calibration between the channels.

Therefore, the data set is processed, and all clusters are identified. For clustering, the ToTs (time-over-threshold values) for an event within a defined time interval, where each event is uniquely assigned are summed. Only excited neighboring strips on a sensor can contribute to a cluster. However, it is also implemented here that if a strip between two adjacent excited strips fails to show a signal, the event is still considered a cluster. In the following, "clustered data" refers to the combined ToT values from multiple strips within one event, which can be used to determine the energy deposited by an event.

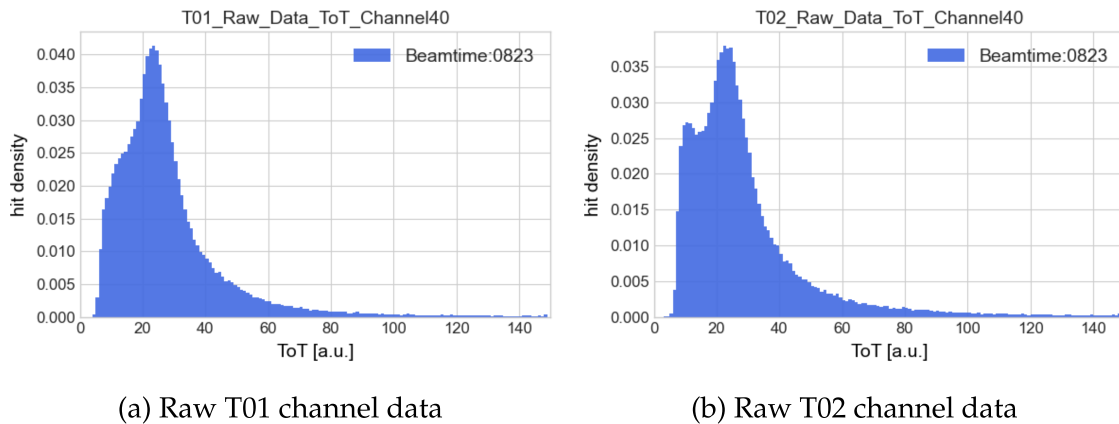

(a) Raw T01 channel data (b) Raw T02 channel data

Figure 7.22: MVD prototype measurements with a proton beam at COSY using T01 (a) and T02 (b) for a randomly chosen channel, based on unclustered raw data.

The clustering process is explained in more detail in Section 7.2.3. It is worth noting that the scaling has been adjusted as the peaks have significantly lost intensity.

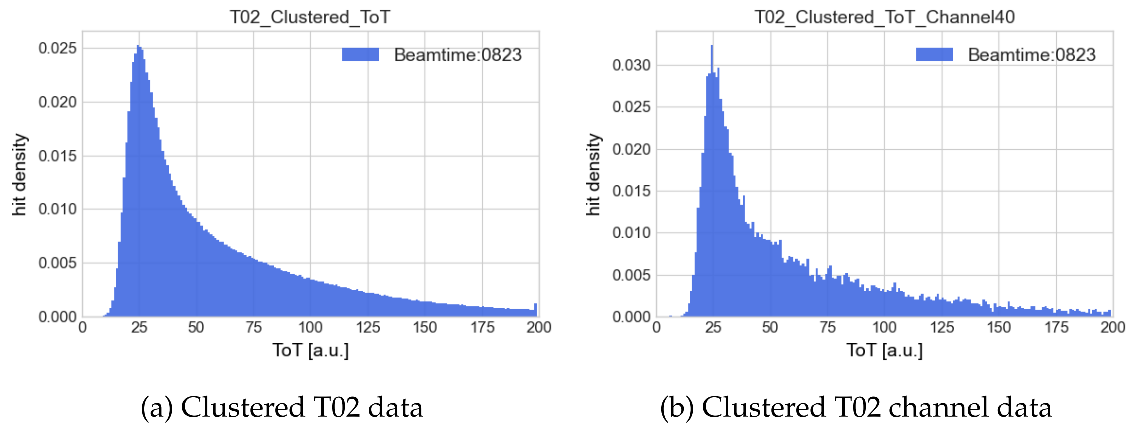

(a) Clustered T02 data

(b) Clustered T02 channel data

Figure 7.23: Summed ToT of event-associated strips, determining total ToT per event, from COSY beam for all T02 Channels (a) and a randomly chosen T02 channel (b).

In Figure 7.23, the clustered data from T02 is plotted, showing that the front peak has completely disappeared. The overlay with the main peak has also significantly reduced its intensity. This suggests that only individual channels are responsible for the front peak, indicative of noise. It will be revealed that this peak is caused by incident light on the sensor, as detailed and explained in Section 7.4.

In the examination of the individual channel, depicted in the right Figure 7.23, it can be observed that the beginning of the curve is slightly truncated, unlike the summed channels. The threshold for this channel was, therefore, set a bit too high. Additionally, a more pronounced decline in the curve is evident. Overall, the curves exhibit the expected behavior of a Landau distribution, illustrating the energy loss of fast charged particles in silicon.

Coincident Hits

Coincident hits are signals that are detected "simultaneously" (within the chosen clock cycle duration of a cluster) on T01 and T02. When the duration of coincident hits is appropriately chosen, it can be assumed that the event indeed involves minimum ionizing particles. This is because it must have had enough energy to traverse both the first and second sensors and is highly likely not noise since noise occurs randomly on the sensors. An explanation can be found in Section 7.2.4, where the most probable time for expecting a "simultaneous" event is discussed.

In total, approximately 1.5 million clusters were identified (2 clock cycle leading edge difference) out of 16.9 million total events in this measurement. Considering the total number of coincident clustered hits, which is 53.5 thousand, it becomes evident how dispersed the beam is and that the sensors are too far apart. Therefore, in Section 7.3.4, the distance will be minimized for Beam Time III.

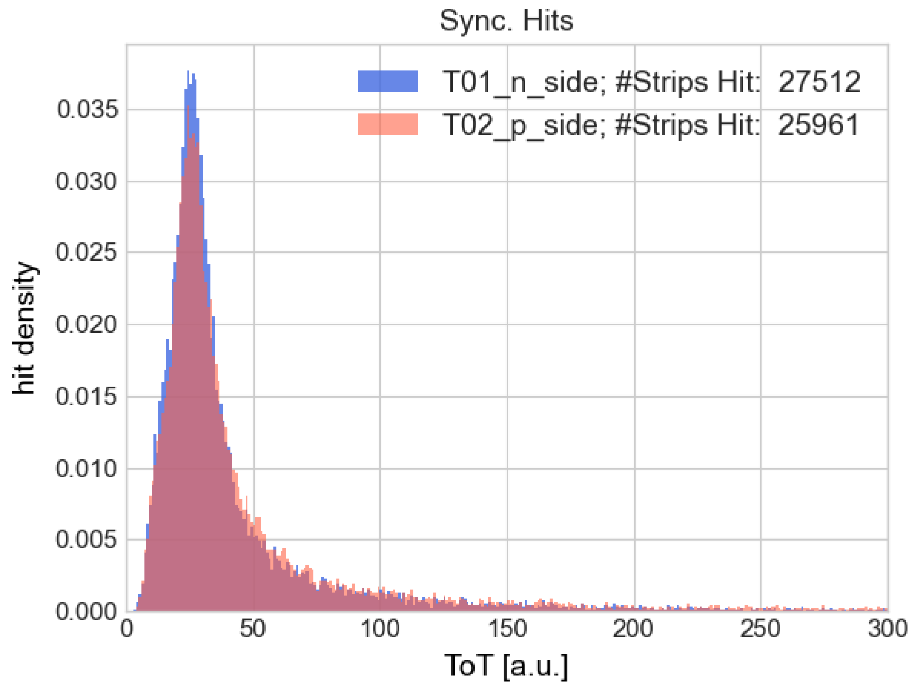

Figure 7.24: Deposited energy for both sensors at COSY Beam Time II for coincident events.

In Figure 7.24, the coincident clustered hits are plotted, representing all simultaneously fired neighboring strips of T01 and T02. Considering the differently zoomed scale, it is evident that the distribution falls off more sharply, resembling a Landau distribution. This indicates that in the data, that was "only" clustered, there are still some events that cannot be attributed to MIPs. A more detailed examination of the Landau function for coincident hits will be discussed for higher statistics in Beam Time III in Section 7.3.5. Also, it is noticeable that this time, for both T01 and T02, the distribution is slightly truncated at the beginning.

In Figure 7.25, the correlation of deposited energy is presented for both sensor readout pairs, T01 and T02. The slight spreading along the x- and y- axes suggests that some noise or not MIPs are still being recorded. However, the trace of fast charged particles on the diagonal is more pronounced, as explained in Section 7.2.4.

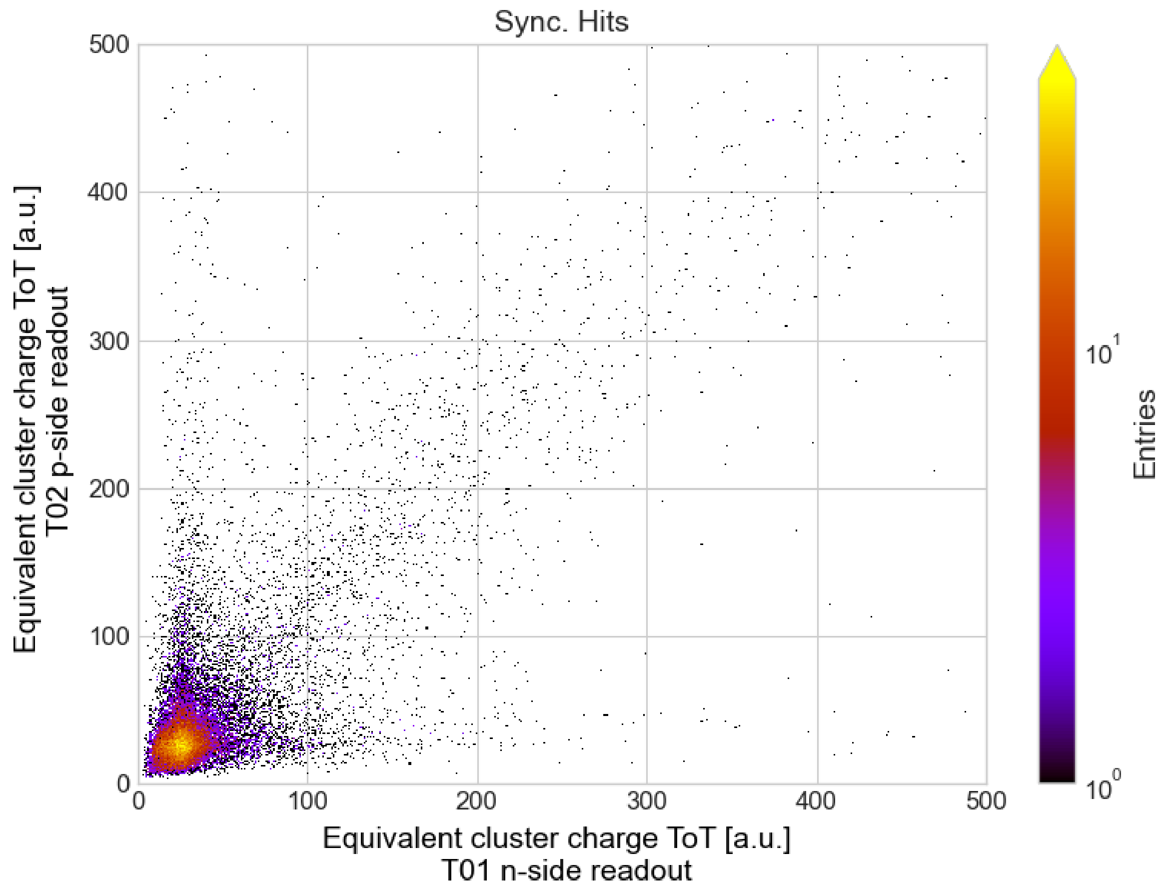

Figure 7.25: Correlation of the energy deposit for both sensors at COSY II Beam Time.

Conclusion Beam Time II

During Beam Time II, the general functionality of the MVD prototype was confirmed. It marked the first successful recording of signals during a beam time. Adjustments for future beam times, such as Beam Time III, were identified to enhance measurements. Various configurations of the ToASt were tested and analyzed, but a comprehensive discussion, along with the results from Beam Time III, is presented in Section 7.3.8.

7.3.4 Beam Time III

In the third beam time, the setup was slightly modified by bringing the sensors closer together, approximately 2 cm apart. This adjustment aims to increase the probability of detecting coincident hits. Additionally, the setup was realigned using a laser system. Two plastic scintillators were attached to both sensors, visible in black in Figure 7.26. This addition was intended for an efficiency measurement, which, unfortunately, could not be carried out. The tripod, the setup was mounted on, was equipped with a scale to enable the adjustment of various rotation angles of the sensors relative to the beam line.

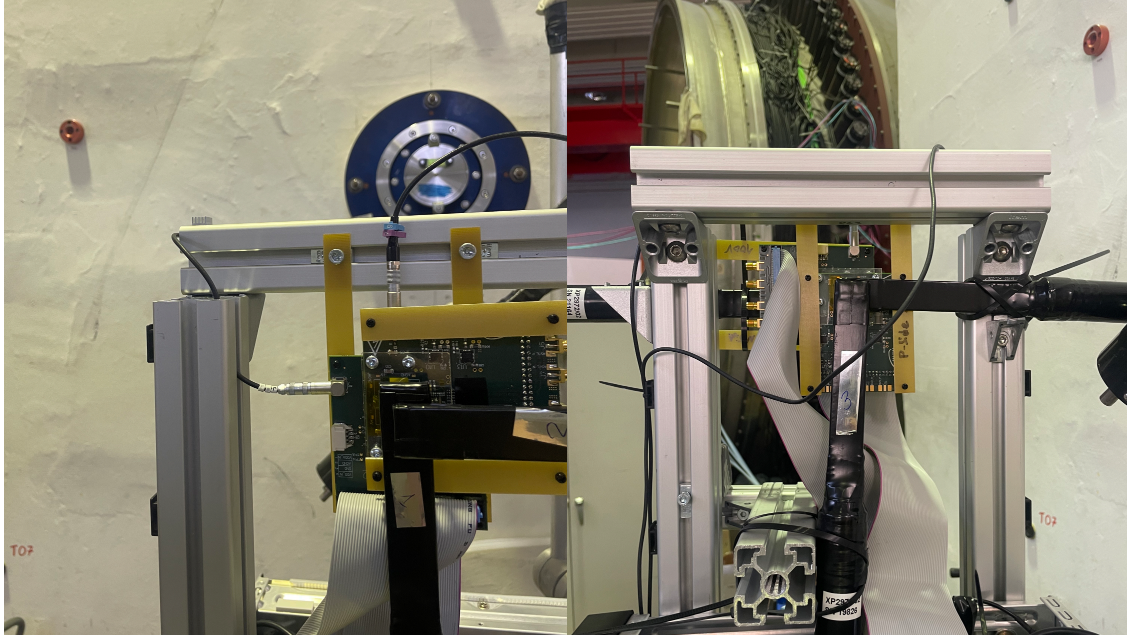

Figure 7.26: Measurement setup for the third COSY beam time conducted in the TOF Hall at FZ Jülich.

Figure 7.26 shows the front and back view of the MVD prototype in the TOF-hall of COSY. It is evident that the ToASt sensor boards are orthogonal to each other, aligning with the orientation of the sensor strips. This is also illustrated in Figure 7.27. In comparison to the previous setup in Figure 7.11, it's noticeable that the sensor boards and sensors are much closer to each other.

The objectives of the third beam time involve repeating the tests conducted in Beam Time II, which includes the investigation of various ToASt parameters and the collection of more statistics from these measurements. New tests include rotating the system to gain insights into multiplicities and energy deposits, as well as measuring coincident hits. It is worth noting that during the beam time, the COSY beam operated very steadily at an momentum of approximately 2740 MeV/c. In previous beam times, the beam was frequently interrupted, leading to the termination of meaningful measurements. Therefore, in the third beam time, a significant amount of data was primarily collected.

7.3.5 Beam Time III Measurements

Rotation of the Sensors

Firstly, we examine the change in cluster strip multiplicities, as explained in Chapter 7.2.3, and the deposited energy when the sensors are rotated in the beam. Here, zero degrees means that the beam impinges perpendicular to the active surface of the sensors. At 90 degrees, the beam would be in line with the active surface. This is illustrated in sketch 7.27.

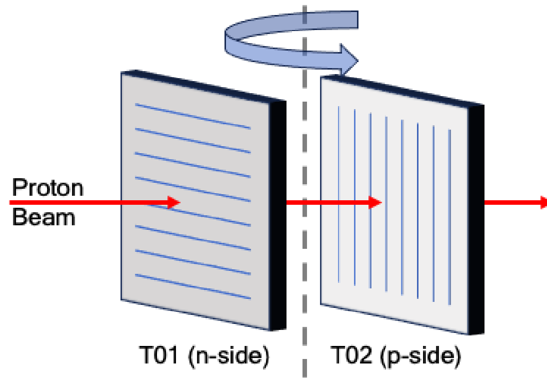

Figure 7.27: Sketch of the sensor rotation and strip configuration to the beam direction.

For zero degrees, it is expected that the beam particles pass approximately perpendicular through the sensors, leaving behind the average energy loss of protons in 285 µm of silicon. With rotation, the particles no longer traverse the sensors perpendicularly but at an angle, covering a longer distance in silicon, resulting in a higher energy deposit.

Similarly, it is expected that the multiplicity increases for the sensor whose strips are oriented horizontally to the axis of rotation. This is because, in this configuration, the particle traverses or "touches" more strips during its passage through the sensor. For the other sensor, whose strips are in the direction of rotation, the multiplicity should not change [65].

Next, we examine the multiplicity for clustered data, distinguishing the clusters for T01 and T02 without considering coincident hits. The calculation is performed with a 2-clock cycle leading-edge separation in the cluster due to the noise behavior, as explained in Section 7.2.4.

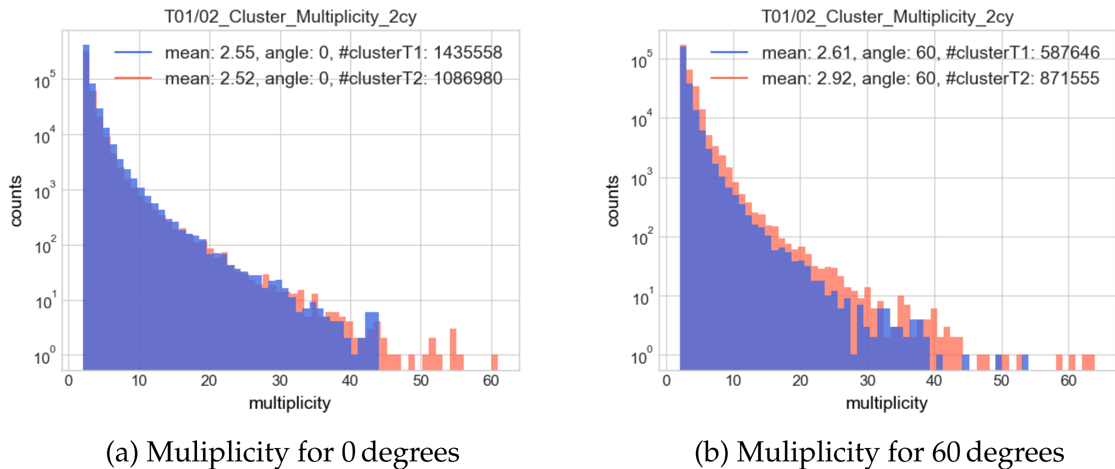

(a) Muliplicity for 0 degrees

(b) Muliplicity for 60 degrees

Figure 7.28: Multiplicity with a rotation angle of the sensors relative to the proton beam set to 0 (a) and 60 degrees (b).

For an angle of 0 degrees, as shown in Figure 7.28a, the cluster multiplicities for T01 and T02 are nearly identical, as expected, with mean values of 2.55 and 2.52, respectively.
For the rotation by 60 degrees in Figure 7.28b, it is initially noticeable that the number of counted clusters has reversed. In contrast to the 0-degree measurement, T02 now has more clusters. T02 was the rear sensor, and through the rotation, it was slightly moved closer towards the beam center, while T01 was moved outward from the center. However, the intensity does not affect the multiplicities.

For T01, the intensity changes only minimally to 2.61, corresponding to an increase of 2.35 %. This is expected since, as shown in the sketch in Figure 7.27, the strips rotate away from the beam direction. A proton traversing the sensor at an angle of 60 degrees "touches" the same number of strips as it does for 0 degrees. However, statistically, it travels longer distance through the strip or strips it touches and therefore has the chance to generate more charge.

On the other hand, T02 exhibits a different behavior. The mean cluster multiplicity for T02 increases to 2.92, corresponding to a 15.87 % increase. This is a significant elevation, as expected. The strips for T02 are perpendicular to the beam. Through rotation, the proton now traverses a shorter distance within a strip, touching multiple strips instead. The total distance covered remains the same for T01 and T02. As a result, the cluster multiplicity increases.

The comparison with the measured and simulated results from Bianco et al. (2013) [110], where a sensor with a comparable pitch and thickness is examined, reveals that the average multiplicities should increase significantly more. The reason for a lower observed increase is explained through the analysis of the deposited energy in figures 7.30 and 7.31.

However, first, we consider the aggregated multiplicity taking into account coincident events.

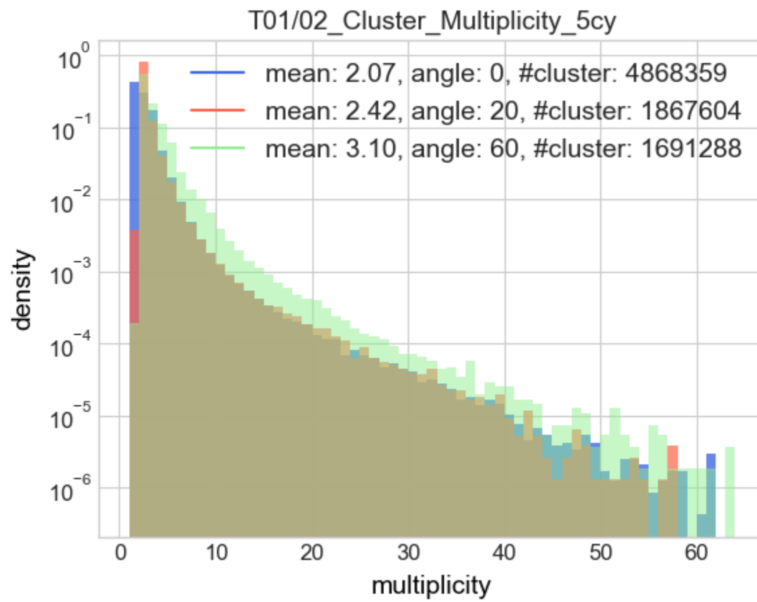

Figure 7.29: Aggregated multiplicity of all clusters recorded on both detectors during a COSY measurement.

In Figure 7.29, the clusters from T01 and T02 are also combined. This time, the angle of 20 degrees is also considered. For this angle, there is no noticeable change in multiplicity, as the proton beam, being relatively broad for secondary users, is already sufficiently fanned out and does not hit the sensors perpendicularly. From the distribution, it can be observed that a larger angle results in fewer coincident hits. This is due to the distance between the sensors, and with the rotation, the rear sensor moves out of the shadow of the front sensor. It should be noted that hits that only stimulate one strip in both sensors are labeled with a multiplicity of one.

To analyze the deposited energy, we examine the deposited energy in Time-over-Threshold for the clustered data from T01 and T02 for angles 0, 20, and 60 degrees.

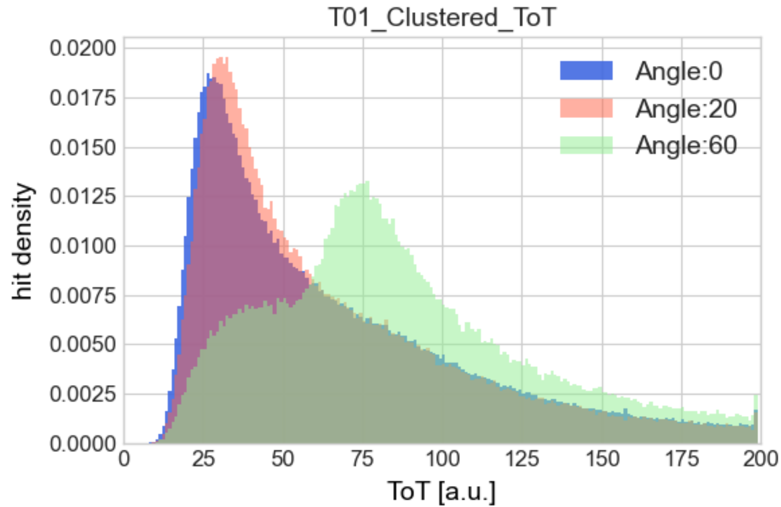

Figure 7.30: Charge deposition of the COSY beam in T01 for three different angles of beam incidence with respect to the sensor surface.

For T01 in Figure 7.30, the expected increase in deposited energy is visible due to the longer path in silicon. It can be observed that, as for 20 degrees, the curve shifts to the right and gains intensity for small energies compared to the 0-degree measurement, which was not expected. The same behavior was observed when reducing the time threshold, as explained in detail in Section 7.3.8. As a result, smaller energies associated with clusters are allowed. The same happens for 20 degrees, except here, the threshold is not reduced but the deposited energy increases. For 60 degrees, the curve moves significantly into the higher energy range. However, another distribution near the peaks of 0 and 20 degrees is visible. These are likely clusters where a part of the deposited particle energy is still below the threshold and thus truncated. This is consistent with the fact that the curve lacks the steeper Landau descent, and the intensity of the MPV is likely significantly reduced due to the truncated clusters.

To determine the change, the center of gravity for the peaks of the curves was calculated and is presented in Table 7.2. One clock cycle corresponds to 6.25 ns, and with the calibration of 60 ns/fC, the deposited energy can be estimated. It's important to note that an error analysis for this estimation is not meaningful since the calibration is an approximation that is significantly less accurate than determining the COGs.

Rotation [°]	**ToT**	**ToT [ns]**	**Energy [keV]**	**Increase [%]**
0	28.65 ± 0.22	179.96 ± 1.38	68.70	-
20	30.44 ± 0.18	190.25 ± 1.13	72.63	6.23 ± 0.06
60	76.50 ± 1.80	478.13 ± 11.25	182.55	167.02 ± 6.28

Table 7.2: Change in deposited energy for T01 with the different incidence angles of the proton beam.

This increase is to be expected to a similar extent. In the work of S. Bianco [110], similar enhancements were measured and simulated, with an increase proportional to $1/\cos(\theta)$ being identified. Additionally, the mean energy per stimulated strip was determined to be 50.46, 64.41, and 72.54 ToT for 0, 20, and 60 degrees, respectively. This is also expected, as more energy is deposited per strip.

When considering detector T02, a different picture emerges. In Figure 7.31, it can be observed that with an angled sensor, the MPV is shifted towards lower energy ranges. It is noticeable that higher energies have significantly lost intensity compared to 0 degrees, while lower energies near the cut-off have increased markedly. Additionally, especially the curve for 60 degrees is noticeably truncated in the low-energy range, which is also apparent for smaller angles.

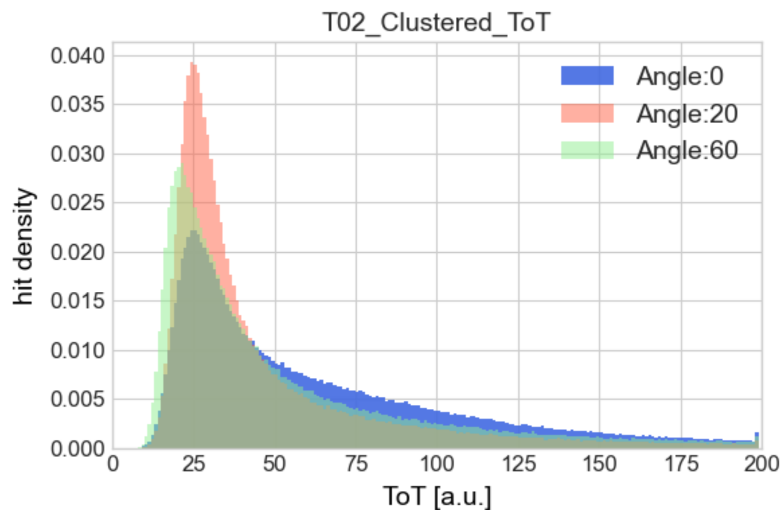

Figure 7.31: Energy deposit of COSY protons in T02 for three different angles of beam incidence with respect to the sensor surface.

Similar behavior to detector T01 would be expected since the proton's path through the silicon is also lengthened [65]. The only difference is that the path per strip is reduced, but more strips are excited, increasing the multiplicity. The deposited energy should remain approximately the same as for T01. Looking at the change in deposited average energy per strip and event, with values of 51.65, 50.29, and 50.25 ToT for 0, 20, and 60 degrees, it is noticeable that these values remain almost constant. A reduction in energy with the angle would be expected. Apparently, signals associated with larger entry angles were not recorded, likely due to a too high time threshold. This explains the observed truncation. Signals with low energies, seemingly caused by a slight rotation, are no longer properly recorded. This results in significant parts of clusters being truncated, especially for higher angles. These low signals would add up to the expected energies through clustering. Even for 0 degrees, parts of the curve are truncated due to the threshold, as shown in Figure 7.30 and in Chapter 7.3.8.

Conclusion Sensor Rotation

Both the multiplicities and the deposited energy caused by the COSY proton beam could be tested in a comprehensible manner. However, it has been shown that the time threshold was chosen too low. During the beam time, reducing the threshold led to instabilities in the ToASt. These issues are now understood and will be addressed in Version-2, as explained in Section 7.3.8.

Coincident Hits

In the analysis of coincident hits on T01 and T02, the immediately noticeable aspect is the higher statistics compared to Beam Time II, attributed to the smaller distance of the sensors. However, the comparison also reveals an increase in events near the x- and y-axes. This suggests that more particles, unable to traverse both sensors, were detected potentially due to ambient light interference. This can be attributed to the use of plastic scintillators, which complicated the coverage of the sensors.

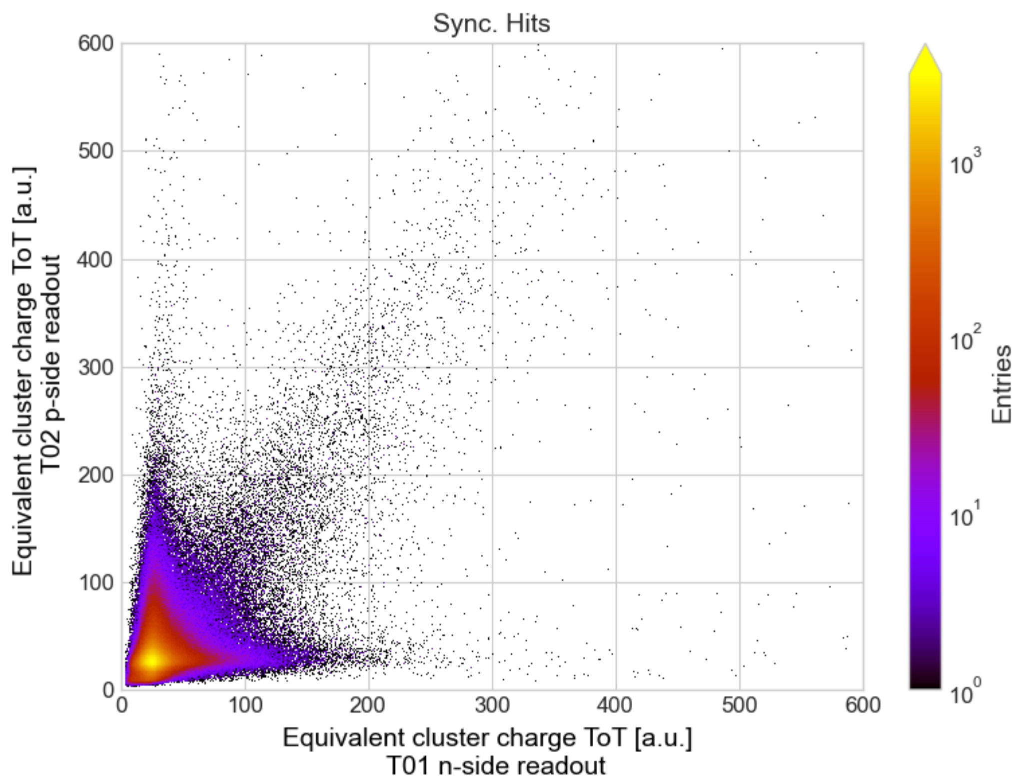

Figure 7.32: Correlation of the deposited energy in both sensors during COSY Beam Time III, synchronized with events caused by incident protons.

The forming diagonal distribution is clearly visible, indicating that indeed, fast charged particles could be detected with high statistics. To gain a more detailed insight into the deposited energy in the sensors, a fit is applied to the coincident event data in the following. This is made possible by the high statistics of Beam Time III.

Evaluation of Data Using Langau Fit

With an increased statistical data set in Beam Time III, a fit for synchronized hits becomes feasible for both detectors T01 and T02. It is important to note that clustering involves the summation of signals from multiple channels. While these channels are calibrated, variations in gain and threshold persist, as demonstrated in Chapter 7.3.3. The fitting approach employed utilizes a convolution of Gaussian and Landau distributions, referred to as "Langau" in the following text, with the fit-function provided by Si-Lab-Bonn [67], as detailed in Chapter 4.3.2. The deposited energy in Time-over-Threshold (ToT) values for COSY protons is plotted for both sensors.

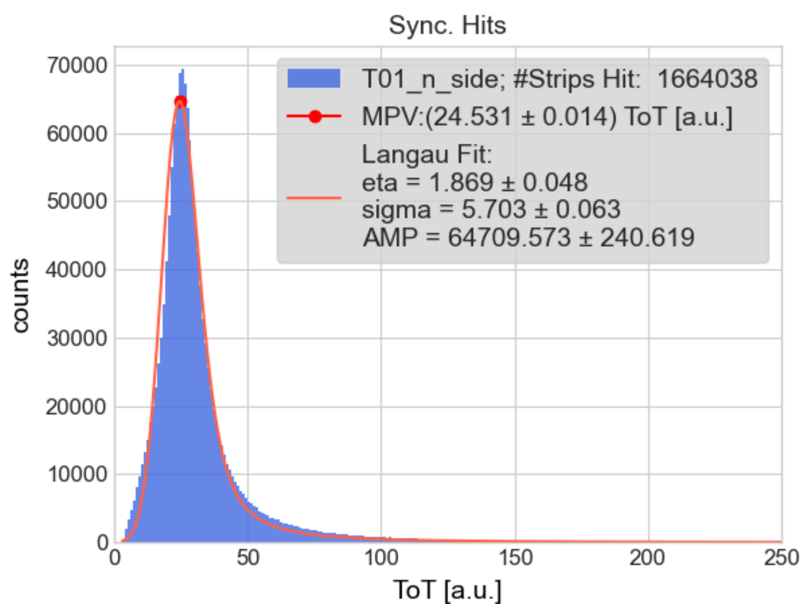

Figure 7.33: Measurement and fit of the deposited energy for T01 at COSY Beam Time III for coincident events.

In Figure 7.33, the fit is presented alongside the distribution of deposited energy in T01. Overall, a good agreement between the fit and the plot is observed. Particularly, the descending tail of the Landau, representing higher energies, is well captured. The rising edge shows a slight deviation from the fit at very low energies. Simultaneously, a minor inaccuracy is evident in the descending tail of the function, around 30 ToT. As mentioned earlier, it is highly probable that parts of clusters were truncated due to an elevated threshold, explaining the broader distribution at lower energies and a lower-than-expected statistics around 30 ToT. A more detailed investigation of this phenomenon has been undertaken in the preceding beam time chapters.

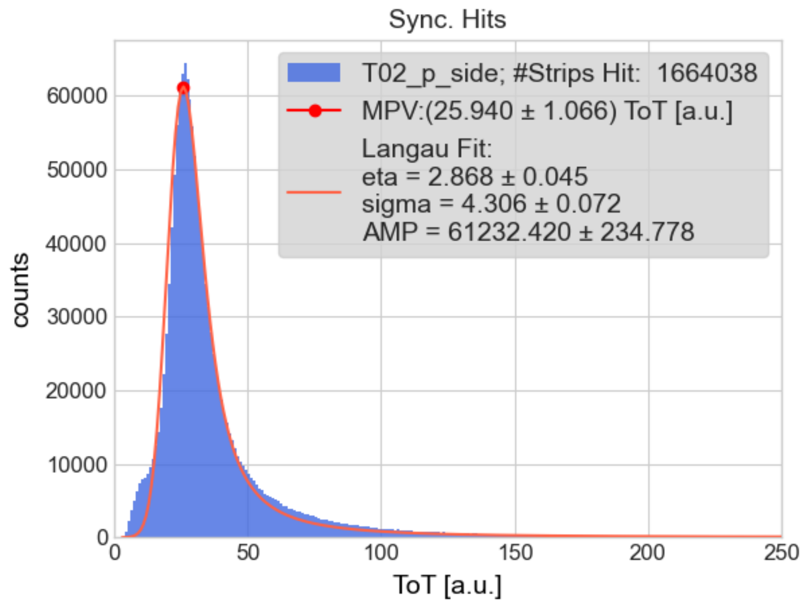

Figure 7.34: Measurement and fit of the deposited energy for T02 at COSY Beam Time III for coincident events.

For detector T02, the insights are even more pronounced. Again, the distribution closely follows the fit very accurately. However, this time, there is higher statistics observed around 50 to 100 ToT than anticipated. This is most likely due to the lack of statistics around the Most Probable Value (MPV) caused by truncated clusters. Therefore the threshold for T02 is chosen to be even higher than T01, significantly truncating signals.

In conclusion, it can be stated that the distributions closely align with the expected convolution of a Landau-Gaussian function. Hence, it is reasonable to assume that, during the measurement of coincident events, primarily Minimum Ionizing Particles (MIPs) were detected.

The most probable energy deposit in 285 µm silicon for a proton beam in the range of 3 GeV/c is approximately 75 keV. With the excitation energy of silicon at about 3.67 eV per electron-hole pair, this corresponds to 24000 electrons as the most likely charge deposit. Consequently, attributing this value to the MPV (Most Probable Value) of the distribution provides an estimation of energy. Assuming only MIPs were measured, this knowledge allows for assessing the calibration quality of the ToASt boards. For T01 and T02, the MPV of the distribution was determined using the fit, resulting in (24.53 ± 0.01) ToT and (25.94 ± 1.07) ToT, respectively. One ToT corresponds to 6.25 ns. With a calibration of 60 ns/fC, the deposited energy for the MPV for T01 is calculated as (58.530 ± 0.239) keV and for T02 as (61.895 ± 2.553) keV, which corresponds to 15,948.36 and 16,865.08 electrons, respectively.

This rough estimation suggests that the calibration operates within the correct

order of magnitude, allowing for meaningful physical results with the MVD prototype. For a very approximate estimation of the following results, the calibration can be back-calculated, considering the Minimum Ionizing Particles (MIPs), resulting in calibration values around 39.87 and 42.16 ns/fC for T01 and T02, respectively. However, it must be noted that the actual deposited energy could be significantly influenced by the primary experiments, so the obtained assessment should only be considered as a guideline. Despite the adverse conditions, an error of 33.6 % and 29.7 % indicates that the deposited energy of the protons can be detected by the prototype.

7.3.6 Leakage Current during Beam Time

During the measurements, it was observed that the leakage current underwent significant changes. Initially, the current rose continuously and then fluctuated around a certain value. Both sensors were fully depleted at 100 V, and the leakage current for the n- and p-side readouts was slightly different. As mentioned in Chapter 7.1.2, the leakage current serves as a crucial indicator for identifying issues with the sensors or connections from the sensors to the ToASt. We maintained a compliance limit of 5 µA for both sensors, which proved to be effective.

The complementary behavior of the sensors in Figure 7.35 from hour 120 onward can be explained by rotating the sensors. Apparently, this rotation exposes the p-side sensor to more scattered light, while the n-side is less burdened. Overall, the increase in leakage current is attributed to temperature variations, as demonstrated in Chapter 7.3.6 and investigated further in Chapter 7.4.

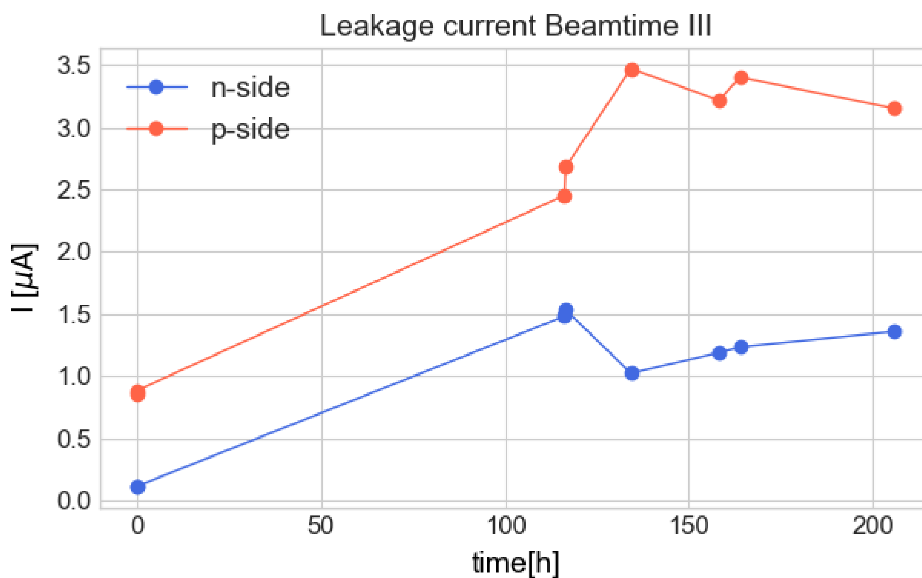

Figure 7.35: The variation in leakage current for both sensors during Beam Time III.

Temperature during Beam Time

The temperature was determined using a thermal imaging camera before the first and after the last measurement, considering the background of increased leakage current during the beam time. Especially, the plastic scintillators contributed significantly to the temperature development, which was trapped in the thick black fabrics. As a result, the temperature visibly increased by 16.5 °C. The impact of this temperature difference will be examined in Chapter 7.4.

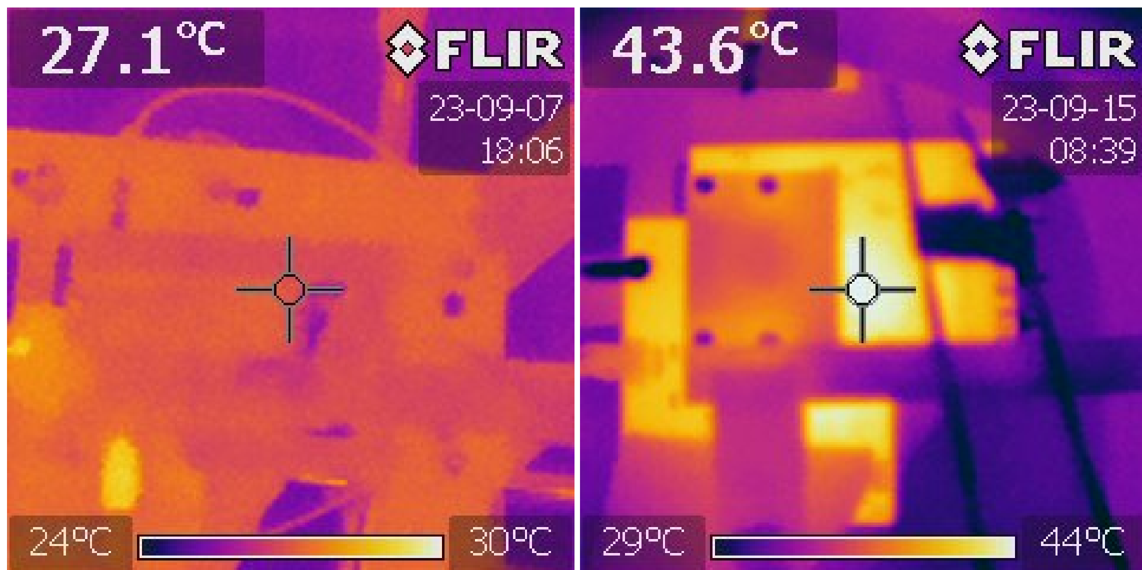

Figure 7.36: Temperature of the COSY Beam Time III setup at the beginning of and at the end of the beam time.

7.3.7 Comparison of Beam times

In comparing the two beam times, slight differences in the distributions become apparent. For instance, in the correlations of deposited energies between T01 and T02 in Figures 7.25 and 7.32 for Beam time II and III, there are noticeably more signals along the x- and y-axes in Beam time III. This suggests that more light exposure and thus more noise were recorded during this beam time compared to Beam time II. The same observation can be made in the examination of raw data, as shown in Figure 7.21 for Beam time II. For Beam time III, the noise peak is more pronounced, attributed to the installation of four scintillators originally intended for an efficiency measurement that unfortunately did not work. The additional setup made covering the sensors more challenging.
However, not every deviation in the measurements is explainable only by observing the data. The following presents two measurements for energy deposition in T01 and T02 for both beam times. The ToASt settings are identical for both measurements, indicating that the changes in the recorded data indeed originate from the measured events. It should be noted, though, that no changes are discernible within a measurement day, while the beam was stable.

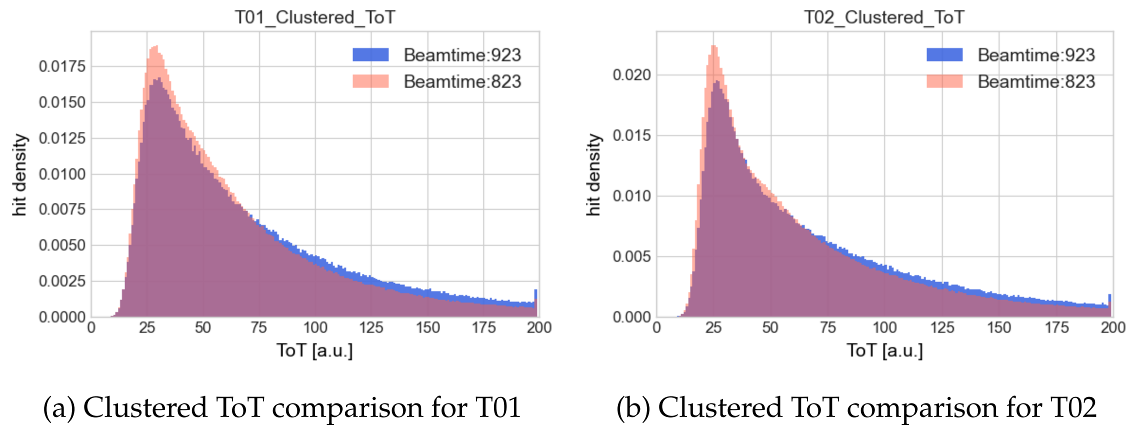

(a) Clustered ToT comparison for T01 (b) Clustered ToT comparison for T02

Figure 7.37: Comparison of measurements with the same ToASt and COSY settings at Beam time II (red) and III (blue).

The variation in the two measurements indicates that external influences have altered the distribution. Possible contributors to these changes include altered beam energy and intensity, light exposure, sensor temperature, or other interfering factors. Although efforts were made to keep the beam at a constant energy and intensity at the particle accelerator, minor fluctuations in both parameters still occurred. To determine the origins of these changes and to ensure that the prototype produces comparable results, the prototype was tested under controlled conditions in Chapter 7.4.
Furthermore, the spatial approximation of the sensors has proven effective, and the alignment with the laser system may have also contributed. The number of coincident hits compared to the total hits is significantly lower in Beam time I and II. However, the number of coincident hits has significantly improved in Beam time III.

7.3.8 Change of ToASt Parameters

In the following section, the behavior of the detectors is tested under different ToASt settings. This involves examining the configuration of individual channels, the discharge current of one of the ToASts, and the global thresholds for time and energy. Clustered data from beam times are evaluated for this purpose. It should be noted that T02 has experienced instability problems with slight changes in the discharge current, which is comparable to the so-called gain and leads to a reset. This problem has also occurred for low thresholds.

The assumption is that for a larger gain the noise is so high that the ToASt is overloaded, the behavior has been addressed for the second version of the ToASt, which is described in the conclusion.

Discharge Current

The discharge current is responsible for discharging the charge on the strips. A high discharge current causes the signal to drop quickly, while a low discharge current contributes to accuracy but makes it challenging to measure rapidly occurring events. For the Time-over-Threshold (ToT) method, a higher discharge current results in a lower ToT since the signal dissipates more rapidly. This is sometimes referred to as gain. The settings in the ToASt have the opposite effect; for instance, increasing the discharge current Digital-to-Analog Converter (DAC) value (labeled as **Disch_Dac_BIAS** in the DAC) actually lowers the discharge current, and the same applies to other settings. Due to the previously described issues, the increase in the discharge current of T01 by one Least Significant Bit (LSB) is considered. For each configuration, two independent measurements were conducted, both yielding the same result except for the altered ToASt.

On the left side of Figure 7.38, the distribution in red represents the increased discharge current DAC-value, resulting in a decrease in the actual discharge current. It is evident that the distribution has shifted to the right, towards the higher energy range.
On the right side, T02 is shown without any modification. Since the curves are identical, it can be assumed that the beam energy and intensity were nearly identical during both measurements. However, due to the nature of the curve, it is noticeable that T01 has captured significantly more clusters than T02. This difference may arise from distinct settings in the two ToASts or from the position of the sensors, although this does not impact the result.

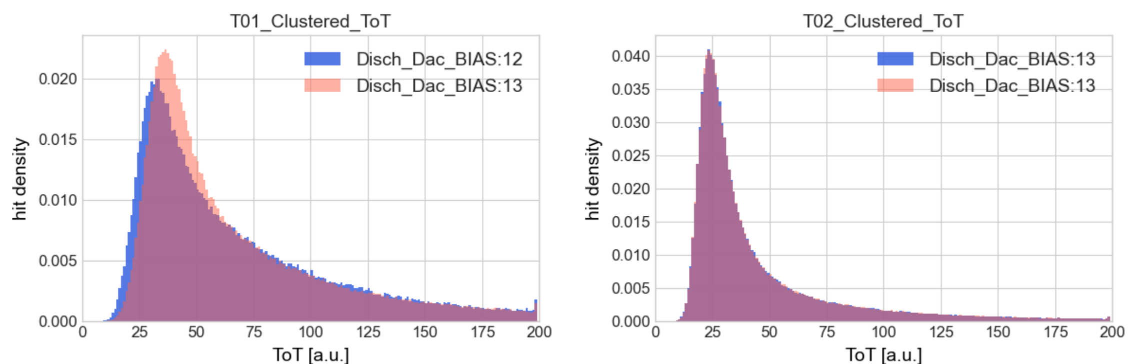

Figure 7.38: COSY proton beam with a variation of the discharge current for T01 for the measurement in red.

The maximum of the distribution increased by 12.2 % due to the modification, and the curve is visibly shifted towards the higher energy range for small cluster energies up to approximately 70 ToT. Above that point, the curves are nearly identical. As a result, the front part of the curve is no longer cut off, leading to an increase in the peak height. It can be assumed that the reduction in the actual discharge current allows for the capture of more signals with lower energies belonging to

clusters in the range between 30 and 70 ToT.

For the shift of the peak towards the higher energy range, the center of gravity of the peak was determined using a Gaussian fit. For T01, with the altered discharge current, the ToT increased by (3.65 ± 0.18) ToT, corresponding to (22.84 ± 1.13) ns or 11.3%. For T02, the maximum remains within the error range of the fit at (24.34 ± 0.14) ToT. Considering the explained energy calibration in Section 7.1.2 with 60 ns/fC, the energy range can be estimated. This results in an increase of the presented energy range by (0.381 ± 0.019) fC, equivalent to 8.727 keV. This result was expected because the reduction in the actual discharge current by 1 LSB prolongs the discharge and thus increases the ToT. For T02, the shift remains within the error, indicating that the measurements are comparable since no parameters were altered for T02.

Global Energy Threshold

The global energy threshold (labeled as **Energy_Th_BIAS** in the DAC) is the level at which the energy level of signals is considered relevant. This allows background noise to be disregarded before measurement, but it may also result in the truncation of signals. Therefore, the following tests the influence of the energy threshold when the DAC value is decreased by 2 LSB. This implies that the actual threshold value (hereafter referred to as real threshold) is increased, and a lower signal quantity is anticipated.

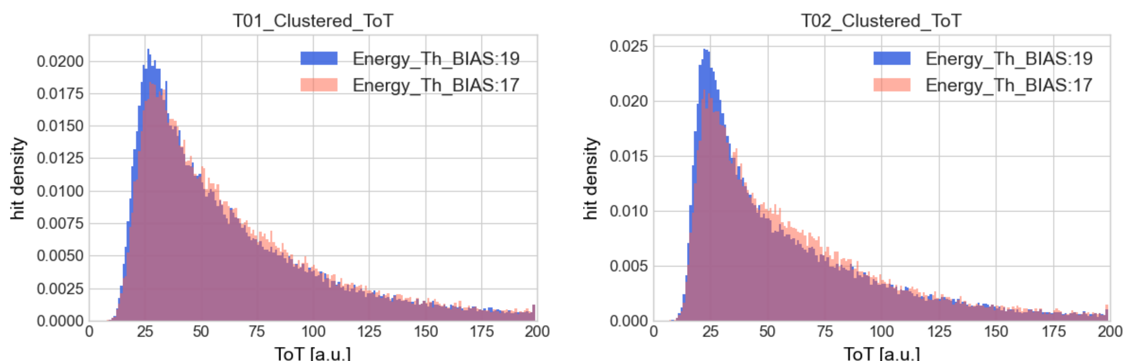

Figure 7.39: COSY beam time measurements for two different global energy thresholds.

In Figure 7.39, a COSY beam time measurement with an energy threshold DAC value of 19 is shown in blue, and one with a threshold of 17 is shown in red. It is immediately noticeable that for lower energies, a lower real threshold (blue curve) allows more events in the lower energy range than the higher one. In the density plot, it is apparent that the higher energy range is more pronounced with the higher threshold, as expected.

Due to the reduction of the real threshold, the maximum for T01 is increased by 14.18 %, and for T02, it is increased by 17.68 %. Considering the curves, it is likely

that especially noise was cut off by the higher threshold, leading to this change. However, it is also likely that some signal was cut off, especially from clusters with an energy around the most probable value (MPV). The center of gravity (CoG) decreases by (-2.069 ± 0.221) ToT for T01 and by (-1.015 ± 0.225) ToT for T02, which corresponds to (-12.93 ± 1.38) ns and (-6.34 ± 1.41) ns. Therefore, the ToT value changes by 7.6 % for T01 and 4.3 % for T02 with the increase in the energy threshold. Therefore, the higher real threshold crops the beginning of the distribution, causing a higher energy range to come more into focus in the measurement.

The changes for T01 and T02 are nearly identical, indicating that the change of 2 LSB affects both detectors almost equally and that the combination of global and channel thresholds is suitable for both detectors. If both sensors were calibrated completely differently, a change in the threshold would strongly alter the curve through noise or signal cutoff.

Global Time Threshold

The global time threshold (labeled as **Time_Th_Bias** in the DAC) represents the temporal threshold above which a signal is stored as an actual event. It directly affects the Time-over-Threshold method since only signals with a minimum duration above the global time threshold are processed. Similar to the energy threshold, this is an essential tool to suppress noise and enable the detection of signals with varying time durations. Again, an increase in the time threshold DAC value implies a reduction in the real threshold.

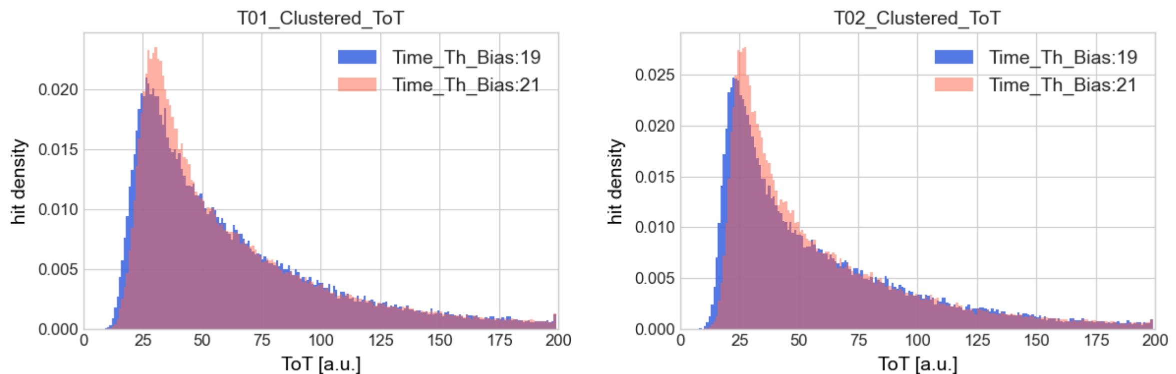

Figure 7.40: COSY beam time measurements for two different global time thresholds.

The DAC value of the global thresholds was increased by 2 LSB, meaning that in reality, the curve in red has a lower threshold, while the one in blue has a higher threshold. In this case, the reduction in the threshold does not cause an increase in noise but most likely contributes to the inclusion of signals in the low-energy range. The curve has gained intensity noticeably for low energies, around the MPV, while the curves remain identical for the higher energy range. Additionally, the

start of the curve has shifted slightly into the higher energy range. The assumption is that a too high time threshold bias removes signals belonging to clusters in the low-energy range, causing the curve to shift to the right and the intensity to increase for small energies. This behavior was also observed when changing the discharge currents, making sense since the discharge current affects the duration of a signal, and the time threshold trims this duration.

The maximum of both measurements shifts by 12.42 % for T01 and 12.16 % for T02. The influence on the ToT, i.e., the measured energy, results in (2.593 ± 0.174) ToT for T01 and (3.207 ± 0.214) ToT for T02, corresponding to 8.68 % and 11.88 %, respectively. This translates to (16.21 ± 1.09) ns for T01 and (20.04 ± 1.34) ns for T02. The adjustment of the ToASts is effective for this parameter as well. It would be interesting for future measurements to determine the actual threshold between noise and signal.

Channel Calibrations

Lastly, two different configurations of the ToASt channels are considered. For T01 and T02, different channel calibrations were applied for one of the two measurements. This time, individual channel settings are tested rather than the global ones.

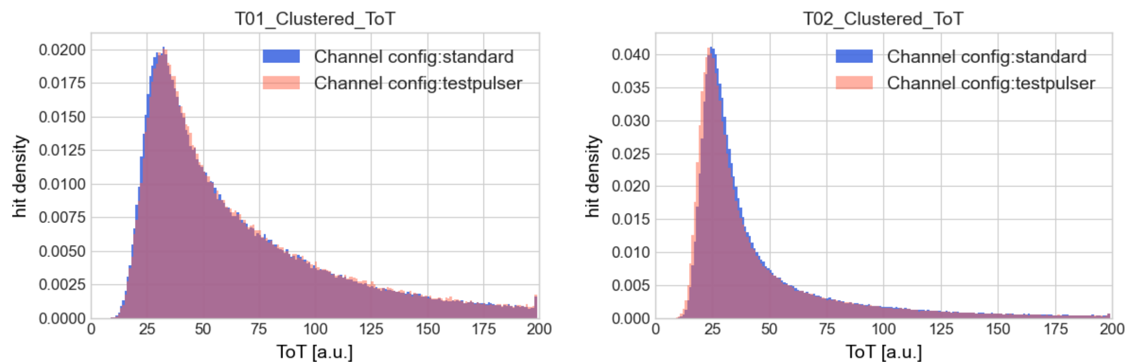

Figure 7.41: COSY beam time measurements for two different calibration settings for T01 and T02.

In the measurements from 7.41, it is immediately noticeable that almost nothing has changed; the intensity has remained almost identical. However, a slight shift on the x-axis is visible. In numbers, the maximum of T01 shifts by 0.89 %, and for T02, it shifts by 0.47 %. The maximum for the Time-over-Threshold shifts by (0.689 ± 0.216) ToT, corresponding to 2.13 %, and for T02, it shifts by (-0.974 ± 0.138) ToT, which is 3.85 %. After converting to the time domain, a temporal shift of (4.31 ± 1.35) ns for T01 and (-6.09 ± 0.86) ns for T02 was measured. A slight change makes sense, as the individual channels have been calibrated upwards and downwards so that the individual calibrations for the entire sensor almost balance each other out. The curve for the entire channels, therefore, changes minimally.

However, it could be demonstrated that channel calibration was successfully applied.

Conclusion

The changes in the ToASt parameters can be altered in a comprehensible manner. The detector system reacts as expected, and can respond to specific scenarios by modifying the parameters. An estimation of the energy range changes for different parameters has been made. Additionally, improvements for the 2nd version of ToASt have been suggested and are to be adopted. This includes addressing the issue previously described, where the system stops working and needs to be restarted for low thresholds, possibly caused by an extra frame sent by the ToASt. Nevertheless, in version 2, the threshold adjustment options will be refined, increasing from 5 to 6 bits.

7.3.9 Conclusion of Beam Time Measurements

In the beam times, a system consisting of $\overline{\text{P}}$ANDA-MVD sensors, the ToASt-ASIC, and the MVD-DAQ was tested for the first time. The system was successfully tested for functionality. A verification of the temporal output of the events demonstrated flawless interaction between the sensor, ASIC, and DAQ.

Energy loss measurements in silicon detectors were carried out with the COSY proton beam. Estimations were made regarding the dead time of the detector strips and the duration of a cluster. The energy loss curve and cluster multiplicities exhibited expected and understandable distributions. The modulation of the distribution due to the rotation of the sensors provided coherent results for multiplicity and energy distribution.

Various ToASt parameters were tested and evaluated to predict the percentage change by adjusting one or more parameters. The custom-made GUI allowed for control of the detectors during operation. It was demonstrated that energy calibration can provide an indication of the actual deposited energy in the sensors. However, more precise calibrations should be carried out to approximate the settings of individual channels and to obtain the exact energy that a particle leaves behind.

Issues were identified for thresholds set too low, leading to the ToASts entering an unstable state. Data analysis revealed that the threshold was actually set too high. This problem has been understood and will be addressed in the next prototype version.
In conclusion, the highly successful beam times have demonstrated the functionality of the detector system. This has led to the decision to release the system for the next iteration.

7.4 Prototype Testing under Controlled Conditions

During the COSY beam periods, measurements were carried out by secondary users of the proton beam, as detailed in Chapter 7.3. As a result, it was not possible to determine with certainty which particles hit the sensors and with what energies and intensities the sensors were hit. Efforts were made to render the experimental setup as light-tight as possible through the use of cloths. However, this aspect could not be conclusively validated. Notably, the prototype lacks active cooling, in contrast to the final design of MVD. As evidenced in the results presented in Subsection 7.3.7, it is observed that measurements conducted under identical settings occasionally exhibit minor variations. In order to clarify the causes of these differences and to improve the next setup to be used during a beam time, measurements carried out under controlled conditions are described in the following section. The focus is on the variation of temperature under conditions of maximum light-tightness.

7.4.1 Measurement Setup

To conduct the measurements as controlled as possible, the same setup used at COSY (see Section 7.2) was placed in a climatic chamber.

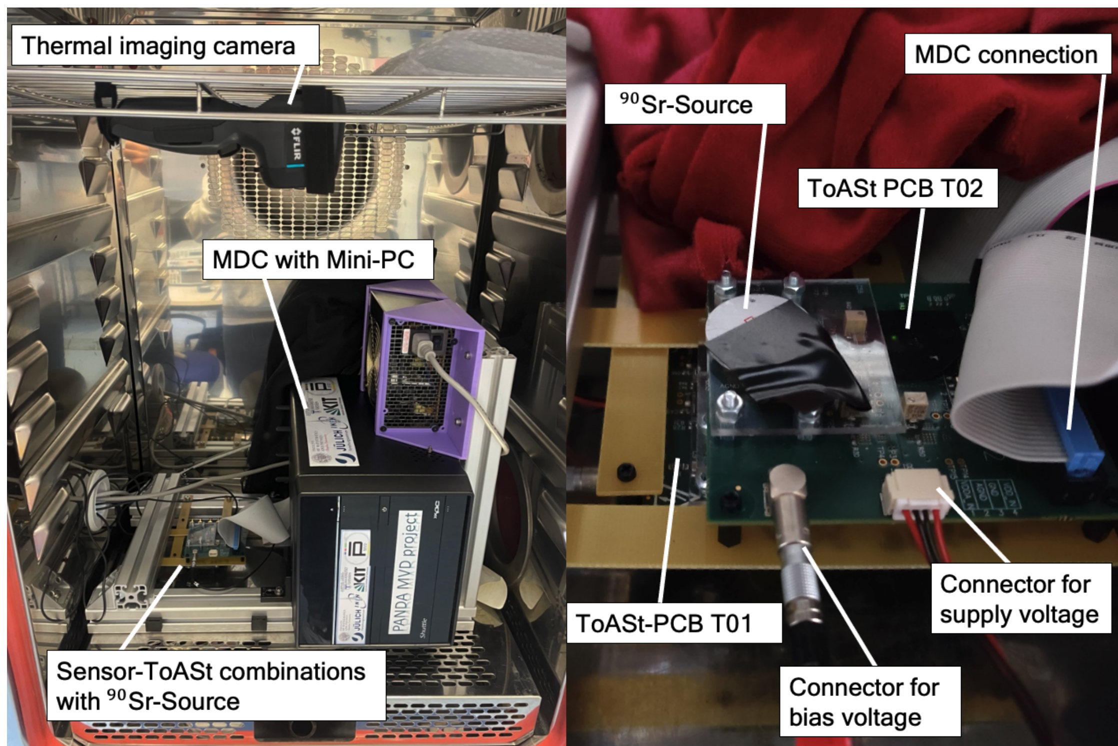

Figure 7.42: Setup of the MVD-Prototype in the climate chamber with a ^{90}Sr-Source.

The temperature was controlled by the climatic chamber, which also ensured light-tight conditions. This was determined through the minimal sensor leakage

current and verified by a camera. Moreover, every LED on the ToASt sensor boards and the PC responsible for controlling the ToASt was covered with tape and the sensors were covered with multiple layers of cloth. Additionally, thermal images were captured before and after the measurements using an infrared camera. The events and a constant event rate were achieved through the use of a Strontium-90 source. The source was positioned as closely and centrally as possible above one of the sensors. The other sensor is located approximately 2 cm below, rotated by 90 degrees, so that together they span a surface. In all measurements, with the exception of one, the ^{90}Sr source was positioned on top of T02, making it closer to T02 than T01.
Both sensors are fully depleted at 100 V during the measurement period. The ToASt sensor boards operate with a supply voltage of 3 and 4.5 V. Consequently, the hardware settings remain consistent with those employed during the beam times. Additionally, the parameters and calibration of the ToASt boards are configured based on the most commonly used and functional settings. Which are the calibrations for ToASt1: **2023-08-11T17-37-27-p-type** and ToASt2: **2023-08-11T18-01-33-n-type**
As in the beam times, ToASt1 reads the n-sensor side, and ToASt2 reads the p-side. It's important to note that in the naming conventions used for calibrations, the n- and p-sides were interchanged. This deviation is due to considering substrate doping rather than strip doping. Therefore, it is crucial to recognize that the p-doped strip side should be calibrated with the n-type calibration, and conversely, the n-doped strip side should undergo calibration with the p-type calibration.

7.4.2 Measurements

The measurements are intended to demonstrate, under constant conditions, how the signal behavior changes with varying temperature. To achieve this, the source is consistently positioned at the exact same location above the detectors. Light-tightness is observed through the variation in leakage current. After setting the temperature, data acquisition is initiated only when the climate chamber stabilizes at the desired temperature. Leakage current is recorded and monitored throughout the measurement. Each measurement is conducted over several hours to ensure an adequate statistical sample in the millions. Measurements are performed for temperatures of 5 °C, 10 °C, 16 °C, 20 °C, 25 °C, 30 °C und 35 °C. Special attention is given to measurements at 16 °C and 20 °C, as 16 °C reflects the anticipated operating temperature of the cooling water [10]. During the measurements, it has been observed that the entire Printed-Circuit-Board (PCB) heats up as a result of the detector operation, similar to the conditions during the beam times, as illustrated in Figure 7.36.

At first, the measured event rate of the sensors is examined for different temperatures. The rate was determined by the measurement duration and the total number of recorded events.

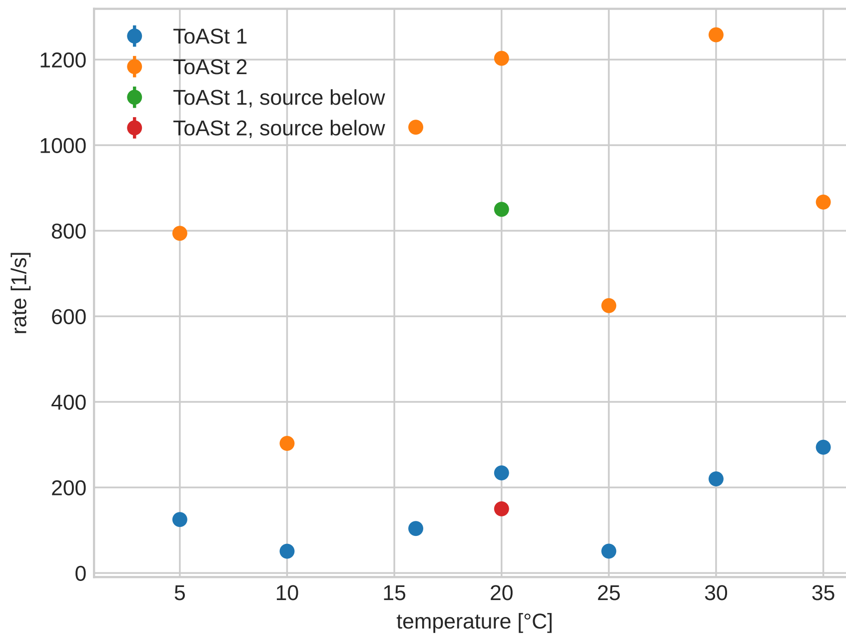

Figure 7.43: T01 and T02 event rate for different temperatures and positions of the ^{90}Sr-Source.

It is clearly evident that T02 has a significantly higher rate than T01, as expected. During the measurements, except for the data plotted in green and dark red, the source was directly placed on T02, with T01 positioned behind T02, which corresponds to setup 1 in Figure 7.54. Since Strontium-90 has a relatively broad energy spectrum due to its composition with Yttrium-90, it can be assumed that T02 already stops many low-energy events (explanation of the energy spectrum of strontium in Chapter 4.4.4). This and the smaller solid angle lead to a lower rate on T01.

As mentioned earlier, for the green and dark red data points at 20 °C, the source was placed closer to T01. Consequently, the event rate reverses as expected in comparison to the other measurements.

For T01, the rate barely changes with temperature, with a slight increase at 30 °C und 35 °C. On the other hand, T02 shows a more pronounced variation in the rate. However, no clear temperature dependence is observed. The differences are likely due to a slightly altered positioning of the source, affecting the actual rate reaching the sensors.
To determine whether temperature has an impact on the signal height, the deposited energy of the β-particles from the ^{90}Sr decay can be examined. First, the clustered events for all channels will be summed up for T01 and T02.

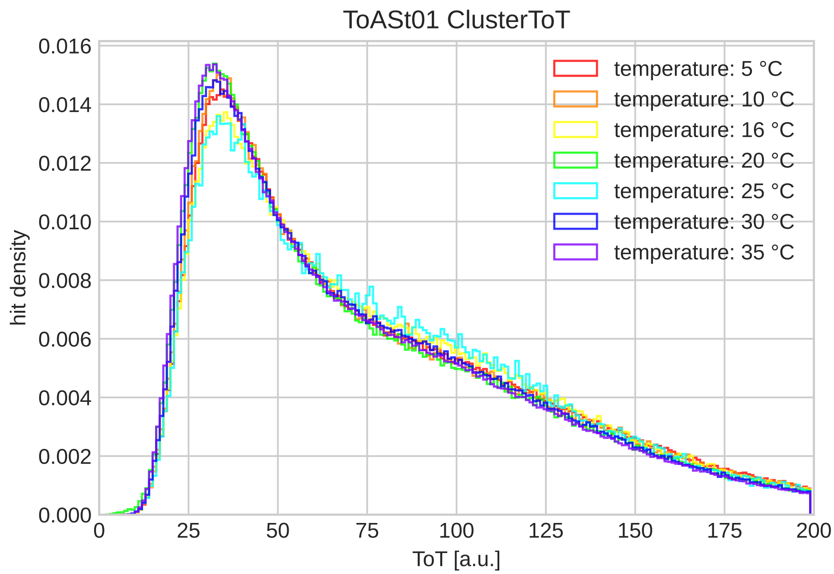

Figure 7.44: Clustered events for T01 with a ^{90}Sr-Source at different temperatures.

For T01, there is generally a very good agreement of the curves. Slight differences are noticeable, especially for 20°C. The slight deviation is likely attributed to the lower statistics of T01. This becomes evident when examining the distributions of T02 in Figure 7.45, where significantly higher statistics were recorded. This will be further investigated in figures 7.49 and 7.50. Overall, no dependence on the ambient temperature can be observed for T01.

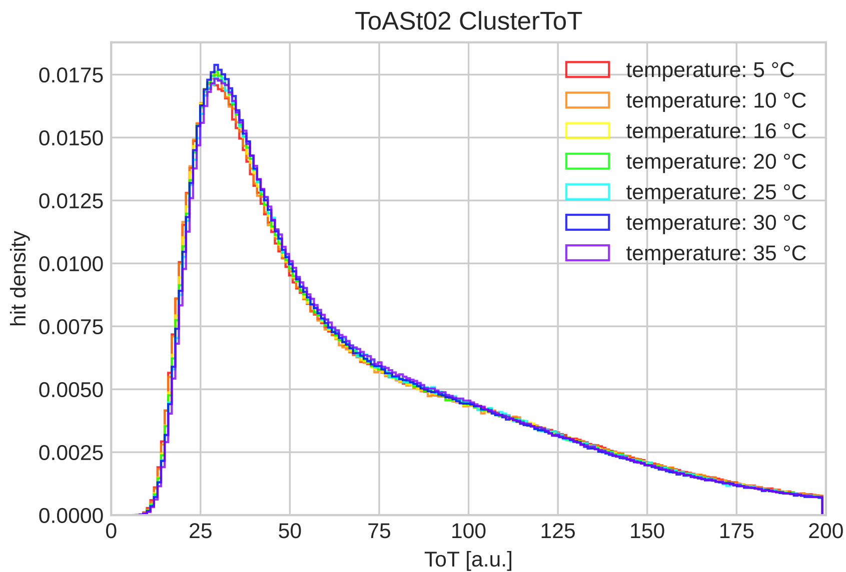

Figure 7.45: Clustered events for T02 with a ^{90}Sr-Source at different temperatures.

The deposited energy distribution for T02 in Figure 7.45 shows no deviation due to temperature as well, the distributions are nearly identical, yielding the desired result.

Since a change could be overlooked through the addition of channels, the following plots show all energies of events from one channel that belong to a cluster. This involves a randomly selected channel, ensuring that no channel selected is adjacent to a non-connected channel and is subject to strong charge sharing (explained in Chapters 7.2.3 and 7.2.2).

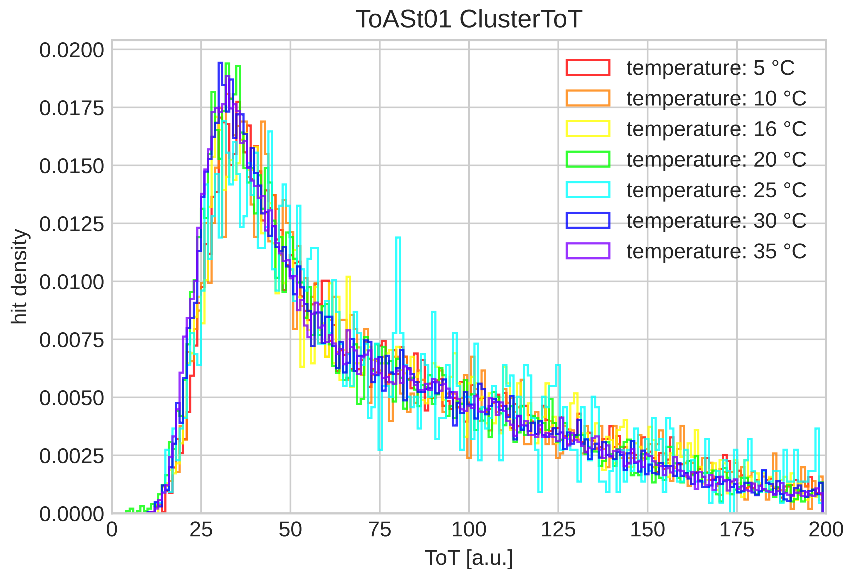

Figure 7.46: Clustered events for channel 42 of T01 with a ^{90}Sr-Source at different temperatures.

As expected, the statistics for a single channel are significantly lower than for the entire sensor. Especially for T01, due to the limited statistics, the measurement is imprecise, but no noticeable change in the curve with temperature is observed. The more accurate measurement of T02 clearly demonstrates that temperature has no measurable impact on the energy deposit and signal processing in the detectors.

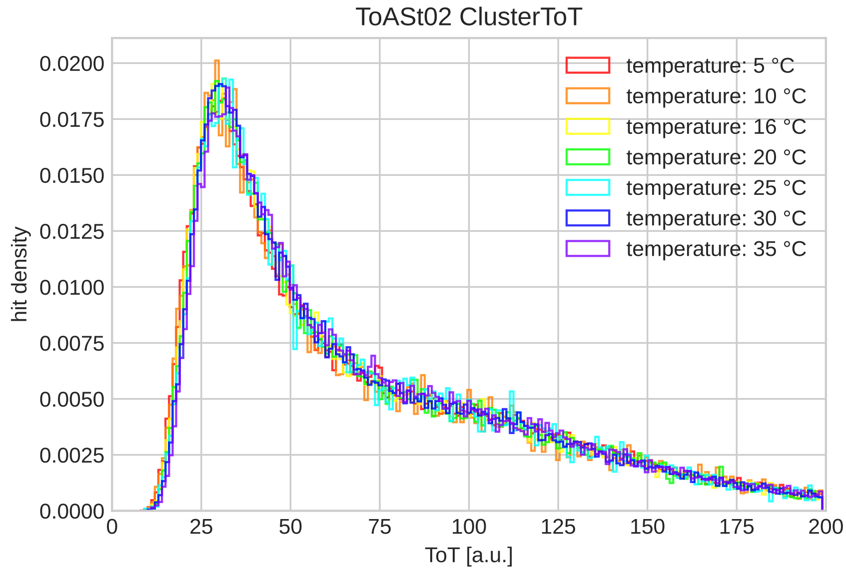

Figure 7.47: Clustered events for channel 42 of T02 with a ^{90}Sr-Source at different temperatures.

The unclustered raw data also show no dependence on temperature. Exemplary, due to statistics, only the raw data of T02 are shown here. The additional associated distributions can be found in the appendix (C.1, C.2, and C.3).

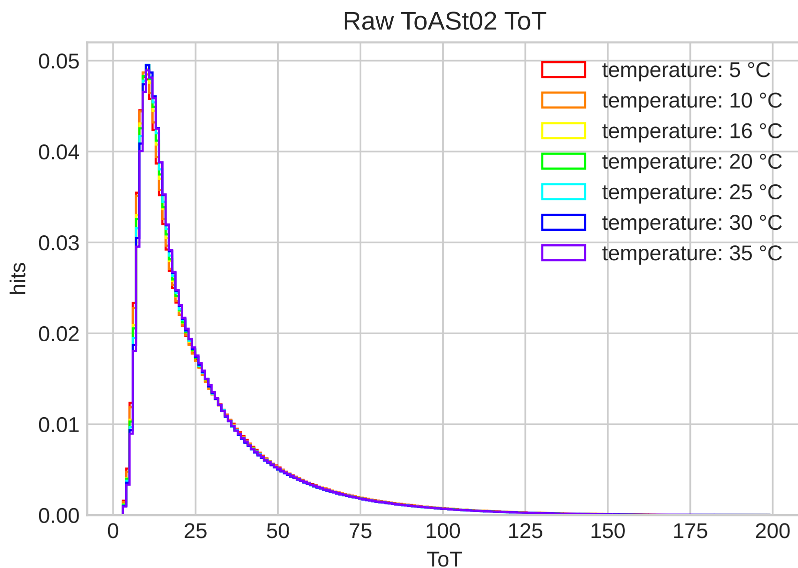

Figure 7.48: Raw events for T02 with a ^{90}Sr-Source at different temperatures.

The distribution of raw data in Figure 7.48 clearly shows that the pre-peak before the actual Landau distribution, as seen in the COSY beam times, has completely disappeared. This pre-peak was illustrated in Figure 7.21, and described in Chapter 7.3.3, it was explained that this accumulation of signals in the low-energy range

vanishes due to clustering. With this understanding and the knowledge that the measurements in Figure 7.48 were taken in darkness, it can be assumed that the bump in the COSY measurements was generated due to stray light. Photons in the visible energy spectrum do not penetrate the sensors and lose their energy in a very limited area, from one strip. As a result, this noise is prevented by clustering or by the absolute light-tightness.

To gain further insights into the behavior of the MVD prototype at different temperatures, the following section investigates the mean deposited energy and the maximum of the distributions.

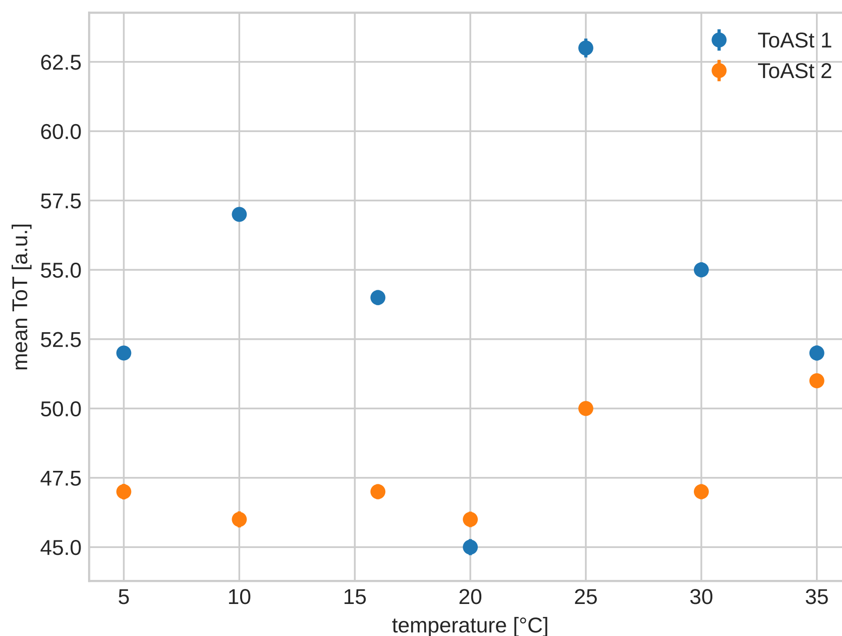

Figure 7.49: Mean deposited energy for clustered MVD-Prototype ^{90}Sr measurements at different temperatures.

Figure 7.49 depicts the mean deposited energy as a function of temperature. Apart from a statistical deviation from the mean of 16.7 % for T01 and 6.9 % for T02, the mean value remains constant for both detectors. The increased uncertainty for T01 can again be attributed to lower statistics, as it is the rear sensor in relation to the source position.

Similarly, the consideration of the MPV, or the maximum of the distribution, shows no dependence on temperature. For T01, the mean deviation is approximately 6.7 %, and for T02, it is 3.0 %, remaining nearly constant with changes in temperature. Thus, the change in temperature from 5 to 35 °C does not measurably alter the deposited energy in the sensors, and the data acquisition captures the signals without a temperature shift.

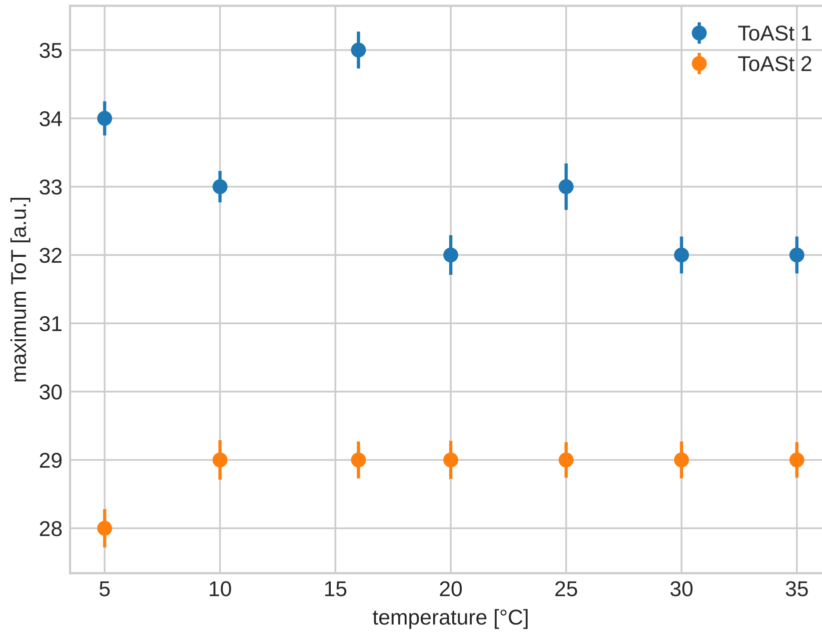

Figure 7.50: Most probable deposited energy value for clustered MVD-Prototype ^{90}Sr measurements at different temperatures.

Finally, the dependence of the leakage current on temperature is examined since an increase in current with measurement duration was observed in the beam times, as depicted in Figure 7.35. For this, the leakage current was plotted multiple times within a temperature measurement, and the mean value was subsequently calculated. The error bars in Figure 7.51 represent the maximum deviation from the mean.

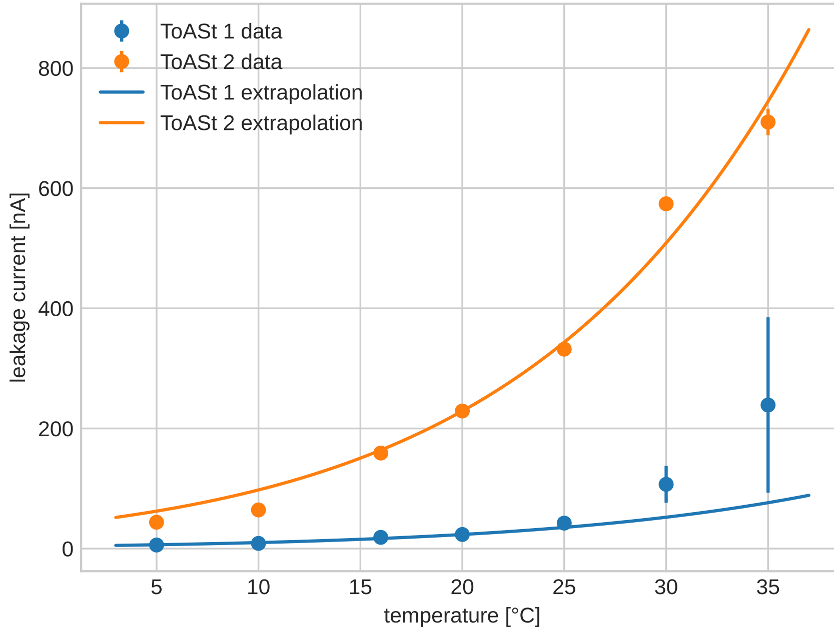

Figure 7.51: Leakage current during ^{90}Sr measurements of the MVD-Prototype at different temperatures.

The dependence of the leakage current on temperature is clearly visible. The leakage current for T01 and T02 increases significantly with temperature, as expected, since the charged particles can more easily cross the band gap at higher temperatures.

Overall, in comparison to the COSY beam time with a maximum leakage current of 3.473 µA, a significantly lower leakage current is observed under controlled conditions. This can be attributed, on the one hand, to a lower temperature and, above all, to the influence of stray light. At the beginning of the measurement, when the detector was still at room temperature, a current of 0.8597 µA,was measured, which exceeds the maximum of the measurements under controlled conditions.
An extrapolation of the leakage currents was performed using Formula 7.5 and is shown by the solid line in Figure 7.51 [111]. In this, a reference temperature T_{ref} of 20 °C was chosen, and the band gap of silicon $E_{g,eff}$ was set to 1.12 eV [53].

$$I(T) = I(T_{ref}) \cdot \left(\frac{T}{T_{ref}}\right)^2 \cdot e^{-\frac{E_{g,eff}}{2k_B}\left(\frac{1}{T}-\frac{1}{T_{ref}}\right)} \tag{7.5}$$

For T02, the exploration corresponds very well to the values actually measured. For T01 at the beginning as well, but for higher temperatures there is an increasing deviation. This is most likely due to the large measurement errors at 30 °C and

especially at 35 °C. To investigate this in more detail, the leakage current for the duration of the 35 °C measurement is plotted below.

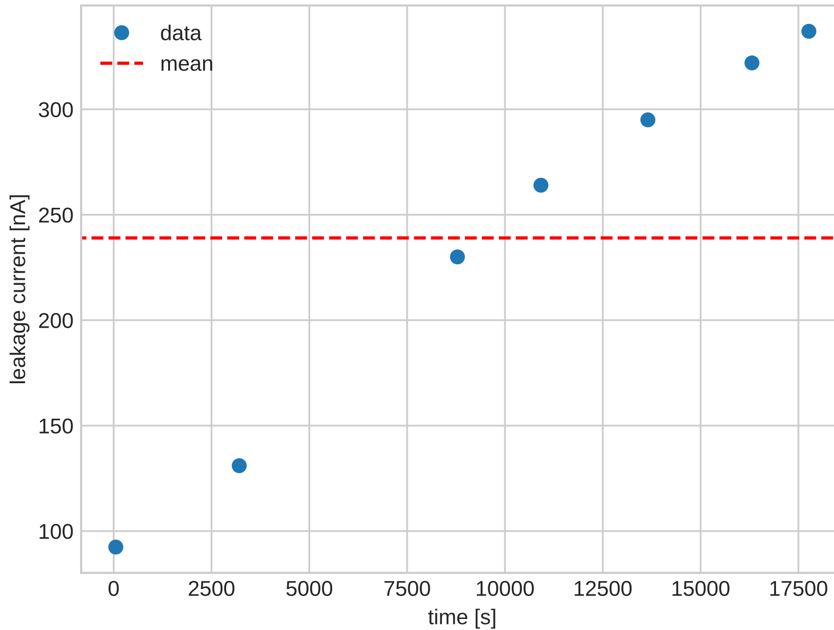

Figure 7.52: Behavior of the leakage current during the 35 °C measurement with ^{90}Sr.

Over time, it becomes apparent that the leakage current steadily increases and, for very long measurement duration's, starts to possibly stabilize, especially after 10,000 s. One possible cause for this could be that the final temperature has not yet been reached on the detector itself, especially due to shielding by the thick textiles. The significant deviation from the mean in red is clearly visible, contributing to the large error in Figure 7.51. Nevertheless, the measurements have demonstrated a understandable dependence of the leakage current on temperature.

Similarly, there is no change in the multiplicities, as observed in the previous results. Therefore, their temperature dependence can be found in Appendix C.4. Interestingly, the measurements with ^{90}Sr in a closed environment show significantly smaller multiplicities than the COSY beam times with proton irradiation in Chapter 7.2.4.

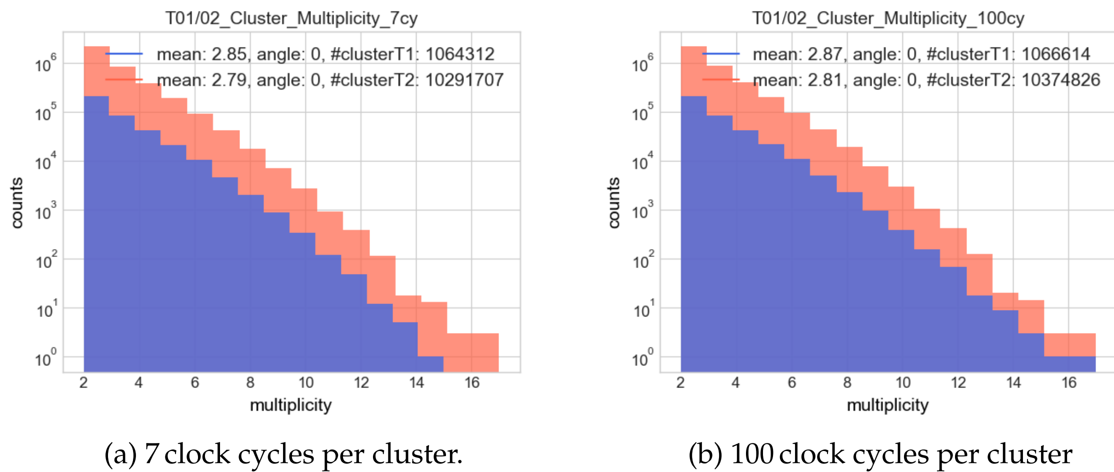

(a) 7 clock cycles per cluster.

(b) 100 clock cycles per cluster

Figure 7.53: Multiplicities for the ^{90}Sr measurements at 16°C with different signal time intervals within an event, given in clock cycles derived from the 6.25 ns clock of the ToASt

Unlike the COSY multiplicity measurements, there is no replenishment of clusters through random events. The multiplicity slightly increases with the cluster time due to the summation of clusters. However, the peak at channel 63 has disappeared, as shown in Figure 7.17b, which was observed in the proton measurement. This proves that the detector itself is not affected by common noise, but rather, actual signals were recorded that caused the peak. A rough estimate of what led to the peak was discussed in Chapter 7.2.4.

7.4.3 Distribution of Strontium-90 Measurements

As a slight elevation in the higher energy range is observed in the distributions with the ^{90}Sr source, along with an accumulation of events on one side of the sensor, clustered events and clustered coincident events for two different measurements with T01 and T02 will be shown in the following.

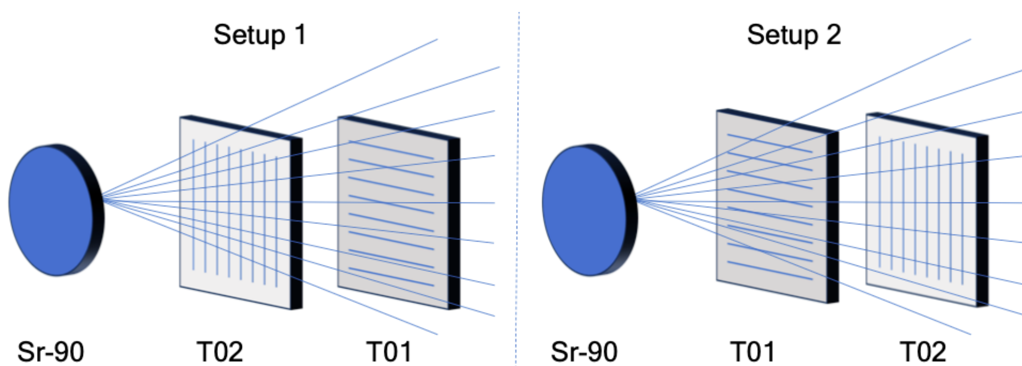

Figure 7.54: Two setups of the sync. measurements with different source positions.

In one of the measurements, T01 is positioned closer to the source, while in the other, it is T02, as illustrated in Figure 7.54. At first, coincident events are considered to get some insights of the physics, happening during the irradiation with ^{90}Sr. In Figure 7.55, the correlation of the deposited energy from coincident hits on T01 and T02 is shown. In this measurement, the ^{90}Sr-Source was positioned directly above the T02 sensor, with the T01 sensor located behind it, corresponding to the setup in Sketch 7.54.

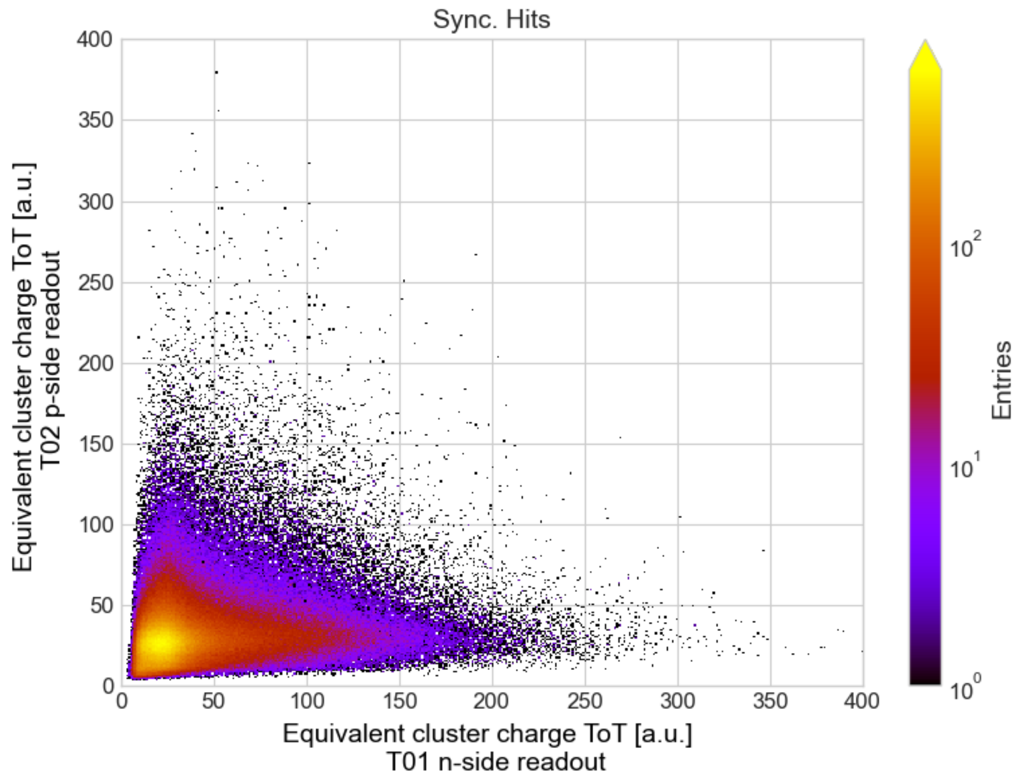

Figure 7.55: Correlation of the deposited energy for T01 behind T02 and the ^{90}Sr-source.

It is clearly noticeable that there is a significant accumulation of events on the x-axis, corresponding to T01. This is most likely due to β-particles that had just enough energy to pass through T02 but got stuck in T01, depositing their entire kinetic energy there. Even if the particles are not stopped but significantly slowed down by the two layers, the ionization is increased due to the deceleration. This localized energy deposit is known as the Bragg peak [64]. This leaves a coincidence signal on T02 and measures a much higher energy on T01.

In Figure 7.56, in comparison to the previous setup, the source is positioned on the opposite side of the detector, directly above the sensor of T01, with T02 located behind it as illustrated in setup of Sketch 7.54.

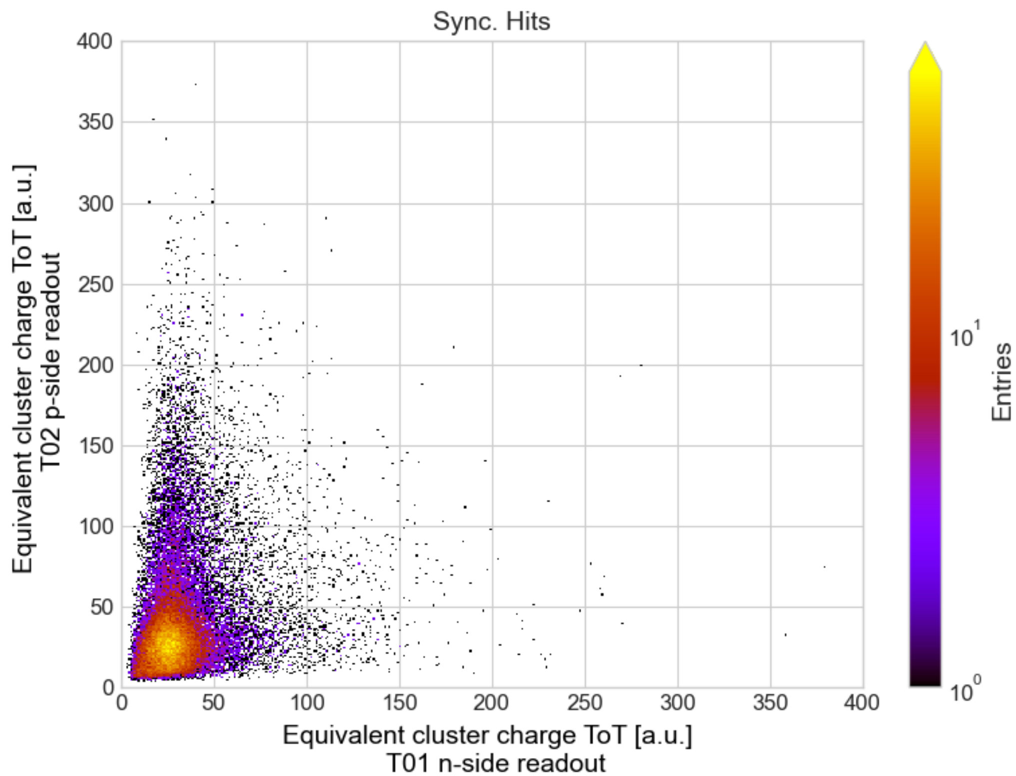

Figure 7.56: Correlation of the deposited energy for T02 behind T01 and the ^{90}Sr-source.

The same behavior can be observed, namely an accumulation of events with higher energies at the rear sensor, confirming the previous hypothesis, this time specifically for T02 near the y-axis.

To highlight the differences in the deposited energies, the deposited cluster energies of coincident events are plotted in Figure 7.57. As anticipated, the distribution for T01, positioned as the rear sensor (Figure 7.57a) facing the source, reveals an increased distribution in the upper energy range compared to T02, introducing a certain distortion to the distribution. Conversely, the front sensor, T02, exhibits heightened intensity in the lower energy spectrum. Upon reversing the source orientation and placing it on the T01 sensor, the distributions are mirrored, presenting a consistent pattern as explained earlier.

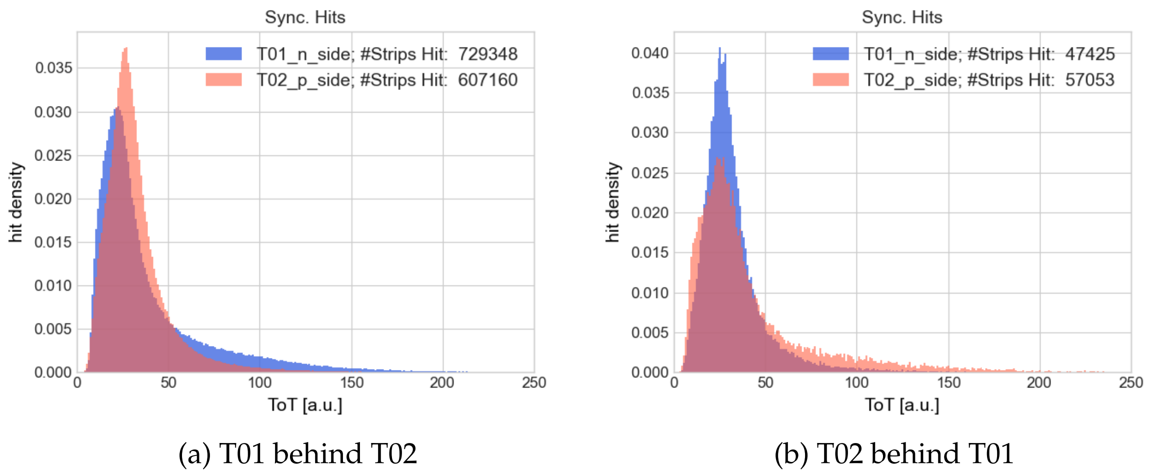

(a) T01 behind T02

(b) T02 behind T01

Figure 7.57: Deposited energy for the sensors with different positions corresponding to the ^{90}Sr-Source for coincident events.

Furthermore, the explanation for the energy shift behavior due to the trapped particles is also influenced by the fact that the particles must pass through T02 with energy loss. The statistically slower particles then, on average, deposit more energy in sensor T01.

The Landau distribution, as elucidated in Chapter 4.3.2, which mirrors the energy loss of minimal ionizing particles in silicon, is more effectively illustrated in the analysis of coincident hits from the front sensor. In this context, it is reasonable to assume that only MIPs have traversed the sensor. In contrast, the rear sensor has a distribution that includes both minimal ionizing particles and electrons, which get stuck in the sensor and release their entire kinetic energy. The deviation in distributions is thus explainable by the positioning of the ^{90}Sr source and does not have a direct correlation with the MVD prototype.

Analysis of Clustered Signals from Events

After verifying the deposited energy in coincident events, an investigation of all measured events can be conducted. In the following figures (see Figure 7.59), the clustered events for T01 and T02 are plotted. T02, as before, represents the sensor closer to the source, corresponding to setup 1 in Figure 7.54. When the positions are swapped, the distributions change accordingly, aligning with the assumption of particles getting stuck in the sensors. Subsequently, a Landau-Gaussian convoluted curve was fitted over the resulting distribution, as discussed in Chapter 4.3.2. Additionally, the fitted distribution minus the actual values was calculated to illustrate the discrepancy. The most probable value (MPV) of the resulting curve was determined using a Gaussian fit. The purpose of this exercise becomes evident when considering the simulated results from Geant4, as presented in the dissertation by K. Koop [23], where simulations were conducted

for an identical sensor to determine which particles from the ^{90}Sr decay passed through the first sensor and left a signal in the second one.

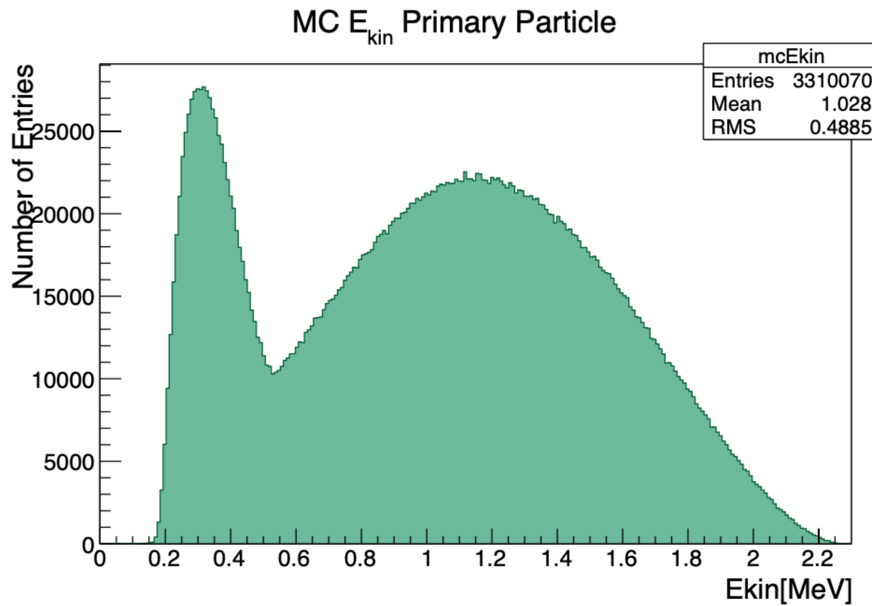

Figure 7.58: Simulated energy spectrum of electrons from a ^{90}Sr-source that deposit a signal in a 300 µm silicon detector without being stopped [23].

In Figure 7.58 it can be observed that primarily electrons from the yttrium decay pass through the sensor. Approximately 24 % of the electrons have an energy above 1 MeV and are therefore nearly minimally ionizing, while the remaining 76 % have too little energy. These electrons mainly originate from the low-energy decay of strontium into yttrium. This, in turn, implies that a large portion of the electrons were already stopped in the first sensor, resulting in the distribution from the MIPs overlapping. However, as seen in the correlation plots 7.55 and 7.56, a significant number of electrons also get stuck in the second sensor, depositing all their kinetic energy there. Consequently, from the two fits explained earlier, the estimated deposited energy of the MIPs as well as the low-energy or stuck electrons can be determined. It is also noteworthy that sources near the sensor for both setups have recorded significantly more events, which is caused by both the sticking of the electrons and the angular distribution, as it is an omnidirectional source.

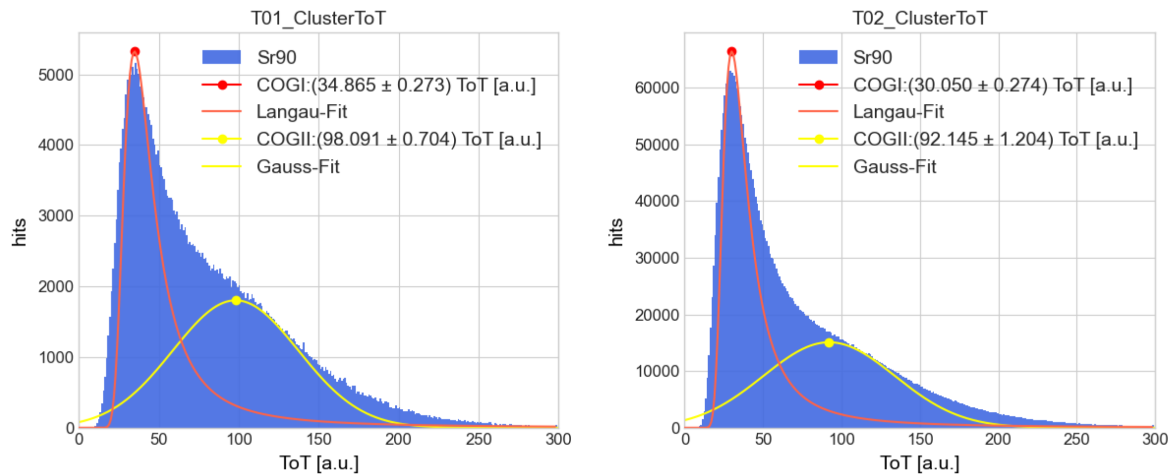

Figure 7.59: ^{90}Sr measurement of T01 behind T02 and the source at 16°C with a Langau fit and Gaussian fit.

Firstly, the center of gravity (COG-I) of the Langau curves is examined in red, with values of 34.865 ToT and 30.05 ToT, corresponding to 22.668 ke and 19.537 ke, respectively, after calibration with 60 ns/fC, in good agreement with the deposited charge of a MIP [65]. As discussed previously in Chapter 7.3.5, the value is slightly lower compared to the simulated target value of 24 ke [23], possibly due to a slightly erroneous channel calibration or an overly high threshold. Nevertheless, a deviation of 5.5 % and 18.59 % from the ideal value are very good indicators of the data acquisition of the deposited energy. Moreover, the measurement error correlates with the measurements from 7.3.5, confirming a slight downward deviation of the calibration.

The second center of gravity (COG-II), determined by the Gaussian fit, reflects a higher energy deposit, with values of 234.053 keV and 205.182 keV leading to 63775 and 55908 free electrons. This could possibly be an overlap of stuck particles and the mean energy loss of electrons with enough energy to pass through the sensors. In the work by Turkington, Gamage, and Graham [112], the second increase is attributed solely to yttrium betas. The average of the yttrium spectrum of 0.8 MeV would deposit an energy of 103.126 keV, leading to 28.65 ke, which is significantly lower than the measured peak. Therefore, it can be ruled out that the second peak consists solely of the deposited energy of the yttrium electrons.

The coincidence measurements depicted in Figure 7.57 clearly indicate the presence of stuck particles. In the synchronicity measurements, it is evident that for the sensor near the source, where the stuck electrons do not contribute to the distribution due to the absence of coincidence, there is only a slightly elevated Landau tail. Conversely, for the rear sensor, as observed in the asynchronous measurements in Figure 7.59, a distinctly slower decay is observed instead of a pure Landau tail.

Therefore, in addition to the distinct MIP peak, another increase in the distribution can be observed, which can be attributed to a combination of stuck electrons from the strontium decay and the mean deposited energy from the yttrium decay. It was also confirmed that the energy calibration of the ToASts is slightly shifted but still within the correct range.

Conclusion prototype under controlled conditions

The measurements of the MVD prototype under controlled conditions have shown that temperature has no measurable influence on the signal acquisition. Therefore, no temperature calibration is required for both intensity and energy deposition. The leakage current changed in a comprehensible manner for the temperatures tested. By comparing with the COSY beam times, it was demonstrated that the light-tightness significantly reduced the leakage current and the number of single events. Additionally, it was shown that the common noise measured during the beam times was not caused by the sensor or the readout but accurately represented events.

An analysis of the composite spectrum from ^{90}Sr and ^{90}Y revealed understandable energy depositions. Besides the MIP peak, a composite enhancement, caused by the overlap of the Yttrium peak and stuck electrons, was observed. This confirmed the suspicion from 7.3.5 that the energy calibration of the ToASts deviates slightly and is closer to 50 ns/fC.

Chapter 8

Summary

In the following sections, the contents of this work are briefly summarized based on the milestones, with detailed descriptions provided in the respective chapters.

Sensor Serial Tests

In this work, detailed quality analyses was conducted for all double-sided silicon strip sensors intended for integration into the MVD, as discussed in Chapter 5.4.1. Additionally, key sensor properties required for operation were identified. A total of 189 S1 sensors, exceeding the required 184, and 123 S2 sensors, exceeding the required 64, were successfully qualified for the MVD. This ensures that more sensors are available than needed for full assembly, providing additional units for backup and experimental use. Furthermore, several sensors, which narrowly missed the specified criteria, are still functional with minor limitations.
In addition to the series tests, several sensors were sample-wise characterized, with their functionality explained in detail based on their specific properties.

Radiation Hardness

In three campaigns, discussed in Chapter 5.5, $\overline{\text{P}}$ANDA MVD diodes were selected to represent the sensor wafers and exhibit similar properties, to investigate radiation damage. The diodes were irradiated with neutrons from an Americium-241/Beryllium source and with a proton beam at MIT. A total fluence of up to $1.121 \times 10^{12}\,n_{1\text{MeV,eq}}\,\text{cm}^{-2}$, was accumulated, which manifested effects on semiconductor structures in terms of leakage current and depletion voltage. These radiation-induced damages were compared with theoretical predictions and found to be within the expected range. Additionally, this allowed an estimation of the sensor lifetime, which falls within the $10^{14}\,n_{1\text{MeV,eq}}\,\text{cm}^{-2}$ range according to the$\overline{\text{P}}$ANDA MVD Technical Design Report [10]. The method of thermal annealing was applied, and its positive effects were verified.

Dosimeter

A dosimeter concept was developed based on MVD diodes as active sensor elements. In three iterations, amplification stages as well as a peak-detect stage were developed and tested. This allowed the detailed signal behavior of the sensors to be obtained. Dosimetry is conducted by counting the incoming radiation particles and their deposited energy. Finally, the dosimeter was adapted to the AmbaSat femto satellite concept to facilitate dosimetry in Low Earth Orbit in the future.

MVD-Prototype

For the first time, sensors were connected to the ToASt-ASIC specifically developed for the MVD. The wire bonding for contacting and fundamental functional tests were discussed. Overall, three fully functional sensor-ASIC combinations were implemented, with limitations imposed by the sensor board allowing only single-sided readout. Therefore, an S4 sensor was contacted for n-side readout and another for p-side readout to test both combinations. Additionally, an S3 sensor was contacted for p-side readout. These modules were then connected to the Data Acquisition System for the PANDA-MVD, resulting in the prototype.

MVD-Prototype Measurements

The system was tested during three beam times at the proton accelerator COSY in Jülich and in the laboratory using sources. During the beam times, the interaction of the components was successfully demonstrated for the first time. Basic functionality tests confirmed the operability of the system. Moreover, important parameters such as deposited energy, multiplicity, or event count were determined by varying prototype parameters or beam parameters. Particular attention was paid to coincident hits, which mimic a double-sided readout by the two single-sided readout sensors. Calibrations were also performed and compared with the actual deposited energy. The measurements proved to be reproducible and comprehensible, confirming good functionality of the prototype. Laboratory tests with a Sr-90 source demonstrated that the measurement results are not significantly dependent on temperature.

The insights gained will be incorporated into the second version of the ToASt-ASIC and into the development of a new sensor board. Improvements for the probe boards include double-sided readout of the detectors with multiple ToASts, a larger mounting area for sensors to accommodate S1 and S2 sensors, and the removal of LEDs for better light immunity.
For the ASIC itself, an automatic feature will be developed to handle missing or excessive headers or trailers. Version two will have the same layout as version one. The reference voltage will be generated via an internal band gap, which can be disabled. The layout will be enclosed. Additionally, the channel DAC threshold voltage resolution will be increased to 6 bits, which should allow for closer or even

within noise measurements without overloading the ToASt. This should enable measurements with lower thresholds to prevent signal clipping.
With this future prototype, full-size sensors will be operated in double-sided readout mode. This will allow setups to fully track particles and determine spatial resolution.

Bibliography

[1] K. J. Peters. (2023). Panda, [Online]. Available: https://www.gsi.de/en/work/research/pandahadrons/experiments/panda.

[2] FAIR. (2024). The accelerator facility. Accessed on March 04, 2024, [Online]. Available: https://fair-center.eu/overview/accelerator.

[3] P. Spiller, R. Balss, P. Bartolome, J. Blaurock, U. Blell, O. Boine-Frankenheim, L. Bozyk, M. Chorowski, T. Eisel, M. Frey, *et al.*, "The fair heavy ion synchrotron sis100," *Journal of Instrumentation*, vol. 15, no. 12, T12013, 2020.

[4] K. Knie, A. Dolinskii, B. Franzke, V. Gostishchev, M. Steck, and P. Sievers, "Concept for the antiproton production target at fair," *Proceedings of IPAC2012, New Orleans, USA*, 2012.

[5] R. Tölle, K. Bongardt, J. Dietrich, F. Esser, O. Felden, R. Greven, G. Hansen, F. Klehr, A. Lehrach, B. Lorentz, R. Maier, D. Prasuhn, A. Raccanelli, M. Schmitt, Y. Senichev, E. Senicheva, R. Stassen, H. Stockhorst, M. Steck, and F. Hinterberger, "Hesr at fair: Status of technical planning," Jul. 2007, pp. 1442–1444. DOI: 10.1109/PAC.2007.4440783.

[6] M. Fritsch. (2019). Panda webpage, hesr schematic overview. Accessed on March 04, 2024, [Online]. Available: https:%20//panda.gsi.de/system/files/user_uploads/m.fritsch/material/HESR_%20Jun2017_2017%5C%20Nov%5C%2009%5C_20190514180033.jpg.

[7] A. Lehrach, O. Boine-Frankenheim, F. Hinterberger, R. Maier, and D. Prasuhn, "Beam performance and luminosity limitations in the high-energy storage ring (hesr)," *Nuclear Instruments and Methods in Physics Research Section A: Accelerators, Spectrometers, Detectors and Associated Equipment*, vol. 561, no. 2, pp. 289–296, 2006, Proceedings of the Workshop on High Intensity Beam Dynamics, ISSN: 0168-9002. DOI: https://doi.org/10.1016/j.nima.2006.01.017. [Online]. Available: https://www.sciencedirect.com/science/article/pii/S0168900206000477.

[8] Group of Prof. Dr. A. Khoukaz. (2023). The panda experiment. Accessed on March 04, 2024, [Online]. Available: https://www.uni-muenster.de/Physik.KP/AGKhoukaz/en/pandagruppe.html.

[9] K.-T. Brinkmann and T. Stockmanns. (2012). The panda detector - mvd, [Online]. Available: https://panda.gsi.de/oldwww/framework/det_iframe.php?section=MVD.

[10] W. Erni, I. Keshelashvili, B. Krusche, M. Steinacher, Y. Heng, Z.-A. Liu, H. Liu, X. Shen, Q. Wang, H. Xu, M. Albrecht, J. Becker, K. Eickel, F. Feldbauer, M. Fink, P. Friedel, F. Heinsius, T. Held, H. Koch, and J. Zmeskal, "Technical design report for the: Panda micro vertex detector," Jan. 2012. DOI: 10.15161/oar.it/1446204374.75.

[11] W. Erni, I. Keshelashvili, B. Krusche, M. Steinacher, Y. Heng, Z. Liu, H. Liu, X. Shen, O. Wang, H. Xu, *et al.*, "Physics performance report for panda: Strong interaction studies with antiprotons," *arXiv preprint arXiv:0903.3905*, 2009.

[12] A. Khoukaz, "Internal targets for the panda experiment," *PoS, vol. STORI11*, p. 036, 2011.

[13] PANDA Collaboration. (2012). Technical design report for the panda internal targets. Accessed on March 05, 2024, [Online]. Available: https://panda.gsi.de/system/files/user_uploads/u.kurilla/RE-TDR-2012-002.pdf.

[14] Group of Prof. Dr. A. Khoukaz. (2023). The cluster-jet target. Accessed on March 08, 2024, [Online]. Available: https://www.uni-muenster.de/Physik.KP/AGKhoukaz/en/clustertargetgroup.html.

[15] PANDA Collaboration. (2018). Target and beamline. Accessed on March 05, 2024, [Online]. Available: https://panda.gsi.de/article/target-and-beamline.

[16] P. Gianotti, V. Lucherini, E. Pace, H. Kozlov, H. Ohm, S. Orfanitski, M. Mertens, J. Ritman, M. Roeder, V. Wintz, M. Idzik, D. Przyborowski, S. Jowzaee, M. Kajanowicz, G. Korcyl, P. Salabura, J. Smyrski, P. Kulessa, K. Pysz, and A. Kashchuk, "Tracking with straw tubes in the panda experiment," vol. 66, Oct. 2011, ISBN: 978-981-4405-06-5. DOI: 10.1051/epjconf/20146611007.

[17] W. Andersson, A. Akram, T. Johansson, R. Kliemt, M. Papenbrock, J. Regina, K. Schoenning, and T. Stockmanns, "A generalized approach to longitudinal momentum determination in cylindrical straw tube detectors," *Computing and Software for Big Science*, vol. 5, Dec. 2021. DOI: 10.1007/s41781-021-00064-0.

[18] PANDA Collaboration. (2018). Straw tube tracker. Accessed on March 14, 2024, [Online]. Available: https://panda.gsi.de/article/straw-tube-tracker.

[19] B. Ratcliff and J. Va'vra, "Dirc: Internally reflecting imaging cherenkov detectors," *Nuclear Instruments and Methods in Physics Research Section A: Accelerators, Spectrometers, Detectors and Associated Equipment*, vol. 970, p. 163 442, 2020, A RICH LEGACY, ISSN: 0168-9002. DOI: https://doi.org/10.1016/j.nima.2020.163442. [Online]. Available: https://www.sciencedirect.com/science/article/pii/S0168900220300401.

[20] A. Belias, "Overview of the panda detector design at fair," *Int. J. Mod. Phys. Conf. Ser.*, vol. 51, 2023. DOI: 10.1142/S2010194523600017.

[21] W. Erni, I. Keshelashvili, B. Krusche, M. Steinacher, Y. Heng, Z.-A. Liu, H. Liu, X. Shen, O. Wang, H. Xu, J. Becker, F. Feldbauer, F. Heinsius, T. Held, H. Koch, B. Kopf, M. Pelizaeus, T. Schroeder, M. Steinke, and J. Zmeskal, "Technical design report for panda electromagnetic calorimeter (emc)," Oct. 2008. DOI: 10.15161/oar.it/1446204388.53.

[22] S. Alef, P. Bauer, D. Bayadilov, R. Beck, M. Becker, A. Bella, J. Bieling, S. Böse, A. Braghieri, K.-T. Brinkmann, P. Cole, R. Di Salvo, D. Elsner, A. Fantini, O. Freyermuth, F. Frommberger, G. Gervino, F. Ghio, S. Goertz, and T. Zimmermann, "The bgood experimental setup at elsa," *The European Physical Journal A*, vol. 56, Apr. 2020. DOI: 10.1140/epja/s10050-020-00107-x.

[23] K. Koop, "Nachweis von vorwärtsgestreuten protonen in photoninduzierten reaktionen am nukleon," PhD thesis, Rheinische Friedrich-Wilhelms-Universitat Bonn, Mar. 2015. [Online]. Available: https://hdl.handle.net/20.500.11811/6441.

[24] F. Frommberger. (2013). Electron accelerator elsa. Accessed on May 16, 2024, [Online]. Available: https://www-elsa.physik.uni-bonn.de/elsa_en.html.

[25] T. Jude, S. Alef, R. Beck, A. Braghieri, P. Cole, D. Elsner, R. D. Salvo, A. Fantini, O. Freyermuth, F. Frommberger, F. Ghio, A. Gridnev, K. Kohl, N. Kozlenko, A. Lapik, P. L. Sandri, V. Lisin, G. Mandaglio, D. Moricciani, V. Nedorezov, D. Novinskiy, P. Pedroni, A. Polonskiy, B.-E. Reitz, M. Romaniuk, G. Scheluchin, H. Schmieden, A. Stuglev, V. Sumachev, and V. Tarakanov, "Evidence of a dibaryon spectrum in coherent $\pi^0\pi^0 d$ photoproduction at forward deuteron angles," *Physics Letters B*, vol. 832, p. 137 277, 2022, ISSN: 0370-2693. DOI: 10.1016/j.physletb.2022.137277. [Online]. Available: https://www.sciencedirect.com/science/article/pii/S0370269322004117.

[26] G. Scheluchin, T. Jude, S. Alef, P. Bauer, D. Bayadilov, R. Beck, A. Braghieri, P. Cole, D. Elsner, R. Di Salvo, A. Fantini, O. Freyermuth, F. Frommberger, F. Ghio, A. Gridnev, D. Hammann, J. Hannappel, K. Kohl, N. Kozlenko, A. Lapik, P. Levi Sandri, V. Lisin, G. Mandaglio, R. Messi, D. Moricciani, A. Mushkarenkov, V. Nedorezov, D. Novinskiy, P. Pedroni, A. Polonskiy, B.-E. Reitz, M. Romaniuk, H. Schmieden, V. Sumachev, and V. Tarakanov, "Photoproduction of $K^+\Lambda(1405) \to K^+\pi^0\Sigma^0$ extending to forward angles and low momentum transfer," *Physics Letters B*, vol. 833, p. 137 375, 2022, ISSN: 0370-2693. DOI: 10.1016/j.physletb.2022.137375. [Online]. Available: https://www.sciencedirect.com/science/article/pii/S0370269322005093.

[27] K. Kohl, T. Jude, S. Alef, R. Beck, A. Braghieri, P. Cole, D. Elsner, R. Salvo, A. Fantini, O. Freyermuth, F. Frommberger, F. Ghio, A. Gridnev, D. Hammann, J. Hannappel, N. Kozlenko, A. Lapik, P. Levi Sandri, V. Lisin, and V. Tarakanov, "Measurement of the $\gamma n \to K^0\Sigma^0$ differential cross section over the K^* threshold," *The European Physical Journal A*, vol. 59, Nov. 2023. DOI: 10.1140/epja/s10050-023-01133-1.

[28] S. Alef, P. Bauer, D. Bayadilov, R. Beck, M. Becker, A. Bella, J. Bieling, S. Böse, A. Braghieri, K.-T. Brinkmann, *et al.*, "The bgood experimental setup at elsa," *The European Physical Journal A*, vol. 56, pp. 1–27, 2020.

[29] O. Bartalini, V. Bellini, J. Bocquet, M. Capogni, L. Casano, M. Castoldi, P. Calvat, A. D'Angelo, R. Di Salvo, A. Fantini, C. Gaulard, G. Gervino, F. Ghio, B. Girolami, A. Giusa, V. Kouznetsov, A. Lapik, P. Levi Sandri, A. Lleres, and A. Turinge, "Measurement of pi photoproduction on the proton from 550 to 1500 mev at graal," *European Physical Journal A*, vol. 26, pp. 399–419, Jan. 2005. DOI: 10.1140/epja/i2005-10191-2.

[30] B. Bantes, D. Bayadilov, R. Beck, M. Becker, A. Bella, P. Bielefeldt, J. Bieling, M. Bleckwenn, S. Böse, A. Braghieri, K.-T. Brinkmann, D. Burdeynyi, F. Curciarello, V. De Leo, R. Di Salvo, H. Dutz, D. Elsner, A. Fantini, O. Freyermuth, and T. Zimmermann, "The bgo calorimeter of bgo-od experiment," *Journal of Physics: Conference Series*, vol. 587, Feb. 2015. DOI: 10.1088/1742-6596/587/1/012042.

[31] C. Wendel, forthe CBELSA/TAPS Collaboration, *et al.*, "The crystal-barrel/taps experiment at elsa current status of the csi (tl) calorimeters," in *Journal of Physics: Conference Series*, IOP Publishing, vol. 160, 2009, p. 012 006.

[32] B. Krusche, "Baryon spectroscopy at elsa and at mami - selected results," *EPJ Web of Conferences*, vol. 72, p. 00 012, May 2014. DOI: 10.1051/epjconf/20147200012.

[33] J. Taylor, C. Waltham, T. Price, N. Allinson, P. Allport, G. Casse, A. Kacperek, S. Manger, N. Smith, and I. Tsurin, "A new silicon tracker for proton imaging and dosimetry," *Nuclear Instruments and Methods in Physics Research Section A: Accelerators, Spectrometers, Detectors and Associated Equipment*, vol. 831, Feb. 2016. DOI: 10.1016/j.nima.2016.02.013.

[34] E. Debrot, M. Newall, S. Guatelli, M. Petasecca, N. Matsufuji, and A. B. Rosenfeld, "A silicon strip detector array for energy verification and quality assurance in heavy ion therapy," *Medical Physics*, vol. 45, no. 2, pp. 953–962, 2018. DOI: https://doi.org/10.1002/mp.12736. eprint: https://aapm.onlinelibrary.wiley.com/doi/pdf/10.1002/mp.12736. [Online]. Available: https://aapm.onlinelibrary.wiley.com/doi/abs/10.1002/mp.12736.

[35] A. Mai. (2019). Panda micro-vertex-detector, [Online]. Available: https://panda-wiki.gsi.de/Mvd/MvdPublic.

[36] G. Lutz *et al.*, *Semiconductor radiation detectors*. Springer, 2007.

[37] M. Kesselkaul, "Untersuchung des einflusses der η-funktion auf die ortsauflösung von si-streifen-detektoren unter verwendung einer automatisierten, örtlich hoch-aufgelösten infrarot-laser-teststation," 2021.

[38] H.-G. Zaunick, "Developments toward a silicon strip tracker for the panda experiment," PhD thesis, Rheinische Friedrich-Wilhelms-Universität Bonn, 2013. [Online]. Available: https://hdl.handle.net/20.500.11811/5668.

[39] Particle Data Group, "Review of particle physics," *Progress of Theoretical and Experimental Physics*, no. 8, 2022, ISSN: 2050-3911. DOI: 10.1093/ptep/ptac097.

[40] A. Ereditao. (2016). Quarks, gluons and strong interaction (qcd). Lecture held as part of the course "Elementarteilchenphysik" at LHEP University of Bern, [Online]. Available: https://www.unibe.ch/unibe/portal/fak_naturwis/b_paw/a_fphyast/content/e41821/e41822/e140946/e148845/e270411/files424471/File7_ger.pdf.

[41] Alice Collaboration and Garibli, A., "Unveiling the strong interaction among hadrons at the lhc," *Nature*, vol. 588, no. 7837, pp. 232–238, 2020.

[42] R. Pohl, A. Antognini, F. Nez, F. D. Amaro, F. Biraben, J. M. Cardoso, D. S. Covita, A. Dax, S. Dhawan, L. M. Fernandes, *et al.*, "The size of the proton," *nature*, vol. 466, no. 7303, pp. 213–216, 2010.

[43] D. Griffiths, *Introduction to elementary particles*. John Wiley & Sons, 2020.

[44] S. Bethke, "Qcd studies at lep," *Physics Reports*, vol. 403–404, 2004, ISSN: 0370-1573. DOI: 10.1016/j.physrep.2004.08.014. [Online]. Available: http://dx.doi.org/10.1016/j.physrep.2004.08.014.

[45] R. L. Workman *et al.*, "Review of Particle Physics," *PTEP*, vol. 2022, p. 083C01, 2022. DOI: 10.1093/ptep/ptac097.

[46] W. Ochs, "The status of glueballs," *Journal of Physics G: Nuclear and Particle Physics*, vol. 40, no. 4, p. 043 001, 2013.

[47] K. N. K. S.M. Sze, "Physics and properties of semiconductors—a review," in *Physics of Semiconductor Devices*. John Wiley & Sons, Ltd, 2006, pp. 5–75, ISBN: 9780470068328. DOI: https://doi.org/10.1002/9780470068328.ch1. eprint: https://onlinelibrary.wiley.com/doi/pdf/10.1002/9780470068328.ch1. [Online]. Available: https://onlinelibrary.wiley.com/doi/abs/10.1002/9780470068328.ch1.

[48] P. Basnet, "Metal oxide photocatalytic nanostructures fabricated by dynamic shadowing growth," PhD thesis, Apr. 2015. DOI: 10.13140/RG.2.1.2393.8408.

[49] E. Riedle. (2017). Grundlagen der halbleiterphysik. Lecture held at the University LMU Munich in 3. 11. 2017, [Online]. Available: http://www.bmo.physik.uni-muenchen.de/~riedle/Elektronik_I/KW045/HalbleiterTeil1.pdf.

[50] S. Morab, M. Minakshi, and A. Pivrikas, "Review on charge carrier transport in inorganic and organic semiconductors," *Coatings*, vol. 13, p. 1657, Sep. 2023. DOI: 10.3390/coatings13091657.

[51] N. Servagent. (2008). Fundamentals of semiconductor physics. Accessed on February 13, 2024, [Online]. Available: http://www.optique-ingenieur.org/en/courses/OPI_ang_M05_C02/co/Contenu_04.html.

[52] R. Beal, J. Dubowski, and V. Aimez, "Laser induced quantum well intermixing: Reproducibility study and fabrication of superluminescent diodes, beal romain phd 2015," PhD thesis, Jul. 2015.

[53] W. H. Strehlow and E. L. Cook, "Compilation of Energy Band Gaps in Elemental and Binary Compound Semiconductors and Insulators," *Journal of Physical and Chemical Reference Data*, vol. 2, no. 1, pp. 163–200, Jan. 1973, ISSN: 0047-2689. DOI: 10.1063/1.3253115. eprint: https://pubs.aip.org/aip/jpr/article-pdf/2/1/163/19223180/163_1_online.pdf. [Online]. Available: https://doi.org/10.1063/1.3253115.

[54] C. Nave. (2017). Fundamentals of semiconductor physics. Accessed on March 21, 2024, [Online]. Available: http://hyperphysics.phy-astr.gsu.edu/hbase/Solids/dope.html#c3.

[55] A. Abadi, "Material properties," Accessed on April 14, 2024. [Online]. Available: https://www.uotechnology.edu.iq/appsciences/filesPDF/material/lectures/2c/3-Materials_prperties6.pdf.

[56] T. Bergauer. (2017). Silicon detectors in high energy physics. Lecture held at HEPHY Vienna in 2017, [Online]. Available: https://www.oeaw.ac.at/fileadmin/Institute/HEPHY/PDF/ausbildung/teilchendetektoren/VO-4-2018-SemiconductorDetectors.pdf.

[57] H. Bethe, J. Ashkin, and I. I953, "Passage of radiations through matter. exp," *Nucl. Phys. I*, p. 166,

[58] H. Bethe and W. Heitler, "On the stopping of fast particles and on the creation of positive electrons," *Proceedings of the Royal Society of London. Series A, Containing Papers of a Mathematical and Physical Character*, vol. 146, no. 856, pp. 83–112, 1934.

[59] F. Bloch, "Zur Bremsung Rasch Bewegter Teilchen beim Durchgang durch Materie," *Annalen Phys.*, vol. 408, pp. 285–320, 1933. DOI: 10.1002/andp.19334080303.

[60] National Institute of Standards and Technology, "Estar : Stopping power and range tables for electrons," U.S. Department of Commerce, Washington, D.C., Tech. Rep. [Online]. Available: https://physics.nist.gov/cgi-bin/Star/e_table.pl (visited on 12/30/2023).

[61] L. D. Landau, "On the energy loss of fast particles by ionization," *J. Phys.*, vol. 8, no. 4, pp. 201–205, 1944. [Online]. Available: https://cds.cern.ch/record/216256.

[62] C. Niebuhr, *Beispiele von de/dx kurven*, DESY Lecture. [Online]. Available: https://www.desy.de/~niebuhr/Vorlesung/Hannover/Vorlesung5.pdf.

[63] S. Meroli, *The landau distribution for ionizing particles*, CERN Lecture. [Online]. Available: https://meroli.web.cern.ch/lecture_landau_ionizing_particle.html.

[64] L. Rossi, *Pixel detectors: From fundamentals to applications*. Springer Science & Business Media, 2006.

[65] J. Baudot *et al.*, "In-Beam Test of Double-Sided Silicon Strip Detector," 2000.

[66] I. Kopsalis, P. Allport, E. Bach, A. Bhardwaj, A. Chisholm, V. Cindro, V. Fadeyev, P. Federicova, J. Fernandez-Tejero, C. Fleta, *et al.*, "Establishing the quality assurance programme for the strip sensor production of the atlas tracker upgrade including irradiation with neutrons, photons and protons to hl-lhc fluences," *Journal of Instrumentation*, vol. 18, no. 05, p. C05009, 2023.

[67] D.-L. Pohl and C. Bespin. (2022). Pylandau. Accessed on February 13, 2024, [Online]. Available: https://github.com/SiLab-Bonn/pylandau/blob/master/README.md.

[68] K. Kölbig and B. Schorr, "A program package for the landau distribution," *Computer Physics Communications*, vol. 31, no. 1, pp. 97–111, 1984, ISSN: 0010-4655. DOI: https://doi.org/10.1016/0010-4655(84)90085-7. [Online]. Available: https://www.sciencedirect.com/science/article/pii/0010465584900857.

[69] M. Moll, "Radiation damage in silicon particle detectors. microscopic defects and macroscopic properties," 1999.

[70] D. Andrew, R. Roshan, and O. Dawson. (2018). Difference between point defect and line defect, [Online]. Available: https://www.differencebetween.com/difference-between-point-defect-and-line-defect/ (visited on 04/12/2024).

[71] V. A. Van Lint, T. M. Flanagan, R. E. Leadon, and J. A. Naber, "Mechanisms of radiation effects in electronic materials. vol. 1," Jan. 1980. [Online]. Available: https://www.osti.gov/biblio/6854931.

[72] M. Moll, "Radiation damage in silicon particle detectors: Microscopic defects and macroscopic properties," PhD thesis, Hamburg U., 2018.

[73] F. Ravotti, L. Dusseau, M. Moll, and E. Tsesmelis, "Development and characterisation of radiation monitoring sensors for the high energy physics experiments of the cern lhc accelerator," Jan. 2006.

[74] A. Ruzin, "Recent results from the rd48 (rose) collaboration," *Nuclear Instruments and Methods in Physics Research Section Accelerators Spectrometers Detectors and Associated Equipment - NUCL INSTRUM METH PHYS RES A*, vol. 447, Jun. 2000. DOI: 10.1016/S0168-9002(00)00179-0.

[75] R. Wunstorf, "A systematic investigation of the radiation hardness of silicon detectors for high-energy physics experiments," Other thesis, Oct. 1992.

[76] National Institute of Standards and Technology, "Standardization of 90sr (srm 4329a)," U.S. Department of Commerce, Washington, D.C., Tech. Rep., 2022. [Online]. Available: https://www.nist.gov/pml/radiation%5C-physics/standartization%5C-90sr%5C-srm%5C-4329a.

[77] J. Dixon, A. Rajan, S. Bohlemann, D. Coso, A. D. Upadhyaya, A. Rohatgi, S. Chu, A. Majumdar, and S. Yee, "Evaluation of a silicon 90sr betavoltaic power source," *Scientific reports*, vol. 6, no. 1, p. 38 182, 2016.

[78] M. Birlea, "A power saving protocol for impedance spectroscopy," vol. 1917, Sep. 2017. DOI: 10.1063/1.5018276.

[79] S. Masciocchi. (2017). Semiconductor detectors - 3. Lecture held at University of Heidelberg in 2017, [Online]. Available: https://www.physi.uni-heidelberg.de/~sma/teaching/ParticleDetectors2/sma_Semiconductors_3.pdf.

[80] D. Campbell, A. Chilingarov, and T. Sloan, "Frequency and temperature dependence of the depletion voltage from cv measurements for irradiated si detectors," *Nuclear Instruments & Methods in Physics Research Section A-accelerators Spectrometers Detectors and Associated Equipment - NUCL INSTRUM METH PHYS RES A*, vol. 492, pp. 402–410, Oct. 2002. DOI: 10.1016/S0168-9002(02)01353-0.

[81] J.-J. Wei, J.-H. Guo, and Y.-M. Hu, "Characterization of silicon microstrip sensors for space astronomy," *Nuclear Science and Techniques*, vol. 31, no. 10, 2020, ISSN: 2210-3147. DOI: 10.1007/s41365-020-00811-9. [Online]. Available: http://dx.doi.org/10.1007/s41365-020-00811-9.

[82] M. Frautschi, M. Hoeferkamp, and S. Seidel, "Capacitance measurements of double-sided silicon microstrip detectors," *Nuclear Instruments and Methods in Physics Research Section A: Accelerators, Spectrometers, Detectors and Associated Equipment*, vol. 378, pp. 284–296, Aug. 1996. DOI: 10.1016/0168-9002(96)00467-6.

[83] E. Riedle. (2015). Silicon detectors lecture 2. Lecture held at the 5th Egytpian School on High Energy Physics in November 2015, [Online]. Available: https://indico.cern.ch/event/453690/sessions/99350/attachments/1184199/1726998/2015-11_SiliconDetectors_manzari_Lecture2.pdf.

[84] M. Frautschi, M. Hoeferkamp, and S. Seidel, "Capacitance measurements of double-sided silicon microstrip detectors," *Nuclear Instruments and Methods in Physics Research Section A: Accelerators, Spectrometers, Detectors and Associated Equipment*, vol. 378, pp. 284–296, Aug. 1996. DOI: 10.1016/0168-9002(96)00467-6.

[85] Marburg Ion Beam Therapy Center. (2023). Technische details, [Online]. Available: https://www.mit-marburg.de/fuer-forscher/technische-details.html (visited on 12/27/2023).

[86] G. P. Summers, E. A. Burke, P. Shapiro, S. R. Messenger, and R. Walters, "Damage correlations in semiconductors exposed to gamma, electron and proton radiations," *IEEE Transactions on Nuclear Science*, vol. 40, pp. 1372–1379, 1993. [Online]. Available: https://api.semanticscholar.org/.

[87] M. Huhtinen and P. Aarnio, "Pion induced displacement damage in silicon devices," *Nuclear Instruments and Methods in Physics Research Section A: Accelerators, Spectrometers, Detectors and Associated Equipment*, vol. 335, no. 3, pp. 580–582, 1993.

[88] B. Dezillie, Z. Li, V. Eremin, M. Bruzzi, S. Pirollo, S. Pandey, and C. Li, "Improved neutron radiation hardness for si detectors: Application of low resistivity starting material and/or manipulation of n/sub eff/ by selective filling of radiation-induced traps at low temperatures," *IEEE Transactions on Nuclear Science*, vol. 46, no. 3, pp. 221–227, 1999. DOI: 10.1109/23.775518.

[89] Z. Li and H. Kraner, "Modeling and simulation of charge collection properties for neutron irradiated silicon detectors," *Nuclear Physics B - Proceedings Supplements*, vol. 32, pp. 398–409, 1993, ISSN: 0920-5632. DOI: 10.1016/0920-5632(93)90052-8. [Online]. Available: https://www.sciencedirect.com/science/article/pii/0920563293900528.

[90] Z. Li, "Radiation damage effects in si materials and detectors and rad-hard si detectors for slhc," *Journal of Instrumentation*, vol. 4, no. 03, P03011, Mar. 2009. DOI: 10.1088/1748-0221/4/03/P03011. [Online]. Available: https://dx.doi.org/10.1088/1748-0221/4/03/P03011.

[91] M. K. Kazimierczuk, *Pulse-Width Modulated DC–DC Power Converters, Second Edition*. John Wiley & Sons, 2016, p. 915. DOI: 10.1002. [Online]. Available: https://onlinelibrary.wiley.com/doi/pdf/10.1002/9781119009597.app3.

[92] M. Krammer. (2011). Silicon detectors. Lecture held as part of the course "Silicon strips and pixels technologies - part 1" at CERN, [Online]. Available: https://indico.cern.ch/event/124392/contributions/1339904/attachments/74582/106976/IntroSilicon.pdf.

[93] AmbaSat Ltd. (2023). Ambasat homepage, [Online]. Available: https://ambasat.com/satellite/ (visited on 12/27/2023).

[94] AmbaSat Ltd. (2024). The things network homepage, [Online]. Available: https://www.thethingsnetwork.org (visited on 01/07/2024).

[95] J. Steininger, M. Bibl, H. Yoo, and G. Schitter, "High bandwidth deflection readout for atomic force microscopes," *Review of Scientific Instruments*, vol. 86, p. 103 701, Oct. 2015. DOI: 10.1063/1.4932188.

[96] C. Newcombe. (2024). Was ist die beziehung zwischen oszilloskopbandbreite und wellenformanstiegszeit? [Online]. Available: https://www.fluke.com/de-de/mehr-erfahren/blog/oszilloskope/was-ist-die-beziehung-zwischen-oszilloskopbandbreite-und-wellenformanstiegszeit (visited on 04/14/2024).

[97] Texas Instruments. (2018). Opax354: 250-mhz, rail-to-rail i/o, cmos operational amplifiers, [Online]. Available: https://www.ti.com/lit/ds/symlink/opa354.pdf?ts=1703863682634&ref_url=https%3A%2F%2Fwww.ti.com%2Fproduct%2Fde-de%2FOPA354 (visited on 12/29/2023).

[98] M. Kákona, J. Šlegl, D. Kyselová, M. Sommer, J. Kákona, M. Lužová, V. Štěpán, O. Ploc, S. Kodaira, J. Chroust, *et al.*, "Airdos—open-source pin diode airborne dosimeter," *Journal of Instrumentation*, vol. 16, no. 03, T03006, 2021.

[99] ATMEL. (2015). Atmega328 datasheet, [Online]. Available: https://ww1.microchip.com/downloads/en/DeviceDoc/Atmel-7810-Automotive-Microcontrollers-ATmega328P_Datasheet.pdf (visited on 01/02/2024).

[100] Espressif Systems. (2024). Esp32 series, [Online]. Available: https://www.espressif.com/sites/default/files/documentation/esp32_datasheet_en.pdf (visited on 01/05/2024).

[101] National Aeronautics and Space Administration. (1999). Space radiation effects on electronic components in low-earth orbit, [Online]. Available: https://llis.nasa.gov/lesson/824.

[102] G. Mazza, D. Calvo, F. Cossio, P. D. Remigis, M. Mignone, R. Wheadon, L. Silvestrin, M. Tessaro, and on behalf of the PANDA MVD collaboration, "A 64 channels asic for the readout of the silicon strip detectors of the panda micro-vertex detector," *Journal of Instrumentation*, vol. 18, no. 01, p. C01020, 2023. DOI: 10.1088/1748-0221/18/01/C01020. [Online]. Available: https://dx.doi.org/10.1088/1748-0221/18/01/C01020.

[103] G. Mazza, "Toast: Torino amplifier for strip detectors," COMPASS DAQFEET 2019, 2019, [Online]. Available: https://indico.cern.ch/event/783347/contributions/3313412/attachments/1794102/2923816/ToASt_slides_2019.02.11.pdf.

[104] O. Manzhura, M. Caselle, L. Ardila-Perez, D. Calvo, S. Chilingaryan, F. Cossio, T. Dritschler, A. Kopmann, F. Lenta, G. Mazza, M. Peter, V. Sidorenko, P. Staněk, T. Stockmanns, L. Tomášek, N. Tröll, K. Unger, H.-G. Zaunick, J. Becker, and K.-T. Brinkmann, "The data acquisition system for the panda micro-vertex detector," *Journal of Instrumentation*, vol. 19, no. 03, p. C03036, Mar. 2024. DOI: 10.1088/1748-0221/19/03/C03036. [Online]. Available: https://dx.doi.org/10.1088/1748-0221/19/03/C03036.

[105] lpGBT design team. (2022). Lpgbt documentation, [Online]. Available: https://cds.cern.ch/record/2809058/files/lpGBT_manual.pdf.

[106] M. Caselle, L. A. Perez, M. Balzer, T. Dritschler, A. Kopmann, H. Mohr, L. Rota, M. Vogelgesang, and M. Weber, "A high-speed daq framework for future high-level trigger and event building clusters," *Journal of Instrumentation*, vol. 12, no. 03, p. C03015, Mar. 2017. DOI: 10.1088/1748-0221/12/03/C03015. [Online]. Available: https://dx.doi.org/10.1088/1748-0221/12/03/C03015.

[107] M. Peter, *Status of the readout system for the micro-vertex-detector of the panda experiment*, Talk presented at SMuK 2023 22.03.2023, Dresden, 2023. [Online]. Available: https://www.dpg-verhandlungen.de/year/2023/conference/smuk/part/hk/session/26/contribution/1.

[108] P. Schleper, *Strip detectors*, DESY Lecture, 2018. [Online]. Available: https://www.desy.de/~schleper/lehre/Det_Dat/SS_2018/03-lecture_Silicon.23-end.pdf.

[109] D. Prasuhn, U. Bechstedt, J. Dietrich, R. Gebel, K. Henn, B. Lorentz, R. Maier, A. Schnase, H. Schneider, R. Stassen, H. Stockhorst, and R. Toelle, "Status of the cooler synchrotron cosy juelich," vol. 5, Feb. 2001, 3350–3352 vol.5, ISBN: 0-7803-7191-7. DOI: 10.1109/PAC.2001.988107.

[110] S. Bianco, "Tracking and vertex reconstruction with the panda micro-vertex-detector," PhD thesis, Bonn, Rheinische Friedrich-Wilhelms-Universität Bonn, Diss., 2013, 2013.

[111] M. Wiehe, "The effective bandgap and current related damage rate of highly irradiated silicon sensors," 27th RD50 Workshop (CERN), 2015, [Online]. Available: https://indico.cern.ch/event/456679/contributions/1126343/.

[112] G. Turkington, K. A. Gamage, and J. Graham, "Beta detection of strontium-90 and the potential for direct in situ beta detection for nuclear decommissioning applications," *Nuclear Instruments and Methods in Physics Research Section A: Accelerators, Spectrometers, Detectors and Associated Equipment*, vol. 911, pp. 55–65, 2018, ISSN: 0168-9002. DOI: https://doi.org/10.1016/j.nima.2018.09.101. [Online]. Available: https://www.sciencedirect.com/science/article/pii/S0168900218312543.

List of Tables

4.1 Overview of the elementary bosons (gauge bosons and the Higgs boson) and their properties within the standard model of particle physics [39]. 28

4.2 Overview of the properties and probable decay channels of some of the best known hadrons [39]. 29

5.1 Capacitances of the $\overline{\text{P}}$ANDA double-sided silicon strip sensors at full depletion, calculated and measured. 73
5.2 Leakage currents of the $\overline{\text{P}}$ANDA sensors at complete depletion, measured for full sensors and divided by the number of strips for strip leakage currents. 76
5.3 Table of lots showing the voltage, leakage current, and capacitance at full depletion, along with the corresponding deviations, as well as the number of sensors S1 and S2. * Lot includes only one wafer, therefore no deviation is measurable. ** No diodes were delivered from CiS; checks were performed by CiS, which did not include measurements of Dep. Current and Dep. Capacitance. 87
5.4 Radiation exposure from neutron irradiation on diodes from different wafers of the MVD lot 352157. 90
5.5 Changes in the properties of silicon diodes after 3795 hours of neutron irradiation with the exp. fluence calculated with the change in the leakage current. 93
5.6 Bonded diode properties before exposure to the neutron source for 3600 hours. 94
5.7 Changes in main properties of the diode # 5 before and after 3600 hours of radiation exposure. 95
5.8 Changes of the $\overline{\text{P}}$ANDA diodes properties after irradiation with protons. 97
5.9 Changes of the $\overline{\text{P}}$ANDA diodes properties after irradiation with protons in MIT Beam Time II. 99
5.10 Changes in $\overline{\text{P}}$ANDA diode properties at full depletion after irradiation with protons and after additional thermal annealing. 105

6.1 $R_F = 1\,\text{M}\Omega$ 113
6.2 $\text{R}_\text{F} = 10\,\text{M}\Omega$ 113
6.3 Measurements of ^{90}Sr signals after the three amplification stages for various reverse bias voltages. 119

7.1 Characteristics and possibilities of the ToASt. 129
7.2 Change in deposited energy for T01 with the different incidence angles of the proton beam. 162

A.1 Result of series measurements for lot 341776. 216
A.2 Result of series measurements for lot 352156. 216
A.3 Result of series measurements for lot 352155. 217
A.4 Result of series measurements for lot 352154. 217
A.5 Result of serial measurements for lot 342563. 217
A.6 Result of series measurements for lot 352157. 218

A.7 Result of serial measurements for lot 341775. 218
A.8 Result of serial measurements for lot 341774. 218
A.9 Result of serial measurements for lot 341773. 219
A.10 Result of serial measurements for lot 341772. 219
A.11 Result of series measurements for lot 413017. 219
A.12 Result of series measurements for lot 413018. 220
A.13 Result of series measurements for lot 413019. 220
A.14 Result of series measurements for lot 410535, which includes only one wafer. 220
A.15 Result of series measurements for lot 410536. 221
A.16 Result of series measurements for lot 410537. 221

List of Figures

2.1 A schematic cross-section of the $\overline{\text{P}}$ANDA experiment with all subsystems highlighted [1]. 9
2.2 The FAIR accelerator facility in red with the existing GSI facility in blue [2]. 10
2.3 Schematic overview of the High Energy Storage Ring (HESR) at FAIR [6]. 11
2.4 Hadrons which can be produced in the $\overline{\text{P}}$ANDA experiment by proton antiproton annihilation [8]. 12
2.5 Sketch of the cluster-jet target production[14]. 15
2.6 The $\overline{\text{P}}$ANDA Straw Tube Tracker is depicted on the left, with its operation principle outlined on the right [17],[18]. 16
2.7 Schematic layout of the Barrel DIRC (a) and Endcap Disc DIRC (b) [19]. 18
2.8 Schematic layout of the Barrel EMC in blue and the Backward Endcap EMC in green [21]. 19

3.1 Schematic overview of the ELSA facility [24]. 21
3.2 Schematic slice view of the BGO Ball Experiment [28]. 22
3.3 Schematic overview of the Crystal Ball/TAPS experiment [32]. . . . 22

4.1 Basic layout of the MVD barrel with the pixel and strip detector parts [9]. 24
4.2 Schematic layout of the silicon strip sensors in the barrel part of the MVD from the side (left), from the front (middle), and the sensor arrangement of the strip disc (right) [35]. 25

4.3 Schematic representation of the silicon strip sensors along with the readout chips. 26
4.4 Illustration of two simultaneously measured particles in red and the resulting "fake" hits in green. 27
4.5 Fermi-Dirac distribution function for different temperatures T_1>T_2>T_3>T_0=0 K [48]. 31
4.6 Schematic representation of the band diagram for a conductor (a), a semiconductor (b), and an insulator (c) [49]. 32
4.7 Illustration of band, energy, occupation probability, Fermi function, and charge carrier density of an intrinsic semiconductor [51] 33
4.8 Schematic energy band diagram for a direct semiconductor with InP as an example on the left, and for an indirect semiconductor with Si as an example on the right [52]. 33
4.9 Illustration of band structure, energy levels, occupation probability, Fermi function, and charge carrier density in an extrinsic semiconductor [51]. 34
4.10 Schematic diagrams illustrating n-type and p-type doping of silicon with antimony and boron, respectively [54]. 35
4.11 The electron concentration is plotted against temperature in Kelvin for doped silicon in green and intrinsic silicon in red [55]. 36
4.12 Diagram showing the effects of donation on the Fermi levels in silicon within the band model [56]. 37
4.13 Schematic depicting energy levels and resulting diffusion in the pn-junction [56]. 38
4.14 The I-V (current vs. voltage) characteristics of a p-n junction diode with the operating range for a silicon detector indicated [56]. 40
4.15 Illustration of the schematic enlargement of the depletion region in a diode while increasing the reverse bias voltage. 41
4.16 Specific energy loss rate for muons, pions and protons corresponding to different absorber materials [45]. 42
4.17 Total stopping power for electrons in silicon [60]. 43
4.18 A schematic illustrates a silicon lattice after particle collisions, with atomic displacements representing typical point defects [70]. 46
4.19 A Monte Carlo simulation was conducted to model the trajectory and defects resulting from a silicon atom knocked out with an initial energy of 50 keV. This initial energy is equivalent to the energy transfer of a 1 MeV neutron to the primary knock-on atom [72]. . . 47
4.20 Displacement damage in silicon and hardness factor of different particles normalized to 95 MeV mb [73]. 48
4.21 The change of the effective doping concentration ΔN_{eff} over time at an annealing temperature of 60 °C is illustrated in [74]. 49
4.22 Change of the leakage current over time at 20 °C to investigate the annealing effect after irradiation with 2×10^{13} n/cm^2 (upper curve) and with (6.4×10^{11} n/cm^2) (lower curve) [75]. 50

4.23 Dependence of the leakage current on the neutron fluence for various detector properties after annealing for 80 minutes at 60 °C [36]. 51
4.24 Normalized energy spectrum of β-particles emitted by the sequential decay of ^{90}Sr and ^{90}Y [77]. 52

5.1 Interface of the General Purpose Device program, which is utilized for the subsequent measurements and operates on a Raspberry Pi. . 54
5.2 The probe station in the clean room consists of needles, the chuck positioned at the bottom, the diode measurement setup in the middle, and the observation system located on top. 56
5.3 Diagram of the bias box designed to shield the measurement setup from over voltage, utilizing four series capacitors C_C for isolation [38]. 57
5.4 Scheme of the parallel two-port model [78]. 57
5.5 The top figure shows a sketch of the diode cross-section, while the bottom features a photograph of the top view of a $\overline{\text{P}}$ANDA MVD diode with an active area of approximately 25 mm^2[79]. 58
5.6 Needle-to-chuck connection measurements, with light and electric shielding on the right-hand side and without shielding on the left. . 59
5.7 On the left-hand side, a diode measurement is shown, in which an aluminum block of the same size as the diode is used to make electrical contact with the entire diode area and ensure an evenly distributed contact force by placing it directly on the diode. On the right-hand side, the measurement was conducted using the final setup described below. 60
5.8 In the sketch on the left, the round electrode is shown above the square diode. The electrode consisting of a round surface similar in size to the active area of the diode. A circular hole in the center of the electrode excludes the passivated layer in the middle of the diode surface. This ensures both optimal electrical contact and an even distribution of the contact force. On the right, a photo of the final setup is shown. 60
5.9 The back side (n-side) of the diode is connected using a circular beryllium copper electrode. Simultaneously, a circular needle exerts pressure on the front side (p-side) of the diode. 61
5.10 Accuracy measurement with the standard deviation error of ten measurements with the same diode. In red, the estimated depletion voltages, calculated with a fit (description in Chapter 5.1.2) of every series. 62
5.11 Two excerpts from two series measurements (cross) of the same diode were applied and evaluated with a fit method (lines). 63
5.12 The capacitance as a function of reverse bias voltage measured for a $\overline{\text{P}}$ANDA diode (marked as a cross). Two fitted lines are shown in color, and the dotted line in red indicating the full depletion voltage is marked at the intersection of the lines. 64

5.13 Probe card with bonded sensor and needle setup in the probe station with observation system on the top right. The reverse bias voltage is applied on the bottom left. 65
5.14 4"-Wafer with the $\overline{\text{P}}$ANDA sensors and test structures. 66
5.15 Specifications of the silicon strip sensors [10]. 67
5.16 The schematic illustrates a cross-section of a Si-sensor, with the p-side at the top and the n-side at the bottom [83]. 68
5.17 The p- and n-side of a double-sided silicon strip detector. 69
5.18 Simple schematic representation illustrating the sensor's function, depicted with an impinging minimal ionizing particle [83]. 70
5.19 Capacitance measurement of a $\overline{\text{P}}$ANDA silicon S2 sensor as a function of the increasing reverse bias voltage. 72
5.20 Single-strip capacitance measurement of a $\overline{\text{P}}$ANDA silicon S2 sensor as a function of increasing reverse bias voltage 74
5.21 Current-voltage curve measured for an S2 sensor with increasing reverse bias voltage. 75
5.22 Schematic capacitance of a silicon strip sensor (not to scale) [84]. . . 77
5.23 CV-measurement carried out by CiS for a diode from lot 341772 wafer 15. 79
5.24 CV-measurement carried out at the probe station of the JLU for a diode from lot 341772 wafer 15. 79
5.25 Section of the capacitance measurement of wafer 20 with the mentioned shift at around 80 V for 100 kHz. 81
5.26 Section of the capacitance measurement of wafer 05 showing a jump around the depletion voltage for 100 kHz (see text). 82
5.27 Leakage current vs. reverse-bias voltage measurement of wafer 05 for 100 kHz. 82
5.28 Section of the capacitance measurement against reverse-bias voltage of wafer 19 for 100 kHz. 83
5.29 Leakage current against reverse-bias voltage measurement of wafer 19 for 100 kHz. 84
5.30 Audit of all available sensors after all requirements are passed. . . . 86
5.31 Overview of the averaged full depletion voltage for each measured lot. 87
5.32 Overview of the averaged leakage current at full depletion for each measured lot. 88
5.33 Overview of the averaged capacitance C_b at full depletion for each measured lot. 88
5.34 The irradiation of the diodes for up to 1600 hours with neutrons is depicted in red and orange, while the unirradiated reference diodes are shown in green. The abbreviations "BM," "BL," and "BR" indicate the original positions of the diodes on the wafer. 91

5.35 On the left, the PCB displays pads for back side contacting and bonding wires, while on the right, the PCB features a diode glued, bonded, and soldered with contacts. 92
5.36 Comparison of the measured fluences in red, derived from the change in leakage current with irradiation and the calculated fluences in blue, from the activity of the neutron source. 94
5.37 Capacitance-to-reverse-bias voltage curve for bonded diode number 5 before and after irradiation. 95
5.38 Leakage current of diode # 5 before and after neutron radiation. . . 96
5.39 Gaussian beam distribution of the proton beam, with the diode dimensions at the center, similar to Beam Time I. The distribution has been calculated based on the beam geometry previously determined by MIT. 97
5.40 Gaussian beam distribution of the proton beam, with the diode dimensions at the center, similar to Beam Time II. The distribution has been calculated based on the beam geometry previously determined by MIT. 98
5.41 Diodes on PCBs are situated in the alignment laser system at MIT, accompanied by an unexposed radiographic dosimeter film on the left and an exposed radiographic dosimeter film on the right. 99
5.42 Leakage current for diodes after irradiation with different proton fluences at MIT; for comparability, the equivalent neutron fluence for 1 MeV neutrons was calculated and plotted. 100
5.43 Measured and calculated change of the leakage current at full depletion to the experienced equivalent neutron fluence. 101
5.44 Comparison of the measured and calculated changes in the full depletion voltage of silicon test structures after irradiation with protons at MIT, converted into 1 MeV equivalent neutron fluence. . 104
5.45 Leakage current versus reverse bias voltage for an unirradiated silicon diode in green, a proton-irradiated one in blue, and one irradiated and thermally annealed in red. 106

6.1 AmbaSat-1 femto-satellite [93]. 109
6.2 Transimpedance amplifier circuit [95]. 110
6.3 PCB of the first iteration dosimeter without attached $\overline{\text{P}}$ANDA-diode. 112
6.4 Signal for R_F=1 MΩ 113
6.5 Signal for R_F=10 MΩ 113
6.6 Histogrammed measurement of ^{90}Sr for R_F = 1 MΩ and 10 MΩ. . . . 114
6.7 Histogrammed measurement of ^{90}Sr for different reverse bias voltages. 115
6.8 Image of the 2nd Iteration Dosimeter with the $\overline{\text{P}}$ANDA Diode. . . . 116
6.9 Circut of the peak-detect stage. 117
6.10 ^{90}Sr-signal after amplification stage one in yellow and three in blue. 118
6.11 ^{90}Sr-signal after amplification stage three in blue and after peak detection in yellow. 118

6.12 Distribution of the deposited energy in the dosimeter due to irradiation with ^{90}Sr. 121
6.13 In blue, the data points from the Yttrium measurement, and in orange, the linear fit. 122
6.14 Dosimeter integrated with the AmbaSat hardware and the $\overline{\text{P}}$ANDA diode. 124
6.15 Third iteration voltage amplifier stage. 124
6.16 The capacitance measurement against the reverse bias voltage of the 50 V $\overline{\text{P}}$ANDA diode. 125
6.17 ^{90}Sr-signal after amplification stage two in yellow. 126
6.18 ^{90}Sr-signal after Peak-Detection stage in yellow. 126
6.19 Bonded diodes, without glob top (left), with glob top and sputter coating (both in the middle), and with glob top and paint coating (right). 127
6.20 Leakage current against reverse bias voltage of a painted diode with illumination in red and without illumination in blue. 127

7.1 Sensor bonding pads for p- and n-side [10]. 131
7.2 S3 sensor connected to the reverse-bias voltage pads and the 64 readout channels of the ToASt Testboard. 132
7.3 Leakage current to bias voltage for a S4 sensor bonded to a ToASt-Board in different configurations. 133
7.4 Capacitance measurement of a single n-side strip against the entire p-side of an S2 sensor. 134
7.5 Capacitance measurement of a single p-side strip against the entire n-side of an S2 sensor. 135
7.6 Distribution of ^{90}Sr-events on a double-sided $\overline{\text{P}}$ANDA S4 strip sensor, readout from a ToASt chip, for each of the 64 channels. 136
7.7 Photograph showing the sensor-front-end assembly with 64 wire-bonded strips of an S4 sensor and the placement of the ToASt-FE on the PCB. 137
7.8 Dual-threshold method employed on the ToASt Chip [102]. 137
7.9 ToT distribution of a single sensor channel. 138
7.10 Data acquisition architecture of the PANDA-MVD detector [104]. . 139
7.11 MVD prototype setup from the COSY08 beam time, mounted on top of a tripod in COSY's TOF Hall. 140
7.12 Leading and trailing edge times for a raw beam time data set with 6.25 ns per time step. 142
7.13 Hit channels of T01/02 for a raw beam time data set. 142
7.14 Schematic representation of a cluster in a silicon strip sensor [108]. . 143
7.15 Drift velocity of electrons and holes versus electric field in Silicon [47].144
7.16 Strips per cluster multiplicity for different signal time intervals within an event. 146

7.17 Strips per cluster multiplicity for different signal time intervals within an event. 147
7.18 Correlation of deposited energy with different signal time intervals within an event of 2 clock cycles on the left and 7 on the right for the same measurement. 149
7.19 Hit cluster channels of T01/02 for 7 clock cycles leding edge difference. 150
7.20 Hit cluster channels of T01/02 for 2 clock cycles leding edge difference. 151
7.21 Measurement with the MVD prototype using a proton beam at COSY, with T01 (a) and T02 (b), based on unclustered raw data. . . 153
7.22 MVD prototype measurements with a proton beam at COSY using T01 (a) and T02 (b) for a randomly chosen channel, based on unclustered raw data. 154
7.23 Summed ToT of event-associated strips, determining total ToT per event, from COSY beam for all T02 Channels (a) and a randomly chosen T02 channel (b). 155
7.24 Deposited energy for both sensors at COSY Beam Time II for coincident events. 156
7.25 Correlation of the energy deposit for both sensors at COSY II Beam Time. 157
7.26 Measurement setup for the third COSY beam time conducted in the TOF Hall at FZ Jülich. 158
7.27 Sketch of the sensor rotation and strip configuration to the beam direction. 159
7.28 Multiplicity with a rotation angle of the sensors relative to the proton beam set to 0 (a) and 60 degrees (b). 159
7.29 Aggregated multiplicity of all clusters recorded on both detectors during a COSY measurement. 161
7.30 Charge deposition of the COSY beam in T01 for three different angles of beam incidence with respect to the sensor surface. 162
7.31 Energy deposit of COSY protons in T02 for three different angles of beam incidence with respect to the sensor surface. 163
7.32 Correlation of the deposited energy in both sensors during COSY Beam Time III, synchronized with events caused by incident protons. 164
7.33 Measurement and fit of the deposited energy for T01 at COSY Beam Time III for coincident events. 165
7.34 Measurement and fit of the deposited energy for T02 at COSY Beam Time III for coincident events. 166
7.35 The variation in leakage current for both sensors during Beam Time III. 167
7.36 Temperature of the COSY Beam Time III setup at the beginning of and at the end of the beam time. 168
7.37 Comparison of measurements with the same ToASt and COSY settings at Beam time II (red) and III (blue). 169

7.38 COSY proton beam with a variation of the discharge current for T01 for the measurement in red. 170
7.39 COSY beam time measurements for two different global energy thresholds. 171
7.40 COSY beam time measurements for two different global time thresholds. 172
7.41 COSY beam time measurements for two different calibration settings for T01 and T02. 173
7.42 Setup of the MVD-Prototype in the climate chamber with a ^{90}Sr-Source. 175
7.43 T01 and T02 event rate for different temperatures and positions of the ^{90}Sr-Source. 177
7.44 Clustered events for T01 with a ^{90}Sr-Source at different temperatures. 178
7.45 Clustered events for T02 with a ^{90}Sr-Source at different temperatures. 178
7.46 Clustered events for channel 42 of T01 with a ^{90}Sr-Source at different temperatures. 179
7.47 Clustered events for channel 42 of T02 with a ^{90}Sr-Source at different temperatures. 180
7.48 Raw events for T02 with a ^{90}Sr-Source at different temperatures. . . 180
7.49 Mean deposited energy for clustered MVD-Prototype ^{90}Sr measurements at different temperatures. 181
7.50 Most probable deposited energy value for clustered MVD-Prototype ^{90}Sr measurements at different temperatures. 182
7.51 Leakage current during ^{90}Sr measurements of the MVD-Prototype at different temperatures. 183
7.52 Behavior of the leakage current during the 35 °C measurement with ^{90}Sr. 184
7.53 Multiplicities for the ^{90}Sr measurements at 16°C with different signal time intervals within an event, given in clock cycles derived from the 6.25 ns clock of the ToASt 185
7.54 Two setups of the sync. measurements with different source positions. 185
7.55 Correlation of the deposited energy for T01 behind T02 and the ^{90}Sr-source. 186
7.56 Correlation of the deposited energy for T02 behind T01 and the ^{90}Sr-source. 187
7.57 Deposited energy for the sensors with different positions corresponding to the ^{90}Sr-Source for coincident events. 188
7.58 Simulated energy spectrum of electrons from a ^{90}Sr-source that deposit a signal in a 300 μm silicon detector without being stopped [23]. 189
7.59 ^{90}Sr measurement of T01 behind T02 and the source at 16°C with a Langau fit and Gaussian fit. 190

B.1 Polysilicon resistor measurement of an S2 sensor. The impedance and the phase angle is measured against the frequency. 222
B.2 Coupling capacitance for one strip of the S2 sensor in dependency of the frequency. 223
B.3 S2 sensor interstrip capacitance for on strip and its four next neighbors.223

C.1 Raw events for T01 with a ^{90}Sr-Source at different temperatures. . . 224
C.2 Raw events for channel 42 of T01 with a ^{90}Sr-Source at different temperatures. 225
C.3 Raw events for channel 42 of T02 with a ^{90}Sr-Source at different temperatures. 225
C.4 Multiplicity of T01/T02 with a ^{90}Sr-Source at different temperatures .226

D.1 Circuit diagram of the first dosimeter iteration in Chapter 6.2 227
D.2 Circut diagram of the second dosimeter iteration in Chapter 6.3 . . 228
D.3 Circuit diagram of the Peak-Detection of iteration two and three. . . 228
D.4 Circut diagram of the third dosimeter iteration in Chapter 6.4 . . . 229
D.5 COSY08 ptoton-beam measurement of the MVD-prototype T01 für every channel. 230
D.6 COSY08 ptoton-beam measurement of the MVD-prototype T02 für every channel. 231

Appendix A

Detailed Tables of Series Measurements

Lot 341776 Measurements		
Parameter	**Average Value**	**Maximum Deviation**
$V_{Depletion}$ [V]	102.824	18.274
I_{leak} [A]	$4.096 \cdot 10^{-7}$	$3.307 \cdot 10^{-6}$
Capacitance [F]	$1.159 \cdot 10^{-11}$	$4.313 \cdot 10^{-13}$
Wafer Issues		
Wafer No.	**Problem**	**Comment**
03	Breakdown at 190 V	-
16	$I_{leak} = 3.716 \cdot 10^{-6}$ A	-
18	$I_{leak} = 6.510 \cdot 10^{-6}$ A	Scratch
CiS Data for lot 341776		
Parameter	**Average Value**	**Maximum Deviation**
$V_{Depletion}$ [V]	91.88	16.12

Table A.1: Result of series measurements for lot 341776.

Lot 352156 Measurements		
Parameter	**Average Value**	**Maximum Deviation**
$V_{Depletion}$ [V]	102.714	7.320
I_{leak} [A]	$3.550 \cdot 10^{-8}$	$4.501 \cdot 10^{-8}$
Capacitance [F]	$1.160 \cdot 10^{-11}$	$3.157 \cdot 10^{-13}$
Wafer Issues		
Wafer No.	**Problem**	**Comment**
20	Shift at 80 V	Under investigation
CiS Data for lot 352156		
Parameter	**Average Value**	**Maximum Deviation**
$V_{Depletion}$ [V]	102.28	21.728

Table A.2: Result of series measurements for lot 352156.

Lot 352155 Measurements		
Parameter	**Average Value**	**Maximum Deviation**
$V_{Depletion}$ [V]	107.791	17.079
I_{leak} [A]	$3.910 \cdot 10^{-8}$	$6.931 \cdot 10^{-8}$
Capacitance [F]	$1.181 \cdot 10^{-11}$	$2.609 \cdot 10^{-13}$
Wafer Issues		
Wafer No.	**Problem**	**Comment**
05	Breakdown at 100 V	Under investigation
CiS Data for lot 352155		
Parameter	**Average Value**	**Maximum Deviation**
$V_{Depletion}$ [V]	98.08	21.92

Table A.3: Result of series measurements for lot 352155.

Lot 352154 Measurements		
Parameter	**Average Value**	**Maximum Deviation**
$V_{Depletion}$ [V]	108.790	-
I_{leak} [A]	$5.397 \cdot 10^{-8}$	-
Capacitance [F]	$1.183 \cdot 10^{-11}$	-
Wafer Issues		
Wafer No.	**Problem**	**Comment**
-	-	-
CiS Data for lot 352154		
Parameter	**Average Value**	**Maximum Deviation**
$V_{Depletion}$ [V]	104	-

Table A.4: Result of series measurements for lot 352154.

Lot 342563 Measurements		
Parameter	**Average Value**	**Maximum Deviation**
$V_{Depletion}$ [V]	105.783	6.343
I_{leak} [A]	$4.110 \cdot 10^{-8}$	$4.415 \cdot 10^{-8}$
Capacitance [F]	$1.141 \cdot 10^{-11}$	$8.040 \cdot 10^{-14}$
Wafer Issues		
Wafer No.	**Problem**	**Comment**
17	Breakdown at 180 V	Under investigation
CiS Data for lot 342563		
Parameter	**Average Value**	**Maximum Deviation**
$V_{Depletion}$ [V]	96.28	26.28

Table A.5: Result of serial measurements for lot 342563.

Lot 352157 Measurements		
Parameter	**Average Value**	**Maximum Deviation**
$V_{Depletion}$ [V]	104.966	6.664
I_{leak} [A]	$3.255 \cdot 10^{-8}$	$1.726 \cdot 10^{-8}$
Capacitance [F]	$1.173 \cdot 10^{-11}$	$2.112 \cdot 10^{-13}$
Wafer Issues		
Wafer No.	**Problem**	**Comment**
-	-	-
CiS Data for lot 352157		
Parameter	**Average Value**	**Maximum Deviation**
$V_{Depletion}$ [V]	101.523	22.478

Table A.6: Result of series measurements for lot 352157.

Lot 341775 Measurements		
Parameter	**Average Value**	**Maximum Deviation**
$V_{Depletion}$ [V]	112.835	2.695
I_{leak} [A]	$4.705 \cdot 10^{-8}$	$6.180 \cdot 10^{-9}$
Capacitance [F]	$1.150 \cdot 10^{-8}$	$4.533 \cdot 10^{-14}$
Wafer Issues		
Wafer No.	**Problem**	**Comment**
-	-	-
CiS Data for lot 341775		
Parameter	**Average Value**	**Maximum Deviation**
$V_{Depletion}$ [V]	95.08	14.08

Table A.7: Result of serial measurements for lot 341775.

Lot 341774 Measurements		
Parameter	**Average Value**	**Maximum Deviation**
$V_{Depletion}$ [V]	104.972	9.577
I_{leak} [A]	$5.237 \cdot 10^{-8}$	$3.176 \cdot 10^{-8}$
Capacitance [F]	$1.160 \cdot 10^{-11}$	$2.882 \cdot 10^{-13}$
Wafer Issues		
Wafer No.	**Problem**	**Comment**
-	-	-
CiS Data for lot 341774		
Parameter	**Average Value**	**Maximum Deviation**
$V_{Depletion}$ [V]	91.88	16.12

Table A.8: Result of serial measurements for lot 341774.

Lot 341773 Measurements		
Parameter	**Average Value**	**Maximum Deviation**
$V_{Depletion}$ [V]	102.909	7.231
I_{leak} [A]	$5.838 \cdot 10^{-8}$	$2.742 \cdot 10^{-8}$
Capacitance [F]	$1.170 \cdot 10^{-11}$	$3.439 \cdot 10^{-13}$
Wafer Issues		
Wafer No.	**Problem**	**Comment**
-	-	-
CiS Data for lot 341773		
Parameter	**Average Value**	**Maximum Deviation**
$V_{Depletion}$ [V]	94.818	9.818

Table A.9: Result of serial measurements for lot 341773.

Lot 341772 Measurements		
Parameter	**Average Value**	**Maximum Deviation**
$V_{Depletion}$ [V]	109.386	4.794
I_{leak} [A]	$4.258 \cdot 10^{-8}$	$3.942 \cdot 10^{-8}$
Capacitance [F]	$1.166 \cdot 10^{-11}$	$6.262 \cdot 10^{-13}$
Wafer Issues		
Wafer No.	**Problem**	**Comment**
19	Breakdown 170 V	Under investigation
CiS Data for lot 341772		
Parameter	**Average Value**	**Maximum Deviation**
$V_{Depletion}$ [V]	101.927	39.083

Table A.10: Result of serial measurements for lot 341772.

Lot 413017 Measurements		
Parameter	**Average Value**	**Maximum Deviation**
$V_{Depletion}$ [V]	110.559	24.019
I_{leak} [A]	$4.970 \cdot 10^{-8}$	$1.250 \cdot 10^{-8}$
Capacitance [F]	$1.250 \cdot 10^{-11}$	$1.140 \cdot 10^{-12}$
Wafer Issues		
Wafer No.	**Problem**	**Comment**
-	-	-
CiS Data for lot 413017		
$V_{Depletion}$ [V]	101.0	9.0

Table A.11: Result of series measurements for lot 413017.

Lot 413018 Measurements		
Parameter	**Average Value**	**Maximum Deviation**
$V_{Depletion}$ [V]	106.058	21.518
I_{leak} [A]	$5.060 \cdot 10^{-8}$	$2.280 \cdot 10^{-8}$
Capacitance [F]	$1.100 \cdot 10^{-11}$	$1.166 \cdot 10^{-12}$
Wafer Issues		
Wafer No.	**Problem**	**Comment**
-	-	-
CiS Data for lot 413018		
$V_{Depletion}$ [V]	98.333	21.667

Table A.12: Result of series measurements for lot 413018.

Lot 413019 Measurements		
Parameter	**Average Value**	**Maximum Deviation**
$V_{Depletion}$ [V]	106.891	24.894
I_{leak} [A]	$4.673 \cdot 10^{-8}$	$2.509 \cdot 10^{-8}$
Capacitance [F]	$1.270 \cdot 10^{-11}$	$3.053 \cdot 10^{-12}$
Wafer Issues		
Wafer No.	**Problem**	**Comment**
-	-	-
CiS Data for lot 413019		
$V_{Depletion}$ [V]	92.0	22.0

Table A.13: Result of series measurements for lot 413019.

Lot 410535 Measurements		
Parameter	**Average Value**	**Maximum Deviation**
$V_{Depletion}$ [V]	113.613	-
I_{leak} [A]	$2.189 \cdot 10^{-8}$	-
Capacitance [F]	$1.189 \cdot 10^{-11}$	-
Wafer Issues		
Wafer No.	**Problem**	**Comment**
-	-	-
CiS Data for lot 410535		
$V_{Depletion}$ [V]	86.0	-

Table A.14: Result of series measurements for lot 410535, which includes only one wafer.

Lot 410536 Measurements		
Parameter	**Average Value**	**Maximum Deviation**
$V_{Depletion}$ [V] I_{leak} [A] Capacitance [F]	97.608 $7.280 \cdot 10^{-8}$ $1.210 \cdot 10^{-11}$	16.108 $2.760 \cdot 10^{-8}$ $1.070 \cdot 10^{-12}$
Wafer Issues		
Wafer No.	**Problem**	**Comment**
-	-	-
CiS Data for lot 410536		
$V_{Depletion}$ [V]	84.0	15.0

Table A.15: Result of series measurements for lot 410536.

Lot 410537 Measurements		
Parameter	**Average Value**	**Maximum Deviation**
$V_{Depletion}$ [V] I_{leak} [A] Capacitance [F]	97.639 $7.610 \cdot 10^{-8}$ $1.200 \cdot 10^{-11}$	4.133 $1.699 \cdot 10^{-8}$ $1.145 \cdot 10^{-12}$
Wafer Issues		
Wafer No.	**Problem**	**Comment**
-	-	-
CiS Data for lot 410537		
$V_{Depletion}$ [V]	100.14	1.14

Table A.16: Result of series measurements for lot 410537.

Appendix B

S2 Sensor Properties

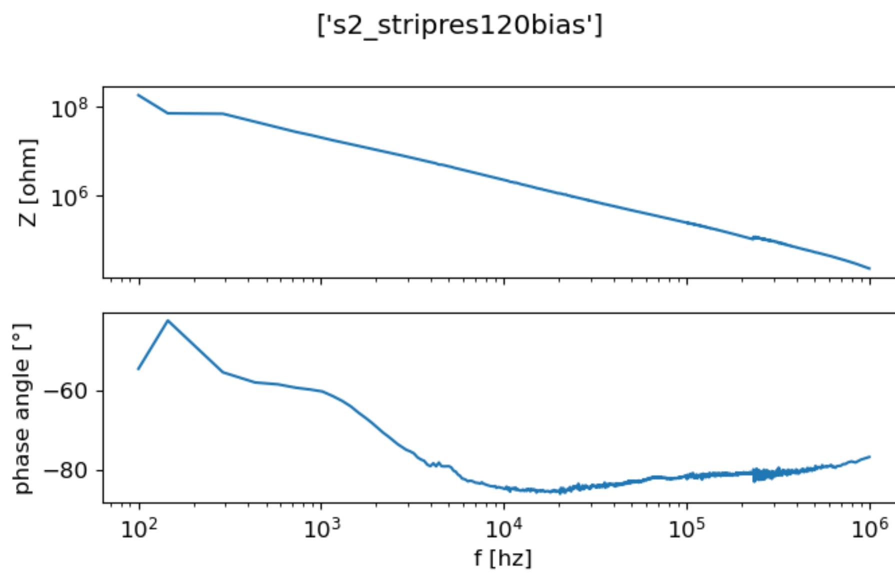

Figure B.1: Polysilicon resistor measurement of an S2 sensor. The impedance and the phase angle is measured against the frequency.

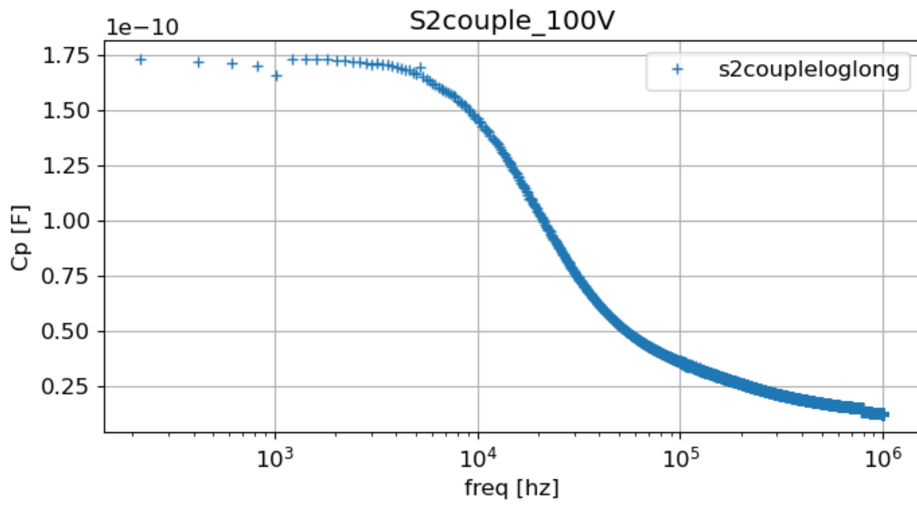

Figure B.2: Coupling capacitance for one strip of the S2 sensor in dependency of the frequency.

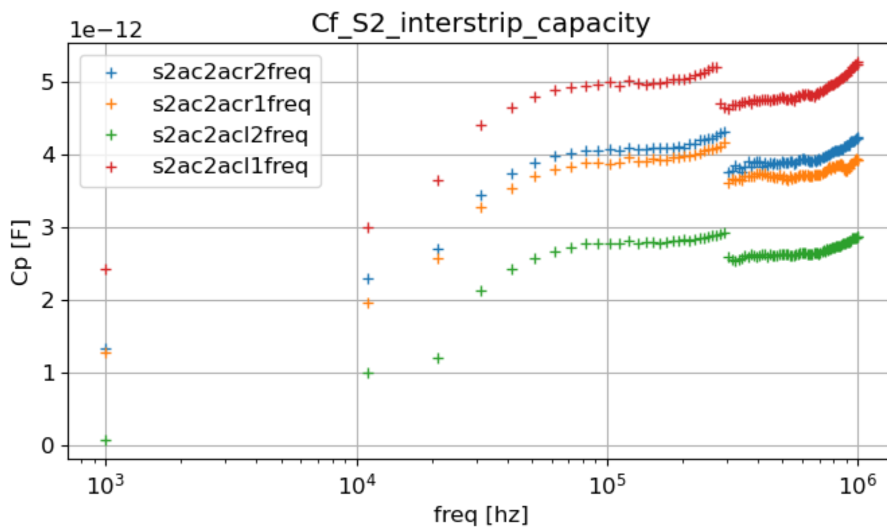

Figure B.3: S2 sensor interstrip capacitance for on strip and its four next neighbors.

Appendix C

Additional Plots

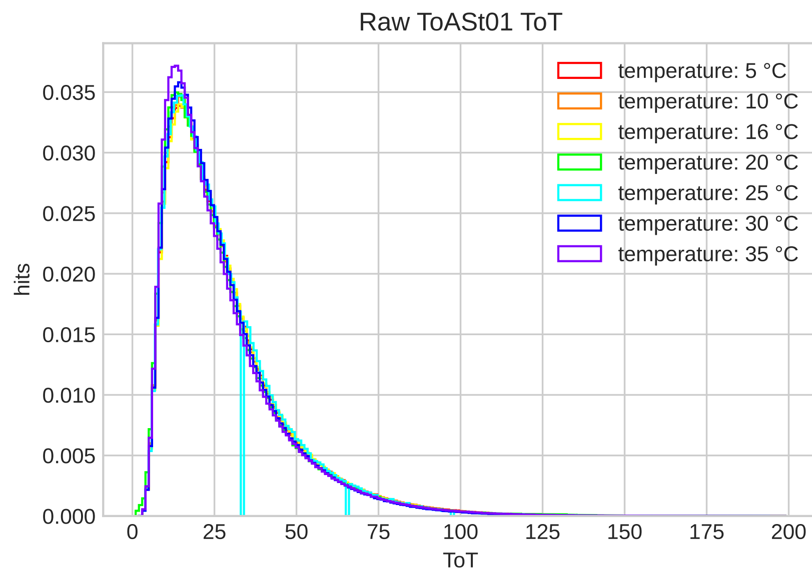

Figure C.1: Raw events for T01 with a ^{90}Sr-Source at different temperatures.

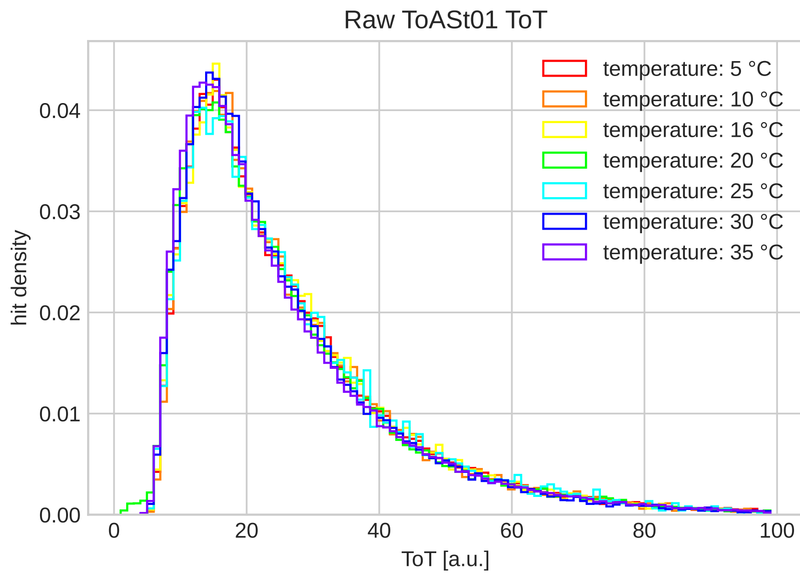

Figure C.2: Raw events for channel 42 of T01 with a ^{90}Sr-Source at different temperatures.

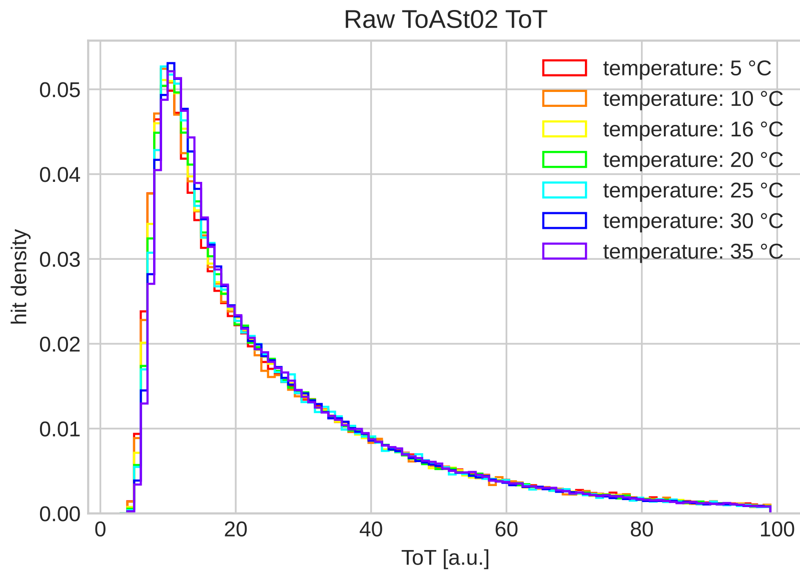

Figure C.3: Raw events for channel 42 of T02 with a ^{90}Sr-Source at different temperatures.

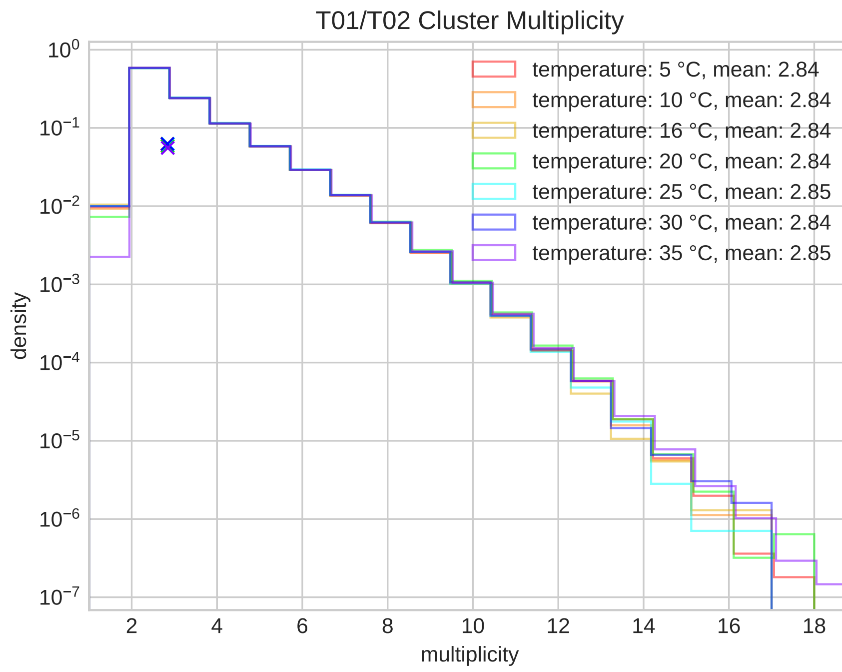

Figure C.4: Multiplicity of T01/T02 with a ^{90}Sr-Source at different temperatures .

Appendix D

Circuit Diagrams

Figure D.1: Circuit diagram of the first dosimeter iteration in Chapter 6.2

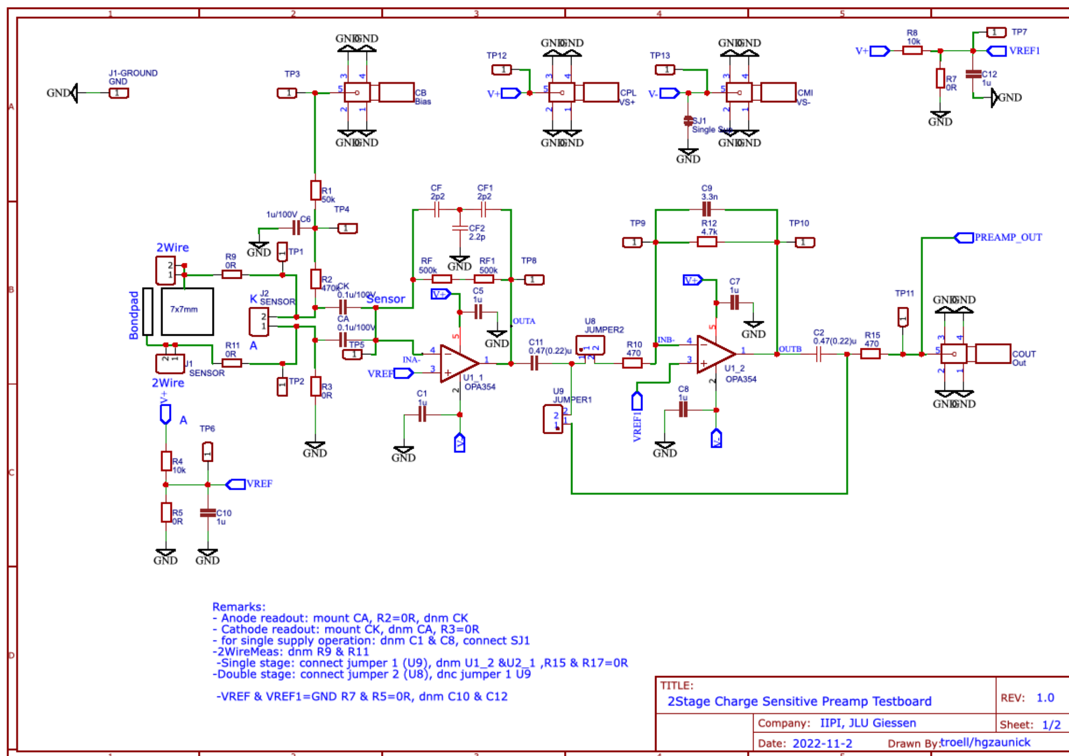

Figure D.2: Circut diagram of the second dosimeter iteration in Chapter 6.3

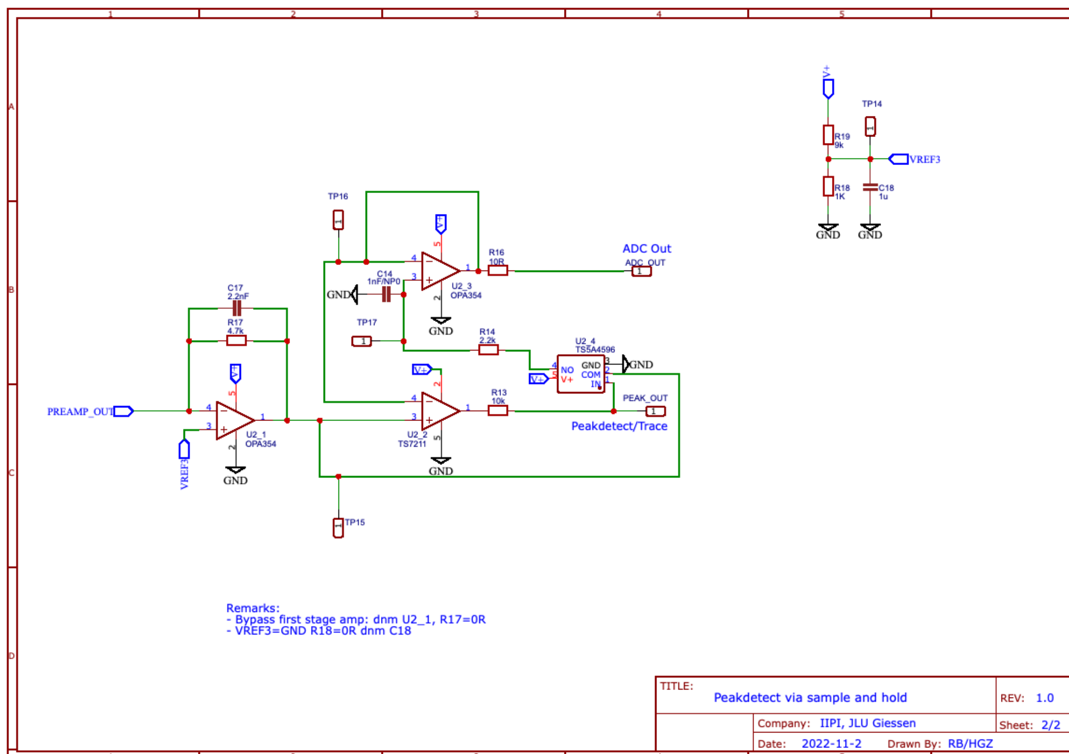

Figure D.3: Circuit diagram of the Peak-Detection of iteration two and three.

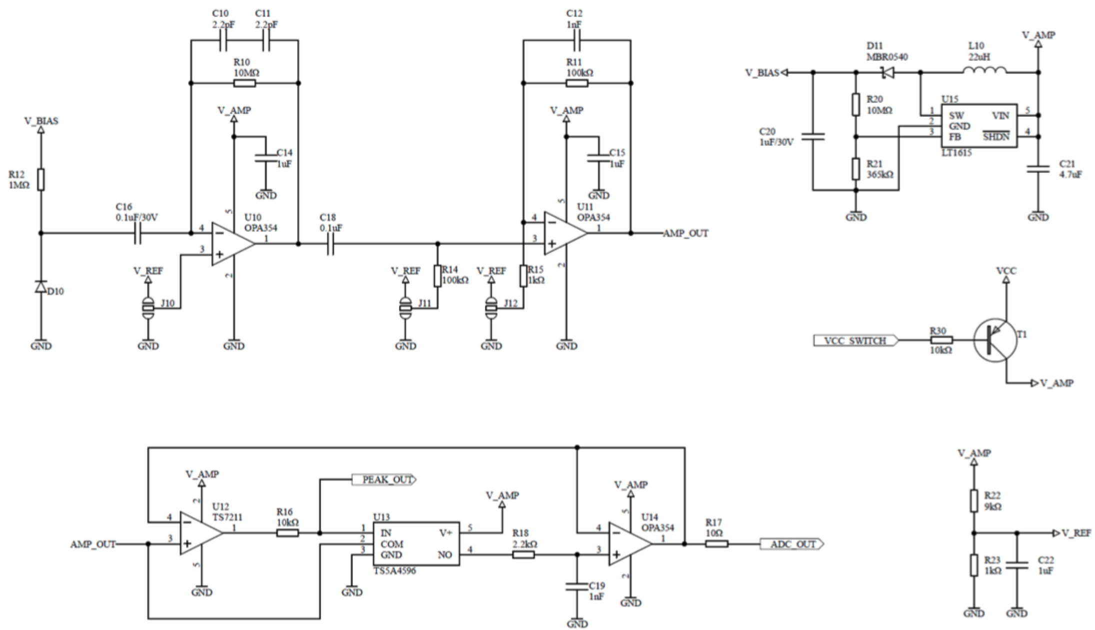

Figure D.4: Circut diagram of the third dosimeter iteration in Chapter 6.4

Figure D.5: COSY08 ptoton-beam measurement of the MVD-prototype T01 für every channel.

Figure D.6: COSY08 ptoton-beam measurement of the MVD-prototype T02 für every channel.

Acknowledgements

I would like to thank Prof. Dr. Kai-Thomas Brinkmann for welcoming me into his research group and for the exciting research topic I had the opportunity to work on. I am especially grateful for his continuous support and trust throughout my years of research.

Additionally, I'd like to extend my thanks to Prof. Dr. Markus Thoma for welcoming me into his research group during my bachelor's and master's studies, and for his support throughout my PhD.

I want to express special gratitude to Dr. Roman Bergert, who has been with me throughout my entire academic journey, offering unwavering support and guidance. Your exemplary approach to research and teaching is truly inspiring.

I would like to extend my gratitude to Dr. Hans Georg Zaunick for his invaluable support and for generously sharing his knowledge.

I am deeply grateful to my fellow students, Ather Ahmad and Ferdinand Ziese, for their support not only within the university but also outside of it.

I would like to thank the whole AG Brinkmann, who I could rely on and who had my back the whole time.

I am very grateful to my friends Tobias, Leon, Carmen, Sascha, Erwin and many others whose encouragement and friendship were invaluable during this trip.

Finally, I would like to express my gratitude to my family - Petra, Joachim and Marc. Without your unwavering love and support, this journey would not have been possible. I would like to express my gratitude to Beatrice. Your love and patience have accompanied me throughout my studies, and I am endlessly grateful for your presence in my life. I am also immensely thankful to my grandparents - Adelheid, Gustav, Inge, and Herbert - for their love and encouragement.

Selbstständigkeitserklärung

Ich erkläre: Ich habe die vorgelegte Dissertation selbstständig und ohne unerlaubte fremde Hilfe und nur mit den Hilfen angefertigt, die ich in der Dissertation angegeben habe. Alle Textstellen, die wörtlich oder sinngemäß aus veröffentlichten Schriften entnommen sind, und alle Angaben, die auf mündlichen Auskünften beruhen, sind als solche kenntlich gemacht. Ich stimme einer evtl. Überprüfung meiner Dissertation durch eine Antiplagiat-Software zu. Bei den von mir durchgeführten und in der Dissertation erwähnten Untersuchungen habe ich die Grundsätze guter wissenschaftlicher Praxis, wie sie in der „Satzung der Justus-Liebig-Universität Gießen zur Sicherung guter wissenschaftlicher Praxis" niedergelegt sind, eingehalten.

____________________	____________________
Datum	Unterschrift